UNIVERSIDADE FEDERAL DE PERNAMBUCO – UFPE
CENTRO DE TECNOLOGIA E GEOCIÊNCIAS
DEPARTAMENTO DE OCEANOGRAFIA
PROGRAMA DE PÓS GRADUAÇÃO EM OCEANOGRAFIA

HUMBERTO LÁZARO VARONA GONZÁLEZ

CIRCULATION, TRANSPORT AND DISPERSION OF HYDROCARBON PLUMES IN THE NORTH BRAZILIAN EQUATORIAL BROADBAND

RECIFE

2018

HUMBERTO LÁZARO VARONA GONZÁLEZ

CIRCULATION, TRANSPORT AND DISPERSION OF HYDROCARBON PLUMES IN THE NORTH BRAZILIAN EQUATORIAL BROADBAND

Tese apresentada ao Programa de Pós-graduação em Oceanografia da Universidade Federal de Pernambuco como requisito parcial para obtenção do título de Doutor em Oceanografia.

Área de concentração: Oceanografia Abiótica

Supervisor: Prof. Dr. Moacyr Cunha de Araújo Filho
Co-supervisor: Profa. Dra. Doris Regina Aires Veleda

RECIFE
2018

Catalogação na fonte
Bibliotecária Margareth Malta, CRB-4 / 1198

V323c Varona González, Humberto Lázaro.
Circulation, transport and dispersion of hydrocarbon plumes in the north Brazilian equatorial broadband / Humberto Lázaro Varona González. - 2018.
160 folhas, il., gráfs., tabs.

Orientador: Prof. Dr. Moacyr Cunha de Araújo Filho.
Coorientadora: Profa. Dra. Doris Regina Aires Veleda.

Tese (Doutorado) – Universidade Federal de Pernambuco. CTG. Programa de Pós-Graduação em Oceanografia, 2018.
Inclui Referências, Apêndice e Anexo.
Texto em Inglês.

1. Oceanografia. 2. Modelo ROMS. 3. Modelo GAS_DOCEAN. 4. Pluma do Rio Amazonas. 5. Vazamentos de óleo e gás. 6. Plataforma continental do Brasil. I. Araújo Filho, Moacyr Cunha de. (Orientador). II. Veleda, Doris Regina Aires. (Coorientadora). III. Título.

UFPE

551.46 CDD (22. ed.) BCTG/2018-283

HUMBERTO LÁZARO VARONA GONZÁLEZ

CIRCULATION, TRANSPORT AND DISPERSION OF HYDROCARBON PLUMES IN THE NORTH BRAZILIAN EQUATORIAL BROADBAND

Tese apresentada ao Programa de Pós-graduação em Oceanografia da Universidade Federal de Pernambuco como requisito parcial para obtenção do título de Doutor em Oceanografia.

Área de concentração: Oceanografia Abiótica

Trabalho aprovado. Recife, 16 de maio de 2018:

Prof. Dr. Moacyr Cunha de Araújo Filho
Orientador/Presidente/Titular Interno – PPGO/UFPE

Dra. Carmen Medeiros Limongi
Titular Interna – PPGO/UFPE

Dr. Alex Costa da Silva
Titular Interno – PPGO/UFPE

Dr. Carlos Esteban Delgado Noriega
Titular Externo – CEERMA/UFPE

Dr. Leonardo Vieira Bruto da Costa
Titular Externo – DOCEAN/UFPE

RECIFE
2018

This Ph. D. thesis is dedicated to:
My beloved parents Ismael Humberto (In Memoriam) and Norka
and to my beloved children Laysun, Humberto Vinlay and Ismael David

Acknowledgements

- To God for his eternal help and for allowing me to finish this thesis.
- To my supervisor Dr. Moacyr Araújo, for the orientation of this work, for his trust, his help, support and friendship.
- To Dra. Doris Veleda for her good advice, support, supervision and friendship.
- To Dr. Marcus Silva for his constant help, support, supervision and for sharing his knowledge.
- To Claudia Von and Fabiana Leite for his constant help.
- To Marcio das Chagas for his support and help.
- To my mother and children for their love, their patience, their collaboration and support in all stages of this work.
- To Ramón Raudel for providing an initial momentum to this Ph. D.
- To William Artiles for his constant help.
- To Human Resources Program (PRH-47) of the Agência Nacional do Petróleo (ANP) for the concession of PhD scholarships, Financiadora de Estudos e Projetos (FINEP) and Ministério da Ciência, Tecnologia, Inovações e Comunicações (MCTI).
- To Centro de Estudos e Ensaios em Risco e Modelagem Ambiental (CEERMA) and Departamento de Oceanografia (DOCEAN)
- To my friends and my colleagues of CEERMA and DOCEAN: Carlos, Severino, Aubains, Pedro, Christine, Marcio Cintra, Marcio das Chagas, Erasmo, Marisa and Ramilla: for your friendship, help and support.
- To Archie, Macuto and Tan for your constant support.
- To Guillermo Palacios y Javier González for sharing their knowledge with me.
- To Leticia and Edgar for your help and friendship.
- To all those who contributed to the realization of this thesis.

"The Lord is with me; I will not be afraid.
What can mere mortals do to me?
The Lord is with me; He is my helper.
I look in triumph on my enemies.
It is better to take refuge in the Lord than to trust in humans."
(Holy Bible, Psalm 118, 6-8)

ABSTRACT

This Ph. D. thesis focuses on a study of hydrodynamics and oil/gas blowouts in deep water using the Regional Ocean Model System (ROMS) and GAS_DOCEAN models. The first objective was to analyze the potential impact of the Amazon and Pará Rivers on salinity, temperature and hydrodynamics in the Western Tropical North Atlantic between 60.5°-24°W and 5°S-16°N. The ROMS was used to simulate the ocean hydrodynamics with 0.25° horizontal resolution and 32 vertical levels. The sea surface temperature and salinity and the surface current were compared with Simple Ocean Data Assimilation (SODA) and Surface Currents from Diagnostic. Vertical profiles at 8°N, 38°W and 12°N, 38°W are validated with the Prediction Research Moored Array in the Tropical Atlantic. In the ROMS model two experiments are carried out, one taking into account the discharge of freshwater from the Amazon and Pará rivers and the second, without releasing freshwater into the Atlantic ocean. The results of both simulations are compared determining the changes in temperature, salinity and surface currents produced by the influence of the rivers discharge. The Sea Surface Temperature difference between the simulations with river and no-river was about 2°C. The Sea Surface Salinity difference was about 8 psu in the plume area confined to the littoral, with maximum from August to December and 4 psu in the area of the North Equatorial Countercurrent (NECC). The surface current velocities are stronger in the experiment with river (mainly in the NECC area from September to December) and the strongest, close to the coast, in June to August. The experiment with river causes a phase shift in the zonal currents anticipating the strongest velocities in the second semester of the year in 2 $months$, changing the seasonal cycle. The Mixed Layer Depth and Isothermal Layer Depth (ILD) in the experiment with river is 20 - 50 m shallower over the entire extension of the Amazon plume. The freshwater river discharge perform a fundamental role in the formation of Barrier Layer. The Oceanic Heat Content in the river experiments is smaller than the experiment without rivers, principally as a result of the shifts of the ILD. The second objective focuses on analyzing the behavior of oil/gas plumes from blowouts into deepwater, located at the northern Brazil continental shelf. For this, the result of the hydrodynamics of ROMS model with release freshwater of the Amazon and Pará Rivers into the Atlantic is used. The simulations with the GAS_DOCEAN model were carried out in three points located at 50°W, 5.25°N, 44.5°W, 0.5°N and 42.75°W, 1°S. Previously, the vertical profiles of the temperature and the current speed in these points were validated comparing them with SODA. The time step was adjusted due to the particular oceanographic conditions at each point, in which, the initial velocity tends to zero and the coefficient 0.1 of the original equation was replaced by 0.0250 for 50°W, 5.25°N and 44.5°W, 0.5°N, and 0.0375 for 42.75°W, 1°S. All the plumes behaved as type 3. The seasonal current speed was small from the bottom to the surface, usually not exceeding 0.25 ms^{-1}; the maximum displacement of the plumes from its point of origin was not greater than 1 m. The mean plumes diameter on the surface varied between 54 and 79.7 m and the arrival time to the surface was from 7.25 to 8.05 $hours$.

Keywords: ROMS model. GAS_DOCEAN model. Amazon River plume. Oil/gas blowouts. Brazil continental shelf.

RESUMO

Esta tese de doutorado tem como foco o estudo da hidrodinâmica e dos vazamentos de óleo/gás em águas profundas usando os modelos Regional Ocean Model System (ROMS) e GAS_DOCEAN. O primeiro objetivo foi analisar o impacto potencial dos rios Amazonas e Pará sobre a salinidade, temperatura e hidrodinâmica no Atlântico Norte Tropical Ocidental entre $60.5° - 24° W$ e $5° S - 16° N$. O ROMS foi usado para simular a hidrodinâmica do oceano com resolução horizontal de 0.25° e 32 níveis verticais. A temperatura da superfície do mar, a salinidade da superfície do mar e a corrente superficial foram comparadas com os bancos de dados Simple Ocean Data Assimilation (SODA) e Surface Currents from Diagnostic. Os perfis verticais em $8° N, 38° W$ e $12° N, 38° W$ foram validados com dados das bóias do projeto Prediction Research Moored Array in the Tropical Atlantic. No modelo ROMS, foram realizados dois experimentos, primeiro considera a descarga de água doce dos rios Amazonas e Pará e o segundo, sem considerar o aporte de água doce no oceano Atlântico. Os resultados de ambas simulações foram comparados determinando as mudanças na temperatura, salinidade e correntes de superfície produzidas pela influência da descarga dos rios. A diferença entre as simulações com rios e sem rios na Temperatura da Superfície do Mar foi de cerca de $2° C$, enquanto a diferença da Salinidade da Superfície do Mar foi de cerca de $8\, psu$ na área da pluma confinada à costa, com valores máximos de Agosto a Dezembro e $4\, psu$ na área da Contracorrente Norte Equatorial (NECC). As velocidades de corrente de superfície foram mais fortes no experimento com rios, principalmente na área NECC de Setembro a Dezembro e foram muito mais intensas perto da costa de Junho a Agosto. O experimento com rios provoca um deslocamento de fase nas correntes zonais, antecipando as velocidades mais fortes no segundo semestre do ano aproximidamente em dois meses, alterando o ciclo sazonal. A Profundidade da Camada de Mistura (MLD) e a Profundidade da Camada Isotérmica (ILD) no experimento com rios foram de 20 a $50\, m$ mais rasas sobre toda a extensão da pluma amazônica. A descarga de água doce dos rios desempenha um papel fundamental na formação da Camada de Barreira. O conteúdo de calor oceânico no experimento com rios é menor do que o experimento sem rios, principalmente como resultado dos deslocamentos do ILD. O segundo objetivo concentrou-se na análise do comportamento das plumas produzidas pelos vazamentos de óleo/gás em águas profundas, localizadas na plataforma continental do norte do Brasil. Para isto, utilizou-se o resultado da hidrodinâmica do modelo ROMS com saída de água doce dos rios Amazonas e Pará no Atlântico. As simulações com o modelo GAS_DOCEAN foram realizadas em três pontos localizados em $50° W, 5.25° N$, $44.5° W, 0.5° N$ e $42.75° W, 1° S$. Anteriormente, os perfis verticais da temperatura e da velocidade da corrente nesses pontos foram validados comparando-os com SODA. O intervalo de tempo foi ajustado devido às condições oceanográficas particulares em cada ponto, o coeficiente 0.1 da equação original foi substituído por 0.0250 para $50° W, 5.25° N$ e $44.5° W, 0.5° N$ e 0.0375 para $42.75° W, 1° S$. Todas as plumas comportaram-se como tipo 3. A velocidade de corrente sazonal foi pequena do fundo para a superfície, geralmente não excedendo $0.25\, ms^{-1}$; o deslocamento máximo das plumas de seu ponto de origem não foi maior do que 1 m. O diâmetro médio das plumas na superfície variou de 54 a 79.7 m e o tempo de chegada à superfície foi de 7.25 a 8.05 $horas$.

Palavras-chave: Modelo ROMS. Modelo GAS_DOCEAN. Pluma do Rio Amazonas. Vazamentos de oléo e gâs. Plataforma continental do Brasil.

RESUMEN

Esta tesis de doctorado se enfoca en un estudio de la hidrodinámica y de los escapes de petróleo y gas en aguas profundas usando los modelos Regional Ocean Model System (ROMS) y GAS_DOCEAN. El primer objetivo fue analizar el impacto potencial que ejercen los ríos Amazonas y Pará sobre la salinidad, la temperatura y la hidrodinámica en el Atlántico Tropical Noroccidental entre 60,5°-24°W y 5°S-16°N. El modelo ROMS fue usado para simular la hidrodinámica del océano con resolución horizontal de 0,25° y 32 niveles verticales. La temperatura y la salinidad de la superficial del mar y la corriente superficial validadas comparándolas con las bases de datos Simple Ocean Data Assimilation (SODA) y el modelo Surface Currents from Diagnostic. Los perfiles verticales en 8°N, 38°W y 12°N, 38°W son validados com los datos de las boyas del proyecto Prediction Research Moored Array in the Tropical Atlantic. En el modelo ROMS fueron realizados dos experimentos, uno que tiene en cuenta la descarga de agua dulce de los ríos en el océano Atlántico y otro que no considera la descarga de los ríos. Los resultados de ambas simulaciones son comparadas determinando las variaciones en la temperatura, la salinidad y las corrientes marinas producida por las descarga de los ríos. Las diferencias entre las simulaciones con ríos y sin ríos en la temperatura de la superficie del mar fue cerca de 2°C, mientras que la diferencia de la salinidad de la superficie del mar fue cerca de 8 psu en el área de la pluma confinada a la costa, con valores máximos de Agosto a Diciembre y 4 psu en el área de la Contracorriente Norte Ecuatorial norte (NECC). La corriente superficial es más fuerte cuando están presentes los ríos, principalmente en el área de la NECC de Septiembre a Diciembre y son más fuertes cerca de la costa de Junio a Agosto. El experimento con ríos provoca un desfase en las corrientes zonales, anticipando las velocidades más grande en el segundo semestre del año en $2\,meses$, alterando el ciclo estacional. La Profundidad de la Capa de Mezcla (MLD) y la Profundidad de la Capa Isotérmica (ILD) en el experimento con ríos son de 20 a $50\,m$ más superficiales sobre toda la extensión de la pluma amazónica. La descarga de agua dulce de los ríos desempeña un papel fundamental en la formación de la Capa de Barrera. El Contenido de Calor Oceánico en el experimento con ríos es menor que en el experimento sin ríos, principalmente como resultado de los desplazamientos de la ILD. El segundo objetivo se concentra en el análisis del comportamiento de las plumas producidas por los derrames de petróleo/gas en aguas profundas, localizadas en la plataforma continental norte de Brasil. Para esto, se utilizaron los resultados de la hidrodinámica del modelo ROMS con la salida de agua dulce de los ríos Amazonas y Pará hacia el Atlántico. Las simulaciones con el modelo GAS_DOCEAN fueron realizadas en tres puntos ubicados en 50°W, 5,25°N, 44,5°W, 0,5°N y 42,75°W, 1°S. Previamente fueron validados los perfiles verticales de la temperatura y la velocidad de la corriente en esos puntos, comparándolos con SODA. El intervalo de tiempo fue ajustado debido a las condiciones oceanográficas particulares en cada punto, el coeficiente 0,1 de la ecuación original fue sustituido por 0,0250 para 50°W, 5,25°N y 44,5°W, 0,5°N y por 0,0375 para 42,75°W, 1°S. El comportamiento de todas las plumas fue de tipo 3, La velocidad de la corriente estacional fue pequeña desde el fondo hasta la superficie, generalmente no excedió de 0,25 ms^{-1}; el desplazamiento máximo de las plumas respecto a su origen no fue mayor que 1 m. El diámetro medio de las plumas en la superficie varió de 54 a 79,7 m e el tiempo de llegada a la superficie osciló de 7,25 a 8,05 $horas$.

Palabras clave: Modelo ROMS. Modelo GAS_DOCEAN. Pluma del Rio Amazonas, Derames de petróleo e gas. Plataforma continental de Brasil.

LIST OF FIGURES

LIST OF TABLES

List of abbreviations and acronyms

ADM	Advection–diffusion model
AGRIF	Adaptive Grid Refinement in Fortran
AM	Adjoint Model
AMIP	Atmospheric Model Intercomparison Project
APDRC/IPRC	Asia Pacific Data Research Center/International Pacific Research Center.
AVHRR	Advanced Very High Resolution Radiometer
AVISO	Archiving Validation and Interpretation of Satellite Data in Oceanography.
BC	Brazil Current
BL	Barrier Layer
BLT	Barrier Layer Thickness
CALTECH	California Institute of Technology (CIT)
CFL	Courant - Friedrichs - Lewy
CNRS	Centre National de la Recherche Scientifique.
COADS	Comprehensive Ocean-Atmosphere Data Set
CONAE	Comisión Nacional de Actividades Espaciales. Argentina
DHN	Diretoria de Hidrografia e Navegação.
DOE	U. S. Department of Energy
ECMWF	European Centre for Medium-Range Weather Forecasts
ESA	European Space Agency
ESMF	Earth System Modeling Framewor
GD	Gabinete do Diretor

GEBCO	General Bathymetric Charts of the Oceans
GES DISC	Goddard Earth Sciences Data Information Services Center
GPCC	Global Precipitation Climatology Centre
GST	Generalized Stability Theory
IFREMER	Institut Français de Recherche pour L'exploitation de la Mer.
IHO	International Hydrographic Organization
ILD	Isothermal Layer Depth
IOM	Inverse Ocean Modeling
INPE	Instituto Nacional de Pesquisas Espaciais
IPRC	International Pacific Research Center
IRD	Institut de Recherche pour le Développement
JPL	Jet Propulsion Laboratory
KPP	K - Profile Parameterization
MIRAS	Microwave Imaging Radiometer using Aperture Synthesis
MLD	Mixed Layer Depth
NASA	National Aeronautics and Space Administration
NBC	North Brazil Current
NCAR	National Center for Atmospheric Research
NCEI (formally NGDC)	National Centers for Enviromental Information
NCEP	National Centers for Environmental Prediction
NEC	North Equatorial Current
NECC	North Equatorial Counter Current
NERSC	Nansen Environmental and Remote Sensing Center
NESDIS	National Environmental Satellite, Data and Information Service
NGDC	National Geophysical Data Center
NLM	Non-Linear model

NOAA	National Oceanic and Atmospheric Administration
OHC	Oceanic Heat Content
OI	Optimum Interpolation
OML	Oceanic Mixed Layer
OSCAR	Ocean Surface Analyses - Real time
PDM	Plume dynamics model
PIRATA	Prediction Research Moored Array in the Tropical Atlantic.
PO.DAAC	Physical Oceanography Distributed Active Archive Cente
QuikSCAT	Quick Scatterometer.
ROMS	Regional Ocean Modeling System
RPM	RePresenter tangent linear Model
SCRUM	S-Coordinate Rutgers University Model
SCUD	Surface CUrrents from Diagnostic model
SEC	South Equatorial Current
SID	Serviço de Informação e Documentação
SMOS	Soil Moisture and Ocean Salinity
SODA	Simple Ocean Data Assimilation
SSH	Sea Surface Height
SSS	Sea Surface Salinity
SST	Sea Surface Temperature
TLM	Tangent Linear Model
UCLA	University of California. Los Angeles
WOA	World Ocean Atlas
WTNA	Western Tropical North Atlantic

List of symbols

u, v, w	Components of the velocity vector $\mathbf{v}$.
$T(u, v, w, t)$	Potential temperature.
$S(u, v, w, t)$	Total salinity.
$\rho_o + \rho(x, y, z, t)$	Total Density.
$\phi(x, y, z, t)$	Dynamic pressure.
P	Total pressure.
f	Parameter of Coriolis.
g	Gravity acceleration.
$K_M(x, y, z, t)$	Eddy Vertical Viscosity.
$K_H(x, y, z, t)$	Eddy vertical diffusivity.
$\mathcal{D}_u, \mathcal{D}_v, \mathcal{D}_T, \mathcal{D}_S$	Terms of viscosity and horizontal diffusivity.
$\mathcal{F}_u, \mathcal{F}_v, \mathcal{F}_T, \mathcal{F}_S$	Forcing terms.
t	Time.
$h(x, y)$	Depth.
$\zeta(x, y, t)$	Surface elevation.
τ_s^x, τ_s^y	Surface wind force.
τ_b^x, τ_b^y	Bottom Forcing.
E	Evaporation.
P_r	Precipitation.
Q_T	Surface heat flow.
T_{ref}	Surface reference temperature.

γ_1	Linear forcing coefficients of the bottom.
γ_2	Quadratic coefficients of the bottom forcing.
Q_T	Strong surface temperature function.
F_c	Compressibility factor
P	Ambient pressure
V	Gas volume
n	Number of gas moles
$R = 8.314\,Pa \cdot mol^{-1} \cdot K^{-1}$	Universal gas constant
T	Ambient temperature
h_s	Phase separation height
d	particle diameter
d_c	critical diameter
ν	Viscosity of seawater
ρ_d	Density of the drop
ρ_w	Seawater density
h	Depth of control volume
V	Total velocity
Δt	Time step
b_0	Ratio of initial control-volume
V_0	Initial blowout velocity
M_0	Momentum excess in the control-volume (gas + oil)
U_0	Velocity of the mixture oil + gas
U_A	Velocity of the currents in the ocean
n	Number of moles of consumed gas
K^*	Rate of diffusion + absorption of the gas
A_P	Surface area of the particle

f	Dissolved gas fugacity
f_{EQ}	Three-phase equilibrium fugacity of the gas
K	Coefficient of mass transfer
A	Surface area of the gas normal to flow direction
C_S	Dissolved saturation gas concentration inside the control-volume
C_0	Dissolved gas concentration inside the control-volume
m_l	Mass of liquid of plume
m_b	Mass of gas of plume
m_h	Mass of hydrates inside the plume
u	Horizontal velocity of plume at x direction
u_a	Ambient horizontal velocity of plume at x direction
v	Horizontal velocity of plume at y direction
v_a	Ambient horizontal velocity of plume at y direction
w	Vertical velocity of plume
w_a	Ambient vertical velocity
w_b	Gas bubbles velocity
ρ_l	Liquid density of plume
ρ_a	Density of ambient seawater
ρ_{com}	Density of hydrates and gas
Q_e	Entrainment water flux
Q_g	Gás flux
g	Acceleration of gravity
b	Plume ratio
ε	Gas fraction
β	Ratio between the bubble core width and the buoyant jet diameter
h	Depth of control volume

P	Ambient pressure
M_g	Gas mol weight
ρ_b	Gas density
T	Temperature
B	Buoyancy of gas plume
N_{BV}	Brunt-Vaisala frequency
Q_B	Gas flux
U_N	Nondimensional velocity
U_S	Bubble slip velocity
H_A	Atmospheric pressure head
H	Local depth
Z_{REF}	Reference depth in the temperature and salinity vertical profiles, It is used for the computation of MLD, ILD and OHC.

CONTENTS

1 INTRODUCTION

In recent decades, oil spills have occurred throughout the world and marine flora and fauna have been a frequent source of environmental impacts caused by these events (TEAL; HOWARTH, 1984). Contamination of marine and coastal environments by oil has been a concern for environmentalists around the world and has been the subject of much debate. This type of impact causes real environmental catastrophes, with incalculable and often irreversible damage to the environment. Human activities such as fishing and the recreational use of the environment are also compromised, causing great economic damages (GARZA-GIL; PRADA-BLANCO; VÁZQUEZ-RODRÍGUEZ, 2006).

From 1978 to 2010, the 12 major disasters occurred due to oil spills, of which only one was in an oil field on land, the rest occurred in marine environments, 9 of them were due to tanker or carrier accidents and 2 in oil rig marine exploration, shedding approximately 3901000 tonnes of oil into the sea (Figure 1).

Figure 1. Map of the world's largest oil spills (from 1978 to 2010).Only Fergana Valley oil spill was terrestrial.

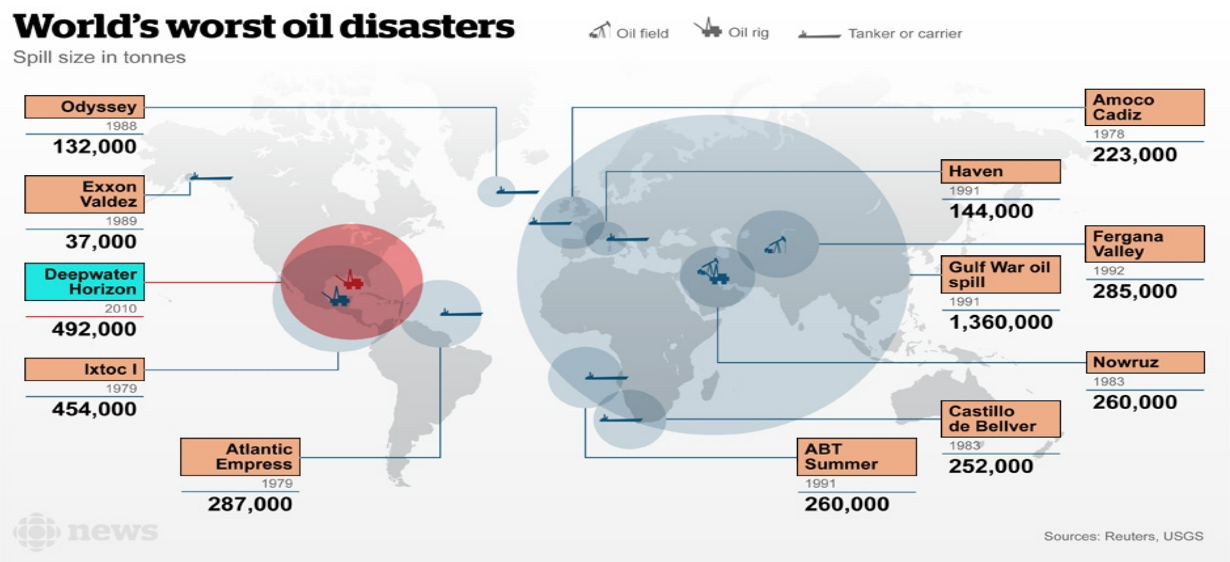

Source: http://www.cbc.ca/news/multimedia/map-12-of-the-worst-oil-spills-1.3037952

The Ixtoc I oil spill involving an oil exploration well drilled by the Mexico's government-owned oil company (Pemex) offshore before an explosion occurred, causing oil to ignite and the drilling rig collapsed. From 10,000 to 30,000 barrels of oil per day went out of the well in the

Bay of Campeche, Gulf of Mexico for almost a whole year. The platform was located about 60 km northwest of Ciudad del Carmen (Bahia de Campeche) in the water (JERNELÖV; LINDÉN, 1981), about 48 m depth. The spill occurred when the drilling rig lost mud circulation and the pressure reduction in the tank caused an explosion, the oil caught fire and the platform collapsed into the ocean. The estimated amount of oil spilled was 476000 tonnes (JERNELÖV; LINDÉN, 1981).

The British Petroleum (BP) Deepwater Horizon oil spill occurred on April 20, 2010 in the Gulf of Mexico. It began when an explosion destroyed the Deepwater Horizon drilling rig, causing a pressurized oil flow near the wellhead at more than 1524 m depth. Many attempts were made to stop the oil leak, but alone they were partially successful, managing to sell the well on July 15, 2010. Oil gushed from the broken well for more than 85 days, spanning about 920 km of the Gulf Coast and killed hundreds of birds and several marine species (SMITH; SMITH; ASHCROFT, 2011). The estimated amount of oil spilled was 492000 tonnes ea (Figure 1).

Oil residues and by-products can have serious consequences for human life, coastal ecosystems and socioeconomic activities. In recent decades, there has been a progressive decrease in the number of accidents and in the volume of oil discharged internationally (ITOPF, 2016). The reduction of accidents is associated with greater control and care in operations involving the exploration, exploitation, transport and oil storage, which reflects an increase in the level of environmental responsibility of society (KIRBY; LAW, 2010; ETKIN, 1999).

Environmental sensitivity to oil spills has been studied some decades ago by Gundlach & Hayes (1978), sensitivity maps contain three types of spatial information: the classification of the sensitivity of environments, biological resources and recreational human resources, subsistence or commercial value. The classification of the environment is made according to its physical characteristics, oil permanence and conditions of cleaning and removal.

The Environmental Sensitivity Charts to Oil Spills, are essential tools and a primary source of information for contingency planning and for the implementation of response actions to oil pollution incidents, allowing the identification of environments with protection priority and possible areas of sacrifice, allowing the correct allocation of resources And the proper mobilization of containment and cleaning equipment (MICHEL; HAYES; BROWN, 1978; CARVALHO; GHERARDI, 2003).

The exploration and production of oil at sea is a risk-filled activity. It requires dangerous tasks such as drilling rocks in ultra-deep regions, facing very high pressures and handling large volumes of oil and gas. It analyzes the large volume of information generated in the initial stages of the investigation, gathering a reasonable knowledge about the depth, thickness and variation of existing rock layers in a sedimentary basin and the hydrodynamics of the region. Based on this knowledge, the best places to drill in the basin are chosen. Research for the exploration and production of oil at sea is considered a high risk activity (JAHN; COOK; GRAHAM, 2008).

The impact of an oil spills and blowout can be minimized if locations most sensitive to contact with the oil can be protected. Knowing previously the variations of spills and explosions of oil help in the distribution of available resources to give a more effective response to these types of accidents.

On the other hand, the dependence of industry and life with the use of oil and gas is very significantly, the demand for these two products and their derivatives is extremely high. Large oil and gas extraction corporations are increasingly expanding into new areas, exploring and exploiting more and more natural gas and oil reserves in the deep ocean. These explorations and exploitation processes are subjects to risk of accidents, which can endanger human life and contaminate the ocean and the coastal line. The understanding of oceanographic processes in the oil and gas blowouts is fundamental for its prevention and mitigation. In case of oil and gas blowouts, companies would have contingency planning and mitigation to reduce the impact on the environment (KIRBY; LAW, 2010).

With the discovery of the pre-salt (Figure 2), the exploration and exploitation of oil in the open sea boosts Brazil's economy by increasing the good prospects of development for the Brazilian coastal states (RODRIGUES; SAUER, 2015). Consequently, also increase the risk of accidents that can produce a threat to the biological resources and socioeconomic development. When a leak occurs in the ocean, oil has a high potential for contamination and the damage it produces in the environment generally has disastrous dimensions, the severity of an accident is closely linked to factors that can make it more drastic, among them, meteorological and oceanic conditions (surface currents, wind, sea surface temperature, etc.), river runoff, seasonal period, area's vulnerability, petroleum type and volume, response time, etc. In order to respond to an oil spill or oil/gas blowout, one must be prepared and planned enough time to minimize the impact of leakage taking into account all possible conditions (LIMA, Novembro, 2008).

Figure 2. Schematic representation of the seabed layers: Pre-salt, salt and post-saltlayers.

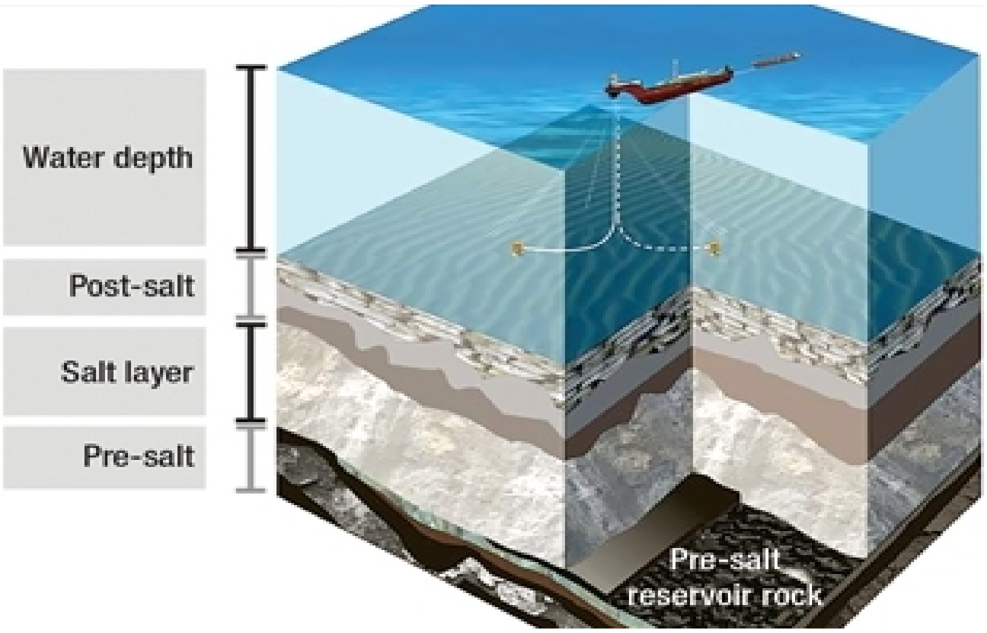

Source: https://innovationhouserio.wordpress.com/2013/09/27/pre-salt-bidders-defined-12th-rounds-details-published/

Therefore, this research contributes to analyze and quantify the risk situations arising from possible oil spills or oil/gas blowouts on the northern continental shelf of Brazil, taking into account the hydrodynamics in the region of study and the flows of the Amazon and Pará Rivers. This type of analysis is essential to reduce the environmental consequences of an oil spill or blowout, to make efficient the containment and cleaning/removal efforts of accidents, simulating both the hydrodynamics of ocean currents forced by the atmosphere and the transport of the hydrocarbon plume as support for contingency plans.

1.1 OBJECTIVE

The main objective of this research is to analyze the variation of hydrocarbon plumes in deepwater oil/gas blowouts on the northern Brazil continental shelf. To get this result specific aims were realized:

- Simulation and verification of a hydrodynamic numerical model in the Western Tropical North Atlantic by comparing numerical data with SODA, PIRATA and SCUD datasets.
- Determine the variability in the marine currents, temperature, salinity, mixed layer depth, isothermal layer depth, formation of barrier layer and oceanic heat content due to the presence of the Amazon and Pará Rivers.

- Execute the GAS_DOCEAN numerical model to characterize the evolution of hydrocarbon plumes in deepwater oil/gas blowouts.

2 THEORETICAL ASPECTS ON DEEPWATER OIL/GAS BLOWOUTS

The circulation in the Western Tropical North Atlantic (WTNA) ocean perform an important role in the interhemispheric transport of mass, heat, and salt and in the thermohaline overturning cell (Schmitz Jr.; MCCARTNEY, 1993; BOURLES et al., 1999; VELEDA et al., 2012). Furthermore, a strong western boundary current, the North Brazil Current (NBC) is the main conduit for cross-equatorial transport of South Atlantic upper-ocean waters, as part of the Atlantic meridional overturning cell (JOHNS et al., 1998). This current flows northwestward, intercepting the Amazon and Pará Rivers freshwater discharges along the Brazilian north coast.

The Amazon River plume enters the WTNA near the equator and is carried northwestward along the Brazilian Shelf by the NBC (SALISBURY et al., 2011; Müller-Karger; MCCLAIN; RICHARDSON, 1988).

The Amazon River is the main source of freshwater in the world, with a discharge that ranges between 200000 $m^3\ s^{-1}$ and 2 240000 $m^3\ s^{-1}$ (RICHEY; NOBRE; DESER, 1989; MOLINIER et al., 1996; SALISBURY et al., 2011), depositing almost 20% of the global discharge of rivers into the continental shelf of the equatorial Atlantic Ocean (GOULDING; BARTHEM; FERREIRA, 2003; BARTHEM et al., 2004). The plume of Amazon River extends thousands of kilometers over the North Atlantic Ocean arriving to Caribbean Sea (Müller-Karger et al., 1989; Johns, W. E. et al., 1990).

The magnitude of Amazon freshwater source is unique in the global oceans. Typically, river discharge is a small component of the open ocean salinity balance, but the Amazon discharge volume is twice the evaporation minus precipitation budget (FERRY; REVERDIN, 2004). The influence of Amazon water is felt far from the river mouth through enhancement of surface stratification leading to the formation of barrier layers (FFIELD, 2007; COLES et al., 2013; GRODSKY et al., 2014). Thus, the Amazon River Plume is thought to contribute to the dynamics of ocean atmosphere interaction and climate in WTNA.

In addition to the physical climate impacts of the Amazon River on the region, the river also injects terrestrially derived sediments, nutrients, and colored as well as transparent dissolved organic matter, which can be traced thousands of kilometers from the Amazon River mouth (HU et al., 2004). Biological community structure is strongly influenced by these dissolved organic matter and nutrient inputs as well as by the plume's role in stratifying the upper ocean (STUKEL et al., 2014), leading to globally significant uptake of atmospheric carbon dioxide in the river plume (COOLEY et al., 2007; SUBRAMANIAM et al., 2008).

Several recent studies have used observed data, satellite products, general circulation models (OGCMs) and regional models to explain the spatial and temporal variability of the Amazon plume and its interaction with the NBC rings (FRATANTONI; GLICKSON, 2002; FFIELD, 2007; KOROSOV; COUNILLON; JOHANNESSEN, 2015). Schmidt et al. (2011) implemented an operational forecasting system using a high resolution model to resolve the migration rate of the NBC rings in a short time scale. Recent studies link the intensification of hurricanes to the spreading of freshwater discharge due to the impact of haline stratification on reduction of vertical heat flux (BALAGURU et al., 2012; GRODSKY et al., 2012; NEWINGER; TOUMI, 2015) and the periodic movement of the NBC rings (FFIELD, 2007).

The WTNA is an area with intense river-sea-land interaction, characterized by complex material transport, mixed layer depth changes (GRODSKY et al., 2012; COLES et al., 2013) and biogeochemical processes (LEFÈVRE; DIVERRÈS; GALLOIS, 2010; IBÁNHEZ; FLORES; LEFÈVRE, 2017). In this context, the Amazon and Pará Rivers are the main continental forcing to the adjacent coastal waters, giving rise to alterations in local and remote physical and biogeochemical processes. However, more studies are necessary to quantify the role of the Amazon and Pará River plumes on the dynamic of this region. Thus, to better understand the role of the plume rivers in the WTNA is crucial to quantify how much it impacts on the dynamics of this region.

The first efforts of Fannelop & Sjoen (1980) focused on the case of the evolution of a single gas plume in the ocean. These authors proposed a simplified analytical modeling approach, with nondimensional solutions, and applicable in cases of spills in shallow waters. In this first model, the gas expansion all through the water column was estimated considering the classical theory of ideal gas. As a result, the solution for this model brings the dimensions of the cone of gas formed along the water column (starting from the ocean floor), and in consequence, the diameter of the gas plume in the surface. Meanwhile, the Fannelop & Sjoen (1980) approach does not consider horizontal advection of gas through the currents. Some advance on this first idea was proposed by Friedl & Fanneløp (2000), when routines were added that considered the elevation in the surface of the sea provoked by the reaching of the gas to the surface (fountain effect, Figure 3).

Figure 3. Standard framework and notation adopted in GAS_DOCEAN model.

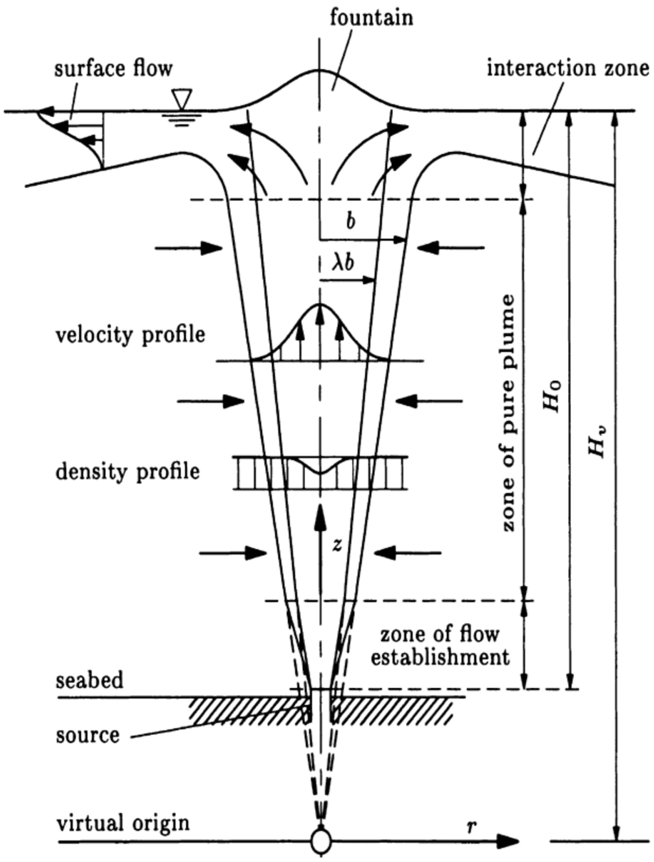

Source: Friedl & Fanneløp (2000)

The increase of the oil and gas production in marine environment verified above all in the mid-year 2000 (E&P Forum/UNEP, 1997; U. S. DOE, 1999; U. S. EIA, 1998; U. S. NOIA., 2005) brought the need of more precise models for evaluation of the transport and dispersion of these mixtures in the oceans, as well as their effects on the environment. In deeper waters, for instance, the gas cannot be treated as an ideal mixture (CHEN; YAPA, 2001), and new interaction processes were observed between the two media (gas and liquid), mainly when the local pressure is very different from the atmospheric pressure. In this new generation of mathematical models, created to represent simultaneously oil and gas plumes in marine environment, two more important physicochemical processes were considered. It is the gas (TOPHAM, 1984a; CHEN; YAPA, 2001) and gas dissolution (JOHANSEN, 2003; ZHENG; YAPA, 2002) in sea.

In shallow waters, the gas dissolution is neglectable (JOHANSEN, 2000). However, in deep waters, the travel time for the gas through the water column is longer, also rising the dysphasic flow time. Adding to this the fact that the gas solubility increases with the environmental pressure (JOHANSEN, 2000), it is observed frequently that under natural conditions of low temperature and high pressure, the gas tends to form hydrates, which significantly change the ascension velocity of the gaseous plume along the water column (TOPHAM, 1984a; CHEN; YAPA, 2001; JOHANSEN, 2003).

The first models of evolution of a plume of gas developed did not foresee in their equations these two mechanisms (dissolution and hydration), limiting itself to its application in deeper ocean areas (CHEN; YAPA, 2001). Yapa & Zheng (1997), for instance, proposed a set of equations to predict the space-time evolution of plumes formed by spills in intermediate waters, considering only the advective transport of the gas as function of its characteristics (volumetric composition) and the environmental thermodynamic conditions (temperature fields, salinity, pressure and density). In the 90s these important mechanisms were introduced into the modeling of a plume of gas in the marine environment (REED et al., 1999; ZHENG; YAPA, 2000; CHEN; YAPA, 2001; YAPA; ZHENG; CHEN, 2001).

The main variables influencing in the variations of oil spills and blowouts are temperature, salinity and marine currents. The Atlantic (central North Atlantic) is the saltiest of the world's major oceans (TALLEY, 2002), The sea surface salinity in the open ocean is $33 - 37\ psu$ and varies with latitude and season. The values of surface salinity are influenced by evaporation, rainfall and river affluence. Although the minimum values of salinity are only to the north of Ecuador (TOMCZAK; Stuart Godfrey, 2003), Because of heavy tropical rainfall, the lowest values are in the high latitudes and along the coasts, where large rivers (Amazon) drain into the ocean (HU et al., 2004). Maximum salinity values occur at approximately $25°N$ and $25°S$, in subtropical regions with low rainfall and high evaporation. The sea surface temperature varies with latitude, marine current, season and other parameters, ranges from below $-2°C$ to $29°C$. The Maximum temperatures occur to the north of the Equator (Figure 4) and the minimum values are found in the polar regions.

The tropical Atlantic region is a complex system of zonal currents and counter-currents (Figure 4) forced by the subtropical gyres and by the action of the trade winds in both hemispheres (STRAMMA et al., 2005). The Benguela current flows north to feed on the southern side of the South Equatorial Current (SEC). The SEC flows westward toward the Brazilian platform and is divided in two branches at Cabo de São Roque, one branch (strongest branch) heading northward as the North Brazil Current (NBC), and the other as the Brazil Current (BC). According to Stramma & England (1999) the SEC is divided into four branches: the southern South Equatorial Current (sSEC), the central South Equatorial Current (cSEC), the northern South Equatorial Current (nSEC) and equatorial South Equatorial Current (eSEC). The eSEC and cSEC give origin to NBC, the latter is fed too by nSEC. At each season the SEC has a strong flow to the westward (about $0.3\ m\, s^{-1}$) near the equator and weaker ($0.1 - 0.15\ m\, s^{-1}$) in a broad band south of $10°S$ (PETERSON; STRAMMA, 1991).

Figure 4. Schematic representation of the main surface (solid lines), subsurface (dashed lines) currents and average SST, 1998 – 2011 (OA_Flux at http://oaflux.whoi.edu/). BC (Brazilian Current). NBC (North Brazilian Current). NBCR (North Brazilian Current Retroflection). NEC (North Equatorial Current). NECC (North Equatorial Countercurrent). nSEC (northern branch of South Equatorial Current). cSEC (central branch of South Equatorial Current). sSEC (southern branch of South Equatorial Current). EUC (Equatorial Undercurrent). NEUC (North Equatorial Undercurrent). SEUC (South Equatorial Undercurrent). NBUC (North Brazil Undercurrent). GD (Guinea Dome). AD (Angola Dome).

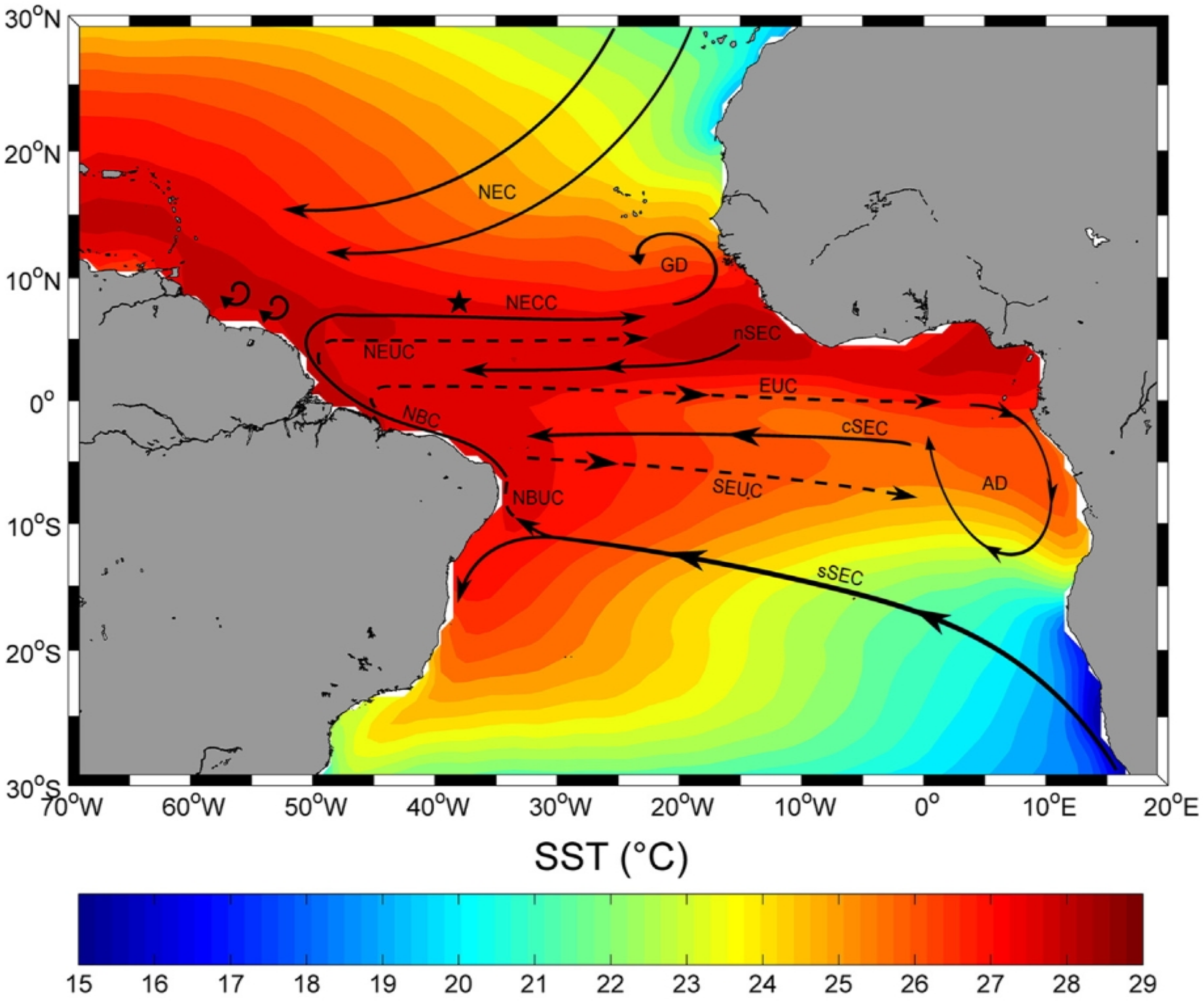

Source: Bruto et al. (2017)

The NBC is considered a low latitude strong western-boundary current (GARZOLI et al., 2004; FRATANTONI; RICHARDSON, 2006; AKUETEVI; WIRTH, 2015), which retroflects and separate away from the boundary turning anti-cyclonically for more than 90° (Figure 4), and form anti-cyclonic eddies. NBC flows from Northeastern to Northwest along the northwestern continental margin of Brazil as a coastal current developing a retroflexion in rings form (DESSIER; DONGUY, 1994; Johns, W. E. et al., 1990; FRATANTONI; JOHNS; TOWNSEND, 1995), this makes a turn to the East driven by the wind and feeds the North Equatorial Counter Current (NECC). Reaching speeds between 0.75 – 1.0 $m\,s^{-1}$ (ARNAULT et al., 1999).

The NBC seasonally retroflects near $6-8°N$ and sheds eddies exceeding 450 km in overall diameter (RICHARDSON et al., 1994; GARZOLI et al., 2004; FRATANTONI; RICHARDSON, 2006). The NBC retroflection feeds the North Equatorial Counter Current (NECC), an eastward zonal current, which contributes to the formation of the anticyclone current rings (CASTELÃO; JOHNS, 2011). The NBC rings are a significant contributor to transporting water across current gyres and between hemispheres in the tropical Atlantic (BOURLES et al., 1999; JOHNS et al., 1998; SCHOTT et al., 2003; STRAMMA et al., 2005).

During the boreal summer, in response to a shift towards the north of the trade winds, the NECC forms eastwards (Figure 4), near $6°N$, intensifying significantly during the boreal winter (GRODSKY; CARTON, 2002; RICHARDSON; WALSH, 1986). The NECC is located between $3°N$ and $10°N$, it is considered as the northern boundary for SEC (PETERSON; STRAMMA, 1991).

Strong seasonal variations in these currents occur in response to the annual migration of the atmospheric Intertropical Convergence Zone (ITCZ) between its southern position in winter, and its northern position in boreal summer (XIE; CARTON, 2004). This leads to northward transport of Amazon water in boreal winter, and eastward transport of Amazon water in the NECC in boreal spring through boreal fall (Müller-Karger; MCCLAIN; RICHARDSON, 1988; LENTZ, 1995b; FRATANTONI; GLICKSON, 2002; COLES et al., 2013; FOLTZ; SCHMID; LUMPKIN, 2015).

The NSEC is a water source that reinforces the NECC (STRAMMA; ENGLAND, 1999). The northern limit of NECC (when it is present) is the North Equatorial Current (NEC). The mean speed to eastward of NECC is 0.42 $m\,s^{-1}$ (FRATANTONI, 2001). The NEC comes from the northwest coast of Africa (Figure 4), where it is fed mainly by the cooler waters that flow from the northeastern Atlantic towards the tropic in the West direction transporting the waters coming from the Canary Current. It is located between 7° and $20°N$, at $10°N$ is the southern part of the subtropical gyre flowing westward as a broad current with a mean velocity about $0 - 0.15$ $m\,s^{-1}$ (RICHARDSON; WALSH, 1986).

Pollutant dispersion models have been developed in the ocean, combining analytical expressions, Eulerian and Lagrangian formalism, e. g. MEDSLIK-II (De Dominicis et al., 2013a; De Dominicis et al., 2013b). One of the advantages of these models is their flexibility to be assimilated from different datasets, as is the case with the output data of other models, such as ROMS (Regional Ocean Modeling System) (NORTH et al., 2011) or data collected in situ with ADCP (Acoustic Doppler Current Profiler) and CTD (Conductivity, Temperature and Depth), e. g. Leite et al. (2014).

2.1 OIL/GAS PLUME EVOLUTION

In agreement with Chen et al. (2015) the underwater oil spill process is divided into three successive stages, namely the turbulent jet stage, the buoyant plume stage and the advection-diffusion stage (Figure 5). The turbulent jet stage exists in the event that the oil and gas mixture is released from a violent underwater burst where the velocity at the orifice can reach $5 - 10\, m \cdot s^{-1}$. At this stage, the movement of the jet is dominated by the initial moment by which the oil breaks into a large number of drops of uneven size due to the high turbulence.

Figure 5. Sketch of underwater oil spill process

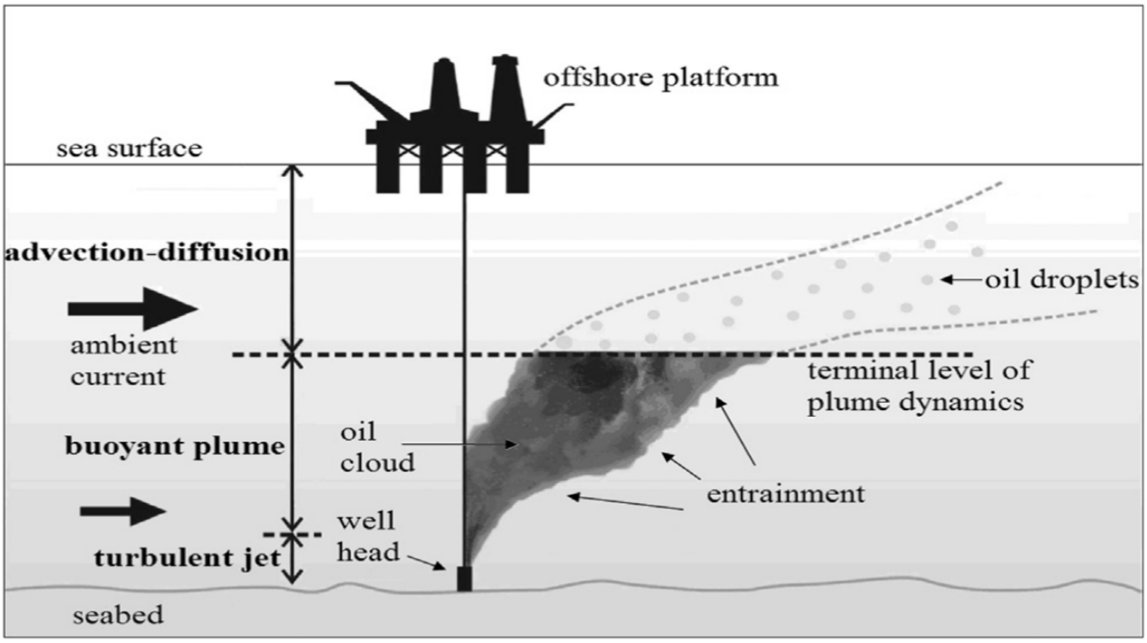

Source: Chen et al. (2015)

As the ambient water is also drawn into the stream, a rapid loss of momentum occurs within a few meters of the release position and then the turbulent jet stage ends. In the buoyant plume stage, the momentum is no longer significant with respect to buoyancy, which then becomes the driving force for the rest of the oil plume.

The plume continues to rise towards the surface of the sea due to buoyancy while the ambient water is continuously drawn into the plume. As a result, the plume is enlarged and its density approaches the ambient density. When the plume is fully developed, a considerable amount of water containing the oil droplets is pumped to the most superficial region because in the deep sea area the sea water environment is usually much denser in the deeper region, the oil plume can reach a level of neutral buoyancy at a certain depth, where buoyancy no longer dominates the movement of the plume.

Thereafter, the dynamics of the plume become insignificant and the oil moves as individual droplets of oil passively following current and ambient turbulence and increasing due to the buoyancy of the droplets. This is the so-called advection-diffusion stage. It should be noted that there is no obvious limit between two successive stages. In fact, the three factors mentioned above exist at each stage and the dominant factor is simply different at a different stage.

Yapa & Zheng (1997) explained a model to simulate oil spills from underwater accidents, their model could also simulate the presence of gas with oil for relatively vertical plume. In Zheng & Yapa (1998), the model simulations were compared in detail with numerous laboratory data and some data obtained from small-scale field experiments using compressed air. A modified version of this model was then used to compare the results of two field experiments conducted in the Norwegian Sea by SINTEF (Norway), consisted of releases of oil and gas at 100 m (RYE; BRANDVIK; STRØM, 1997). The results of these comparisons are set forth in Yapa, Zheng & Nakata (1999).

Yapa & Zheng (1997) is not suitable for deepwater simulations due to important differences in gas variations in relatively shallow water. As stated in Cooper, Forristall & Joyce (1990) the existence of strong currents in some deepwater regions may cause the gas phase to separate from the plume. Another argument by which the previous model needed a major modification. Yapa, Zheng & Chen (2001) developed a module for the formation and decomposition of the hydrate by coupling it with its previous model (YAPA; ZHENG, 1997) to calculate several scenarios of deepwater blowouts. Johansen (2000) developed a deepwater oil/gas blowouts model based only on thermodynamics capable of simulating the formation and decomposition of gas hydrates, the dissolution of the gas and the separation of the gas from the main plume, ignoring reaction rates of formation and decomposition.

Yapa, Zheng & Chen (2001) developed a model that did not include the complete model formulation or comparisons with data from the field experiment "Deepspill" (JOHANSEN; RYE; COOPER, 2003). Spaulding et al. (2000) presented a model in deep waters that could simulate the formation of hydrates, without detailing this one. Vysniauskas & Bishnoi (1983) developed a model taking into account the empirical hydration formation that was later integrated by Barbosa Jr, Bradbury & Silva Freire (1996) and by Topham (1984a), Topham (1984b) with a plume model to simulate scenarios of deepwater blowouts. None of these studies compared the results of numerical simulations with field data.

Zheng, Yapa & Chen (2002) describes a complete mathematical model to simulate the variations of oil and gas released from deep water, the formulation of the model integrates the hydrodynamics and thermodynamics of the plume; the thermodynamics and the kinetics of the formation and decomposition of the hydrate and the dissolution of the gas, uses an improvement for the calculation of the buoyant velocity of gases and hydrates and the dissolution of gases, obtaining good results. Gas behavior may be no-ideal.

The model can simulate the variations of oil and gas under conditions of a strong transverse flow where gases can be separated from the main plume. Each module was tested by comparing the numerical results with the available data. Zheng, Yapa & Chen (2002) called for convenience "CDOG" to this model. Subsequently, Chen & Yapa (2003) used CDOG model for computing and compare results with large-scale field experiments, "Deepspill".

Figure 6. Sketch of control element of PDM submodel. b_k is the plume radius and h_k is the plume thickness

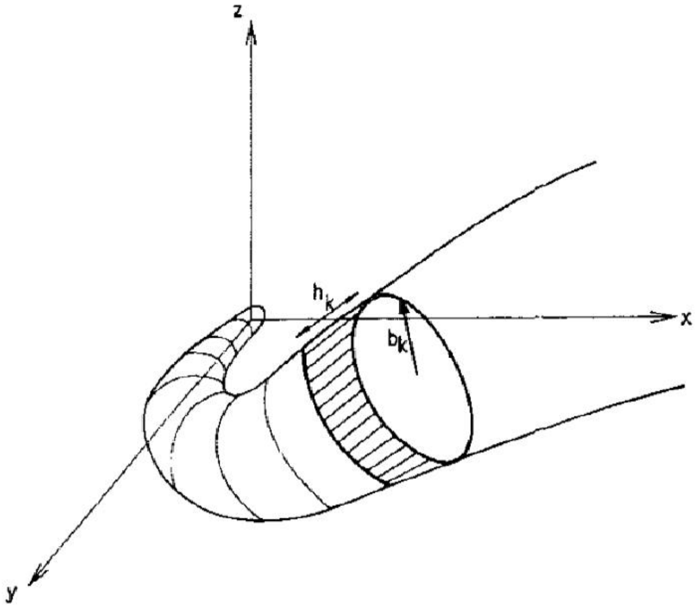

Source: Taken and modified from Lee & Cheung (1990)

Conforming to Dasanayaka & Yapa (2009), the time for oil to appear on the surface and its approximate location are two key aspects that must be solved with the oil spill model for contingencies and emergency responses. This requires that the explanation of the underwater oil spill process be as accurate as possible. Yapa et al. (2012) summarized the most recent models of underwater oil spills, making successive improvements to the simulations that illustrate the behavior of the oil, demonstrates the impact of the dimensions of oil drops, also explains how the behavior of the oil changes when additives are supplied as dispersants. The results of the simulations reveal that underwater plumes with low concentrations of oil can form and remain submerged for long periods of time when very small oil droplets with diameters less than 0.5 mm are present.

The oil slick model presented by Chen et al. (2015) it is formed by two submodels: the dynamics model of the plume (PDM) and the advection-diffusion model (ADM). The PDM submodel is used to simulate the turbulent jet phase and the floating plume phase where the water mixture and a small amount of spilled oil is treated as a whole and takes into account the interaction between the oil and its environment. The Lagrangian integral technique is used to simulate the turbulent jet stage and the floating plume phase. The duration of the oil spills is divided into a series of equal time intervals (Figure 6) and each time interval corresponds to a small amount of oil spilled (LEE; CHEUNG, 1990).

As a result, the oil and water plume is represented by a series of non-interfering control elements. At some point, the line connecting the central points of all control elements is considered as the oil path. It is assumed that each control element is a cylindrical section of a curved cone and its lower plane is perpendicular to the trajectory of the plume. In the submodel ADM the oil spilled is divided into a large number of discrete particles, each particle represents a set of oil droplets of equal size and is characterized by its spatial coordinate, velocity, volume, oil concentration, drop diameter, etc. These particles are introduced into the water, in the last place of the plume and then move in response to the shear current, turbulence and buoyancy.

When the oil plume moves up to a certain depth, its density may be very close to the density of the environment because a large amount of water has been drawn into the plume, mainly in a water environment stratified by density, when the oil boom rises to the depth where the water is less dense, the fluid of the boom can reach a level of neutral or even negative buoyancy below of the sea surface.

2.2 HYDRATE FORMATION

According to Zheng, Yapa & Chen (2002) in low temperatures and high pressures in the deep ocean, oil/gas blowouts, in addition to their long travel to the surface, are more subject to more complex processes than if they were on the surface or in shallow waters (Figure 7), including hydrate formation, non-ideal gas behavior, etc. Gas hydrates consist of gas and water, and it is a compound. For CH_4, the hydrate formation can be described as equation (2.1).

$$(CH_4)_{gas} + n_h(H_2O)_{water} \leftrightarrow (CH_4 \cdot n_h\, H_2O)_{hydrate} \tag{2.1}$$

Where $n_h = 5.75$ for CH_4. When a plume rises to a lower pressure level, the hydrate can decompose in water and gas again. Figure 7 shows the variation of potential temperature and thermodynamic equilibrium conditions for CH_4 and natural gas (80% methane, 10% ethane, 10% propane) in the Norwegian Sea and Gulf of Mexico. Below the thermodynamic equilibrium line, the pressure and temperature satisfy the hydrate formation conditions, above this, the hydrates will begin to decompose. In these places, the thermodynamic conditions to form hydrates will gather close to $500\,m$ (CH_4) and $200\,m$ (natural gas) at Norwegian Sea; and near $600\,m$ (CH_4) and $300\,m$ (natural gas) at Gulf of Mexico. The formation and decomposition of the hydrate significantly affects the buoyancy of the plume.

Figure 7. Diagrams of thermodynamic equilibrium for hydrate from CH_4 and natural gas (80% methane, 10% ethane, 10% propane) superimposed on the temperature distribution at a place in the Norwegian Sea and Gulf of Mexico.

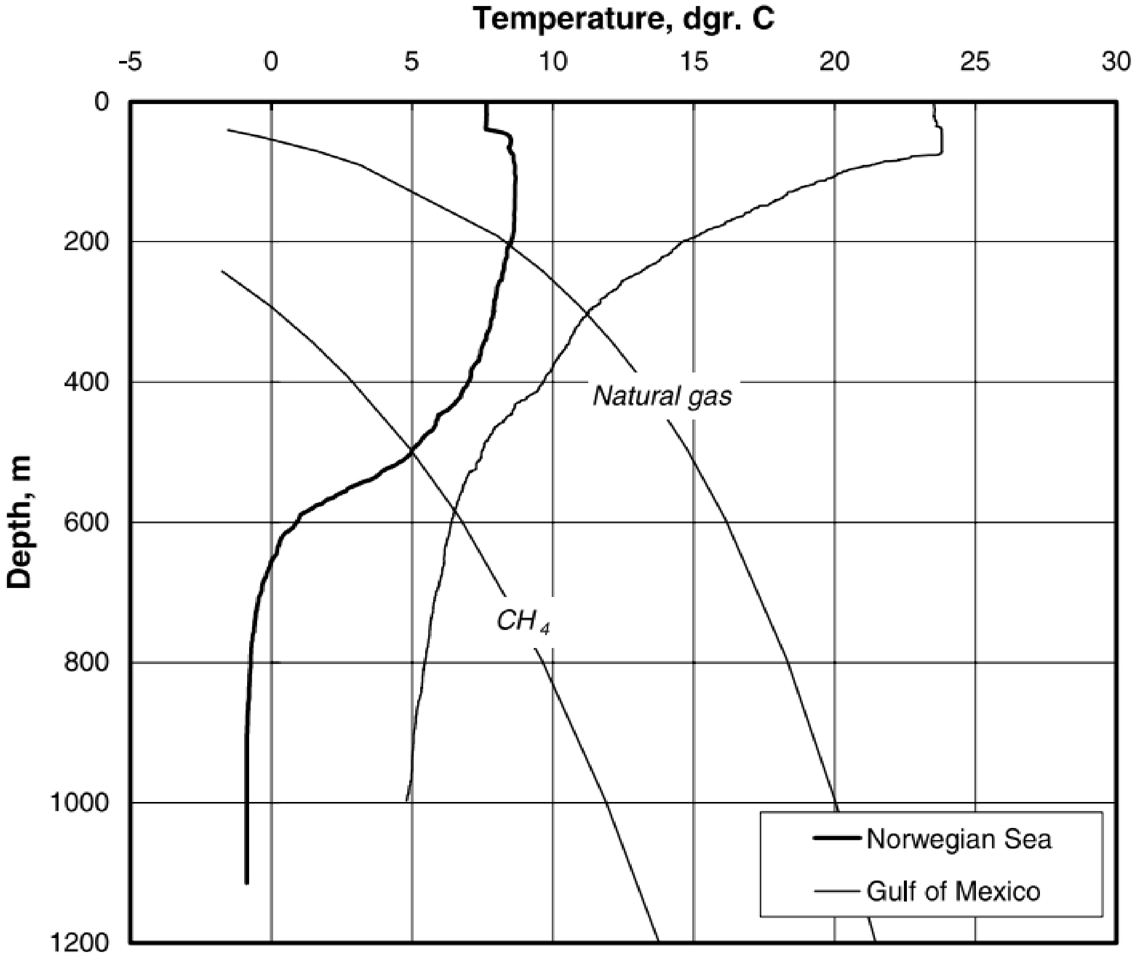

Source: Johansen (2003)

Conforming to Zheng, Yapa & Chen (2002) the free gas can dissolve in water during its long journey, changing the buoyancy of the plume. Under high pressures the behavior of the gas is best described by an equation of non ideal gas state. The size of the gas bubbles and their buoyancy velocities cannot be approximated as constants, considering the processes of hydrate formation, decomposition, dissolution and gas expansion. The gas can be separated from the plume due to the slip velocity of the gas bubble if the plume is significantly bent in a transversal flow.

2.3 RELATIONSHIP OF KINETICS OF HYDRATE FORMATION WITH MASS AND HEAT TRANSFER

To model the rate of hydrate formation in the gas phase of the plume the relationship between hydrate kinetics, mass and heat transfer should be considered. The mass transfer carries the gas for the formation of hydrates to the point of reaction. Heat transfer redistributes the released heat of hydrate formation around the solid hydrate to change the temperature of the water.

Before integrating the hydrate kinetics with the hydrodynamics and thermodynamics of the plume, Englezos et al. (1987) constructed a module for the hydrate kinetics that helped to verify the adaptation and the numerical algorithms, this module takes into account that the gas molecules diffuse through the porous hydrate layer due to the concentration gradient of the gas and react with the water to form hydrates at the hydrate-water interface; the hydrate layer is at the same temperature as the hydrate-water interface, the heat released by the hydrate formation at the hydrate-water interface is transferred only through the aqueous phase since the thermal conductivity of the phase gaseous phase is much lower than that of the liquid phase; the transfer of mass and heat in any cross-section is the same for a given time; the pressure on the inside and the outside of the bubble is the same; any hydrate particles that emanate from the border of the bubbles are not taken into account in the calculations and the hydrate sheathing evenly covers the surface of the bubble (Figure 8). This module is for a single bubble and is applied in the same way to several bubbles. The nucleation process is not taken into account because the experimental data show that the period of this process is very short (BISHNOI; NATARAJAN, 1996; BREWER et al., 1998).

Figure 8. Scheme of a gas bubble with a homogeneous sheathing of hydrate

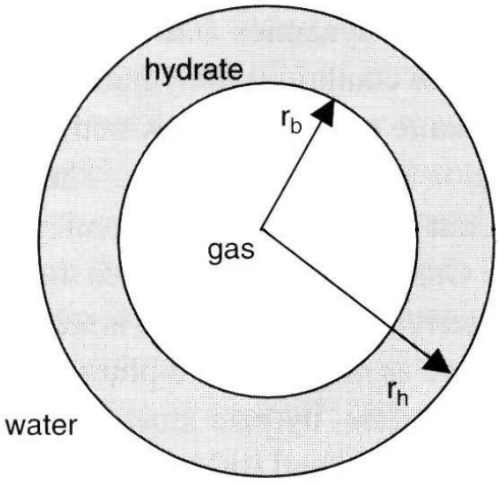

Source: Taken and modified from Zheng, Yapa & Chen (2002)

2.4 NON IDEAL GAS BEHAVIOR IN DEEP WATER

The gas behavior is not ideal in deep water because of the high ambient pressure, the solubility of the gas in water depends to a large extent on the ambient pressure, temperature and salinity (ZHENG; YAPA; CHEN, 2002; JOYE et al., 2011). Therefore, a correction for compressibility factor (F_c) is necessary.

$$PV = F_c nRT \tag{2.2}$$

Where:

$F_c = 1$ for ideal gas
P Ambient pressure (Pa)
V Gas volume (m^3)
n Number of gas moles
$R = 8.314\, Pa \cdot mol^{-1} \cdot K^{-1}$ Universal gas constant
T Ambient temperature (K)

The values of F_c for CH_4, CO_2 and an ideal gas are shown in figure 9 up to $500\,m$ depth in the Gulf of Mexico, where can see a significant difference between the ideal gas and the real gases CH_4 and CO_2, this difference increases with the increase of depth.

Figure 9. Comparison of the compressibility factor of an ideal gas with the real CH_4 and CO_2 gases in the Gulf of Mexico. The compressibility factor is computed according to Sloan Jr & Koh (2008) method.

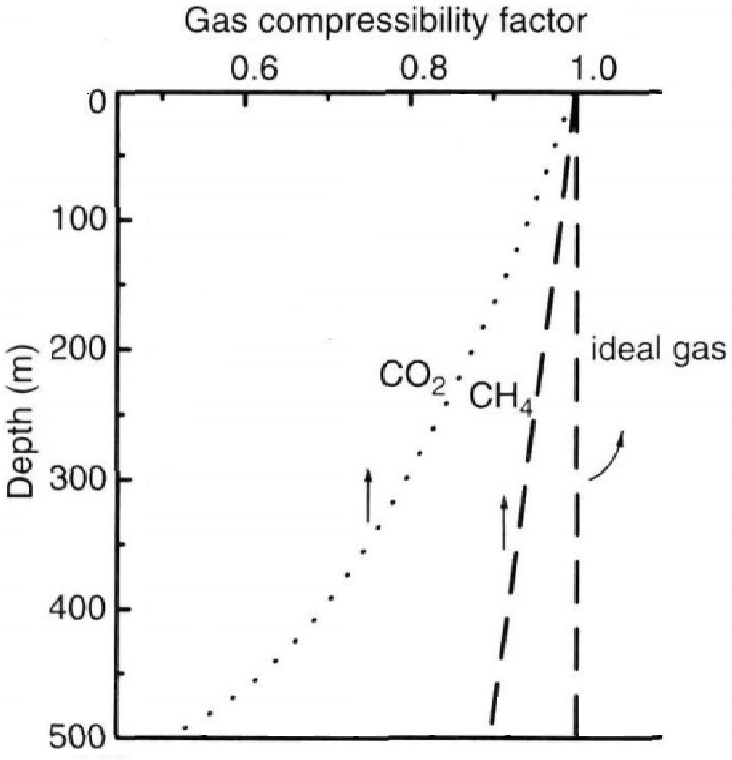

Source: Taken and modified from Zheng, Yapa & Chen (2002)

2.5 PHASE SEPARATION

In a transverse flow the difference in velocity between the sliding bubbles and rising entrained fluid can lead to a phase separation. Figure 10 shows single-phase and biphasic plume in a uniform cross-flow. If the cross-flow is strong enough to push the fluid out of the plume and advect it with the flow, the bubbles will separate from the entrained fluid at some height h_s, forming a column of bubbles that rises as a result of the velocity of sliding the bubble alone. Above h_s, fluid diverted at the front of the bubble column by the current rises a short distance while interacting with the floating bubbles before it is thrown to leeward of the plume (SOCOLOFSKY; ADAMS, 2002).

Figure 10. Representation of single-phase and biphasic plumes in a uniform cross-flow. h_s is the phase separation height

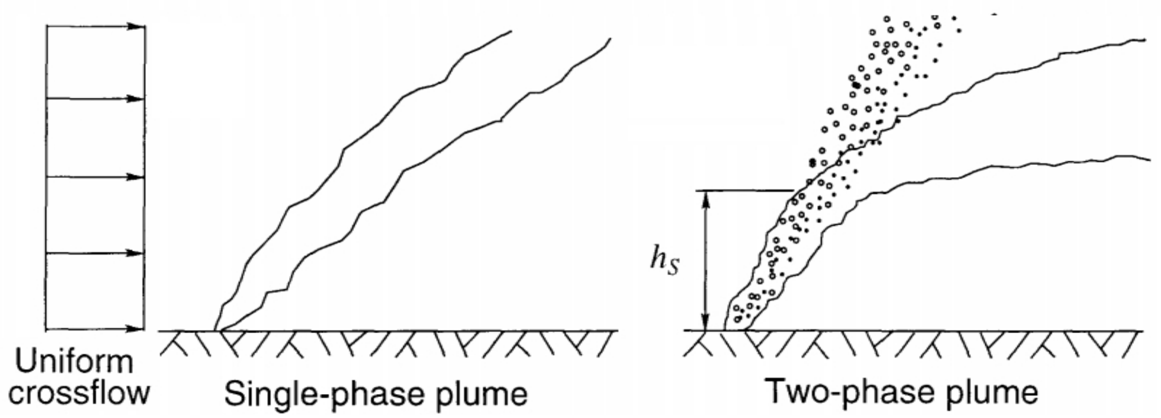

Source: Socolofsky (2001)

Cross-flows affect a wide range of plume properties, changing the basic dynamics of the plume. Even in the case of single-phase plume, cross flows improve entrainment, divert the plume center line, deform it into a pair of vortices and can cause fluid to leak in the downstream wake of the plume (FISCHER et al., 1979; DAVIDSON; PUN, 1999). The bubble plumes are similarly affected and have additional complications due to the sliding velocity of the dispersed phase.

Socolofsky & Adams (2002) performed several experiments confirming fractionation and separation, determining the coding for phase separation taking into account the cross-flow force, for plumes with high buoyancy and low cross-flow velocity (weak cross-flows), the separation did not occur at the time the bubbles reached the surface of the water, occurring the separation in other experiments with high cross-flow rate (strong cross-flows).

2.6 SOLUBILITY

Experimental values for the water-solubility of natural gases are available as a function of pressure and temperature (FOGG; GERRARD, 1991), for small pressures, the solubility increases in proportion to the pressure in the gas phase according to Henry's law, while at higher pressures, this simple law must be substituted by the modified form of Henry's law (Krichevsky & Kasarnovsky (1935) relation). In this law, the pressure term is replaced by the fugacity that accounts or non-ideal gas behavior (LEKVAM; BISHNOI, 1997).

Figure 11 shows the Comparison between the calculated data of CH_4 solubility in water through Henry's law and the modified Henry's law and those observed by Lekvam & Bishnoi (1997). In this comparison has taken into account 3 different temperatures ($1.20\,^{\circ}C$, $10.22\,^{\circ}C$ and $12.46\,^{\circ}C$). Evidently it can be seen that for higher temperatures and for higher pressures the observed data are much closer to the modified Henry's law. Therefore, at higher pressures modified Henry's law provide better computational values for solubility. The higher pressures in this plot correspond to what is expected in deepwater spills.

Figure 11. Comparison between calculated CH_4 solubility in water data and those observed by Lekvam & Bishnoi (1997)

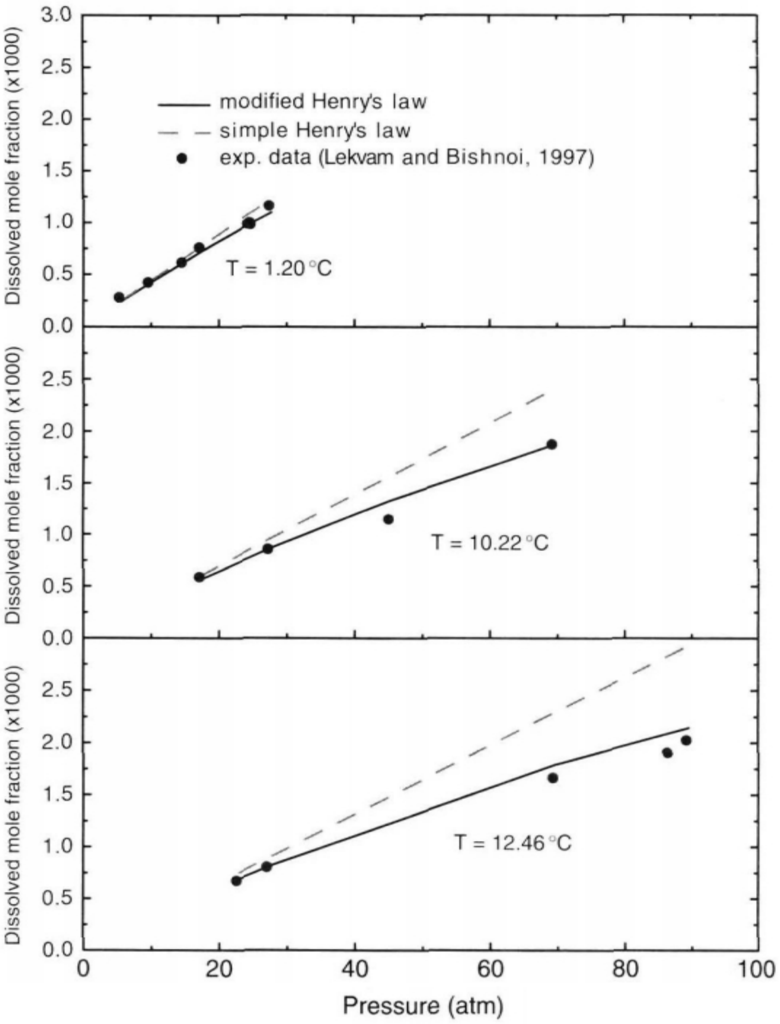

Source: Zheng & Yapa (2002)

2.7 LIFTING SPEED OF OIL PARTICLES

When the oil drop are in the water column, its trajectory is described by the advection-diffusion equation with a buoyant velocity as part of the vertical velocity (YAPA; ZHENG; NAKATA, 1999). The bouyant velocity of the oil particles using Stokes's law or Reynolds's law was calculated by Elliott (1986) and depends on the particle diameter d relative to the critical diameter d_c given by:

$$d_c = \frac{9.52\nu^{2/3}}{[g(1-\rho_d/\rho_w)]^{1/3}} \tag{2.3}$$

Where:

d particle diameter (m)

d_c critical diameter (m)

ν Viscosity of seawater ($m^2 \cdot s^{-1}$)
ρ_d Density of the drop ($kg \cdot m^{-3}$)
ρ_w Seawater density ($kg \cdot m^{-3}$)

$$W = \begin{cases} \dfrac{gd^2(1 - \dfrac{\rho_d}{\rho_w})}{18\nu} & \text{Stokes law} \quad if \quad d < d_c \\ \left[\dfrac{8}{3} - gd\left(1 - \dfrac{\rho_d}{\rho_w}\right)\right]^{1/3} & \text{Reynolds law} \quad if \quad d \geq d_c \end{cases} \tag{2.4}$$

Using equation (2.4), Elliott (1986) successfully simulated the vertical mixing of oil particles in the North Sea.

3 DATA AND METHODOLOGY

3.1 STUDY AREA

The Atlantic Ocean is limited to the west by North and South America, in the north and northeast is separated by the Arctic Ocean and by the Canadian Arctic Islands, Iceland, Greenland, Jan Mayen, Svalbard Islands and continental Europe. It connects to the Arctic Ocean through the Strait of Denmark, the Greenland Sea, the Norwegian and Barents Seas. To the east, the boundaries of the ocean are Europe, the Strait of Gibraltar (which connects it with the Mediterranean Sea) and Africa. In the southeast, the Atlantic merges with the Indian Ocean, divided by the eastern meridian, running south of the Cape Agulhas to Antarctica. While some authorities show the Atlantic Ocean, extending south to Antarctica, others show it as delimited to the south by the South Ocean (IHO, 1953). In the southwest, the Drake Pass connects to the Pacific Ocean. The Caribbean Sea, the Gulf of Mexico, the Hudson Bay, the Mediterranean Sea, the North and the Baltic Seas are the large bodies of water adjacent to the Atlantic Ocean.

The Atlantic Ocean with its adjacent seas occupies an area of about 106.4 million square kilometers and without them, 82.6 million square kilometers. The width of the Atlantic ranges from 2848 km (between Brazil and Liberia) to about 4830 km (between the United States and North Africa) (AKINDE; OBIRE, 2011). The average depth of the Atlantic Ocean without its adjacent seas is 3926 m. The mean depth between $60^{\circ}N$ and $60^{\circ}S$ is 3730 m, finding the modal depth between 4000 m and 5000 m (LEVIN; GOODAY, 2003) and the maximum depth in the Puerto Rico Trench with a value of 8605 km (FOX et al., 2009).

The study area of this work is located in the equatorial band of the tropical Atlantic, limited in the southeast by the north coast of Brazil, where the rivers Amazonas and Pará release freshwater. This area is framed in $60.5^{\circ}W - 24^{\circ}W/5^{\circ}S\breve{}16^{\circ}N$ (Figure 12), covering an area of $4916 \times 10^3\ Km^2$. Special attention is given to these two oceanic regions: REG1, the retroflexion area of NBC and REG2, which corresponds to the plume of the Amazon River spreading eastwards. Figure 13 shows the Amazon river delta with very irregular coast and where are located multiple islands that define four fundamental inputs: North channel, Santa Rosa Bay, Dangerous channel and Jurupari channel.

Figure 12. The model domain framed in $60.5°W - 24°W/5°S - 16°N$, bathimetry and regions for data validation (Red rectangles). REG1($48° - 45°W/4° - 12°N$). REG2 ($40° - 28°W/6° - 10°N$)

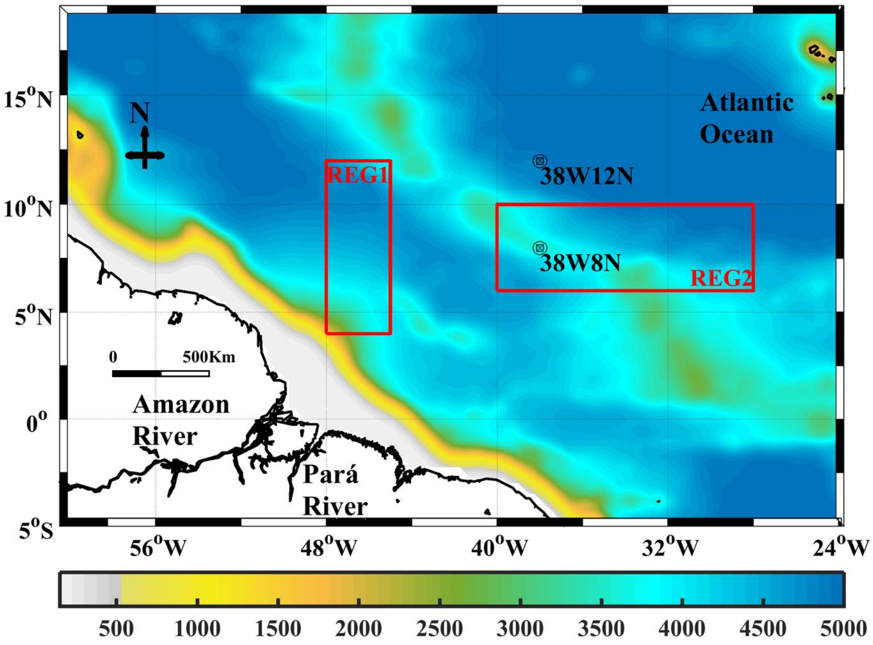

Source: The author

Figure 13. Map of location of the Amazon River delta and its four inputs (North channel, Santa Rosa Bay, Dangerous channel and Jurupari channel)

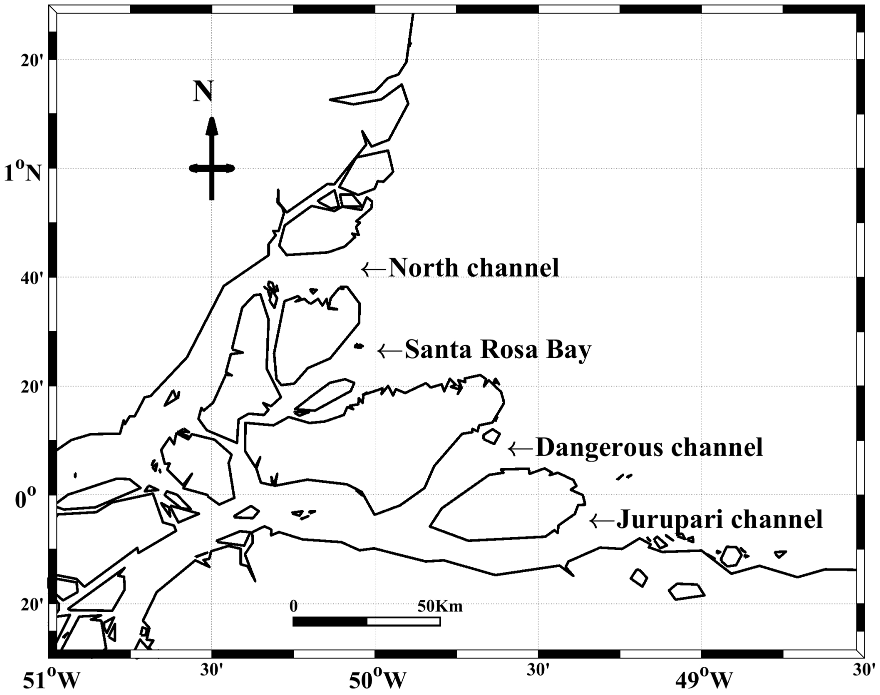

Source: The author

3.2 OBSERVATIONAL DATA

3.2.1 World Ocean Atlas (WOA)

World Ocean Atlas (WOA) is a climate data service created in 1994 by the Ocean Climate Laboratory (OCL) of the National Oceanographic Data Center (NODC), includes monthly, seasonal and annual data of temperature (LOCARNINI et al., 2013), salinity (ZWENG et al., 2013), dissolved oxygen, apparent oxygen utilization, oxygen saturation (GARCIA et al., 2014b) and dissolved inorganic nutrients (GARCIA et al., 2014a) in a global grid with spatial resolution of 1° and 33 levels of standard depths between 0 and 5500 m. This climatology is made from 1900 to 2013. Development of the World Ocean products has been updated in 1994, 1998, 2001, 2005, 2009, and 2013.

3.2.2 Comprehensive Ocean-Atmosphere Data Set (COADS)

Comprehensive Ocean-Atmosphere Data Set is the result of a cooperative project to collect observations of weather measurements near to ocean's surface. The first observations were made by merchant ships. The variables observed are air temperature, SST, wind, pressure, humidity and cloudiness, from these are generated other variables such as surface forcings. From these variables a monthly climatology is made, which are used as inputs of the ROMS model. The spatial resolution of COADS is 2°x2° and the period of time used for this dataset was from 1945 to 1989 (SLUTZ et al., 1985; WOODRUFF et al., 1987).

3.2.3 Simple Ocean Data Assimilation (SODA)

There are several datasets that can be used to validate of the SST and SSS result of the ROMS model, such as SMOS (SST and SSS), Aquarius (Only SSS) and SODA (SST, SSS and currents). In this work it is not convenient to use the data of SMOS and Aquarius because in both there is absence of data in the regions that correspond to the Amazon River mouth and to the band that forms the NBC (blue polygon in figure 14). Being SODA selected for the validations of SST and SSS throughout the study region.

The SODA reanalysis dataset (CARTON; GIESE, 2008) is composed of temperature, salinity, ocean currents and other physical oceanographic variables, these data are produced by a general ocean circulation model based on Smith, Dukowicz & Malone (1992), with a spatial resolution of 0.25°x0.4° and 40 vertical levels with a spacing of 10 meters on the surface. Salt, heat and vertical diffusion of momentum are done through K-profile parameterization (KPP) mixing with modifications to address issues such as diurnal heating, meanwhile lateral subgrid-scale processes are resolved using biharmonic mixing (LARGE; MCWILLIAMS; DONEY, 1994). Sea level is computed by a linearized continuity equation, determined for small ratios of sea level to fluid depth (DUKOWICZ; SMITH, 1994). Daily surface wind speed data is provided by the ERA-40 project of ECMWF (SIMMONS; GIBSON, 2000; UPPALA et al., 2005) and surface freshwater flow is provided by GPCC.

Figure 14. Representation of the SSS of SMOS and Aquarius in November. The blue polygon represents the area where there is no data in both datasets.

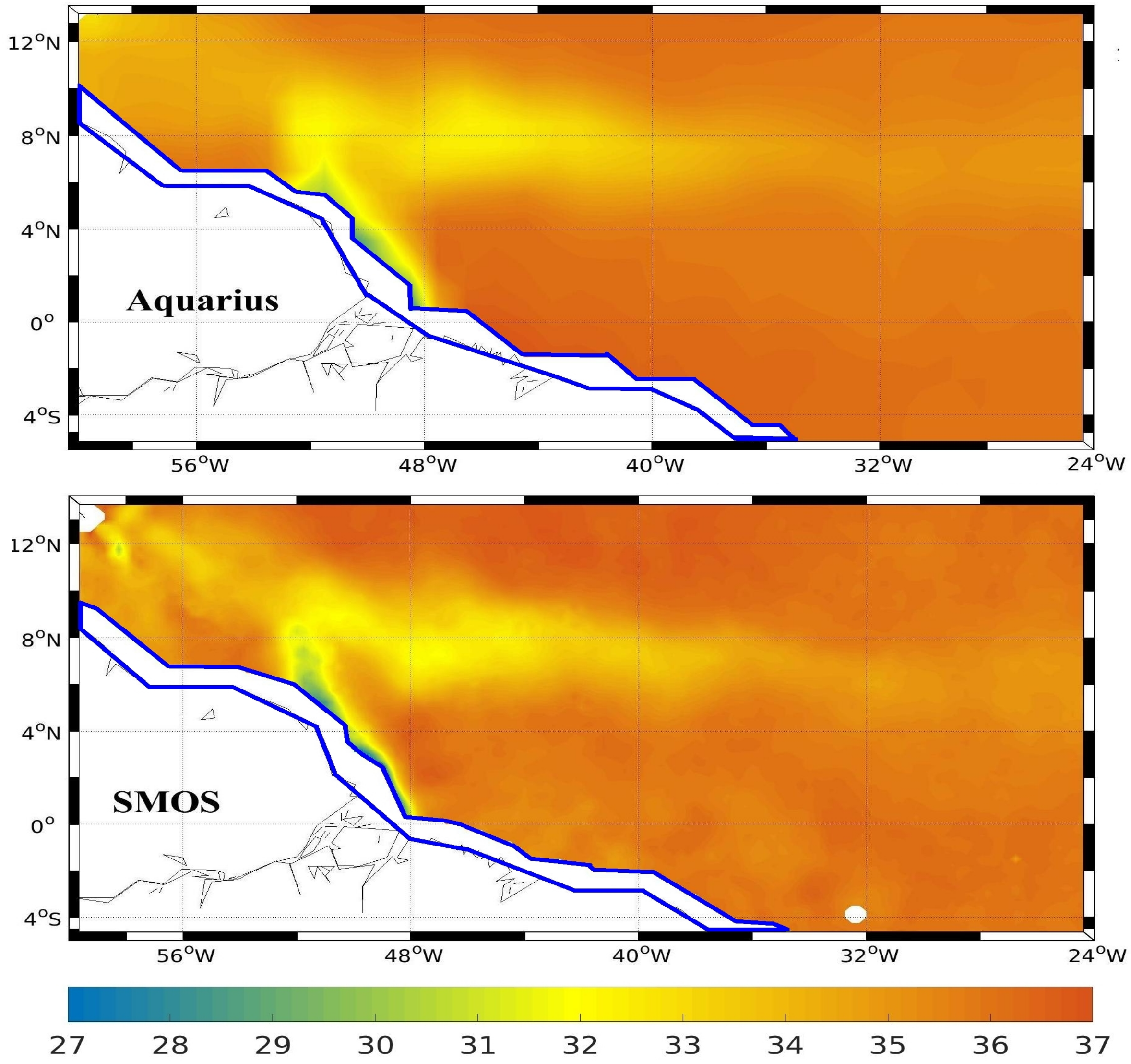

Source: The author

Data assimilation is done every 10 days using incremental analysis (BLOOM et al., 1996), where a time analysis is performed, followed by a simulation of 5 days. On the fifth day there is an update of temperature and salinity. The simulation is repeated from time to time with gradual corrections of temperature and salinity. This maintains a relationship between the geostrophic component of the flux and the pressure and velocity fields. In this way, the average fields are remapped to a uniform global field of horizontal grid with a resolution of 0.5°x0.5° (CARTON; CHEPURIN; CAO, 2000a; CARTON; CHEPURIN; CAO, 2000b). Temperature, salinity, and zonal and meridional velocity components of ocean currents are three-dimensional and Sea Surface Height (SSH) and zonal and meridional components of the vertically integrated velocity are two-dimensional.

SST operational data from AVHRR (NASA) and NOAA are used to update the SODA SST, binned into 1° × 1° bins (CARTON; GIESE, 2008; VAZQUEZ; PERRY; KILPATRICK, 1998; REYNOLDS et al., 2002). The Reynolds & Smith (1994) SST are also used for update SODA SST. The SST of Reynolds & Smith (1994) is obtained from the combination of the satellite, shipboards and buoys observations. The period of time used for this dataset was from 1991 to 2010.

3.2.4 Prediction and Research Moored Array in the Tropical Atlantic (PIRATA)

The Prediction and Research Moored Array in the Tropical Atlantic (PIRATA) dataset (SERVAIN et al., 1998; BOURLÈS et al., 2008) was implemented in the mid-1990s to measure the oceanographic and atmospheric variables in the tropical Atlantic Ocean that affect the climatic variability of this region in seasonal, interannual and longer duration scales. The name of the project was renamed in 2008 as Prediction and Research Moored Array in the Tropical Atlantic. It is supported by INPE, DHN, NOAA, IRD, IFREMER, Meteo-France and CNRS. The period of time used for this dataset was from 2000 to 2015.

3.2.5 Bathymetry

Ocean circulation models, the effect of bathymetry on ocean dynamics is essential. There are international databases obtained from satellite altimetry and depth soundings with ships (SMITH; SANDWELL, 1997) that are used by most models, in this study we use eTOPO2v2 (NCEI, 2006). The vertical datum is Mean Sea Level with 1 meter of precision. The horizontal datum is WGS-84, the horizontal grid spacing is 2-minutes of latitude and longitude, averaged over the cell's area.

3.2.6 Tide TPXO7

TPXO7 is a version 7 of a TOPEX/Poseidon Global Inverse Solution model of ocean tides described by Egbert, Bennett & Foreman (1994) and also by Egbert & Erofeeva (2002). The tides are supplied as amplitudes of earth-relative sea-surface elevation. The main harmonic constituents provided are: Principal lunar (M_2), Principal solar (S_2), Major lunar elliptical (N_2), Luni-solar declinational (K_2), Luni-solar declinational (K_1), Principal lunar (O_1), Principal solar (P_1) and Major lunar elliptical (Q_1); harmonic constituents of long period, Lunar fortnightly (Mf) and Lunar monthly (Mm); and harmonic constituents nonlinear Shallow water overtides of principal lunar constituent (M_4), Shallow water quarter diurnal constituent (MN_4) and Shallow water quarter diurnal constituent (MS_4). The spatial resolution of TPXO7 is 0.25°.

3.2.7 Freshwater river runoff. Dai and Trenberth Global River Flow and Continental Discharge Dataset

Temporary series of monthly river flows at the furthest downstream station of the world's largest 925 rivers (mean and climatological monthly volume at stations), more long-term river flows and continental discharge into the global and individual oceans (DAI; TRENBERTH, 2002). The period of time used for this dataset was from 1948 to 2004. Figure

Figure 15. (a) Monthly distribution of discharge ($m^3 s^{-1}$) of Amazon River (blue lines) and Pará River (black line), from Obidos and Tucuruí gauge stations. (b) Monthly distribution of temperature (°C) of of Amazon River (blue line) and Pará River (black line).

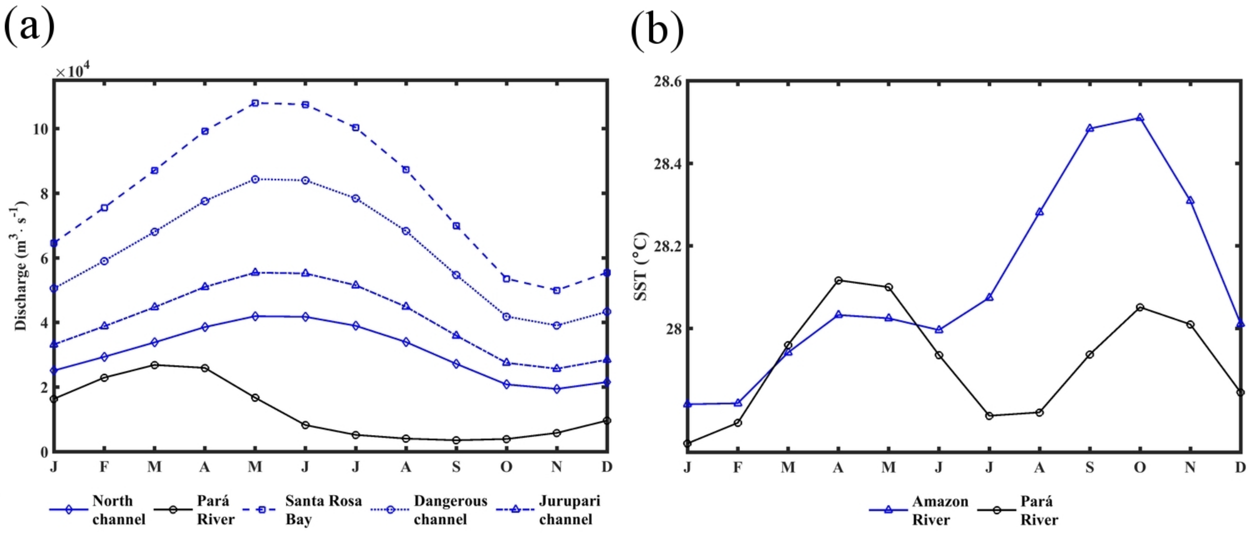

Source: The author

3.3 SURFACE CURRENTS FROM DIAGNOSTIC MODEL (SCUD)

The surface velocities are taken from the SCUD program (MAXIMENKO; HAFNER, 2010), implemented by the Asia Pacific Data Research Center of the International Pacific Research Center (APDRC/IPRC). The SCUD dataset, with spatial resolution of 0.25°, comprises nearly global and daily surface velocities as a result of a simple diagnostic model that combines three sources of scientific information: geostrophic components produced by the sea level anomaly from the Archiving Validation and Interpretation of Satellite Data in Oceanography (AVISO) project and mean dynamic ocean topography from Maximenko et al. (2009). Wind components using satellite daily winds (QuikSCAT) and drifter trajectories which provide consistent data for tuning the diagnostic model. The period of time used for this dataset was from 2000 to 2008.

3.4 NUMERICAL SIMULATION TOOLS

Numerical models are a tool to evaluate and understand the dynamics of the natural environment, simulating computational physical conditions of the same, allowing preventive and corrective to evaluate alternatives for technical and scientifical environmental studies, to reach the improvement and protection of the conditions of the marine - river ecosystem. Numerical models are very useful in assessing impacts on environmental impact studies in the marine environment.

Ocean numerical models are useful for the study of ocean dynamics and are applied to characterize hydrodynamics, for the assessment of environmental impact in the marine environment, for the design of marine works, submarine issuers, dredging, etc.

3.4.1 ROMS model

The ROMS (Regional Oceanic Modeling System) model is an open source software that is actively developed by a large community of programmers and scientists (UCLA, IDR and Rutgers University), with hundreds of thousands of lines of FORTRAN code, which integrates primitive equations into a rotational, surface system free, using the Boussinesq approximation, the hydrostatic approximation and the vertical momentum balance (SHCHEPETKIN; MCWILLIAMS, 2005; SONG; HAIDVOGEL, 1994; PANZER et al., 2013).

ROMS uses orthogonal curvilinear coordinates in the horizontal dimension and generalized sigma coordinates that follow the shape of the ocean floor in the vertical dimension. This was adapted to different geographic regions of world where good results were obtained (HAIDVOGEL et al., 2000; PENVEN et al., 2000; Malanotte-Rizzoli et al., 2000; SHE; KLINCK, 2000; SHE; KLINCK, 2001; PENVEN et al., 2001; LUTJEHARMS; PENVEN; ROY, 2003; CORREA et al., 2008; SILVA et al., 2009).

3.4.1.1 Basic equations of the ROMS AGRIF model

Figure 16 shows several computational pathways for the execution of the ROMS model, the OCEAN model can be used standalone or coupled to waves (**WAVE_OCEAN**) and/or atmospheric (**AIR_OCEAN**) models. These follow the Earth System Modeling Framework (ESMF) conventions for coupling models in the execution sequence (**INITIALIZE**, **RUN** and **FINALIZE**). ROMS dynamic kernel consists of four independent models, including:

NLM Non-Linear model.

TLM Tangent Linear Model.

RPM RePresenter tangent linear Model.

AM Adjoint Model.

There are several drivers to run each model (NLM, TLM, RPM and AM) separately and together. The drivers that are shown in the **PROPAGATOR** group are used for the analysis of Generalized Stability Theory (GST) (MOORE et al., 2004) to study the dynamics, sensitivity and stability of oceanic circulations to naturally occurring perturbations, errors or uncertainties in the system of forecasting and adaptive sampling. The driver for adjoint sensitivities (**ADSEN_OCEAN**) calculates the response of a chosen function of the model's circulation to variations in all physical attributes of the system (MOORE et al., 2004). Includes drivers for strong (**IS4DVAR_OCEAN**) and weak (**W4DVAR_OCEAN**) constraint variational data assimilation (Di Lorenzo et al., 2006). Strong Constraint drivers: Conventional S4DVAR, outer loop, NLM, AM; Incremental **S4DVAR_OCEAN**, inner and outer loops, NLM, TLM, AM (Courtier et al., 1994) and efficient incremental S4DVAR (WEAVER; VIALARD; ANDERSON, 2003). Weak Constraint drivers: Inverse Ocean Modeling (IOM), Indirect Representer Method, inner and outer loops, NLM, TLM, RPM, AM (EGBERT; BENNETT; FOREMAN, 1994). A driver for ensemble prediction is available to perturb forcing and/or initial conditions along the most unstable directions of the state space using singular vectors. Finally, several controllers are included in the sanity check group to test the accuracy and correctness of the TLM, RPM, and AM algorithms.

Figure 16. Working structure of the ROMS model.

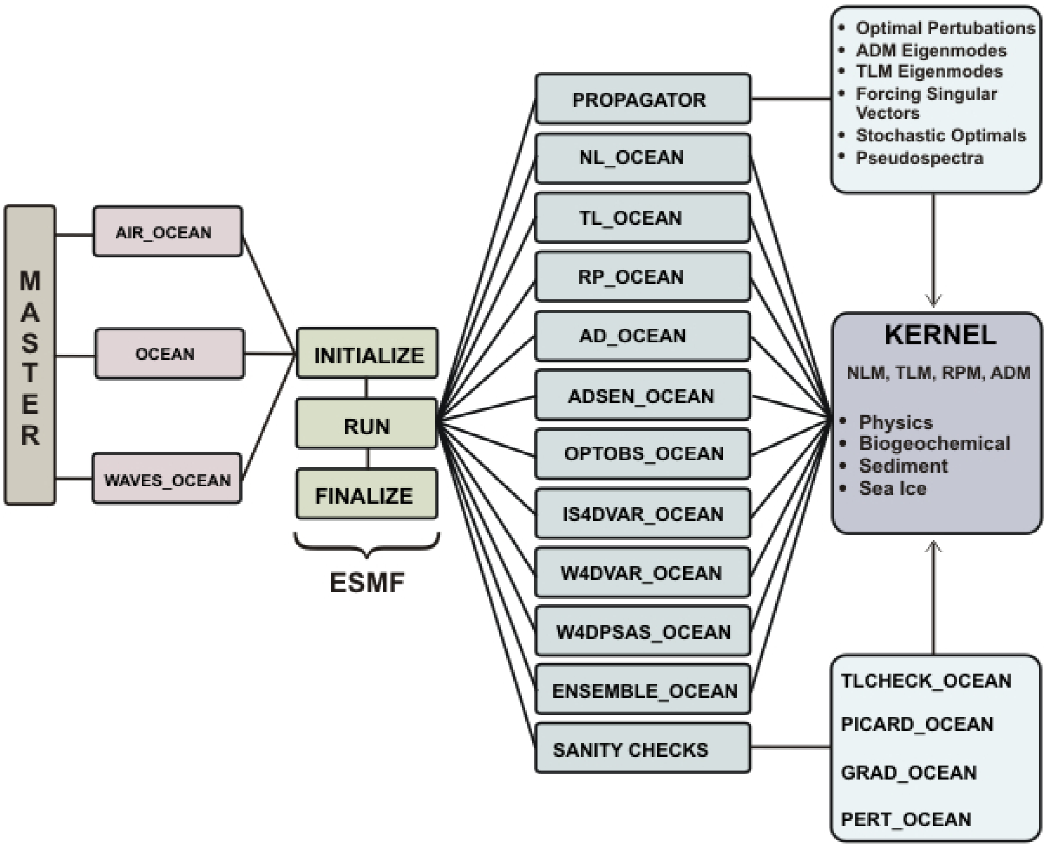

Source: https://www.myroms.org/wiki/Regional_Ocean_Modeling_System_(ROMS)

The primitive equations in Cartesian coordinates are:

$$\frac{\partial u}{\partial t} + \mathbf{v} \cdot \nabla u - fv = -\frac{\partial \phi}{\partial x} - \frac{\partial}{\partial z}(K_M \frac{\partial u}{\partial z}) + \mathcal{F}_u + \mathcal{D}_u \tag{3.1}$$

and

$$\frac{\partial v}{\partial t} + \mathbf{v} \cdot \nabla v - fu = -\frac{\partial \phi}{\partial y} - \frac{\partial}{\partial z}(K_M \frac{\partial v}{\partial z}) + \mathcal{F}_v + \mathcal{D}_v \tag{3.2}$$

The temperature and salinity equations can be written as:

$$\frac{\partial T}{\partial t} + \mathbf{v} \cdot \nabla T = \frac{\partial}{\partial z}(K_H \frac{\partial T}{\partial z}) + \mathcal{F}_T + \mathcal{D}_T \tag{3.3}$$

and

$$\frac{\partial S}{\partial t} + \mathbf{v} \cdot \nabla S = \frac{\partial}{\partial z}(K_H \frac{\partial S}{\partial z}) + \mathcal{F}_S + \mathcal{D}_S \tag{3.4}$$

The advective-diffusive equation is:

$$\rho = \rho(S, T, P) \tag{3.5}$$

The equation of state is given by:

$$\frac{\partial \phi}{\partial z} = -\frac{\rho g}{\rho_o} \tag{3.6}$$

Finally, the continuity equation is:

$$\frac{\partial u}{\partial x} + \frac{\partial v}{\partial y} + \frac{\partial w}{\partial z} = 0 \tag{3.7}$$

The equation (3.5) is the general equation of state, it is taken into account the form of the international equation of state of the sea water (GILL, 1982). The notation used in these equations is:

u, v, w Components of the velocity vector $\mathbf{v}$.

$T(u, v, w, t)$ Potential temperature.

$S(u, v, w, t)$ Salinity.

$\rho_o + \rho(x, y, z, t)$ Total density.

$\phi(x, y, z, t)$ Dynamic pressure. $\phi = P/\rho_o$

P Total pressure. $P \approx \rho_o g z$

f Parameter of Coriolis.

g Acceleration of gravity.

$K_M(x, y, z, t)$ Eddy vertical viscosity.

$K_H(x, y, z, t)$ Eddy vertical diffusivity.

$\mathcal{D}_u, \mathcal{D}_v, \mathcal{D}_T, \mathcal{D}_S$ Vertical Eddy viscosity and diffusivity.

$\mathcal{F}_u, \mathcal{F}_v, \mathcal{F}_T, \mathcal{F}_S$ Forcing terms.

t Time.

3.4.1.2 Horizontal boundary conditions

The domain of the model is logically rectangular, but it is possible to mask the land areas in the contour and in the interior. The boundary conditions on these masked regions are straightforward, with a choice of no-slip or free-slip walls.

If biharmonic friction is used, a higher order boundary condition must also be provided. The model currently has this built-in code where the biharmonic terms are calculated. The higher-order contour conditions used for u are:

$$\frac{\partial}{\partial x}\left(\frac{h\nu}{mn}\frac{\partial^2 u}{\partial x^2}\right) = 0 \tag{3.8}$$

on the east and west limits.

and

$$\frac{\partial}{\partial y}\left(\frac{h\nu}{mn}\frac{\partial^2 u}{\partial y^2}\right) = 0 \tag{3.9}$$

on the north and south limits. Where ν is the horizontal viscosity.

The boundary conditions for v, T and S are similar. These contour conditions were chosen because they preserve the property of no gain or loss of momentum of the integrated volume, temperature or salinity.

3.4.1.3 Vertical boundary conditions

The vertical boundary conditions can be prescribed as follows:

On the surface ($z = \zeta(x, y, t)$)

$$K_M \frac{\partial u}{\partial z} = \tau_s^x(x, y, t) \tag{3.10}$$

$$K_M \frac{\partial v}{\partial z} = \tau_s^y(x, y, t) \tag{3.11}$$

$$K_T \frac{\partial T}{\partial z} = \frac{Q_T}{\rho_o c_p} + \frac{1}{\rho_o c_p}\frac{dQ_T}{dT}(T - T_{ref}) \tag{3.12}$$

$$K_S \frac{\partial S}{\partial z} = (E - P_r)S \tag{3.13}$$

$$w = \frac{\partial \zeta}{\partial t} \tag{3.14}$$

On the seabed ($z = -h(x, y)$)

$$K_M \frac{\partial u}{\partial z} = \tau_b^x(x, y, t) \tag{3.15}$$

$$K_M \frac{\partial v}{\partial z} = \tau_b^y(x, y, t) \tag{3.16}$$

$$K_T \frac{\partial T}{\partial z} = 0 \tag{3.17}$$

$$K_S \frac{\partial S}{\partial z} = 0 \tag{3.18}$$

$$-w + \mathbf{v} \cdot \nabla h = 0 \tag{3.19}$$

Where:

$h(x, y)$ Depth.

$\zeta(x, y, t)$ Surface elevation.

τ_s^x, τ_s^y Surface wind stress.

τ_b^x, τ_b^y Bottom stress.

$E - P_r$ Evaporation minus precipitation.

Q_T Surface heat flux.

T_{ref} Surface reference temperature.

Q_T is a strong function of surface temperature, it is also prudent to include a correction term for the Q change, as the surface temperature moves away from the reference temperature that was used to calculate Q_T. In the background, $z = -h(x, y)$, the horizontal velocity components are limited to accommodate the background forcing which is a sum of linear and quadratic terms:

$$\tau_b^x = (\gamma_1 + \gamma_2 \sqrt{u^2 + v^2})u \tag{3.20}$$

$$\tau_b^y = (\gamma_1 + \gamma_2 \sqrt{u^2 + v^2})v \tag{3.21}$$

γ_1, γ_2 are the linear and quadratic coefficients of the bottom forcing.

A better description of the ROMS model can be found in Hedstrom (1997), Hedstrom (2009).

3.4.1.4 Vertical coordinates

ROMS vertically uses the so-called sigma-coordinate (σ coordinate) system (SONG; HAIDVOGEL, 1994; HAIDVOGEL et al., 2000). The σ coordinate models, or "terrain-following" are especially suitable in regions with variable bottom topography and in which the processes of interaction with the background boundary layer are important. The main attraction of such models lies in the smooth representation of topography and in its ability to simulate the interactions between flow and bathymetry (EZER; ARANGO; SHCHEPETKIN, 2002).

3.4.1.5 Spatial and temporal discretization

The model is discretized horizontally in a rectangular and isotropic Arakawa type C structured mesh (ARAKAWA; LAMB, 1977), is discretized vertically in a curvilinear σ coordinate system that follows the shape of the bottom and the coastline (SONG; HAIDVOGEL, 1994). It uses two time steps, one for the barotropic external oscillation mode (with a shorter time interval) that satisfies the continuity equation and another baroclinic internal (with a longer time interval), both fulfilling the CFL convergence condition (SHCHEPETKIN, 2015).

3.4.1.6 Pre and post-processing of data

The grids of bathymetry, forcing, initial and contour conditions were constructed using the ROMSTOOLS package developed by the IRD (PENVEN et al., 2007). This package includes tools like **nestgui** for nesting the meshes and **roms_gui** for visualizing the results. Finally it has scripts to run it in inter-annual and climatic modes. The operation of such tools is described in Penven et al. (2010).

3.4.1.7 Lateral boundary and initial conditions

The grid generated from the bathymetry has a spatial resolution of 0.25° and 32 vertical levels in sigma-coordinates. The four lateral boundaries are considered open, in the lateral boundary and initial conditions all variables were obtained from the monthly mean of World

Ocean Atlas 2009 (WOA09) with a resolution of 1°. The surface forcings were obtained from monthly mean climatology of Comprehensive Ocean–Atmosphere Data Set (COADS05) (Da Silva; YOUNG; LEVITUS, 1994) with 0.5° of resolution. Tides are an important process in mixing the river freshwater plumes with the open ocean and are obtained from the TPXO7 (EGBERT; BENNETT; FOREMAN, 1994; EGBERT; EROFEEVA, 2002), which has altimetry data from several satellites to improve the accuracy of the results obtained through the hydrodynamic model (WANG, 2004; D'ONOFRIO; OREIRO; FIORE, 2012). The monthly means river discharge were obtained from Obidos and Tucurui gauge stations (DAI; TRENBERTH, 2002), the monthly climatology of SST in the rivers discharge points was also obtained from WOA09.

3.4.1.8 Experiment configuration

We have carried out two numerical experiments to estimate the potential impact of Amazons and Pará rivers in the salinity, temperature and surface currents on the WTNA. In the first experiment, River Runoff (RRF), the Amazon and Pará Rivers release freshwater into the WTNA, given the geographical configuration of Amazon River Delta, there are four inputs from the river to WTNA (Figure 13): Canal do Norte, Baia de Santa Rosa, Canal Perigoso and Canal do Jurupari, the inputs are placed in four cells of the grid, considering the width of each channel the contribution was calculated for each one, distributed in 14.47%, 37.27%, 29.13% and 19.13% respectively (Figure 15(a)), with the same monthly temperature distribution for the four inputs nodes in the Amazon River Delta and different in the input node of the Pará River (Figure 15(b)). In the second experiment, No-River Runoff (NRF), the Amazon and Pará Rivers do not release freshwater into the WTNA, with the same parametrization as the first experiment. We run each experiment for 11 years, but our analyses are restricted to the last 3 years.

3.4.2 GAS_DOCEAN model

In this study the evolution of the plumes of oil and gas through the water column was estimated based on the theory proposed by Leite et al. (2014), Fannelop & Sjoen (1980), Zheng & Yapa (1998), Friedl & Fanneløp (2000), Zheng & Yapa (2000), Yapa, Zheng & Chen (2001), Zheng & Yapa (2002), Chen & Yapa (2004). These studies were used for the elaboration of computational routines that could represent the simultaneous transport of oil and natural gas. This model was also previously used in the evaluation of the evolution of plumes of natural gas and/or oil resulting from an eventual blowout on the oceanic floor (LEITE et al., 2014).

The new implementations to the GAS_DOCEAN code (version 3.0) allow the simulations of engaged/simultaneous evolution of the plumes of oil and natural gas. The adopted methodology follows the theoretical-experimental approach proposed by Chen & Yapa (2004). The decrease of the pressure that makes the gas expand in volume, the temperature decrease may induce the formation of hydrates starting from lighter hydrocarbon chains (ZHENG; YAPA, 2002; CHEN;

YAPA, 2004). So, under these new conditions of pressure and temperature, the mixture tends to hydrate. With the formation of hydrates, the upwelling time for the gas along the water column will be incremented since their presence will induce the reduction of ascending velocity of the gas plume (TOPHAM, 1984a; CHEN; YAPA, 2001; JOHANSEN, 2003). The physical-chemical characteristics of the oil, necessary for simulations, were then calculated from each depth through parameterized equations inserted in the mathematical model, and taken from experimental curves obtained in laboratory (LEITE et al., 2014).

3.4.2.1 Basic equations of the GAS_DOCEAN model

The equations are discretized using a lagrangean control-volume, and local variations of mass inside the plumes are treated taking into account the prime mechanisms of water entrainment, oil dissolution and gas hydrate formation. In order to follow the usual framework and notations concerning previous modelling approaches we have adopted here the scheme proposed by Friedl & Fanneløp (2000) (Figure 3).

The position of each control volume along the simulation is obtained as follows:

$$h = |V|\Delta t \tag{3.22}$$

$$\Delta t = \frac{0.1 \cdot b_0}{|V_0|} \tag{3.23}$$

where:

h Depth of control volume (m).
V Total velocity ($m \cdot s^{-1}$).
Δt Time step (s).
b_0 Ratio of initial control-volume (m).
V_0 Initial blowout velocity ($m \cdot s^{-1}$).

Recent implementations in the GAS_DOCEAN code are mainly related to the inclusion of the coupled/simultaneous dynamics of evolution of the plumes of oil and gas. The adopted methodology follows the theoretical-experimental approach proposed by Chen & Yapa (2004) and illustrated in figure 17.

Separation between the two plumes occurs in regard to their speed of ascension and the strength of horizontal advection imposed by the oceanic currents. The critical length, from which the separation is observed between the plumes of oil and gas, is calculated comparing the momentum in the control-volume (gas and oil) with the horizontal momentum induced by environmental current fields.

The GAS_DOCEAN model uses the theoretical concept developed by Davidson & Pun (1999) and Davidson & Wang (2002) for estimating the eventual separation between oil and gas plumes along the seawater column. This approach defines, for each step of time, the excess momentum (per unit density - M_0) of the mixture according to the environment forcing, as follows:

Figure 17. Theoretical-experimental scheme for displacement of oil and gas plumes used in simulations.

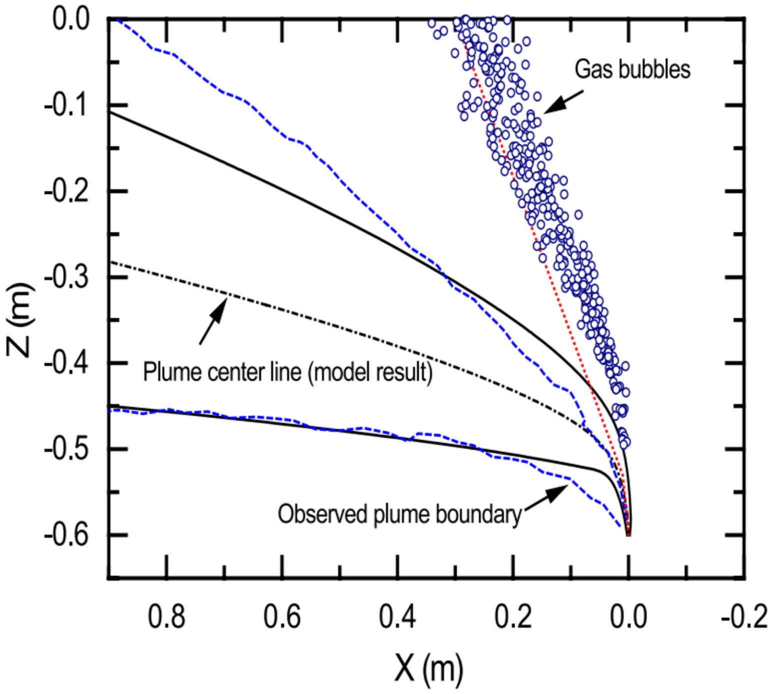

Source: Chen & Yapa (2004)

$$M_0 = \pi \cdot (U_0 - U_A) \cdot U_0 \cdot b_0^2 \tag{3.24}$$

where:

M_0 Momentum excess in the control-volume (gas + oil) ($m^4 \cdot s^{-4}$).
U_0 Velocity of the mixture oil + gas ($m \cdot s^{-1}$).
U_A Velocity of the currents in the ocean ($m \cdot s^{-1}$).

The characteristic length scale X_{SW} (m) that relates the excess momentum in the mixture (oil + gas) to the ocean momentum (always by units of density) is given by:

$$X_{SW} \simeq \frac{M_0^{1/2}}{U_A} \tag{3.25}$$

The characteristic length scale X_{SW}, estimated by the equation 3.25 and calculated at each numerical step of time, furnishes an indication of the location along the water column of the transition between the strong advective behavior and the weak advection. Laboratory experiments indicate that the separation between the two plumes (oil and gas) occurs, indeed X_{SEP}, when the excess of momentum in the external environment (in this case the ocean) is about 100−fold the plumes momentum, or:

$$\frac{X_{SEP}}{M_0^{1/2}/U_A} \leq 100 \tag{3.26}$$

A second upgrade in this new version of the GAS_DOCEAN model is the routines that consider hydration mechanisms of the gas (TOPHAM, 1984a; CHEN; YAPA, 2001) and the dissolution of the gas (JOHANSEN, 2003; ZHENG; YAPA, 2002) in the liquid environment.

In the hydration mechanism of the gas, each particle (considered spherical) is treated considering that it is involved by a diffusive layer, superimposed to an absorption layer. From this sub-model, the transformation of the gas into hydrates is driven by the equation 3.27. More details can be found in the works of Englezos et al. (1987).

$$\left(\frac{dn}{dt}\right)_P = K^* \cdot A_P \cdot (f - f_{EQ}) \tag{3.27}$$

where:

n Number of moles of consumed gas ($moles$).
K^* Rate of diffusion + absorption of the gas ($m \cdot s^{-1}$).
A_P Surface area of the particle (m^2).
f Dissolved gas fugacity ($mol \cdot m^{-3}$).
f_{EQ} Three-phase equilibrium fugacity of the gas ($mol \cdot m^{-3}$).

The process of gas dissolution in the liquid environment is considered through the following expression (ZHENG; YAPA, 2002):

$$\frac{dn}{dt} = K \cdot A \cdot (C_S - C_0) \tag{3.28}$$

where:

K Coefficient of mass transfer ($m \cdot s^{-1}$).
A Surface area of the gas normal to flow direction (m^2).
C_S Dissolved saturation gas concentration inside the control-volume ($mol \cdot m^{-3}$).
C_0 Dissolved gas concentration inside the control-volume ($mol \cdot m^{-3}$).

The main set of derivative mass-balance equations in GAS_DOCEAN model are presented following and more details can be found in Yapa & Zheng (1997).

$$\begin{aligned}
\frac{d}{dt}[(m_l + m_b + m_h)\,u] &= u_a\rho_a Q_e - u\rho_{com}Q_g \\
\frac{d}{dt}[(m_l + m_b + m_h)\,v] &= v_a\rho_a Q_e - v\rho_{com}Q_g \\
\frac{d}{dt}[m_l w + (m_b + m_h)(w + w_b)] &= w_a\rho_a Q_e - w\rho_{com}Q_g + \\
&\quad +(\rho_a - \rho_l)g\pi b^2(1-\beta\varepsilon)h + \\
&\quad +(\rho_a - \rho_{com})g\pi b^2\beta^2\varepsilon h
\end{aligned} \tag{3.29}$$

where:

m_l Mass of liquid of plume (kg).

m_b Mass of gas of plume (kg).

m_h Mass of hydrates inside the plume (kg).

u Horizontal velocity of plume at x direction ($m \cdot s^{-1}$).

u_a Ambient horizontal velocity of plume at x direction ($m \cdot s^{-1}$).

v Horizontal velocity of plume at y direction ($m \cdot s^{-1}$).

v_a Ambient horizontal velocity of plume at y direction ($m \cdot s^{-1}$).

w Vertical velocity of plume ($m \cdot s^{-1}$).

w_a Ambient vertical velocity ($m \cdot s^{-1}$).

w_b Gas bubbles velocity ($m \cdot s^{-1}$).

ρ_l Liquid density of plume ($kg \cdot m^{-3}$).

ρ_a Density of ambient seawater ($kg \cdot m^{-3}$).

ρ_{com} Density of hydrates and gas($kg \cdot m^{-3}$).

Q_e Entrainment water flux ($m^3 \cdot s^{-1}$).

Q_g Gás flux ($m^3 \cdot s^{-1}$).

g Acceleration of gravity ($m^2 \cdot s^{-1}$).

b Plume ratio (m).

ε Gas fraction, defined as $\varepsilon = (\rho_l - \rho)/(\rho_l - \rho_{com})$.

β Ratio between the bubble core width and the buoyant jet diameter, varies from 0.65 to 0.8

h Depth of control volume (m).

At the deep ocean the gas is considered as non-ideal, so we have:

$$PM_g = \rho_b F_c RT \tag{3.30}$$

where:

P Ambient pressure from (Pa).

M_g Gas mol weight ($kg \cdot mol^{-1}$).

F_c Compress factor.
R Universal gas constant ($8,314 J \cdot mol^{-1} \cdot K^{-1}$).
ρ_b Gas density ($kg \cdot m^3$).
T Temperature (K).

In geophysical deep ocean situations, the important independent variables are the total kinematics buoyancy flux (B) and the buoyancy frequency (N), defined by Socolofsky & Adams (2005) as:

$$B = \frac{gQ_B(\rho_a - \rho_b)}{\bar{\rho}_a} \tag{3.31}$$

$$N_{BV} = \left[-\frac{g}{\bar{\rho}_l} \left(\frac{\partial \rho_l}{\partial z} \right) \right]^{1/2} \tag{3.32}$$

where:
B Buoyancy of gas plume ($m^4 \cdot s^{-3}$).
N_{BV} Brunt-Vaisala frequency (s^{-1}).
Q_B Gas flux ($m^3 \cdot s^{-1}$).

The dimensional analysis performed by Socolofsky & Adams (2005) introduces a single nondimensional number that describes the first-order effects of the dispersed phase:

$$U_N = \frac{U_S}{(B \cdot N)^{1/4}} \tag{3.33}$$

where:
U_N Nondimensional velocity.
U_S Bubble slip velocity ($m \cdot s^{-1}$).

Asaeda & Imberger (1993) presents three different plume types as observed in laboratory studies and Socolofsky & Adams (2005) identified the behavior of another type of plume (Figure 18). For each kind of plume shape, it is possible to estimate the corresponding U_N as presented in Table 1 (SOCOLOFSKY; ADAMS, 2005). The plume Type 1* is different to Type 1, defined by:

$$H_T = H + H_A \tag{3.34}$$

Figure 18. Schematic of plume type classification: H_T is trap height of the first peel and H is reservoir depth.

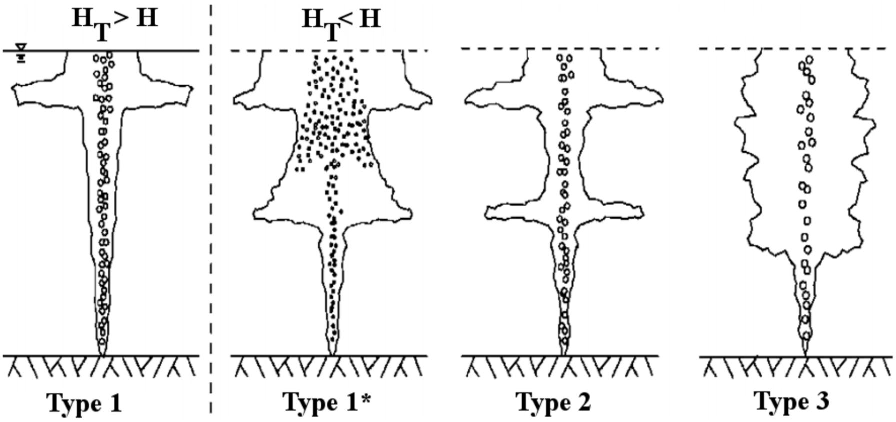

Source: Socolofsky & Adams (2005)

H_T is the local H depth plus the atmospheric pressure head H_A. If the height of the plume trap is higher then H_T (i.e., $h > H_T$) the plume is classified as Type 1. Otherwise if $h < H_T$, the plume has a Type 1* behavior.

Table 1. U_N intervals for plume classification

U_N range	Type
$0 < U_N < 1.5$	1
$0 < U_N < 1.5$	1*
$1.5 \leq U_N < 2.5$	2
$U_N \geq 2.5$	3

Source: Socolofsky & Adams (2005)

3.4.2.2 Parameterization of GAS_DOCEAN model

Table 2 shows the values of the main parameters of the GAS_DOCEAN model.

Table 2. Parameterization of GAS_DOCEAN

Parameters	**Value**
Ratio between the bubble core width and the buoyant jet diameter	0.8
Gas density	$5 \times 10^{-3}\, kg \cdot m^{-3}$
Density of hydrates and gas	$912, kg \cdot m^{-3}$
Initial shear entrainment coefficient	0.083
Gas flow	$50\, kg \cdot s^{-1}$
Oil flow	$100\, kg \cdot s^{-1}$
Mass transfer coefficient of dissolution	$10^{-9}\, m \cdot s{-}1$

Source: Yapa & Chen (2004)

The points $P1$, $P2$ and $P3$ (Figure 19) were selected according to the position of the oil and gas exploration blocks in the north continental shelf of Brazil and the analysis of oil sensitivity charts (SAO charts) of the areas subject to oil spill and blowouts in the region comprising the continental shelves of Amazonas and Pará - Maranhão – Barreirinhas. The Amazon Continental Shelf (ACS) is a high priority area for the conservation of biodiversity (JUNIOR; MAGRINI, 2014; SANTOS; MENDES; SILVEIRA, 2016), the Amazon River mouth represents the limit of the distribution of several sponges, lobster, stony corals and snapper and others shallow water fish, among other groups of coastal and reef organisms (MOURA et al., 2016).

Figure 19. The bathymetry and distribution of the slope in the continental shelf northwest of Brazil. The green rectangle represent the Amazon mouth basin and the magenta rectangle represent Pará-Maranhão-Barreirinhas basin. The oil and gas exploration blocks are represented by black polygons. The location of P1, P2 and P3 is represented by blue points above of exploration blocks where P1, P2 and P3 are placed, block FZA-M-88 ($P1$), block PAMA-M-337 ($P2$) and block BAR-M-21 ($P3$). The coral reef appears in red color.

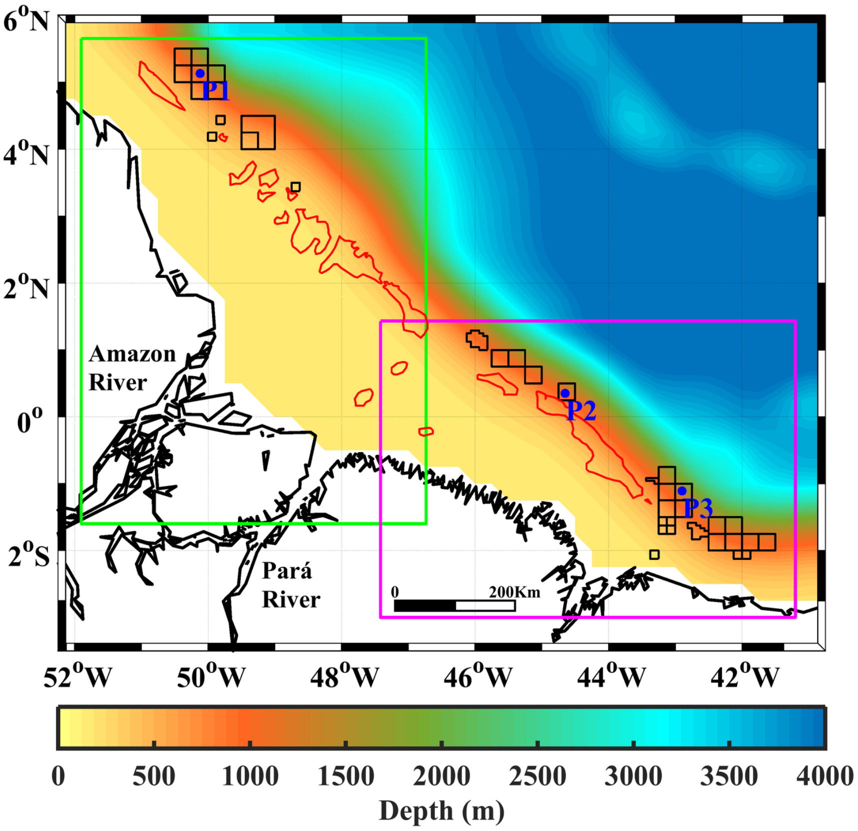

Source: The author

$P1$ is located on it, at $(50.12°W, 5, 12°N)$ and belongs to the exploration block FZA-M-88; $P2$ is in the Pará - Maranhão basin at $(44.63°W, 0.38°N)$, coinciding with the exploration block PAMA-M-337 and $P3$ it's located in exploration block BAR-M-21 at $(42.75°W, 1°S)$ in the Barreirinhas basin.

The dilution capacity of the effluent overflow will be analyzed in a blowout event at

P1, P2 and P3 as a result of the simultaneous effects of sea currents, winds and surface and subsurface thermodynamic processes acting at the adjacent oceanic area. This analysis will be held through hydrodynamics simulation, mathematical modeling and numeric simulation of the dispersion mechanism acting over the plumes of oil and natural gas in the study region. The simulations of the oil and gas blowouts were performed taking into account a flow of 100 and $50\,kg \cdot s^{-1}$ respectively (Table 2) and the other parameters were taken from (YAPA; CHEN, 2004).

3.5 MIXED LAYER DEPTH (MLD), ISOTHERMAL LAYER DEPTH (ILD) AND BARRIER LAYER THICKNESS (BLT) CRITERION

MLD defined as the depth where the density increases from the surface value due to a prescribed temperature decrease of $0.2°C$ ($\Delta T = -0.2°C$) from the surface value while maintaining constant surface salinity value. The MLD was mathematically defined by Sprintall & Tomczak (1992) and Montégut et al. (2007) as:

$$\Delta\sigma = \sigma(T + \Delta T, S, P_0) - \sigma(T, S, P_0) \tag{3.35}$$

where $\Delta\sigma$ is densities difference for the same change in temperature (ΔT) at constant salinity, T, S are the values of temperature and salinity at Z_{REF} (reference depth in the temperature and salinity vertical profiles) and P_0 is the pressure at the ocean surfaces.

In this study we consider $Z_{REF} = 5\ m$, also used by Hounsou-Gbo et al. (2016) and different from that used by other authors, e.g. Montégut et al. (2007), this value was chosen because in the region of the Atlantic the MLD can be found at depths less than 10 m; and in the outputs of the RRF and NRF experiments we have 32 vertical levels, corresponding the level 32 to the ocean surface and the level 31 to $4.8\,m$ depth. The ILD is the depth at which the temperature is equal to $T + \Delta T$.

The Barrier Layer (BL) prevents heat exchange between the Oceanic Mixed Layer (OML) and deeper water, influencing the SST, ensuring greater isolation of the OML, while thicker it is, less heat exchange will exist between deep water and the OML. The BLT can be calculated according Montégut et al. (2007) as:

$$BLT = ILD - MLD$$

3.6 OCEANIC HEAT CONTENT (OHC) CRITERION

The transfer of mass, momentum and energy through the mixing layer is the source of almost all oceanic movements, and its thickness determines the heat content and the mechanical inertia of the layer that interacts directly with the atmosphere (MONTÉGUT et al., 2004). Changes in oceanic heat content play an important role in sea level rise due to thermal expansion. The quantity of energy stored per unit area in the ocean (OHC) between levels Z_{REF} and h is defined according to Jayne, Wahr & Bryan (2003) as:

$$OHC = \rho_0 C_p \int_{Z_{REF}}^{h} T(Z)\, dZ$$

where: OHC is the Oceanic Heat Content in $J\, m^{-2}$, $\rho_0 = 1025\, kg\, m^{-3}$ is the density of seawater at the sea surface, $C_p = 4 \cdot 10^3 J\, (kg -^{\circ} C)^{-1}$ is the specific heat of seawater at constant pressure at the sea surface, according to Levitus, Antonov & Boyer (2005), $T(Z)$ is the potential temperature ($^{\circ}C$), Z is the depth (m) and $Z_{REF} = 5\ m$.

As the depth increases, the temperature oscillation decreases and below the active ocean layer, there are practically no annual variations in temperature, so we are only going to study the quantity of heat in the active layer of the ocean, numerically integrating the temperature in each vertical profile in the grids of the RRF and NRF experiments, from Z_{REF} to $h = ILD$. For the determination of MLD, ILD, BLT and OHC, the temperature and salinity are linearly interpolated every $1\, m$ depth from Z_{REF}, following the procedures and equations described above.

4 HYDRODYNAMIC MODEL: RESULTS AND DISCUSSIONS

In this chapter the following results are detailed:

- Hydrodynamical model: Two hydrodynamical simulations are carried out with the ROMS model, in the first one (RRF experiment), the release of freshwater from the Amazon and Pará rivers in the tropical Atlantic is taken into account; and the second one (NRF experiment) is supposed not to release freshwater.
- Validation of model results with rivers: The salinity, temperature and currents of the ROMS model (RRF experiment) are compared with the SODA, PIRATA and SCUD datasets.
- Influence of rivers on WTNA: The variations produced by the rivers in the SST, SSS, MLD, ILD, BLT and OHC fields are quantified, finally, the NECC offset is determined due to the influence of the rivers.

These results correspond to the article "Amazon River plume influence in the western Tropical Atlantic dynamic variability" that was submitted in the Dynamics of Atmospheres and Oceans journal.

4.1 VALIDATION OF THE HYDRODYNAMIC MODEL

The difference of SSS between the model simulation with river (RRF) and SODA is shown in figure 20. Modeled mean SSS present lower salinities than SODA in the area of the NBC retroflection mainly during April to June. From September to December, the lower salinities are following the NECC.

Figure 20. Mean monthly cycle of the difference between SSS (psu) of RRF experiment and SODA dataset.

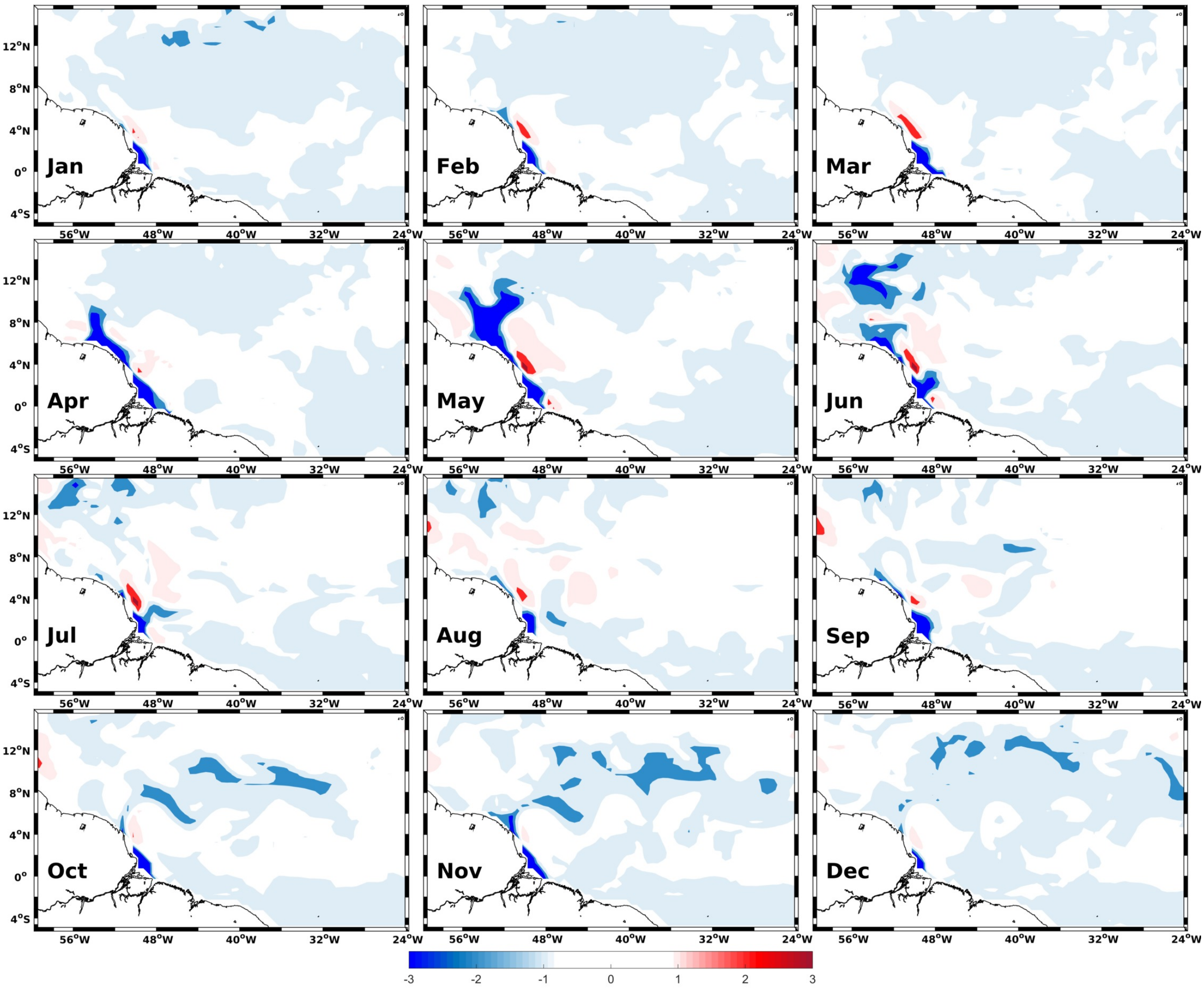

Source: The author

Table 3 (columns 1 and 2) shows a summary of the seasonal cycles averaged for the area REG2 (defined in figure 12). The SSS maximum difference is from June to August (0.27 *psu*) and a minimum difference is from March to May (0.06 *psu*).

Table 3. Comparison between the SSS RRF and SODA in REG2, area defined in figure 12. In the first rows mean value ± standard deviation and in the second rows minimum − maximum.

	SODA (psu)	RRF (psu)	SODA ($°C$)	RRF ($°C$)
DJF	35.86 ± 0.02 (35.56 – 36.10)	35.63 ± 0.07 (34.94 – 36.19)	26.90 ± 0.04 (26.02 – 27.48)	28.17 ± 0.14 (26.47 – 29.12)
MAM	36.09 ± 0.02 (35.87 – 36.32)	36.15 ± 0.01 (35.81 – 36.47)	26.74 ± 0.10 (25.60 – 27.61)	27.05 ± 0.27 (25.73 – 28.31)
JJA	35.82 ± 0.03 (35.43 – 36.15)	36.09 ± 0.05 (35.46 – 36.51)	27.77 ± 0.07 (27.15 – 28.30)	27.77 ± 0.23 (26.27 – 28.84)
SON	35.41 ± 0.07 (34.89 – 35.87)	35.23 ± 0.13 (34.19 – 36.26)	28.26 ± 0.04 (27.84 – 28.74)	28.63 ± 0.13 (27.63 – 29.69)
Annual	35.79 ± 0.03 (35.44 – 36.11)	35.78 ± 0.08 (35.10 – 36.36)	27.42 ± 0.07 (26.65 – 28.03)	27.91 ± 0.19 (26.53 – 28.99)

Source: The author

The difference of SST between the model simulation with river (RRF) and SODA is shown in figure 21. Modeled mean SST present higher temperatures than SODA in the area of the NBC retroflection, mainly during October to February and also in the NECC area. The cause of this large seasonal variation is assumed to be a dynamic adjustment due to changes in wind forcing over the tropical Atlantic and both local and remote wind stress that may play a role in the SST variability (JOHNS et al., 1998; BOURLES; GOURIOU; CHUCHLA, 1999b; SHARMA et al., 2009).

Figure 21. Mean monthly cycle of the difference between SST (°C) of RRF experiment and SODA dataset.

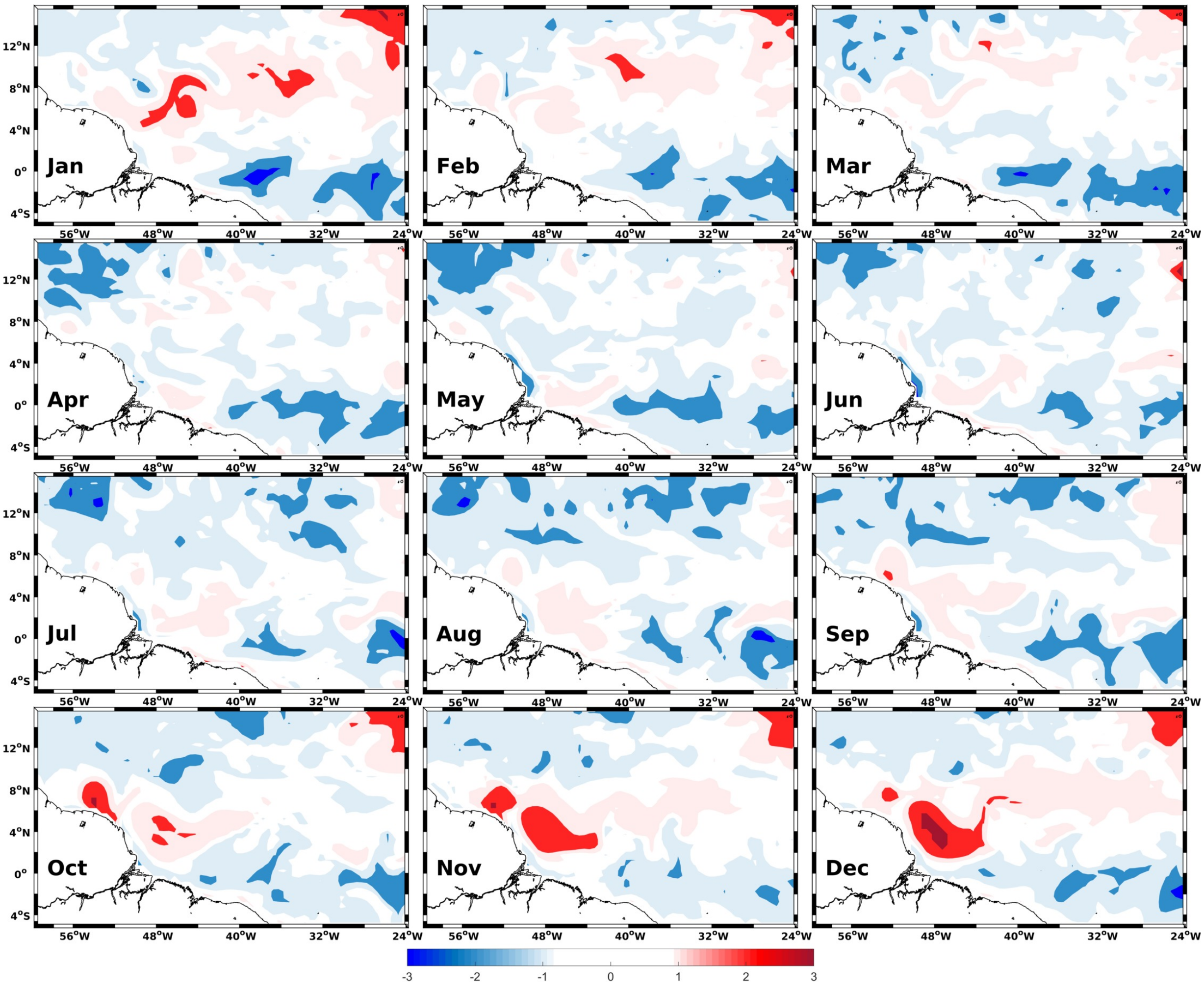

Source: The author

The Table 3 (columns 3 and 4) resume the main results of modeled SST and SODA, evidencing higher difference in December to February, when we have the plume feeding the NECC. The RRF is well adjusted in June to August.

The figure 22 shows the comparison of RRF simulation and PIRATA salinity and temperature profiles. The modeled salinity at the position $8^\circ N 38^\circ W$ (Figure 22(a)) shows similar vertical structure, mainly from August to December, period of lower salinities from the plume. The main differences are from June to October, mainly in the first 40 m, which is coincident with the period that the freshwater of the Amazon plume flows into the NECC (COLES et al., 2013; GRODSKY et al., 2014).

Figure 22. Hovmüller diagram of RRF (red dashed lines) and PIRATA buoy (blue solid lines), monthly mean calculated from 2000 to 2015 at $38°W8°N$ (a) salinity vertical profile (psu) and (b) temperature vertical profile ($°C$) and at $38°W12°N$ (c) salinity vertical profile (psu) and (d) temperature vertical profile ($°C$).

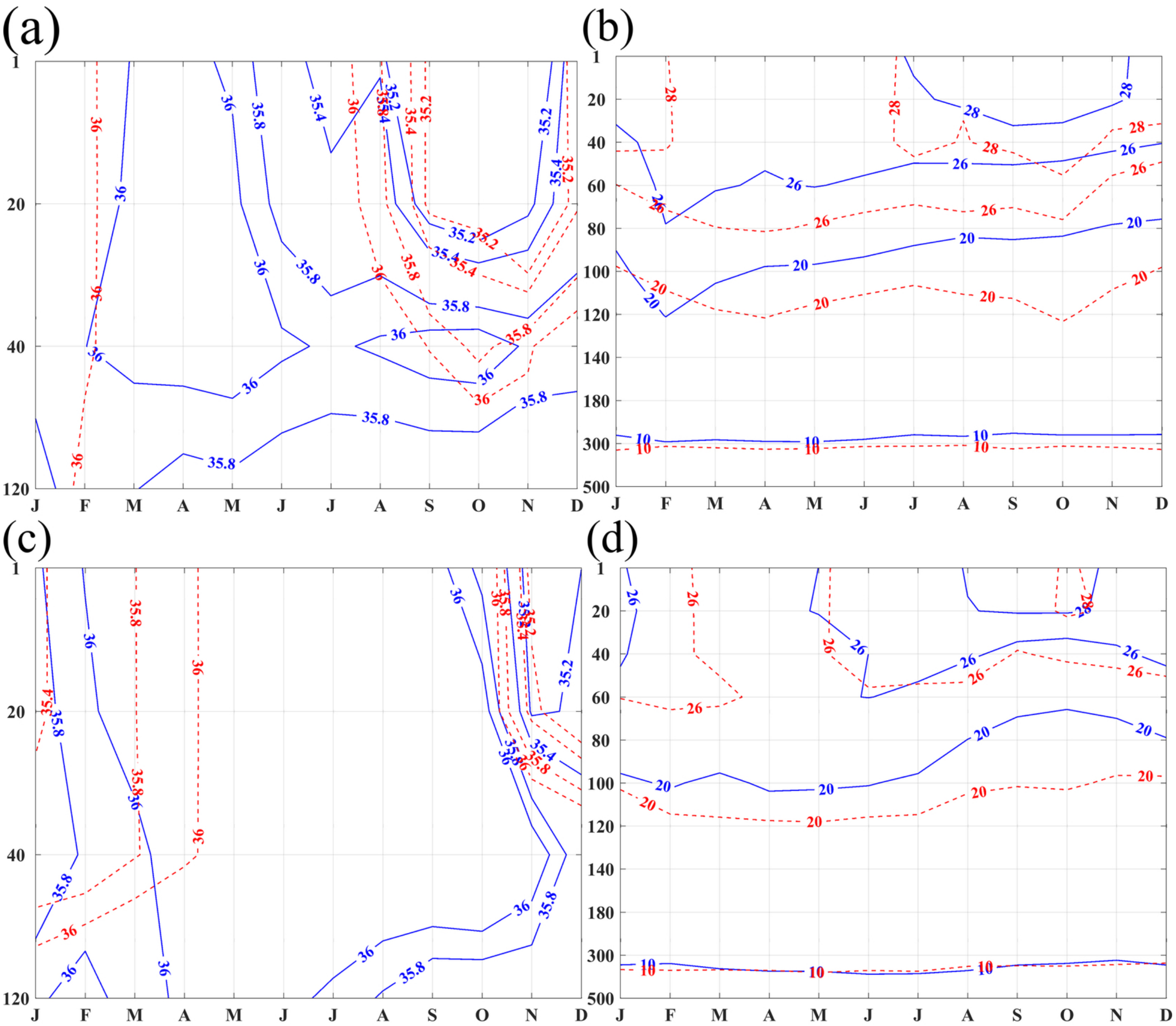

Source: The author

In order to compare the vertical profiles of salinity and temperature of the RRF experiment with the PIRATA dataset, we used the two-sample t-student test. Prior to performing the t-test, data were normalized by dividing each profile by its norm, since the initial dataset showed a non-normal distribution (one-sample Kolmogorov-Smirnov test). The t-student test also no statistically significant differences were found between salinity vertical profile of RRF experiment and PIRATA dataset ($p = 0.9966, \alpha = 0.05$). The temperature vertical profile is well adjusted to the measurements (Figure 22(b)). However, the RRF underestimate the measurements between 80 and 180 m depth. There were no significant differences between potential temperature of RRF experiment and PIRATA dataset ($p = 0.8287, \alpha = 0.05$).

At the position $38°W12°N$ (Fig. 22(c)), the vertical profile of modeled salinity is consistent with measurements, with mean difference of 0.4 psu. No significant differences were found between potential salinity of RRF experiment and PIRATA ($p = 0.9857, \alpha = 0.05$). The temperature vertical structure is similar to the measurement along the year (Figure 22(d)), With main differences between $100 - 180\,m$. The main differences found in these results are limited by the thermocline depth. The t-student test also did not show significant differences ($p = 0.8137$) for a significance level of 0.05.

The NECC is the main current that transports the Amazon plume eastward (GRODSKY et al., 2014). We compare the resulting zonal components in the RRF simulation in the area REG2 (Figure 23(a)), associated to the NECC pathway, with SCUD zonal components (Figure 23(b)). The values of the zonal component are gradually decreasing in the RRF experiment, from 0.3 to $0.2\,ms^{-1}$, from July to October, between 4.5 and $9.5°N$. The maximum difference with SCUD was found between 5.5 and $6.5°N$ in July and between 4 and $5°N$ in October (Figure 23(b)), being $0.2\,ms^{-1}$. The mean differences are $0.1\,ms^{-1}$. These results reveal the RRF simulation is representing quite well the dynamics of the NECC variability.

Figure 23. Hovmüller diagram of the zonal component in REG2 (a) RRF experiment, (b) SCUD dataset

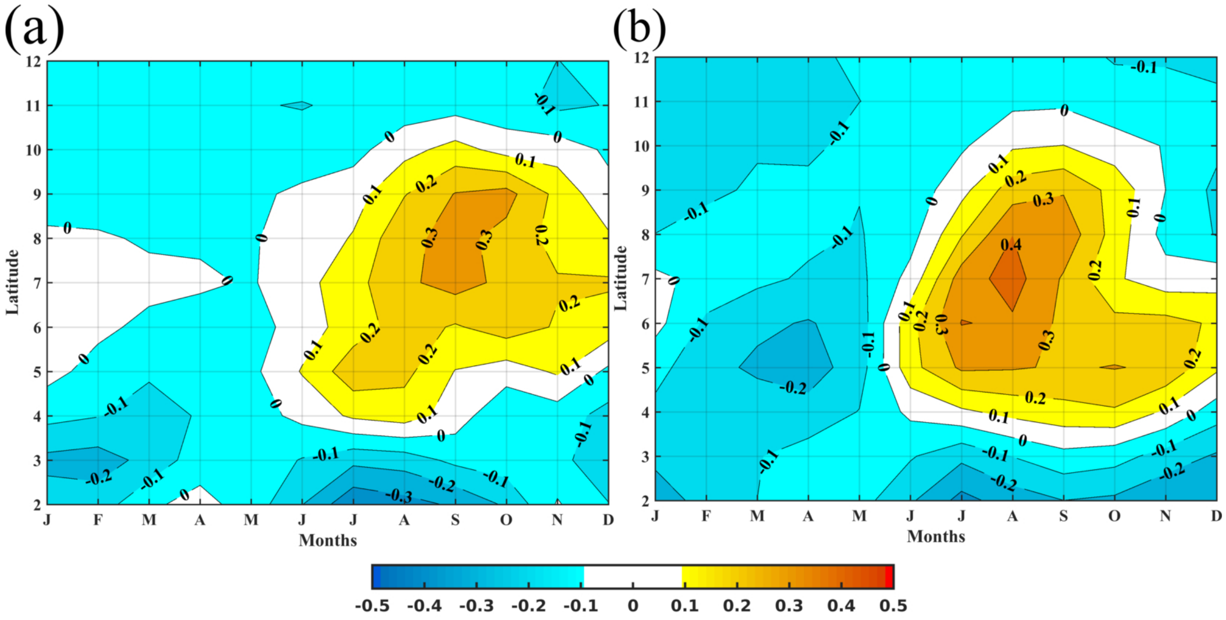

Source: The author

We also calculated the average of the zonal component in WNECC (framed in $50° - 40°W/5° - 8°N$) and ENECC (framed in $30° - 25°W/5° - 8°N$) regions, in the boreal fall, being $0.384\,ms^{-1}$ and $0.226\,ms^{-1}$ respectively. Similar averages in the same regions were reported by Richardson & Reverdin (1987), being $0.410\,ms^{-1}$ and $0.215\,ms^{-1}$ respectively.

Figures 24(a) and (b) show the monthly mean differences between the zonal and meridional components of ROMS model and SODA dataset at $38°W, 8°N$. The zonal component of ROMS at the surface is $0.1\,m \cdot s^{-1}$ higher than SODA, in January and from July to October, conversely SODA is stronger $0.1\,m \cdot s^{-1}$, in March from $600\,m$ to just over $1000\,m$; and in

May and November around $3500\,m$. In the meridional component the biggest differences are found in the first $250\,m$, from April to June and August, reaching a little more than $500\,m$ in March. In December ROMS is $0.1\,m \cdot s^{-1}$ higher than SODA. Predominating the differences between $-0.05\,m \cdot s^{-1}$ and 0 for both components.

Figures 24(c) and (d) show the monthly mean differences between the zonal and meridional components of ROMS model and SODA at $38°W, 12°N$. For both components the maximum variation range of this difference is between $-0.13, m\,s^{-1}$ and $0.12, m\,s^{-1}$, locating the extreme values only in the first $500\,m$, from this depth the difference oscillates between $-0.05, m\,s^{-1}$ and $0.07, m\,s^{-1}$, being the ROMS model consistent with SODA.

Figure 24. Monthly mean differences between the vertical profile of (a) zonal ($m\,s^{-1}$) and (b) meridional components ($m\,s^{-1}$) at $38°W, 8°N$, the vertical profile of (c) zonal ($m\,s^{-1}$) and (d) meridional components ($m\,s^{-1}$) at $38°W, 12°N$.

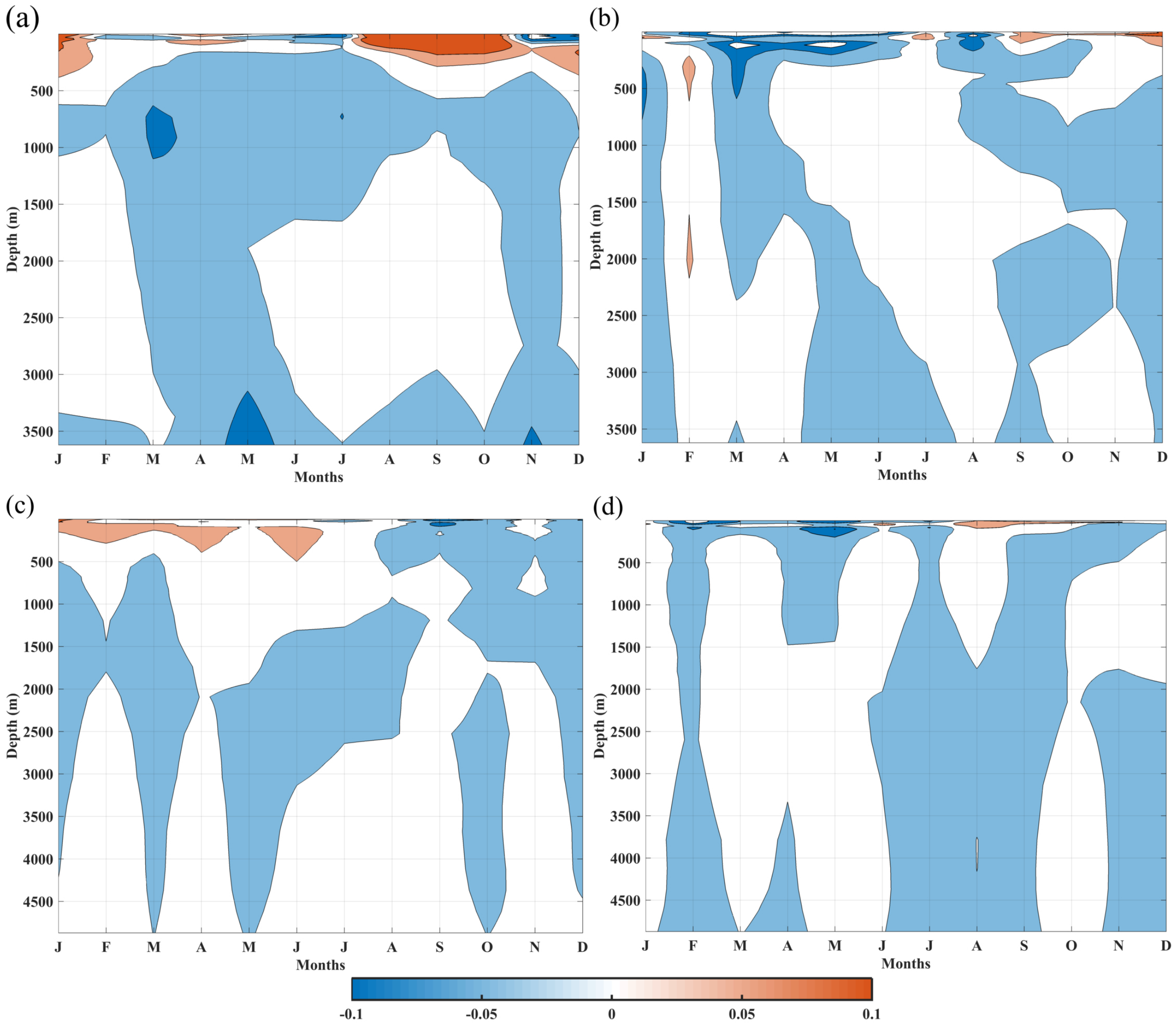

Source: The author

4.2 INFLUENCES OF THE AMAZON AND PARÁ RIVERS ON HYDRODYNAMICS

In the figure 25, the seasonal cycles of SSS differences are compared in the RRF and NRF experiments. The RRF experiment shows lower salinities confined to the coast from December to February. From March to May, the RRF experiment shows lower salinities in the NBC retroflection area, from June to August the plume spreads northward and from September to November the plume is eastward along the NECC. The RRF experiment is $10-12\,psu$ lower along the coast than NRF, which represents well the seasonal cycle of the Amazon freshwater discharge into the WTNA. In the NECC area the RRF create a lower SSS area of $4\,psu$. These results are in agreement with others authors (COLES et al., 2013; KOROSOV; COUNILLON; JOHANNESSEN, 2015; NEWINGER; TOUMI, 2015).

Figure 25. Mean seasonal cycle of difference of SSS between RRF and NRF simulations. Boreal winter (DJF-December, January, February), boreal spring (MAM-March, April, May), boreal summer (JJA-June, July, August), and boreal fall (SON-September, October, November).

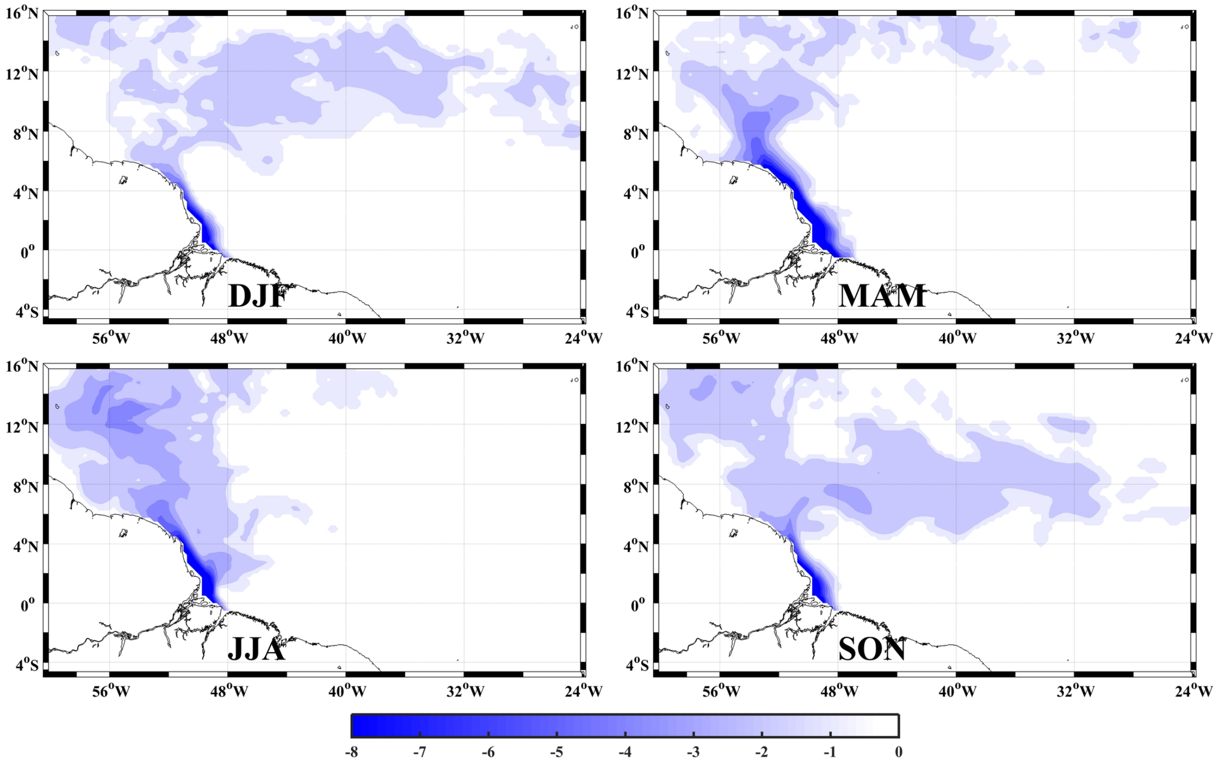

Source: The author

There is no significant change in SST, except near the Amazon River mouth (Figure 26). The differences show variable river temperatures ($0-2\,°C$) at the left side of the Amazon mouth from September to November. In the open ocean the SST changes are not sensitive to the river temperature. These results are in agreement with others authors (NEWINGER; TOUMI, 2015).

Figure 26. Mean seasonal cycle of difference of SST between RRF and NRF simulations. Boreal winter (DJF-December, January, February), boreal spring (MAM-March, April, May), boreal summer (JJA-June, July, August), and boreal fall (SON-September, October, November).

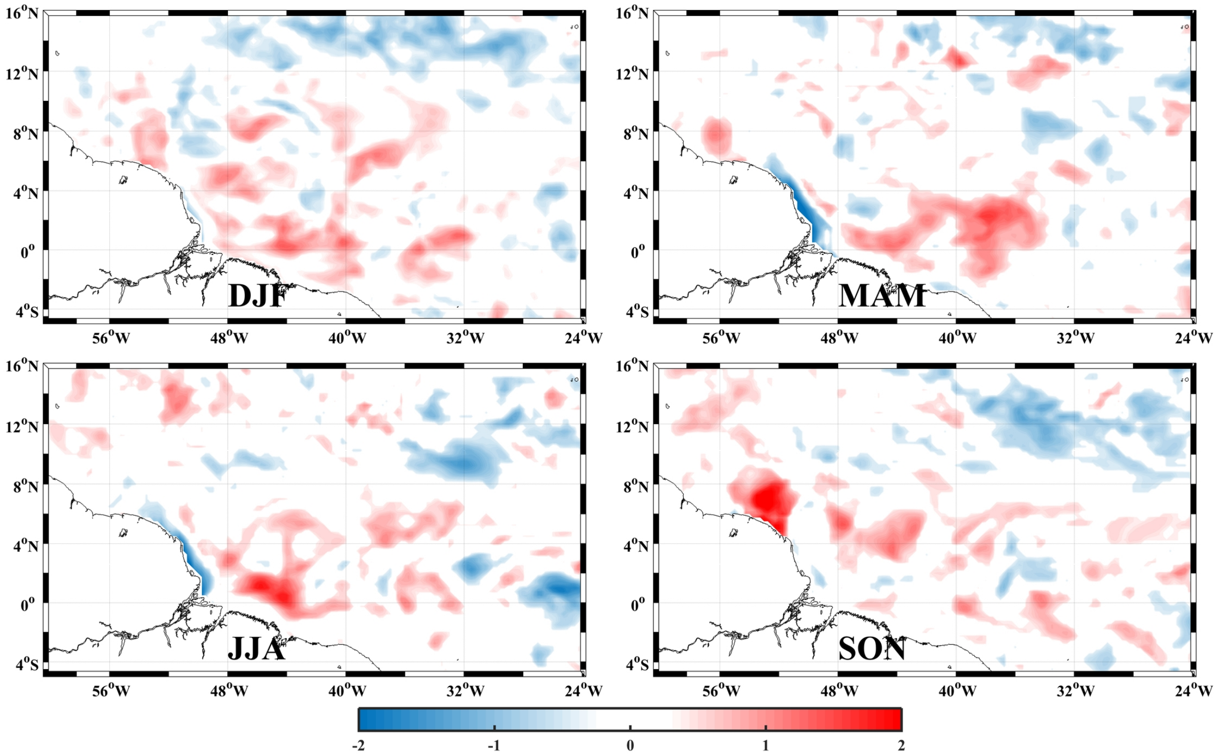

Source: The author

Figure 27 shows the differences between RRF and NRF velocities of surface currents. The seasonal cycle shows a strong impact of the river plume on the WTNA. These strongest velocities are from June to November. From September to November a well-defined rings structure eastward is highlighted. These differences emphasize the role of the Amazon plume in the dynamics of the NBC retroflection as well as in the NBC rings into the NECC, with maximum differences of 1 ms^{-1}.

Figure 27. Mean seasonal cycle of difference of surface currents between RRF and NRF simulations. Boreal winter (DJF-December, January, February), boreal spring (MAM-March, April, May), boreal summer (JJA-June, July, August), and boreal fall (SON-September, October, November).

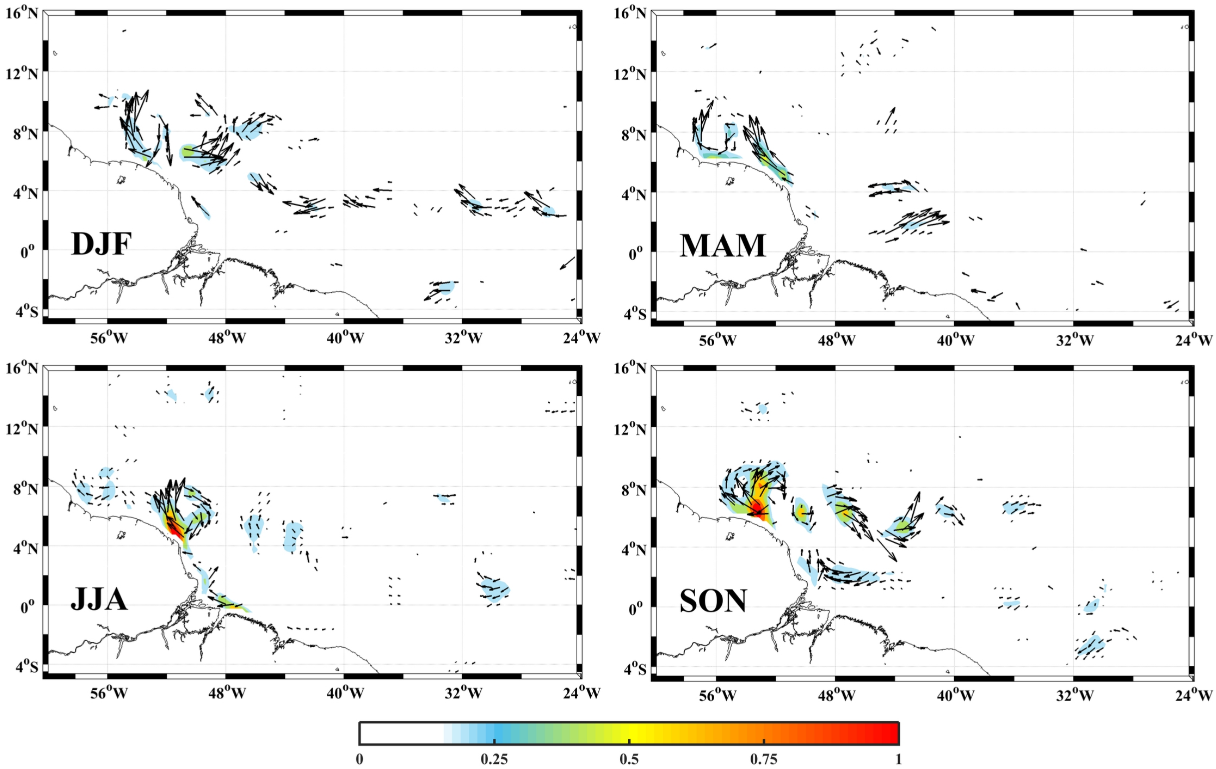

Source: The author

Comparing the zonal component of RRF and NRF experiments (Figure 28(a) RRF and (b) NRF), similar patterns are present in the zonal current intensities, reaching a maximum value of 0.5 ms^{-1}. These areas have a phase shift, in the RRF experiment the maximum value appears in February (between 7° and 8°N), from middle of August to end of September and from middle October to middle November.

Figure 28. Comparison of zonal component between RRF and NRF simulations in REG1, area defined in figure 12. The black arrow represents the phase shift of the zonal component of the current.

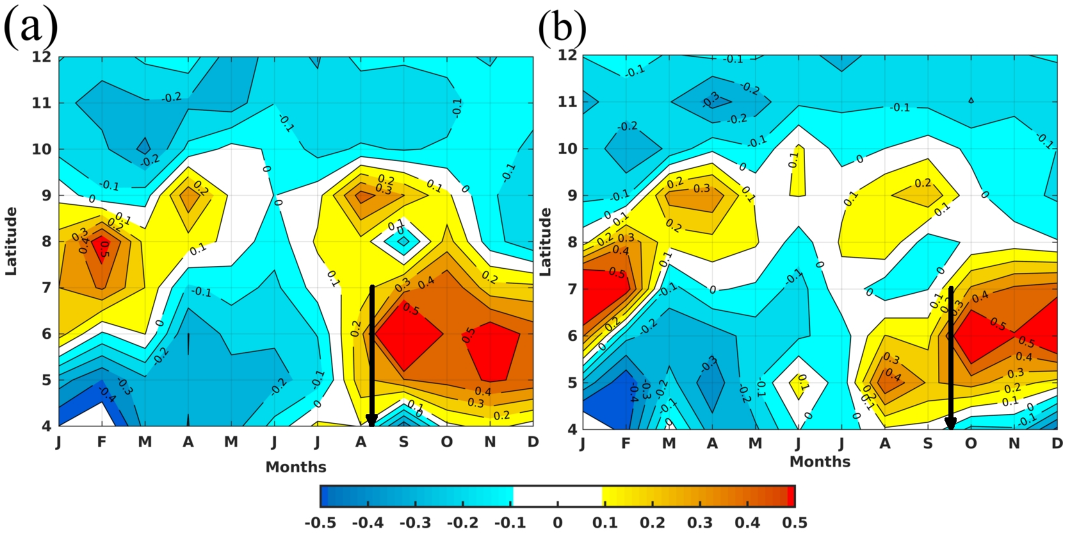

Source: The author

In the NRF experiment (Figure 28) a phase shift exists. From January to February the maximum values are similar to the RRF experiment (between 6.5° and 7.5°N). However, in the second part of the year the strongest velocities occur after September, lagging in two months relating to the RRF experiment, where the maximum values start in August. This phase shifts in the second part of the year reveals that the river plume changes the seasonal cycle of the zonal currents.

Figure 29 shows how the OML is shallower in the RRF experiment than in the NRF, due mainly to the low-density layer formed by the freshwater input discharged by the rivers. The MLD in the RRF experiment is $20-50\,m$ shallower over the entire extension of the plume. The MLD minimum for the RRF experiment is $6\,m$ throughout the year and the maximum fluctuates between $88-102\,m$, being deeper in the SON period, while for the NRF experiment the MLD minimum is between $6-22\,m$ and the maximum oscillates between $99-120\,m$, found the most extreme values in the SON period.

Figure 29. Mean seasonal cycle of difference in MLD (m). Boreal winter (DJF - December, January, February), boreal spring (MAM - March, April, May), boreal summer (JJA - June, July, August), and boreal fall (SON - September, October, November).

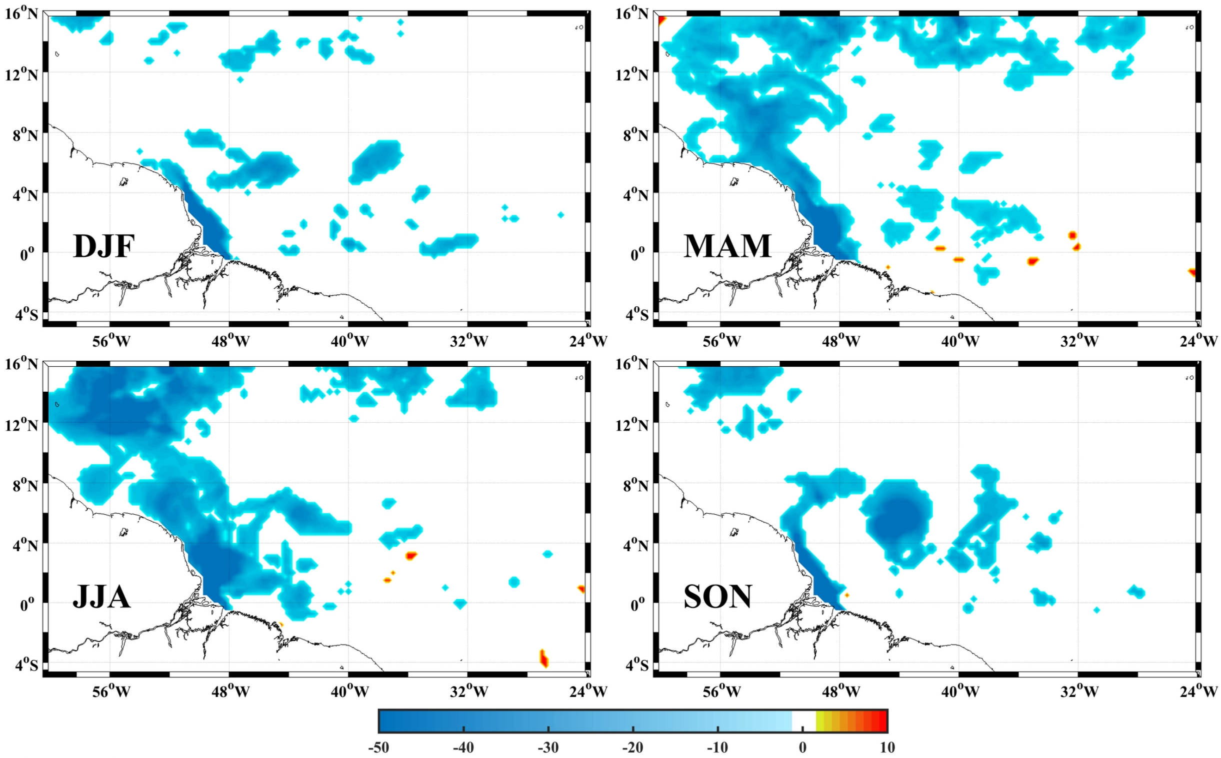

Source: The author

Figure 30 shows the spatial distribution of ILD between the RRF and NRF experiments, here we also find that the ILD is $20 - 50\,m$ shallower in the RRF experiment, mainly in the periods JJA and SON. In the variation of ILD there is a clear influence of SST, being up to $1\,°C$ higher in the RRF experiment (Figure 26).

Figure 30. Mean seasonal cycle of difference in ILD (m). Boreal winter (DJF - December, January, February), boreal spring (MAM - March, April, May), boreal summer (JJA - June, July, August), and boreal fall (SON - September, October, November).

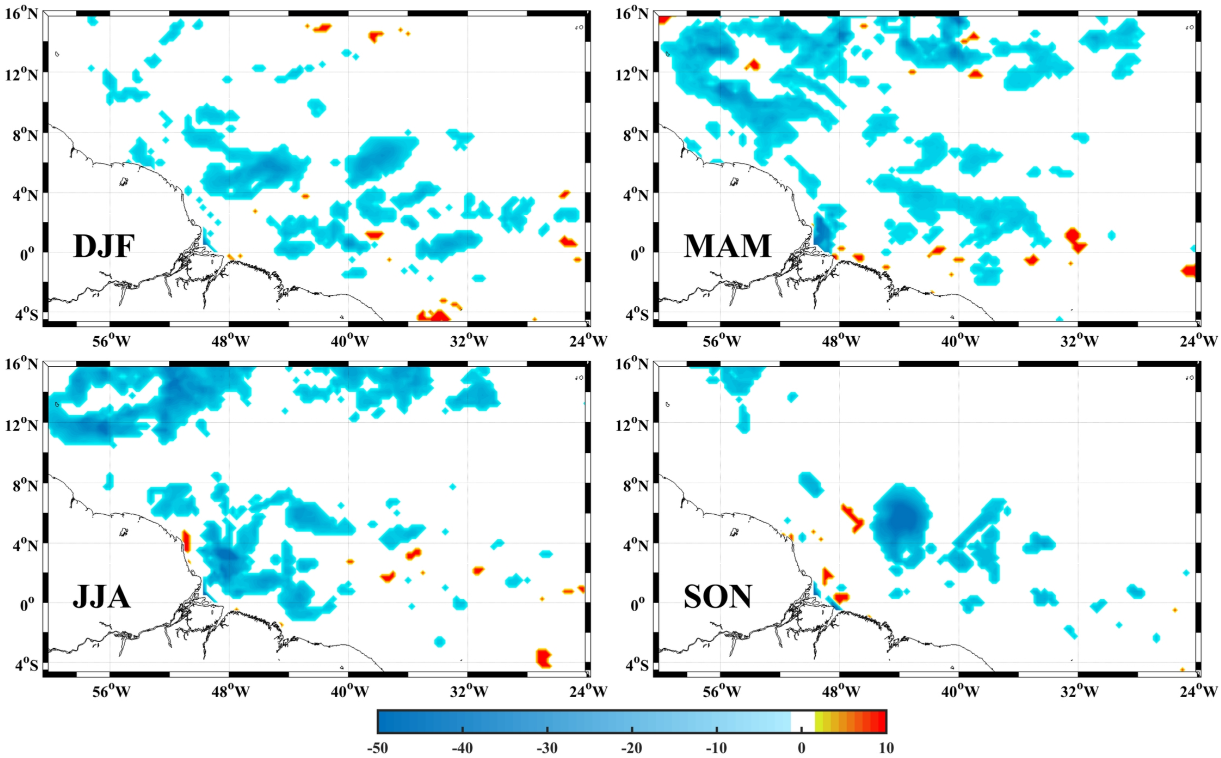

Source: The author

Figure 31 shows the spatial distribution of the difference of BLT between the RRF and NRF experiments. The discharge of fresh water from the rivers plays a fundamental role in the formation of BL, following the extension of the plume. In the NRF experiment, the BL is almost non-existent in the extension of the plume, when the maximum thickness of the BL is at the mouth of the river and extending northwestward, gradually decreasing its thickness as it moves away in the same direction of the river discharge, mainly in the MAM and JJA periods. In SON the BL extends towards the Northwest and then makes a turn to the East accompanying the plume and the NECC. In the NRF experiment we can find 100% of the BLT between $1-35\,m$. In the RRF experiment the BLT reaches $82-94\,m$ in the periods DFJ, MAM and JJA and up to $110\,m$ in the SON period. A similar result was reported by Pailler, Bourlès & Gouriou (1999).

Figure 31. Mean seasonal cycle of difference in BLT (m). Boreal winter (DJF - December, January, February), boreal spring (MAM - March, April, May), boreal summer (JJA - June, July, August), and boreal fall (SON - September, October, November). The nodes of the grid where the thickness of the layer is less than 10% of the maximum depth ($ILD\ or\ MLD$) are shown with value 0 and in white color.

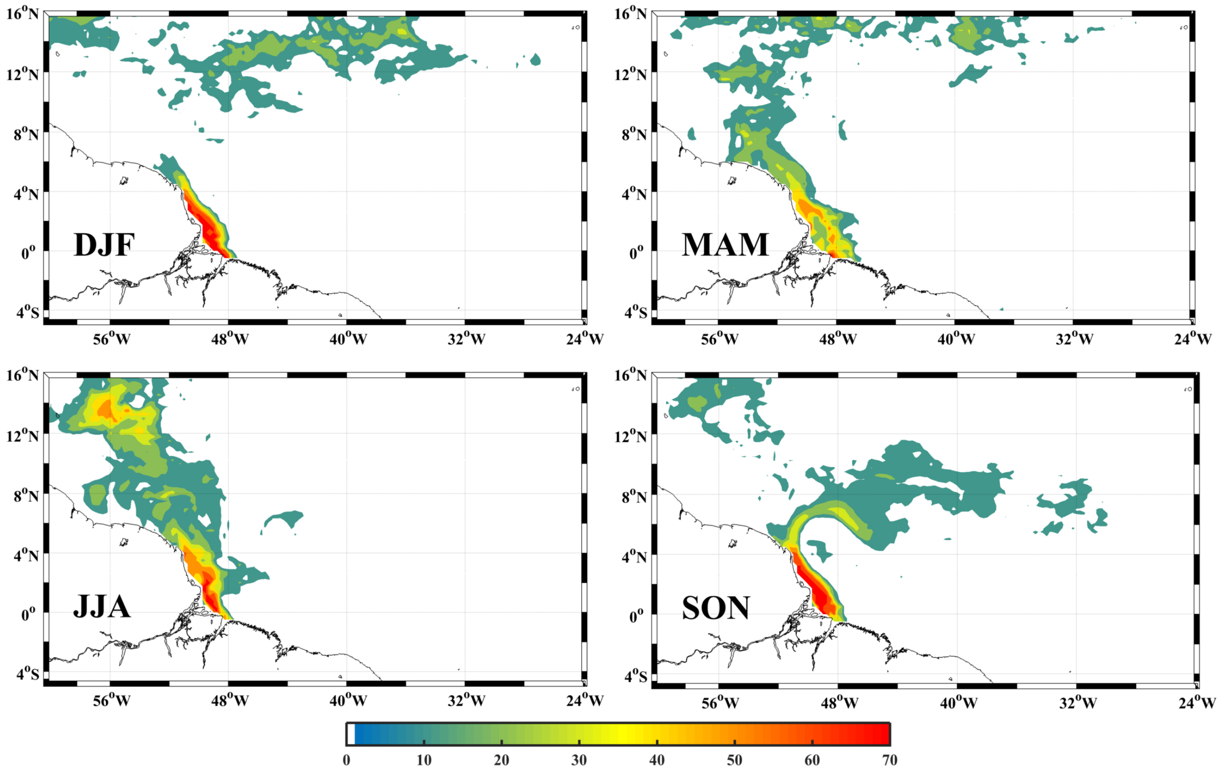

Source: The author

It was calculated the OHC between Z_{REF} and ILD, the biggest difference was between -0.7 and $-0.3 \times 10^{10}\ J\,m^{-2}$, storing more energy in the NRF experiment, mainly in the periods MAM, JJA and SON (Figure 32). These differences stand out fundamentally in the region near the nodes of the grid and northwest region in the periods MAM and JJA; in the SON period the biggest difference is observed in the region of the plume extension eastward, the opposite phenomenon is also highlighted in the same direction, coinciding with the maximum values of the BLT near river mouth and with the retroflection, with higher energy stored in that region in the experiment RRF. The largest accumulation of energy in the NRF experiment was from 1.1 to $1.3 \times 10^{10}\ J\,m^{-2}$, while in the RRF experiment it was from 1.0 to $1.2 \times 10^{10}\ J\,m^{-2}$, with maximum difference of $0.1 \times 10^{10}\ J\,m^{-2}$. Variations in ILD are the main factor influencing the OHC difference between the RRF (shallower) and NRF experiments.

Figure 32. Mean seasonal cycle of difference in $OHC(J\,m^{-2})$ integrated from Z_{REF} to ILD. Boreal winter (DJF - December, January, February), boreal spring (MAM - March, April, May), boreal summer (JJA - June, July, August), and boreal fall (SON - September, October, November).

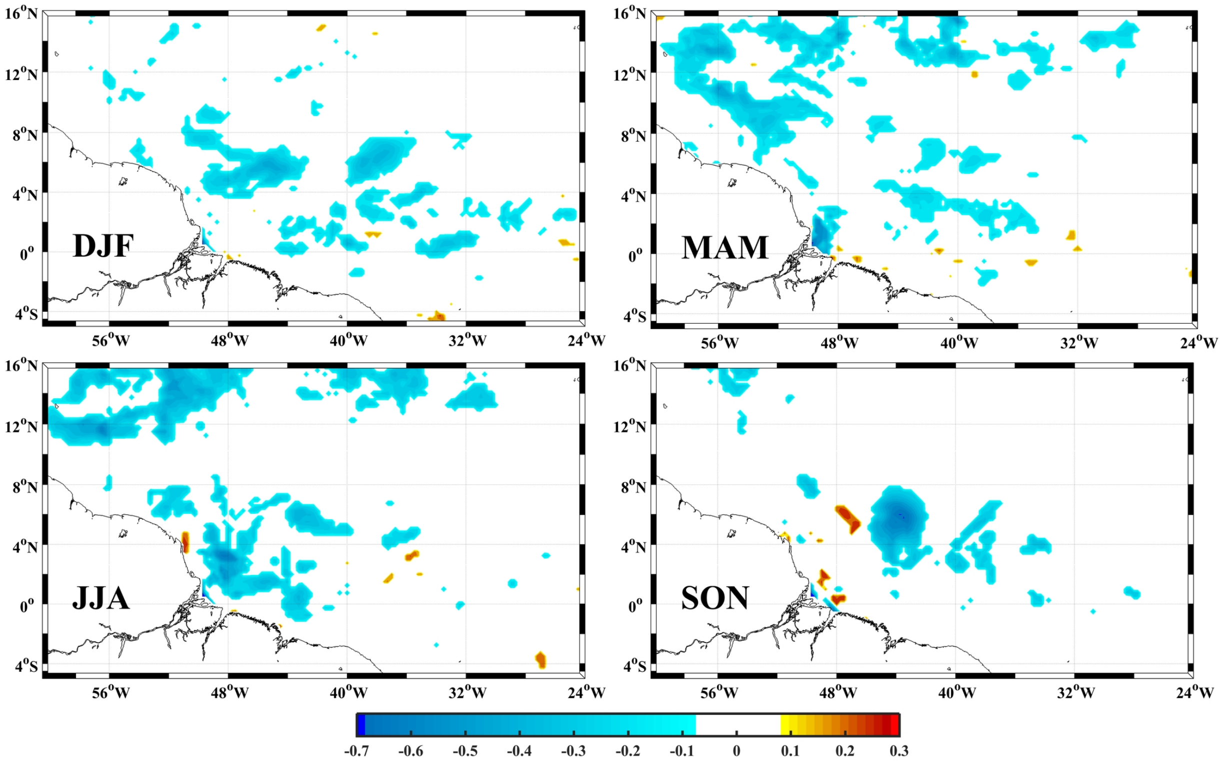

Source: The author

5 DEEPWATER OIL/GAS BLOWOUTS SIMULATIONS: RESULTS AND DISCUSSIONS

This chapter presents the results of the temporal evolution of plumes generated from oil/gas blowouts at points located on the continental shelf of the northern coast of Brazil. These results correspond to the article "Influence of underwater hydrodynamics on oil and gas blowouts off Amazon River mouth" that was accepted by the Tropical Oceanography journal.

In order to perform the numerical simulations, the GAS_DOCEAN model was used, which has three-dimensional fields of marine currents, temperature and salinity as input. These three three-dimensional fields were obtained from the RRF experiment.

Before running the GAS_DOCEAN model, it was necessary to evaluate the temperature and current speed in the vertical profiles of the ROMS model at points P1, P2 and P3. Resulting in good agreement when compared with the SODA dataset.

Figure 33(a) shows the vertical profiles of the temperature at point P1 of the SODA dataset and the ROMS model in the DJF and JJA periods. The vertical profiles of the temperature are better adjusted below 300 m depth in both periods. In depths above 300 m the ROMS model overestimates the temperature and the main differences range between 0.7 to 1.7$^{\circ}C$.

Figure 33. (a) Temperature and (b) current speed vertical profiles in DJF (December-January-February) and JJA (June-July-August) periods for SODA and ROMS at point P1.

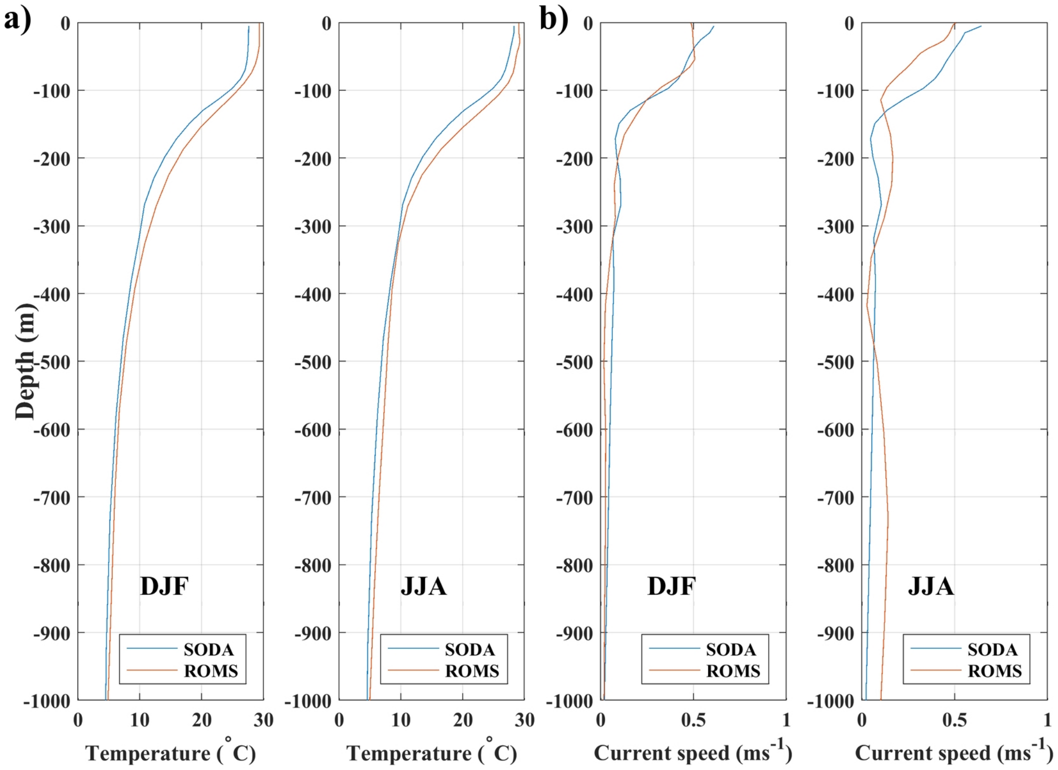

Source: The author

In JJA period there is a maximum difference of 0.04 ms^{-1} below 300 m and above this depth, the average difference was 0.17 ms^{-1} with a maximum difference of 0.21 ms^{-1} from 150 to 180 m depth (Figure 33(b)). The profile of the current speed is well adjusted below the 300 m depth in the DJF period. The maximum difference in the DJF period was 0.18 ms^{-1} on the surface.

Once the results of the ROMS model were validated, the GAS_DOCEAN model it ran with the parameters summarized in table 2. In the interest of improve the understanding of the results of oil/gas plumes simulations, the figure 34(a) shows the mean seasonal velocity of the marine current, averaged between the surface and 100 m depth.

Figure 34. ROMS output of mean seasonal cycle of the currents measured (a) between the surface and 100 *m* depth; and (b) between 1000 and 1200 m depth during the winter (DJF-December, January, February), spring (MAM-March, April, May), summer (JJA-June, July, August), and fall (SON-September, October, November). The centers of the red circle represent the positions of the simulation points P1, P2 and P3.

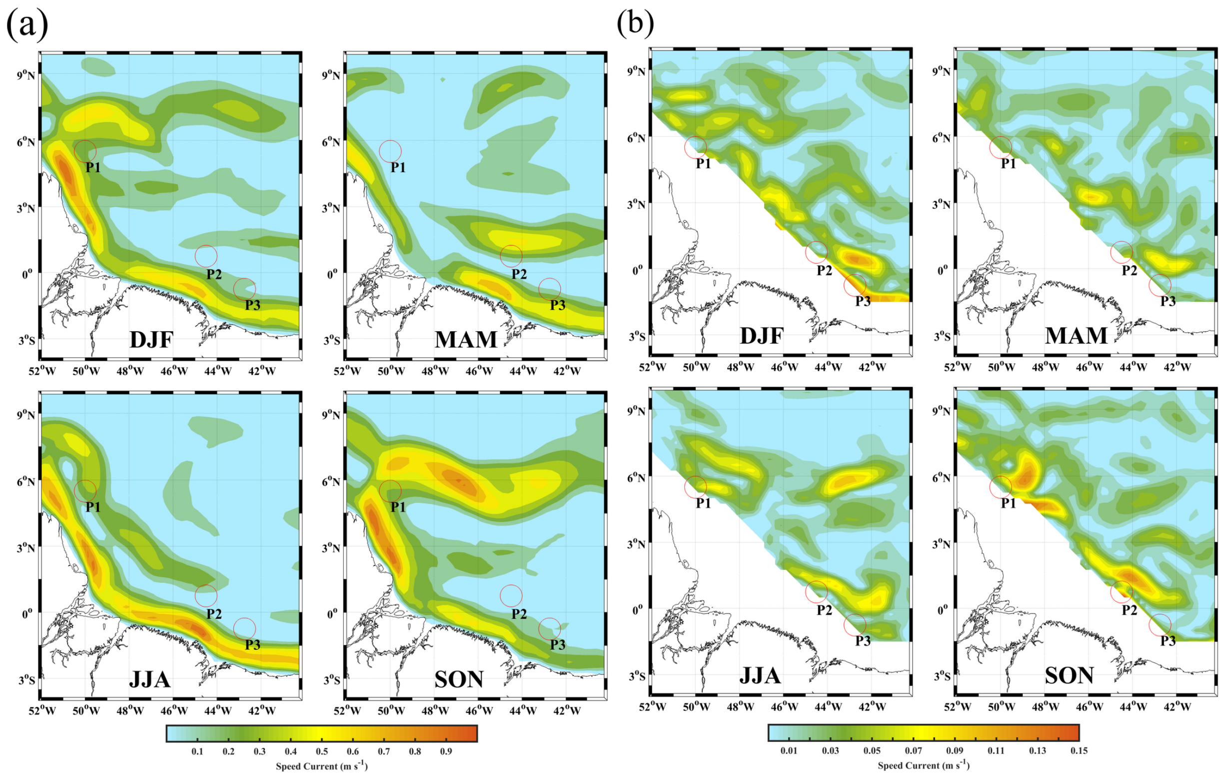

Source: The author

The most intense currents form a wide band and confined to the coastline, corresponds to the NBC. This current is more intense in the winter especially over the northwest part of the coast, where it turns toward the east (following the NBC retroflection), reaching speeds higher than 0.9 ms^{-1}. In the boreal spring, we found the less intense currents of the whole year with maximum values eastward of the Amazon River mouth, reaching up to 0.7 ms^{-1}. In the boreal summer, the NBC velocities vary from 0.5 ms^{-1} to speeds higher than 0.9 ms^{-1}. In the autumn, as in the winter, the eastward turning appears, better defining the NBC retroflection. Higher speeds are found along the coast more to the northwest and in the NBC retroflection, oscillating the current speed from 0.5 ms^{-1} to speeds higher than 0.9 ms^{-1}.

The center of the red circles represents the positions of the P1, P2 and P3 simulation points. In winter the average speed is 0.25 ms^{-1}, at P1, extremely low (0.01 ms-1) at P2 and it reaches 0.15 ms^{-1} at P3. In the spring, we find the lowest speeds of the year at P1, P2 and P3, oscillating between 0.01 and 0.25 ms^{-1}. In the boreal summer and autumn at P2 and P3, current speeds reach the minimum value (0.01-0.15 ms^{-1}), increasing at P1 with respect to spring.

Figure 34(b) shows the mean seasonal behavior of currents dynamic between 1000 and

$1200\,m$ depth. In general, at these depths the currents are very slow, oscillating their speed between 0.01 and $0.15\,ms^{-1}$. These currents are slightly less intense in the spring and a little more intense in the fall, mainly above 4°N and between 47 and 50°W; and between 0.5-2°N and 42-45°W, reaching $0.15\,ms^{-1}$, moving this last pattern towards the southeast in the winter.

In the winter we find speeds of $0.15\,ms^{-1}$ at P3 and between 0.01-0.03 ms^{-1} at P1 and P2. The least intense currents are in the spring at all 3 points (0.03-0.04 ms^{-1}). Similar speeds are found at P2 and P3 in the summer, increasing slightly at P1 to $0.06\,ms^{-1}$. In the autumn, speeds at P3 do not differ from the summer, being somewhat lower at P1 and reaching up to $0.15\,ms^{-1}$ at P2.

5.1 OIL AND GAS PLUMES EVOLUTION

Figure 35 shows the monthly evolution of oil/gas plumes at P1. During the entire evaluated period, the plumes were type 3, with exception to September, where they reached the maximum entrainment below $1000\,m$ depth. Above this level, the radius of the plumes began to decrease gradually until reaches the surface, oscillating between 54-76.5 m. The plumes reached the largest radius in August, November and December and the lowest radius was observed between May-July (table 4).

Figure 35. Oil/gas plumes evolution in the middle of each month (simulation day 15) at P1. The solid lines represent the west (-) and east (+) directions. The dashed lines represent the north (-) and south (+) directions. The red color is the displacement of the plumes from the bottom. The black color represents the radius to the west and north. The blue color represents the radius to the east and south.

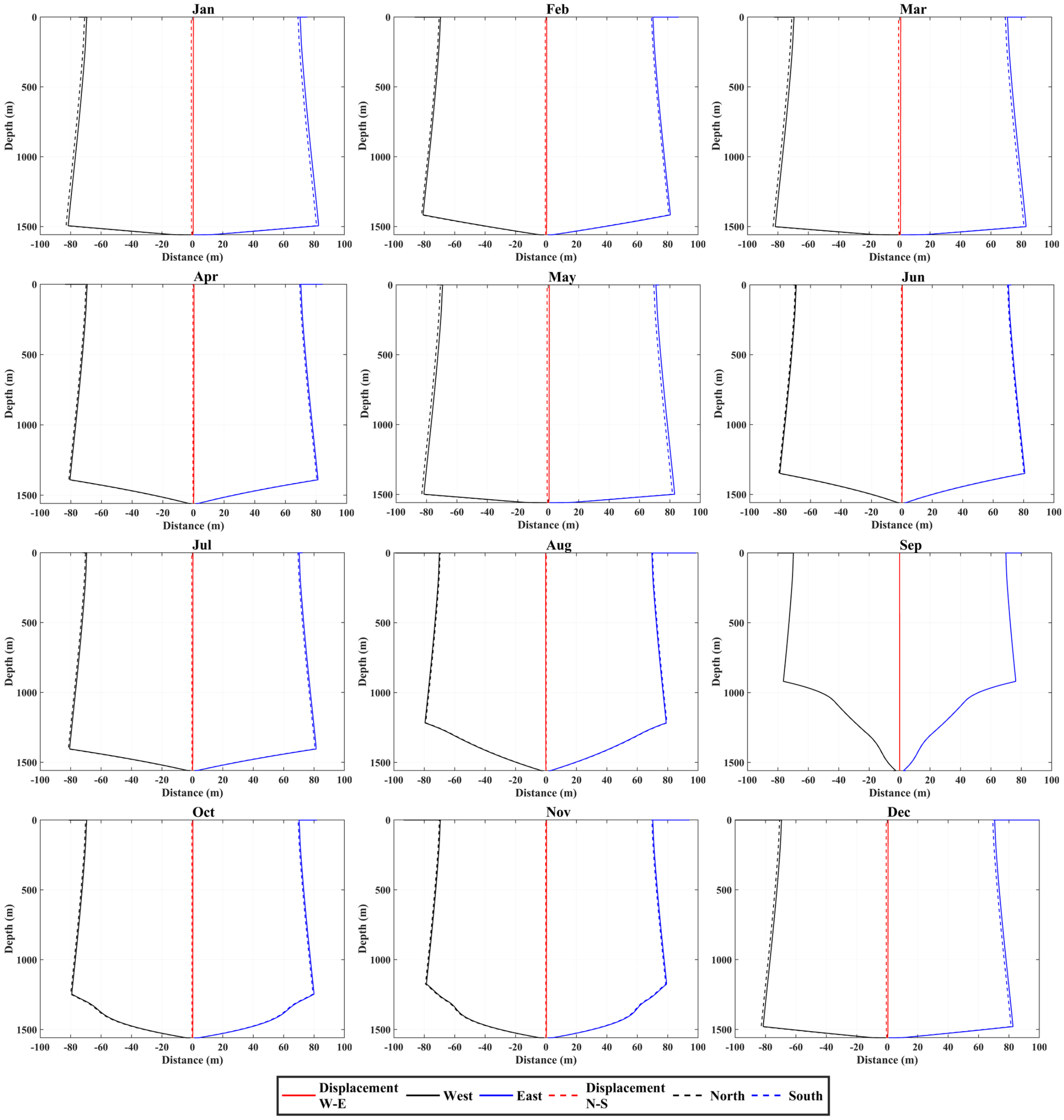

Source: The author

The largest displacements of the plume from the blowout point were approximately 1 m in January and May. The mean arrival time of the oil/gas plumes to the surface was 7.99 *hours* and difference between the months was minimal.

Figure 36 shows the monthly evolution of the oil/gas plumes at P2. As already verified in P1, all the plumes are were of type 3. All the plumes reach their maximum entrainment

Table 4. Monthly radius and displacement of oil/gas plumes at points P1, P2 and P3

	P1			P2			P3		
	Mean radius (m)	Displacement (m)	Evolution time (hours)	Mean radius (m)	Displacement (m)	Evolution time (hours)	Mean radius (m)	Displacement (m)	Evolution time (hours)
Jan	56.4	(0.71,-0.70)	8.04	75.5	(-0.30,0.20)	7.26	58.9	(0.37,-0.32)	6.30
Feb	65.3	(0.50,-0.45)	7.97	60.1	(-0.35,0.26)	7.25	58.7	(-0.13,0.22)	6.30
Mar	62.1	(0.71,-0.71)	8.06	54.1	(-0.33,0.24)	7.25	58.7	(-0.09,0.23)	6.30
Apr	63.3	(0.36,-0,36)	7.96	58.4	(0.14,-0.15)	7.26	58.7	(-0.19,0.26)	6.30
May	54.5	(0.69,-0.73)	8.05	60.7	(-0.10,0.15)	7.25	58.8	(0.20,-0.18)	6.30
Jun	54.0	(0.30,-0.28)	7.95	55.3	(-0.52,0.34)	7.26	58.8	(0.18,0.24)	6.30
Jul	54.3	(0.38,-041)	7.96	73.1	(-0.54,0.32)	7.27	58.8	(0.10,-0.03)	6.30
Aug	74.1	(-0.24,0.22)	7.96	61.0	(-0.56,0.30)	7.26	58.8	(-0.44,0.64)	6.33
Sep	60.3	(-0.02,-0.01)	7.96	56.5	(-0.47,0.25)	7.26	58.7	(-0.28,0.36)	6.30
Oct	61.4	(0.35,-0.33)	7.97	79.5	(-0.44,0.26)	7.25	58.7	(-0.39,0.47)	6.31
Nov	70.6	(0.36,-0.24)	7.97	54.5	(-0.42,0.19)	7.25	58.7	(-0.19,0.32)	6.30
Dec	76.5	(0.54,-0.69)	8.02	79.7	(-0.26,0.16)	7.26	58.7	(-0.37,0.55)	6.32

Source: The author

below 1000 m, decreasing their radius until they reach the surface (54.1-79.7 m). The largest diameters in the surface corresponded to the months of January, October and December. The largest displacements of P2 plume occurred from June to August and were approximately 0.64 m (table 4). The average time of arrival at the surface was 7.26 $hours$.

Figure 36. Oil/gas plumes evolution in the middle of each month (simulation day 15) at P2. The solid lines represent the west (-) and east (+) directions. The dashed lines represent the north (-) and south (+) directions. The red color is the displacement of the plumes from the bottom. The black color represents the radius to the west and north. The blue color represents the radius to the east and south.

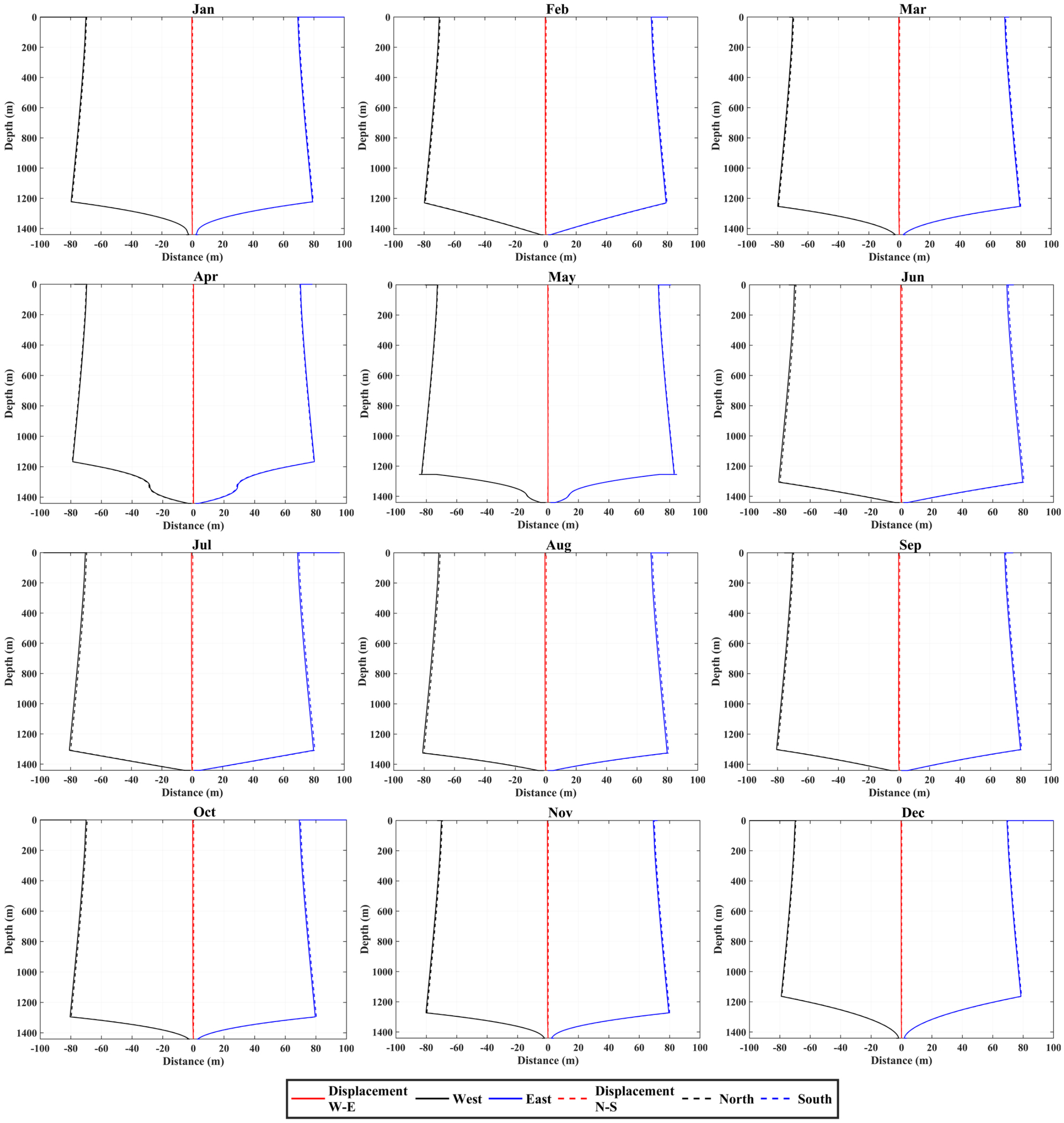

Source: The author

The pattern of oil/gas plume evolution already observed at the points P1 and P2 (type

3) was also verified at P3 (Figure 37). The plumes at P3 reaching its largest entrainment below 1000 m depth except for the months of May and July, where the diameter at the surface was almost invariant during all months (58.7-58.9 m). As shown in table 4, the displacement of the plumes from its point of origin occurred in August and was 0.78 m. The plumes evolution time was practically the same, oscillating between 6.30 and 6.33 $hours$.

Figure 37. Oil/gas plumes evolution in the middle of each month (simulation day 15) at P3. The solid lines represent the west (-) and east (+) directions. The dashed lines represent the north (-) and south (+) directions. The red color is the displacement of the plumes from the bottom. The black color represents the radius to the west and north. The blue color represents the radius to the east and south.

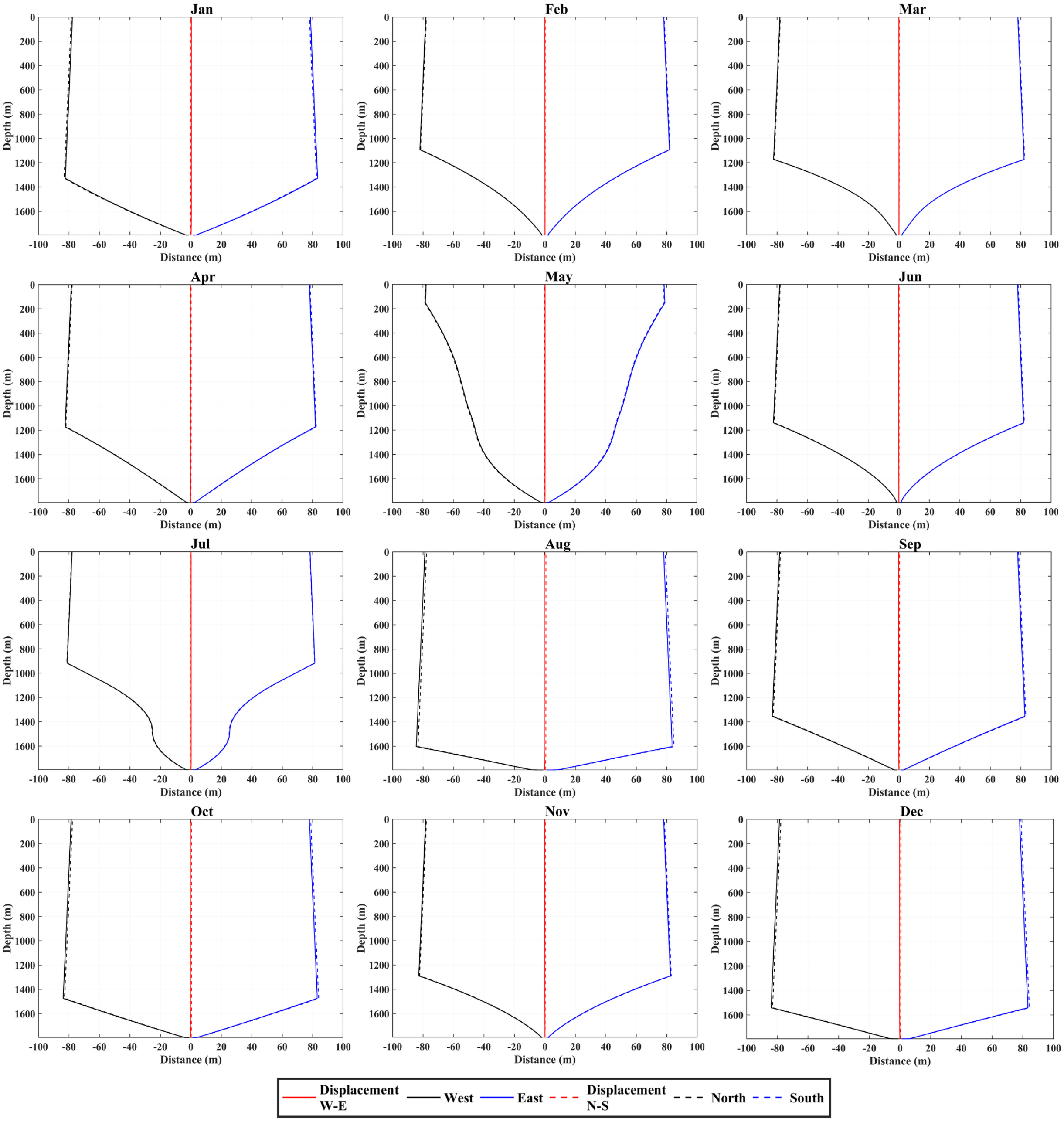

Source: The author

Figure 38(a) shows the vertical profiles of the current velocity for March at point P1 and for November at point P3. In both profiles, the plume simulations show that the maximum entrainment of these were reached below $1000\,m$ depth (Figure 35 and figure 37). The bottom speed of points P1 and P3 is greater than $0.1\,ms^{-1}$ and less than $0.2\,ms^{-1}$, thus maintaining the entire water column up to $200\,m$ depth. This behavior is very similar to the rest of the profiles at all points, with the exception of September, at point P1, and of May and July, at point P3.

Figure 38. Vertical profiles of the current speed (a) at P1 (March) and P3 (November) and (b) at P1 (September) and P3 (May and July).

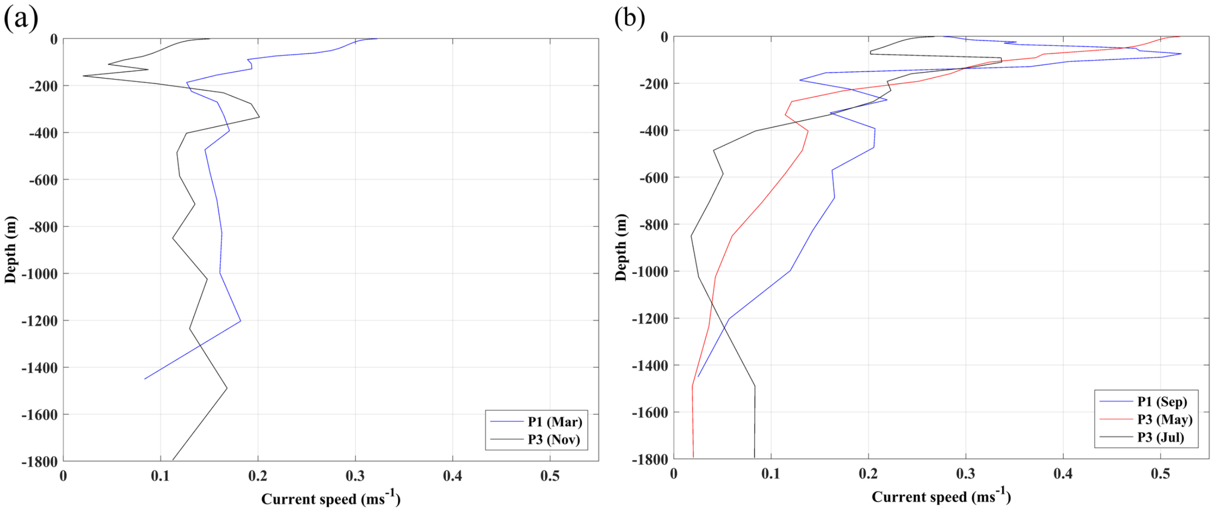

Source: The author

In September, at P1 (Figure 38(b)), the current speed at the bottom was almost zero (approximately $0.02\,ms^{-1}$). From the bottom, the velocity grew very slowly as the depth decreased to $1000\,m$ ($0.12\,ms^{-1}$). The speed began to increase a little faster from $1000\,m$ depth to the surface, which means that the maximum entrainment was reached between 900 and $1000\,m$ depth. In May at P3 (Figure 38(b)) the behavior of the plume in the bottom was also almost zero, but the increase in speed began near the $1500\,m$ depth, which was much slower than in the previous case. Up to almost 200 m depth the speed did not exceed $0.2\,ms^{-1}$ and, above that, where the plume reached its maximum entrainment, it began to grow sharply until exceeding $0.5\,ms^{-1}$ on the surface. At this same point, in July (Figure 38(b)), the current speed was less than $0.1\,ms^{-1}$ and maintained that value up to $1500\,m$ depth. It began to decrease to approximately $850\,m$ depth and then, it increased from above this depth, reaching its maximum entrainment.

Using the coefficient 0.2 in the equation 3.23 did not get good results because the bottom current speed at the three points was very small, $|V_0| \to 0$, which this implied that $\Delta t \to \infty$. Thus it was necessary to adjust the coefficient to estimate Δt. The equation 5.1 below was then considered

$$\Delta t = \begin{cases} 0.025\ b_0/|V_0| & \text{for P1 and P2} \\ 0.0375\ b_0/|V_0| & \text{for P3} \end{cases} \tag{5.1}$$

where Δt is the time step in s, b_0 is the ratio of initial control-volume in m and V_0 is the initial blowout velocity in ms^{-1}.

6 CONCLUSIONS

In the first place, this study quantify how much the Amazon plume impacts on the dynamics of the Western Tropical North Atlantic. We investigate the role of Amazon and Pará River plumes in the temperature, salinity and dynamics of the main surface currents, as the North Brazil Current retroflection, rings and North Equatorial Countercurrent, using a regional ocean model with and no-river input.

The rivers freshwater impact on the WTNA is evident in the SSS fields. The seasonal cycle of the experiment with rivers is in good agreement with profiles of the PIRATA buoys and with spatial distribution of satellite and reanalysis products. Compared to some previous studies about salinity fields in the region of the WTNA, we find similar patterns of the plume distribution, as the salinity, temperature and mixed layer depth values (COLES et al., 2013; KOROSOV; COUNILLON; JOHANNESSEN, 2015; NEWINGER; TOUMI, 2015). The structure of the SSS on the area of the NBC retroflection and NECC is clearly identified in the seasonal cycle, showing a confinement of the lower salinities close to the coast from December to February and spreading eastward along the NECC region from September to November.

The SST fields don't show significant changes, except near the Amazon River mouth. A warm core of SST is concentrated at the left side of the Amazon mouth from September to November, following the NBC retroflection area. This river output warming core is due to the influence of the river temperature. However, in the open ocean, SST changes are not sensitive to the river temperature. The seasonal cycle of the differences in the experiments with river and no-river is stronger from October to November.

The seasonal cycle of the differences between RRF and NRF experiments in the surface current fields show a strong impact of the river plume on the WTNA dynamics. The strongest velocities are from June to November and a well-defined rings structure eastward is highlighted from September to November. The differences in the surface currents emphasize the role of the Amazon plume in the dynamics of the NBC retroflection, as well as in the NBC rings following the NECC. The experiment with river increase the surface currents in $1\,ms^{-1}$ compared to the experiment with no-river.

In the comparisons of zonal components of RRF and NRF experiments we found similar patterns in the zonal current intensities, reaching a maximum value of $0.5\,ms^{-1}$. However, the maximum values in the second semester of the year show a phase delay of the experiment NRF relating to the RRF. The zonal component of the NRF lags the RRF in two months, with strongest values occurring after September. This phase shifts in the second part of the year reveals that the river plumes change the period of maximum intensities of the zonal currents, anticipating the seasonal cycle.

The MLD and ILD in the RRF experiment is $20-50\,m$ shallower over the entire extension of the plume. The discharge of fresh water from the rivers plays the fundamental role in the formation of BL. The maximum thickness of the BL is at the mouth of the rivers and extending northwestward, gradually decreasing its thickness as it moves away following the plume, mainly in the MAM and JJA periods. In SON, the plume extends northwestward and then retroflects eastward accompanying the plume and the NECC.

In the RRF experiment less energy is accumulated than in the NRF, there being a maximum difference of the OHC of $0.1 \times 10^{10}\,J\,m^{-2}$ between both experiments, mainly due to the variations of the ILD, being shallower in the RRF experiment.

In this work, the physical properties, as the dynamic variability of the Amazon River plume are well represented by the ocean regional modeling. The results with-river and no-river show a significative difference of the thermodynamic at the Amazon plume. The SSS spatial pattern is much altered by the river presence, reducing the salinity in about 8 psu.

Besides, the surface currents are intensified with the river input. The main difference is along the plume trajectory, where strong velocities are found. Other important characteristic are the rings formation. Considering river input, the presence of the Amazon rings are evident, highlighting the importance of the river in the rings dynamic into the WTNA region.

The formation and intensification of these rings due to the presence of the river, as well as the low salinities, evidence the role of the river in the dynamics, stratification and its contribution to heat transport in the WTNA.

As a summary, figure 39 shows a diagram of the logical sequence in which the processes described above in the study area are manifested.

Figure 39. Outline of the logical sequence of oceanic processes due to the effect of the Amazon and Pará rivers in WTNA

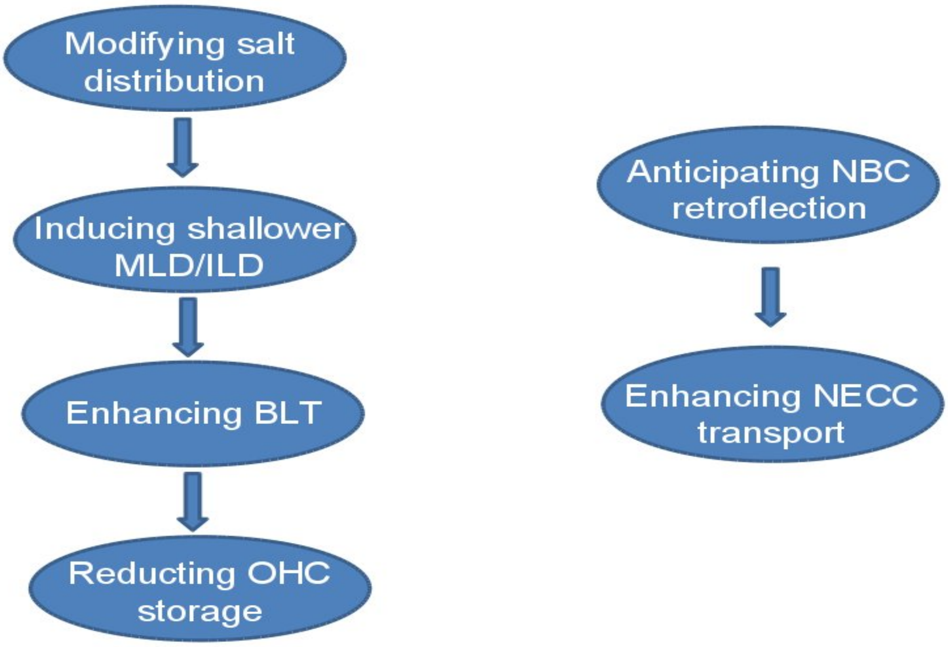

Source: The author

In the second place, the behavior of the oil/gas plumes of the deepwater blowout, located on the continental shelf of northern Brazil, was analyzed. Three parameters were estimated, the time of arrival at the surface, the plume radius on the surface and the deviation at surface from its origin.

All the plumes were type 3. At $P1$ the mean radius at the surface varied between $54-76.5\,m$, displacement the plume approximately $1\,m$ from its origin in the bottom, the average time it delayed to reach the surface was $7.99\,hours$, this time was a little lower in $P2$, delaying $7.26\,hours$, the greatest distance displaced from its point of origin was $0.64\,m$ and its average radius on the surface ranged from $54.1-79.7\,m$. At $P3$ the displacement of the plume with respect to its origin was $0.78\,m$, at this point the mean radius on the surface and the time of evolution to the surface of the plume remained almost invariant, oscillating between $58.7-58.9\,m$ and $6.30-6.33\,hours$ respectively. The little displacement of the plume with respect to their origin is due to the low speeds in the vertical profile.

To obtain good results in the numerical simulations of the plumes, it was necessary to adjust the coefficient for computation Δt. The equation suggested by Lee & Cheung (1990) will be modified as $\Delta t = 0.025\ b_0/|V_0|$ for P1 and P2; and $\Delta t = 0.0375\ b_0/|V_0|$ for P3.

REFERENCES

AKINDE, S. B.; OBIRE, O. In-situ Physico-chemical Properties of the Deep Atlantic Ocean Water Column and their Implications on Heterotrophic Bacterial Distribution in the Gulf of Guinea . *Advances in Applied Science Research*, v. 2, n. 6, p. 470–482, 2011. Cited on page 49.

AKUETEVI, C. Q. C.; WIRTH, A. Dynamics of turbulent western-boundary currents at low latitude in a shallow-water model. *Ocean Science*, v. 11, n. 3, p. 471–481, 2015. ISSN 1812-0792. doi: 10.5194/os-11-471-2015. Cited on page 36.

ARAKAWA, A.; LAMB, V. R. Methods of computational physics. *Methods of computational physics*, v. 17, p. 174–265, 1977. Cited on page 60.

ARNAULT, S. et al. Intercomparison of upper layer circulation of the western equatorial Atlantic Ocean: In situ and satellite data. *Journal of Geophysical Research*, v. 104, n. C9, p. 21,171–21,194, set. 1999. Cited on page 36.

ASAEDA, T.; IMBERGER, J. Structure of bubble plumes in linearly stratified environments. *Journal of Fluid Mechanics*, Cambridge University Press, v. 249, p. 35–57, 1993. Cited on page 66.

BALAGURU, K. et al. Ocean barrier layers' effect on tropical cyclone intensification. *Proceedings of the National Academy of Sciences*, v. 109, n. 36, p. 14343–14347, 2012. ISSN 0027-8424. Cited on page 33.

Barbosa Jr, J. R.; BRADBURY, L. J. S.; Silva Freire, A. P. On the numerical calculation of bubble plumes, including an experimental investigation of its mean properties. In: *Society of Petroleum Engineers (SPE) Eastern Regional Meeting*. [S.l.: s.n.], 1996. p. 23–25. Cited on page 39.

BARTHEM, R. B. et al. Amazon Basin, GIWA Regional assessment 40b. *UNEP*, University of Kalmar on behalf of United Nations Environment Programme, 2004. ISSN 1651-9402. Disponível em: <http://www.unep.org/dewa/giwa/areas/reports/r40b/giwa_regional_assessment_40b.pdf>. Cited on page 32.

BISHNOI, P. R.; NATARAJAN, V. Formation and decomposition of gas hydrates. *Fluid phase equilibria*, Elsevier, v. 117, n. 1-2, p. 168–177, 1996. Cited on page 43.

BLOOM, S. C. et al. Data Assimilation Using Incremental Analysis Updates. *Monthlyu Weather Review*, v. 124, n. 6, p. 1256–1271, jun. 1996. Cited on page 52.

BOURLES, B.; GOURIOU, Y.; CHUCHLA, R. On the circulation in the upper layer of the western Equatorial Atlantic. *Journal of Geophysical Research*, v. 104, n. C9, p. 21151–21170, set. 1999b. Cited on page 73.

BOURLÈS, B. et al. The PIRATA program: history, accomplishments, and future directions. *Bulletin of the American Meteorological Society*, v. 89, n. 8, p. 1111–1125, 2008. Cited on page 53.

BOURLES, B. et al. Upper layer currents in the western tropical North Atlantic (1989-1991). *Journal of Geophysical Research*, v. 104, n. C1, p. 1361–1375, jan. 1999. Cited 2 times on pages 32 and 37.

BREWER, P. G. et al. Gas hydrate formation in the deep sea: In situ experiments with controlled release of methane, natural gas, and carbon dioxide. *Energy & Fuels*, ACS Publications, v. 12, n. 1, p. 183–188, 1998. Cited on page 43.

BRUTO, L. et al. Variability of CO_2 fugacity at the western edge of the tropical Atlantic Ocean from the $8°N$ to $38°W$ PIRATA buoy. *Dynamics of Atmospheres and Oceans*, Elsevier, v. 78, p. 1–13, 2017. doi:10.1016/j.dynatmoce.2017.01.003. Cited on page 36.

CARTON, J. A.; CHEPURIN, G.; CAO, X. A Simple Ocean Data Assimilation Analysis of the Global Upper Ocean 1950–95. Part I: Methodology. *Journal of Physical Oceanography*, v. 30, n. 2, p. 294–309, fev. 2000a. doi:10.1175/1520-0485(2000)030<0294:ASODAA>2.0.CO;2. Cited on page 52.

CARTON, J. A.; CHEPURIN, G.; CAO, X. A Simple Ocean Data Assimilation Analysis of the Global Upper Ocean 1950–95. Part II: Results. *Journal of Physical Oceanography*, v. 30, n. 2, p. 311–326, fev. 2000b. doi:10.1175/1520-0485(2000)030<0311:ASODAA>2.0.CO;2. Cited on page 52.

CARTON, J. A.; GIESE, B. S. A reanalysis of ocean climate using Simple Ocean Data Assimilation (SODA). *Monthly Weather Review*, v. 136, n. 8, p. 2999–3017, 2008. doi:10.1175/2007MWR1978.1. Cited 2 times on pages 51 and 53.

CARVALHO, M.; GHERARDI, D. F. M. Uso de transformação IHS e classificação não supervisionada por regiões para o mapeamento da sensibilidade ambiental ao derramamento de óleo. *Simp. Bras. de Sens. Rem*, v. 11, n. 2003, p. 1515–1523, 2003. Cited on page 28.

CASTELÃO, G. P.; JOHNS, W. E. The sea-surface structure of North Brazil Current Rings derived from shipboard and moored acoustic Doppler current profiler observations. *Journal of Geophysical Research*, v. 116, n. C01010, jan. 2011. Cited on page 37.

CHEN, F.; YAPA, P. D. Estimating hydrate formation and decomposition of gases released in a deepwater ocean plume. *Journal of marine systems*, Elsevier, v. 30, n. 1, p. 21–32, 2001. Cited 4 times on pages 34, 35, 62, and 64.

CHEN, F.; YAPA, P. D. A model for simulating deep water oil and gas blowouts-Part II: Comparison of numerical simulations with "Deepspill" field experiments. *Journal of Hydraulic Research*, Taylor & Francis Group, v. 41, n. 4, p. 353–365, 2003. Cited on page 40.

CHEN, F.; YAPA, P. D. Modeling gas separation from a bent deepwater oil and gas jet/plume. *Journal of Marine Systems*, Elsevier, v. 45, n. 3, p. 189–203, 2004. Cited 3 times on pages 61, 62, and 63.

CHEN, H. et al. Numerical study of underwater fate of oil spilled from deepwater blowout. *Ocean Engineering*, Elsevier, v. 110, p. 227–243, 2015. Cited 2 times on pages 38 and 40.

COLES, V. J. et al. The pathways and properties of the Amazon river plume in the tropical North Atlantic Ocean. *Journal of Geophysical Research C: Oceans*, v. 118, n. 12, p. 6894–6913, dez. 2013. Cited 6 times on pages 32, 33, 37, 74, 78, and 96.

COOLEY, S. R. et al. Seasonal variations in the Amazon plume-related atmospheric carbon sink. *Global Biogeochemical Cycles*, Wiley Online Library, v. 21, n. 3, p. 1–15, 2007. Cited on page 33.

COOPER, C.; FORRISTALL, G. Z.; JOYCE, T. M. Velocity and hydrographic structure of two Gulf of Mexico warm-core rings. *Journal of Geophysical Research: Oceans*, Wiley Online Library, v. 95, n. C2, p. 1663–1679, 1990. Cited on page 39.

CORREA, D. et al. Modelado de la circulación marina y descargas hipotéticas en la bahía del Callao, Perú. *Instituto del Mar del Perú*, v. 35, n. 3, p. 181–192, 2008. Cited on page 55.

Da Silva, A.; YOUNG, A. C.; LEVITUS, S. *Atlas of sur face marine data 1994, volume 1: Algorithms and procedures*. [S.l.], 1994. Cited on page 61.

DAI, A.; TRENBERTH, K. E. Estimates of Freshwater Discharge from Continents: Latitudinal and Seasonal Variations. *Journal of Hydrometeorology*, v. 3, n. 6, p. 660–687, 2002. Cited 2 times on pages 54 and 61.

DASANAYAKA, L. K.; YAPA, P. D. Role of plume dynamics phase in a deepwater oil and gas release model. *Journal of Hydro-environment Research*, Elsevier, v. 2, n. 4, p. 243–253, 2009. Cited on page 40.

DAVIDSON, M.; PUN, K. Weakly advected jets in cross-flow. *Journal of Hydraulic Engineering*, American Society of Civil Engineers, v. 125, n. 1, p. 47–58, 1999. Cited 2 times on pages 45 and 63.

DAVIDSON, M.; WANG, H. Strongly advected jet in a coflow. *Journal of hydraulic engineering*, American Society of Civil Engineers, v. 128, n. 8, p. 742–752, 2002. Cited on page 63.

De Dominicis, M. et al. MEDSLIK-II, a Lagrangian marine surface oil spill model for short-term forecasting–Part 1: Theory. *Geoscientific Model Development*, Copernicus GmbH, v. 6, n. 6, p. 1851–1869, 2013. Cited on page 37.

De Dominicis, M. et al. MEDSLIK-II, a Lagrangian marine surface oil spill model for short-term forecasting–Part 2: Numerical simulations and validations. *Geoscientific Model Development*, Copernicus GmbH, v. 6, n. 6, p. 1871–1888, 2013. Cited on page 37.

DESSIER, A.; DONGUY, J. R. The sea surface salinity in the tropical Atlantic between 10 S and 30 N-seasonal and interannual variations (1977-1989) . *Deep Sea Research Part I: Oceanographic Research Papers*, v. 41, n. 1, p. 81–100, 1994. Cited on page 36.

Di Lorenzo, E. et al. Weak and strong constraint data assimilation in the inverse Regional Ocean Modeling System (ROMS): Development and application for a baroclinic coastal upwelling system. *Ocean Modelling*, Elsevier, v. 16, n. 3, p. 160–187, 2006. Cited on page 56.

D'ONOFRIO, E.; OREIRO, F.; FIORE, M. Simplified empirical astronomical tide model—An application for the Río de la Plata estuary. *Computers & Geosciences*, v. 44, p. 196–202, jul. 2012. Cited on page 61.

DUKOWICZ, J. K.; SMITH, R. D. Implicit free-surface method for the Bryan-Cox-Semtner ocean model. *Journal of Geophysical Research*, v. 99, n. C4, p. 7991–8014, abr. 1994. Cited on page 52.

EGBERT, G. D.; BENNETT, A. F.; FOREMAN, M. G. G. TOPEX/POSEIDON tides estimated using a global inverse model. *Journal of Geophysical Research: Oceans*, v. 99, n. C12, p. 24821–24852, dez. 1994. Cited 3 times on pages 53, 56, and 61.

EGBERT, G. D.; EROFEEVA, S. Y. Efficient inverse modeling of barotropic ocean tides. *Journal of Oceanic and Atmospheric Technology*, v. 19, n. 2, p. 183–204, 2002. Cited 2 times on pages 53 and 61.

ELLIOTT, A. J. Shear diffusion and the spread of oil in the surface layers of the North Sea. *Ocean Dynamics*, Springer, v. 39, n. 3, p. 113–137, 1986. Cited 2 times on pages 47 and 48.

ENGLEZOS, P. et al. Kinetics of gas hydrate formation from mixtures of methane and ethane. *Chemical Engineering Science*, Elsevier, v. 42, n. 11, p. 2659–2666, 1987. Cited on page 43.

E&P Forum/UNEP. *Environment al management in oil and gas exploration and production: An overview of issues and management approache*. [S.l.], 1997. v. 2, n. 37, 76pp p. Cited on page 34.

ETKIN, D. S. Estimating cleanup costs for oil spills. In: AMERICAN PETROLEUM INSTITUTE. *International oil spill conference*. [S.l.], 1999. v. 1999, n. 1, p. 35–39. Cited on page 28.

EZER, T.; ARANGO, H.; SHCHEPETKIN, A. Developments in terrain-following ocean models: Intercomparisons of numerical aspects. *Ocean Modelling*, n. 4, p. 249–267, 2002. Cited on page 60.

FANNELOP, T.; SJOEN, K. Hydrodynamics of underwater blowouts. In: *18th Aerospace Sciences Meeting*. [S.l.: s.n.], 1980. p. 219p. Cited 2 times on pages 33 and 61.

FERRY, N.; REVERDIN, G. Sea surface salinity interannual variability in the western tropical Atlantic: An ocean general circulation model study. *Journal of Geophysical Research: Oceans*, v. 109, n. C5, p. 1–11, maio 2004. doi:10.1029/2003JC002122. Cited on page 32.

FFIELD, A. Amazon and Orinoco River Plumes and NBC Rings: Bystanders or Participants in Hurricane Events? *Journal of Climate*, v. 20, n. 2, p. 316–333, jan 2007. ISSN 0894-8755. Cited 2 times on pages 32 and 33.

FISCHER, H. B. et al. *Mixing in Inland and Coastal Waters*. [S.l.: s.n.], 1979. ISBN 978-0-08-051177-1. Cited on page 45.

FOGG, P. G.; GERRARD, W. *Chapter 7. Solubilities of methane and other gaseous hydrocarbons*. [S.l.]: John Wiley. New York, 1991. Cited on page 46.

FOLTZ, G. R.; SCHMID, C.; LUMPKIN, R. Transport of Surface Freshwater from the Equatorial to the Subtropical North Atlantic Ocean. *Journal of Physical Oceanography*, v. 45, n. 4, p. 1086–1102, 2015. ISSN 0022-3670. Disponível em: <http://journals.ametsoc.org/doi/abs/10.1175/JPO-D-14-0189.1;http://dx.doi.org/10.1175/JPO-D-14-0189.1>. Cited on page 37.

FOX, C. et al. Transregional linkages in the north-eastern Atlantic: an end-to-end analysis of pelagic ecosystems. *Oceanography and marine biology:an annual review.*, CRC Pess Inc, v. 47, p. 1–76, 2009. Cited on page 49.

FRATANTONI, D. North Atlantic surface circulation during the 1990's North Atlantic surface circulation during observed with satellite-tracked drifters . *Journal of Geophysical Research: Oceans*, Wiley Online Library, v. 106, n. C10, p. 22067–22093, 2001. Cited on page 37.

FRATANTONI, D. M.; GLICKSON, D. a. North Brazil Current Ring Generation and Evolution Observed with SeaWiFS*. *Journal of Physical Oceanography*, v. 32, n. 3, p. 1058–1074, 2002. ISSN 0022-3670. Cited 2 times on pages 33 and 37.

FRATANTONI, D. M.; JOHNS, W. E.; TOWNSEND, T. L. Rings of the North Brazil Current: Their structure and behavior inferred from observations and a numerical simulation. *Journal of Geophysical Research*, v. 100, n. C6, p. 10633–10654, jun. 1995. Cited on page 36.

FRATANTONI, D. M.; RICHARDSON, P. L. The evolution and demise of North Brazil Current rings. *Journal of Physical Oceanography*, v. 36, n. 7, p. 1241–1264, 2006. Cited 2 times on pages 36 and 37.

FRIEDL, M. J.; FANNELØP, T. Bubble plumes and their interaction with the water surface. *Applied Ocean Research*, Elsevier, v. 22, n. 2, p. 119–128, 2000. Cited 4 times on pages 33, 34, 61, and 62.

GARCIA, H. E. et al. *World Ocean Atlas 2013: Dissolved Inorganic Nutrients (phosphate, nitrate, silicate)*. [S.l.]: NOAA Atlas NESDIS 76, 2014. v. 4. 33 p. Cited on page 51.

GARCIA, H. E. et al. *World Ocean Atlas 2013: Dissolved Oxygen, Apparent Oxygen Utilization, and Oxygen Saturation*. [S.l.]: NOAA Atlas NESDIS 75, 2014. v. 3. 35 p. Cited on page 51.

GARZA-GIL, M. D.; PRADA-BLANCO, A.; VÁZQUEZ-RODRÍGUEZ, M. X. Estimating the short-term economic damages from the Prestige oil spill in the Galician fisheries and tourism. *Ecological Economics*, Elsevier, v. 58, n. 4, p. 842–849, 2006. Cited on page 27.

GARZOLI, S. L. et al. North Brazil Current retroflection and transports. *Journal of Geophysical Research*, v. 109, n. C1, p. 1–14, 2004. ISSN 0148-0227. Cited 2 times on pages 36 and 37.

GILL, A. E. *Atmosphere-Ocean Dynamics*. [S.l.]: Academic Press, 1982. v. 30. (International Geophysics, v. 30). ISBN 0-12-283520-4. Cited on page 57.

GOULDING, M.; BARTHEM, R.; FERREIRA, E. *Smithsonian Atlas of the Amazon*. 1. ed. [S.l.]: Smithsonian Institution Press, 2003. 256–269 p. ISBN 2901588341357. Cited on page 32.

GRODSKY, S. A.; CARTON, J. A. Surface drifter pathways originating in the equatorial Atlantic cold tongue. *Geophysical research letters*, Wiley Online Library, v. 29, n. 23, p. 62–1—62–4, 2002. doi:10.1029/2002GL015788. Cited on page 37.

GRODSKY, S. A. et al. Haline hurricane wake in the Amazon/Orinoco plume: AQUARIUS/SACD and SMOS observations. *Geophysical Research Letters*, v. 39, n. 20, p. 4–11, 2012. ISSN 00948276. Cited on page 33.

GRODSKY, S. A. et al. Year-to-year salinity changes in the Amazon plume: Contrasting 2011 and 2012 Aquarius/SACD and SMOS satellite data. *Remote Sensing of Environment*, Elsevier Inc., v. 140, p. 14–22, 2014. ISSN 00344257. Cited 3 times on pages 32, 74, and 76.

GUNDLACH, E. R.; HAYES, M. O. Vulnerability of coastal environments to oil spill impacts. *Marine technology society Journal*, v. 12, n. 4, p. 18–27, 1978. Cited on page 28.

HAIDVOGEL, D. et al. Model evaluation experiments in the North Atlantic basin: Simulations in nonlinear terrain-following coordinates. *Dynamics of Atmospheres and Oceans*, v. 32, p. 239–282, 2000. Cited 2 times on pages 55 and 60.

HEDSTROM, K. S. *SCRUM Manual*. [S.l.]: Institute od Marine and Coastal Sciences. Rutgers University. USA, 1997. Cited on page 60.

HEDSTROM, K. S. *DRAFT Technical Manual for a Coupled Sea-Ice/Ocean Circulation Model*. 3. ed. [S.l.]: U.S Department of the Interior, Mine ral Management Service, Anchorage, Alaska, Arctic Region Supercomputing Center, U niversity of Alaska Fair- banks, Contract M07PC13368, 2009. Cited on page 60.

HOUNSOU-GBO, G. A. et al. Oceanic Indices for Forecasting Seasonal Rainfall over the Northern Part of Brazilian Northeast. *American Journal of Climate Change*, Scientific Research Publishing, v. 5, Scientific Research Publishing, n. 02, p. 261, 2016. http://www.scirp.org/journal/PaperDownload.aspx?paperID=67809. Cited on page 69.

HU, C. et al. The dispersal of the Amazon and Orinoco River water in the tropical Atlantic and Caribbean Sea: Observation from space and S-PALACE floats. *Deep Sea Research Part II: Topical Studies in Oceanography*, v. 51, n. 10-11, p. 1151–1171, may-jun 2004. Cited 2 times on pages 32 and 35.

IBÁNHEZ, J. S. P.; FLORES, M.; LEFÈVRE, N. Collapse of the tropical and subtropical North Atlantic CO_2 sink in boreal spring of 2010. *Scientific Reports*, Nature Publishing Group, v. 7, p. 41694, 2017. doi:10.1038/srep41694. Cited on page 33.

IHO. *Limits of Oceans and Seas*. 3rd. ed. [S.l.]: International Hydrographic Organization Special Publication, 1953. 42 p. Cited on page 49.

ITOPF, I. T. O. P. F. *Oil Tanker Spill Statistics 2016*. 2016. <http://www.itopf.com/knowledge-resources/data-statistics/statistics/>. Accessed: 2017-07-7. Cited on page 28.

JAHN, F.; COOK, M.; GRAHAM, M. *Hydrocarbon exploration and production*. [S.l.]: Elsevier, 2008. v. 55. Cited on page 28.

JAYNE, S. R.; WAHR, J. M.; BRYAN, F. O. Observing ocean heat content using satellite gravity and altimetry. *Journal of Geophysical Research: Oceans*, Wiley Online Library, v. 108, n. C2, p. 13–1——13–12, 2003. doi:10.1029/2002JC001619. Cited on page 70.

JERNELÖV, A.; LINDÉN, O. Ixtoc I: a case study of the world's largest oil spill. *Ambio*, JSTOR, p. 299–306, 1981. Cited on page 28.

JOHANSEN, Ø. DeepBlow–a Lagrangian plume model for deep water blowouts. *Spill Science & Technology Bulletin*, Elsevier, v. 6, n. 2, p. 103–111, 2000. Cited 2 times on pages 34 and 39.

JOHANSEN, Ø. Development and verification of deep-water blowout models. *Marine Pollution Bulletin*, Elsevier, v. 47, n. 9, p. 360–368, 2003. Cited 4 times on pages 34, 42, 62, and 64.

JOHANSEN, Ø.; RYE, H.; COOPER, C. DeepSpill—-field study of a simulated oil and gas blowout in deep water. *Spill Science & Technology Bulletin*, Elsevier, v. 8, n. 5-6, p. 433–443, 2003. doi:10.1016/S1353-2561(02)00123-8. Cited on page 39.

Johns, W. E. et al. The North Brazil Current Retroflection: Seasonal Structure and Eddy Variability. *Journal of Geophysical Research*, v. 95, n. 11, p. 22103–22120, 1990. Cited 2 times on pages 32 and 36.

JOHNS, W. E. et al. Annual cycle and variability of the North Brazil Current. *Journal of Physical Oceanography*, v. 28, n. 1, p. 103–128, 1998. Cited 3 times on pages 32, 37, and 73.

JOYE, S. B. et al. Magnitude and oxidation potential of hydrocarbon gases released from the BP oil well blowout. *Nature Geoscience*, Nature Publishing Group, v. 4, n. 3, p. 160, 2011. Cited on page 43.

JUNIOR, O. M. da S.; MAGRINI, A. Exploração de hidrocarbonetos na Foz do Rio Amazonas: perspectivas de impactos ambietais no âmbito das áreas ofertadas na 11o rodada de licitações da Agência Nacional do Petroléo. *Revista GeoAmazônia*, v. 2, n. 04, p. 159–172, jul-dez 2014. Cited on page 68.

KIRBY, M. F.; LAW, R. J. Accidental spills at sea–Risk, impact, mitigation and the need for co-ordinated post-incident monitoring. *Marine pollution bulletin*, Elsevier, v. 60, n. 6, p. 797–803, 2010. Cited 2 times on pages 28 and 29.

KOROSOV, A.; COUNILLON, F.; JOHANNESSEN, J. A. Monitoring the spreading of the Amazon freshwater plume by MODIS, SMOS, Aquarius, and TOPAZ. *Journal of Geophysical Research C: Oceans*, v. 120, n. 1, p. 268–283, 2015. ISSN 21699291. Cited 3 times on pages 33, 78, and 96.

KRICHEVSKY, I.; KASARNOVSKY, J. Thermodynamical calculations of solubilities of nitrogen and hydrogen in water at high pressures. *Journal of the American Chemical Society*, ACS Publications, v. 57, n. 11, p. 2168–2171, 1935. Cited on page 46.

LARGE, W. G.; MCWILLIAMS, J. C.; DONEY, S. C. Oceanic vertical mixing: A review and a model with a nonlocal boundary layer parameterization. *Reviews of Geophysics*, v. 32, n. 4, p. 363–403, nov. 1994. Cited on page 51.

LEE, J. H.; CHEUNG, V. Generalized Lagrangian model for buoyant jets in current. *Journal of Environmental Engineering*, American Society of Civil Engineers, v. 116, n. 6, p. 1085–1106, 1990. Cited 2 times on pages 40 and 98.

LEFÈVRE, N.; DIVERRÈS, D.; GALLOIS, F. Origin of CO_2 undersaturation in the western tropical Atlantic. *Tellus B*, Wiley Online Library, v. 62, n. 5, p. 595–607, 2010. Cited on page 33.

LEITE, F. S. et al. Modeling Subsurface Gas Release in Tropical and Shallow Waters: Comparison with Field Experiments off Brazil's Northeast Coast. *Human and Ecological Risk Assessment: An International Journal*, Taylor & Francis, v. 20, n. 1, p. 150–173, 2014. Cited 3 times on pages 37, 61, and 62.

LEKVAM, K.; BISHNOI, P. R. Dissolution of methane in water at low temperatures and intermediate pressures. *Fluid Phase Equilibria*, Elsevier, v. 131, n. 1, p. 297–309, 1997. Cited 3 times on pages 13, 46, and 47.

LENTZ, S. J. Seasonal variations in the horizontal structure of the Amazon Plume inferred from historical hydrographic data. *Journal of Geophysical Research: Oceans*, Wiley Online Library, v. 100, n. C2, p. 2391–2400, 1995b. Cited on page 37.

LEVIN, L. A.; GOODAY, A. The Atlantic: The Deep Atlantic Ocean. In: ____. [S.l.]: Elsiever, 2003. cap. 5, p. 111–178. Cited on page 49.

LEVITUS, S.; ANTONOV, J.; BOYER, T. Warming of the world ocean, 1955–2003. *Geophysical Research Letters*, Wiley Online Library, v. 32, n. 2, 2005. Cited on page 70.

LIMA, P. C. R. Os desafios, os impactos e a gestão da exploração do pré-sal. *Estudo da Consultoria Legislativa da Câmara dos Deputados*, Novembro, 2008. Cited on page 29.

LOCARNINI, R. A. et al. *World Ocean Atlas 2013: Temperature*. [S.l.]: NOAA Atlas NESDIS 73, 2013. v. 1. 40 p. Cited on page 51.

LUTJEHARMS, J.; PENVEN, P.; ROY, C. Modelling the shear edge eddies of the southern Agulhas Current. *Continental Shelf Research*, v. 23, n. 11-13, p. 1099–1115, jul. 2003. Cited on page 55.

Malanotte-Rizzoli, P. et al. Water mass pathways between the subtropical and tropical ocean in a climatological simulation of North Atlantic. *Dynamics of Atmospheres and Oceans*, v. 32, n. 3-4, p. 331–371, 2000. Cited on page 55.

MAXIMENKO, N.; HAFNER, J. SCUD: Surface CUrrents form Diagnostic model. *IPRC Technical Note No. 5. International Pacific Research Center - School of Ocean and Earth Science and Technology - University of Hawaii*, University of Hawaii, 2010. http://iprc.soest.hawaii.edu/users/hafner/NIKOLAI/SCUD/BAK/SCUD_manual_02_16.pdf. Cited on page 54.

MAXIMENKO, N. et al. Mean dynamic topography of the ocean derived from satellite and drifting buoy data using three different techniques. *Journal of Atmospheric and Oceanic Technology*, v. 26, n. 9, p. 1910–1919, 2009. Cited on page 54.

MICHEL, J.; HAYES, M. O.; BROWN, P. J. Application of an oil spill vulnerability index to the shoreline of lower Cook Inlet, Alaska. *Environmental Geology*, Springer, v. 2, n. 2, p. 107–117, 1978. Cited on page 28.

MOLINIER, M. et al. Les regimes hydroiogiques de l'Amazone et de ses affluents. *IAHS publication*, p. 209–222, 1996. Cited on page 32.

MONTÉGUT, C. de B. et al. Mixed layer depth over the global ocean: An examination of profile data and a profile-based climatology. *Journal of Geophysical Research*, v. 109, p. C12003, 2004. Cited on page 70.

MONTÉGUT, C. de B. et al. Control of salinity on the mixed layer depth in the world ocean: 1. General description. *Journal of Geophysical Research: Oceans*, Wiley Online Library, v. 112, n. C6, 2007. Cited on page 69.

MOORE, A. M. et al. A comprehensive ocean prediction and analysis system based on the tangent linear and adjoint of a regional ocean model. *Ocean Modelling*, Elsevier, v. 7, n. 1, p. 227–258, 2004. Cited on page 56.

MOURA, R. L. et al. An extensive reef system at the Amazon River mouth. *Science advances*, American Association for the Advancement of Science, v. 2, n. 4, p. e1501252, 2016. Cited on page 68.

Müller-Karger, F. E. et al. Pigment distribution in the Caribbean Sea Observations from space. *Progress in Oceanography*, v. 23, p. 23–64, 1989. Cited on page 32.

Müller-Karger, F. E.; MCCLAIN, C. R.; RICHARDSON, P. L. The dispersal of the Amazons water. *Nature*, v. 333, p. 56–59, maio 1988. Cited 2 times on pages 32 and 37.

NCEI. https://www.ngdc.noaa.gov/mgg/fliers/06mgg01.html. NOAA, jun. 2006. http:// www.ngdc.noaa.gov/mgg/fliers/ 06mgg01.html. Cited on page 53.

NEWINGER, C.; TOUMI, R. Potential impact of the colored Amazon and Orinoco plume on tropical cyclone intensity. *Journal of Geophysical Research: Oceans*, v. 120, n. 2, p. 1296–1317, fev. 2015. Cited 3 times on pages 33, 78, and 96.

NORTH, E. W. et al. Simulating oil droplet dispersal from the Deepwater Horizon spill with a Lagrangian approach. *Monitoring and Modeling the Deepwater Horizon Oil Spill: A Record-Breaking Enterprise*, Wiley Online Library, p. 217–226, 2011. Cited on page 37.

PAILLER, K.; BOURLÈS, B.; GOURIOU, Y. The barrier layer in the western tropical Atlantic Ocean. *Geophysical Research Letters*, Wiley Online Library, v. 26, n. 14, p. 2069–2072, 1999. Cited on page 83.

PANZER, I. et al. High Performance Regional Ocean Modeling with GPU Acceleration. *IEEE/MTS OCEANS*, p. 1–4, set. 2013. doi:10.23919/OCEANS.2013.6741366. Cited on page 55.

PENVEN, P. et al. *ROMS_AGRIF/ROMSTOOLS User's Guide*. [S.l.]: Institut de Recherche pour le D´eveloppement (IRD). France, 2010. Cited on page 60.

PENVEN, P. et al. Software tools for pre- and post-processing of oceanic regional simulations. *Environmental Modelling & Software*, v. 23, n. 5, p. 660–662, jul. 2007. Cited on page 60.

PENVEN, P. et al. A regional hydrodynamic model of upwelling in the Southern Benguela. *South African Journal of Science*, v. 97, p. 472–776, nov. 2001. Cited on page 55.

PENVEN, P. et al. Simulation of a coastal jet retention process using a barotropic model. *Oceanologica Acta*, v. 23, n. 5, p. 615–634, 2000. Cited on page 55.

PETERSON, R. G.; STRAMMA, L. Upper-level circulation in the South Atlantic Ocean. *Progress in Oceanography*, v. 26, n. 1, p. 1–73, 1991. Cited 2 times on pages 35 and 37.

REED, M. et al. Oil spill modeling towards the close of the 20th century: overview of the state of the art. *Spill Science & Technology Bulletin*, Elsevier, v. 5, n. 1, p. 3–16, 1999. Cited on page 35.

REYNOLDS, R. W. et al. An improved in situ and satellite SST analysis for climate. *Journal of climate*, v. 15, n. 13, p. 1609–1625, 2002. doi:10.1175/1520-0442(2002)015<1609:AIISAS>2.0.CO;2. Cited on page 53.

REYNOLDS, R. W.; SMITH, T. M. Improved global sea surface temperature analyses using optimum interpolation. *Journal of climate*, v. 7, n. 6, p. 929–948, 1994. doi:10.1175/1520-0442(1994)007<0929:IGSSTA>2.0.CO;2. Cited on page 53.

RICHARDSON, P. L. et al. North Brazil Current retroflection eddies. *Journal of Geophysical Research*, v. 99, n. C3, p. 5081–5093, 1994. ISSN 0148-0227. Disponível em: <http://doi.wiley.com/10.1029/93JC03486>. Cited on page 37.

RICHARDSON, P. L.; REVERDIN, G. Seasonal cycle of velocity in the Atlantic North Equatorial Countercurrent as measured by surface drifters, current meters, and ship drifts. *Journal of Geophysical Research: Oceans*, v. 92, n. C4, p. 3691–3708, abr. 1987. Cited on page 76.

RICHARDSON, P. L.; WALSH, D. Mapping climatological seasonal variations of surface currents in the tropical Atlantic using ship drifts. *Journal of Geophysical Research*, v. 91, n. C9, p. 10537–10550, set. 1986. Cited on page 37.

RICHEY, J. E.; NOBRE, C.; DESER, C. Amazon River discharge and climate variability: 1903 to 1985. *Science*, American Association for the Advancement of Science, v. 246, n. 4926, p. 101–103, 1989. Cited on page 32.

RODRIGUES, L. A.; SAUER, I. L. Exploratory assessment of the economic gains of a pre-salt oil field in Brazil. *Energy Policy*, Elsevier, v. 87, p. 486–495, 2015. Cited on page 29.

RYE, H.; BRANDVIK, P. J.; STRØM, T. Subsurface blowouts: Results from field experiments. *Spill Science & Technology Bulletin*, Elsevier, v. 4, n. 4, p. 239–256, 1997. Cited on page 39.

SALISBURY, J. et al. Spatial and temporal coherence between Amazon River discharge, salinity, and light absorption by colored organic carbon in western tropical Atlantic surface waters. *Journal of Geophysical Research*, v. 116, p. C00H02, jul 2011. ISSN 0148-0227. Disponível em: <http://doi.wiley.com/10.1029/2011JC006989>. Cited on page 32.

SANTOS, V. F. dos; MENDES, A. C.; SILVEIRA, O. F. M. da. *Atlas de sensibilidade ambiental ao óleo da Bacia Marítima da Foz do Amazonas*. [S.l.]: Macapá: IEPA, 2016. 106p p. ISBN 978-85-87794-29-1. Cited on page 68.

SCHMIDT, A. C. K. et al. A Feature Oriented Regional Modeling System for the North Brazil Current Rings Migration after Retroflection. *Offshore Technology Conference*, n. OIC 21532, 2011. Cited on page 33.

Schmitz Jr., W. J.; MCCARTNEY, M. S. On the North Atlantic Circulation. *Reviews of Geophysics*, v. 31, n. 1, p. 29–49, fev. 1993. Cited on page 32.

SCHOTT, F. A. et al. The zonal currents and transports at 35 W in the tropical Atlantic. *Geophysical Research Letters*, v. 30, n. 7, p. 1349, abr. 2003. Cited on page 37.

SERVAIN, J. et al. A pilot research moored array in the tropical Atlantic (PIRATA). *Bulletin of the American Meteorological Society*, v. 79, p. 2019–2031, 1998. Cited on page 53.

SHARMA, N. et al. Quantifying the Seasonal and Interannual Variability of the Formation and Migration Pattern of North Brazil Current Rings. In: *OCEANS 2009, MTS/IEEE Biloxi-Marine Technology for Our Future: Global and Local Challenges*. [S.l.]: IEEE, 2009. p. 1–7. ISBN 978-1-4244-4960-6. Cited on page 73.

SHCHEPETKIN, A. F. An Adaptive, Courant-number-dependent Implicit Scheme for Vertical Advection in Oceanic Modeling. *Ocean Modelling*, v. 91, p. 38–69, 2015. Cited on page 60.

SHCHEPETKIN, A. F.; MCWILLIAMS, J. C. The regional oceanic modeling system (ROMS): a split-explicit, free-surface, topography-following-coordinates oceanic model. *Ocean Modelling*, v. 9, p. 347–404, 2005. Cited on page 55.

SHE, J.; KLINCK, J. M. Flow near submarine canyons driven by constant wind. *Journal of Geophysical Research*, v. 105, n. C12, p. 28671–28694, dez. 2000. Cited on page 55.

SHE, J.; KLINCK, J. M. Correction to "Flow near submarine canyons driven by constant wind". *Journal of Geophysical Research*, v. 106, n. C2, p. 2689, fev. 2001. Cited on page 55.

SILVA, M. et al. High-resolution regional ocean dynamics simulation in the southwestern tropical Atlantic. *Ocean Modelling*, v. 30, p. 256–269, 2009. Cited on page 55.

SIMMONS, A. J.; GIBSON, J. K. *The ERA-40 Project Plan, ERA- 40 Project Report Series No. 1*. [S.l.], 2000. 1–63 p. Cited on page 52.

Sloan Jr, E. D.; KOH, C. *Clathrate hydrates of natural gases*. Third. [S.l.]: CRC press. Taylor & Francis Group, 2008. Cited 2 times on pages 13 and 44.

SLUTZ, R. J. et al. Comprehensive Ocean-Atmosphere Data Set: Release 1. *Climate Research Program, Boulder, Colorado*, 1985. Cited on page 51.

SMITH, L.; SMITH, M.; ASHCROFT, P. Analysis of environmental and economic damages from British Petroleum's Deepwater Horizon oil spill. *Marine pollution bulletin*, v. 74, n. 1, p. 563–585, 2011. Cited on page 28.

SMITH, R.; DUKOWICZ, J.; MALONE, R. Parallel ocean general circulation modeling. *Physica D: Nonlinear Phenomena*, v. 60, n. 1-4, p. 38–61, nov. 1992. Cited on page 51.

SMITH, W. H. F.; SANDWELL, D. T. Global sea floor topography from satellite altimetry and ship depth soundings. *Science*, v. 277, n. 5334, p. 1956–1962, set. 1997. Cited on page 53.

SOCOLOFSKY, S.; ADAMS, E. Multi-phase plumes in uniform and stratified crossflow. *Journal of Hydraulic Research*, Taylor & Francis, v. 40, n. 6, p. 661–672, 2002. Cited on page 45.

SOCOLOFSKY, S. A. *Laboratory experiments of multi-phase plumes in stratification and crossflow*. Tese (Doutorado) — Massachusetts Institute of Technology, 2001. Cited on page 45.

SOCOLOFSKY, S. A.; ADAMS, E. E. Role of slip velocity in the behavior of stratified multiphase plumes. *Journal of Hydraulic Engineering*, American Society of Civil Engineers, v. 131, n. 4, p. 273–282, 2005. Cited 2 times on pages 66 and 67.

SONG, Y.; HAIDVOGEL, D. B. A Semi-implicit Ocean Circulation Model Using a Generalized Topography-following Coordinate System. *J. Comput. Phys.*, Academic Press Professional, Inc., San Diego, CA, USA, v. 115, n. 1, p. 228–244, nov. 1994. ISSN 0021-9991. doi:10.1006/jcph.1994.1189. Disponível em: <http://dx.doi.org/10.1006/jcph.1994.1189>. Cited 2 times on pages 55 and 60.

An integrated model for prediction of oil transport from a deep water blowout, v. 2. 611–635 p. Cited on page 39.

SPRINTALL, J.; TOMCZAK, M. Evidence of the barrier layer in the surface layer of the tropics. *Journal of Geophysical Research: Oceans*, Wiley Online Library, v. 97, n. C5, p. 7305–7316, 1992. Cited on page 69.

STRAMMA, L.; ENGLAND, M. On the water masses and mean circulation of the South Atlantic Ocean. *Journal of Geophysical Research*, v. 104, n. C9, p. 20863–20883, set. 1999. Cited 2 times on pages 35 and 37.

STRAMMA, L. et al. Upper ocean circulation in the western tropical Atlantic in boreal fall 2000. *Deep Sea Research Part I: Oceanographic Research Papers*, v. 52, n. 2, p. 221–240, fev. 2005. Cited 2 times on pages 35 and 37.

STUKEL, M. R. et al. Top-down, bottom-up and physical controls on diatom-diazotroph assemblage growth in the Amazon River plume. *Biogeosciences*, v. 11, n. 12, p. 3259–3278, 2014. ISSN 17264189. Cited on page 32.

SUBRAMANIAM, A. et al. Amazon River enhances diazotrophy and carbon sequestration in the tropical North Atlantic Ocean. *Proceedings of the National Academy of Sciences of the United States of America*, v. 105, n. 30, p. 10460–5, jul 2008. ISSN 1091-6490. Cited on page 33.

TALLEY, L. D. The Earth system: physical and chemical dimensions of global environmental change. In: MACCRACKEN, M. C.; PERRY, J. S.; MUNN, T. (Ed.). *Salinity Patterns in the Ocean*. [S.l.]: John Wiley & Sons, Ltd, 2002, (Encyclopedia of Global Environmental Change, v. 1). ISBN 0-471-97796-9. Cited on page 35.

TEAL, J. M.; HOWARTH, R. W. Oil spill studies: a review of ecological effects. *Environmental Management*, Springer, v. 8, n. 1, p. 27–43, 1984. Cited on page 27.

TOMCZAK, M.; Stuart Godfrey, J. Regional Oceanography: an Introduction. In: ____. 2nd. ed. [S.l.]: Daya Publishing House, 2003. cap. 15. ISBN 8170353068. Cited on page 35.

TOPHAM, D. The formation of gas hydrates on bubbles of hydrocarbon gases rising in seawater. *Chemical Engineering Science*, Elsevier, v. 39, n. 5, p. 821–828, 1984. Cited 4 times on pages 34, 39, 62, and 64.

TOPHAM, D. R. The modelling of hydrocarbon bubble plumes to include gas hydrate formation. *Chemical Engineering Science*, Elsevier, v. 39, n. 11, p. 1613–1622, 1984. Cited on page 39.

U. S. DOE. Environmental benefits of advanced oil and gas exploration and production technology. *Department of Energy*, p. 168pp, 1999. Cited on page 34.

U. S. EIA. Future supply potential of natural gas hydrates. In: *International Energy Outlook. Energy Information Administration*. [S.l.: s.n.], 1998. v. 98, n. DOE/EIA-0484, p. 73–90. Cited on page 34.

U. S. NOIA. What are environmental challenges and regulatory barriers to expanding our natural gas supply and how can they be remedied ? In: *Natural Gas Conference, Senate Energy and Natural Resources Committee. National Ocean Industries Association*. [S.l.: s.n.], 2005. p. 9–11. Cited on page 34.

UPPALA, S. M. et al. The ERA-40 re-analysis. *Quarterly Journal of the royal meteorological society*, Wiley Online Library, v. 131, n. 612, p. 2961–3012, 2005. Cited on page 52.

VAZQUEZ, J.; PERRY, K.; KILPATRICK, K. NOAA/NASA AVHRR oceans pathfinder sea surface temperature data set user's reference manual. *Jet Propulsion Laboratory Tech. Rep. D-14070*, 1998.

https://www.nodc.noaa.gov/woce/woce_v3/wocedata_2/sat_sst/avhrr/docs/usr_gde4_0.htm. Cited on page 53.

VELEDA, D. et al. Intraseasonal variability of the North Brazil Undercurrent forced by remote winds. *Journal of Geophysical Research*, v. 117, n. C11, p. C11024, nov 2012. ISSN 0148-0227. Disponível em: <http://doi.wiley.com/10.1029/2012JC008392>. Cited on page 32.

VYSNIAUSKAS, A.; BISHNOI, P. A kinetic study of methane hydrate formation. *Chemical Engineering Science*, Elsevier, v. 38, n. 7, p. 1061–1072, 1983. Cited on page 39.

WANG, Y. *Ocean Tide Modeling in the Southern Ocean*. [S.l.], 2004. Cited on page 61.

WEAVER, A.; VIALARD, J.; ANDERSON, D. Three- and Four-Dimensional Variational Assimilation with a General Circulation Model of the Tropical Pacific Ocean. Part I: Formulation, Internal Diagnostics, and Consistency Checks. *Monthly Weather Review*, v. 131, n. 7, p. 1360–1378, 2003. Cited on page 56.

WOODRUFF, S. D. et al. A comprehensive ocean-atmosphere data set. *Bulletin of the American meteorological society*, American Meteorological Society, v. 68, n. 10, p. 1239–1250, 1987. Cited on page 51.

XIE, S.-P.; CARTON, J. A. Tropical Atlantic variability: Patterns, mechanisms, and impacts. *Earth's Climate: The Ocean–Atmosphere Interaction, Geophys. Monogr.*, v. 147, Amer. Geophys. Union 100, p. 121–142, 2004. doi:10.1029/147GM07. Cited on page 37.

YAPA, P. D.; CHEN, F. Behavior of oil and gas from deepwater blowouts. *Journal of Hydraulic Engineering*, American Society of Civil Engineers, v. 130, n. 6, p. 540–553, 2004. Cited 2 times on pages 67 and 69.

YAPA, P. D. et al. How does oil and gas behave when released in deepwater? *Journal of hydro-environment research*, Elsevier, v. 6, n. 4, p. 275–285, 2012. Cited on page 40.

YAPA, P. D.; ZHENG, L. Simulation of oil spills from underwater accidents I: Model development. *Journal of Hydraulic Research*, Taylor & Francis Group, v. 35, n. 5, p. 673–688, 1997. Cited 3 times on pages 35, 39, and 64.

YAPA, P. D.; ZHENG, L.; CHEN, F. A model for deepwater oil/gas blowouts. *Marine pollution bulletin*, Elsevier, v. 43, n. 7, p. 234–241, 2001. Cited 3 times on pages 35, 39, and 61.

YAPA, P. D.; ZHENG, L.; NAKATA, K. Modeling underwater oil/gas jets and plumes. *Journal of Hydraulic Engineering*, American Society of Civil Engineers, v. 125, n. 5, p. 481–491, 1999. Cited 2 times on pages 39 and 47.

ZHENG, L.; YAPA, P. D. Simulation of oil spills from underwater accidents II: Model verification. *Journal of Hydraulic Research*, Taylor & Francis, v. 36, n. 1, p. 117–134, 1998. Cited 2 times on pages 39 and 61.

ZHENG, L.; YAPA, P. D. Buoyant velocity of spherical and nonspherical bubbles/droplets. *Journal of Hydraulic Engineering*, American Society of Civil Engineers, v. 126, n. 11, p. 852–854, 2000. Cited 2 times on pages 35 and 61.

ZHENG, L.; YAPA, P. D. Modeling gas dissolution in deepwater oil/gas spills. *Journal of Marine Systems*, Elsevier, v. 31, n. 4, p. 299–309, 2002. Cited 5 times on pages 34, 47, 61, 62, and 64.

ZHENG, L.; YAPA, P. D.; CHEN, F. A model for simulating deepwater oil and gas blowouts-Part I: Theory and model formulation. *Journal of Hydraulic Research*, Taylor & Francis, v. 41, n. 4, p. 339–351, 2002. Cited 5 times on pages 39, 41, 42, 43, and 44.

ZWENG, M. et al. *World Ocean Atlas 2013: Salinity*. [S.l.]: NOAA Atlas NESDIS 74, 2013. v. 2. 47 p. Cited on page 51.

A PAPER "INFLUENCE OF UNDERWATER HYDRODYNAMICS ON OIL AND GAS BLOWOUTS OFF AMAZON RIVER MOUTH"

This annex presents the manuscript entitled *Influence of underwater hydrodynamics on oil and gas blowouts off amazon river mouth*, submitted Feb 21, 2018 in *Tropical Oceanography*. Current status: Accepted.

the main objective is to determine the behavior of the oil/gas plumes of the deepwater blowout, located on the continental shelf of northern Brazil, was analyzed. Three parameters were estimated, the time of arrival at the surface, the plume radius on the surface and the deviation at surface from its origin.

Tropical Oceanography
ISSN 1679-3013 (online) / ISSN 1679-3005 (print)

INFLUENCE OF UNDERWATER HYDRODYNAMICS ON OIL AND GAS BLOWOUTS OFF AMAZON RIVER MOUTH

Humberto L. VARONA[1,2]*; Marcus A. SILVA[1,2]; Dóris VELEDA[1,2]; Fabiana S. LEITE[1,2]; Márcio das Chagas MOURA[3]; Moacyr ARAUJO[1,2]

[1]Department of Oceanography, DOCEAN, Federal University of Pernambuco, Recife, PE, Brazil. E-mail: humberto.varona@yandex.com, marcus.oceano@gmail.com, doris.veleda@ufpe.br, fasoaresl@yahoo.ca, moa.ufpe@gmail.com
*Autor correspondente

[2]Center for Risk Analysis and Environmental Modeling - CEERMA. Federal University of Pernambuco, Recife, PE, Brazil.

[3]Department of Production Engineering, Federal University of Pernambuco, Recife, PE, Brazil. E-mail: marcio@ceerma.org

RESUMO. O estudo está focado na análise do comportamento das plumas de vazamento de óleo/gás em águas profundas, localizadas na plataforma continental do norte do Brasil. O modelo Regional Ocean Modeling System (ROMS) é utilizado para simular a dinâmica oceânica na região 60.5°-24°W/5°S-16°N com 0.25° de resolução, 32 níveis verticais e considerando as descargas dos rios Amazonas e Pará. A saída do modelo ROMS é comparada com o conjunto de dados SODA (Simple Ocean Data Assimilation). Três pontos foram selecionados para fazer as simulações numéricas, localizados em (50°W, 5.25°N), (44.5°W, 0.5°N) e (42.75°W, 1°S). O passo do tempo sugerido por Lee e Cheung (1990) foi ajustado devido às condições oceanográficas particulares em cada ponto, em que a velocidade inicial tende a zero. O coeficiente 0.1 da equação original foi substituído por 0.0250 e 0.0375. Todas as plumas se comportaram como tipo 3. A velocidade de corrente sazonal foi pequena do fundo á superfície, não excedendo 0.25 ms^{-1}; o deslocamento máximo das plumas de seu ponto de origem não foi maior do que 1 m. O diâmetro médio das plumas na superfície variou de 54 a 79.7 m e o tempo de chegada à superfície foi de 7.25 a 8.05 horas.

Palavras-Chave: Vazamento de Óleo/Gás, Foz do Rio Amazonas, Oceano Atlântico, Modelo ROMS, Modelo GAS_DOCEAN.

ABSTRACT. This study is focused on analyzing the behavior of oil/gas plumes from blowouts into deepwater, located at the northern Brazil continental shelf. The Regional Ocean Modeling System (ROMS) model is used to simulate ocean dynamics in the region 60.5°-24.0°W/5°S-16°N with 0.25° of resolution, 32 vertical levels and considering the discharges of the Amazon and Pará Rivers. The ROMS output are compared to Simple Ocean Data Assimilation (SODA) dataset. Three points were selected to make the numerical simulations, located at (50°W, 5.25°N), (44.5°W, 0.5°N) and (42.75°W, 1°S). The time step suggested by Lee and Cheung (1990) was adjusted due to the particular oceanographic conditions at each point, in which, the initial velocity tends to zero and the coefficient 0.1 of the original equation was replaced by 0.0250 and 0.0375. All the plumes behaved as type 3. The seasonal current speed was small from the bottom to the surface, usually not exceeding 0.25 ms^{-1}; the maximum displacement of the plumes from its point of origin was not greater than 1 m. The mean plumes diameter on the surface ranged 54 - 79.7 m and the arrival time to the surface was from 7.25 to 8.05 hours.

Keywords: Oil/Gas Blowouts, Amazon River mouth, Atlantic Ocean, ROMS model, GAS_DOCEAN model.

INTRODUCTION

The dependence of industry and life with the use of oil and gas is very significant; the demand for these two products and their derivatives is extremely high (IEA, 2009; EIA, 2011; Lara, 2014; Prates *et al.,* 2006). Large oil and gas extraction corporations are increasingly expanding into new areas, exploring and exploiting more and more natural gas and oil reserves in the deep ocean. These exploration and exploitation processes are subject to risk of accidents (O'Rourke and Connolly, 2003; Skogdalen *et al.,* 2011), which can endanger human life and contaminate the ocean and the littoral.

The exploration and production of oil at sea is a risk-filled activity (Skogdalen and Vinnem, 2012; Small *et al.,* 2014), as well its research (Abimbola *et al.,* 2014; Neff *et al.,* 1987). It requires dangerous tasks such as drilling rocks in ultra-deep regions, facing very high pressures and handling large volumes of oil and gas. This activity analyzes the large volume of information generated in the initial stages of the investigation, gathering a reasonable knowledge about the depth, thickness and behavior of existing rock layers in a sedimentary basin and the hydrodynamics of the region. Based on this knowledge, the best places to drill in the basin are chosen.

In recent decades, the environmental impacts of oil spills have occurred throughout the world and marine flora and fauna have been frequently submitted to environmental impacts caused by these events (Teal and Howarth, 1984; Ugochukwu and Ertel, 2008). Contamination of marine and coastal environments by oil has been a concern for environmentalists around the world (Mendelssohn *et al.,* 2012). Oil residues and by-products can cause serious consequences for human life (Charrouf and Guillaume, 2008), coastal ecosystems and socioeconomic activities (de Andrade *et al.,* 2010), and has been the subject of many debates. This type of impact causes real environmental catastrophes, with incalculable and often irreversible damage to the environment. Human activities, such as fishing and tourism are also compromised (Garza-Gil *et al.,* 2006), causing great economic damages.

Finally, there has been a progressive decrease in the number of accidents and in the volume of oil discharged internationally (ITOPF, 2016). The reduction of accidents is associated with greater control and care in operations involving the exploration, exploitation, transport and storage of oil, which reflects an increase in the level of environmental responsibility of the society.

Environmental sensitivity to oil spills has been studied some decades ago by Gundlach and Hayes (1978). These authors constructed sensitivity maps containing three types of spatial information: the classification of the sensitivity of environments, biological resources and human resources of recreational, subsistence or commercial value. Thus, the classification of the environment is made according to its physical characteristics, oil permanence and conditions of cleaning and removal.

The Environmental Sensitivity Charts to Oil Spills are essential tools and a primary source of information for contingency planning and for the implementation of response actions to oil pollution incidents, allowing the identification of environments with protection priority and possible areas of sacrifice, allowing the correct allocation of resources and the proper mobilization of containment and cleaning equipment (Carvalho and Gherardi, 2003; Michel *et al.,* 1978).

The impacts of an oil spill and blowout can be minimized if locations most sensitive to contact with the oil can be protected. The previous knowledge of oil spills and explosions under the sea can help in the distribution of available resources to give a more effective response to these types of accidents. The understanding of oceanographic processes in the oil and gas blowouts is fundamental for its prevention and mitigation. In case of oil and gas blowouts, companies would have contingency planning and mitigation to reduce the impact on the environment.

The increase of the oil and gas production in marine environment verified above all in the mid-year 2000 (E&P Forum/UNEP, 1997; U.S. DOE, 1999; U.S. EIA, 1998; U.S. NOIA, 2005) brought the need of more precise models for evaluation of the transport and dispersion of these mixtures in the oceans, as well as their effects on the environment. Initially, Fannelop and Sjoen (1980) focused on the case of the evolution of a single gas plume in the ocean. These authors proposed an approach of simplified analytical modeling, with non-dimensional solutions, and applicable in cases of spills in shallow waters. In this model, the gas expansion all through the water column was estimated considering the classical theory of ideal gas. As a result, the solution for this model brings the dimensions of the cone of gas formed along the water column (starting from the ocean floor), and in consequence, the diameter of the gas plume in the surface.

Meanwhile, the Fannelop and Sjoen (1980) approach does not consider horizontal advection of gas through the currents. Some advance on this initial idea was proposed by Friedl and Fanneløp (2000), when routines were added that considered the elevation in the surface of the sea provoked by the reaching of the gas to the surface (fountain effect, Fig. 1 in Friedl and Fanneløp (2000)). In deeper waters, for instance, the gas cannot be treated as an ideal mixture (Chen and Yapa, 2001), and new interaction processes among the two means gas and liquid was observed, mainly when the local pressure is very different to the atmospheric pressure. In this new generation of mathematical models, created to represent simultaneously oil and gas plumes in marine environment, two more important physiochemical processes were considered, formation of gas hydrate (Chen and Yapa, 2001; Topham, 1984) and gas dissolution (Johansen, 2003; Zheng and Yapa, 2002) in seawater. In shallow waters, the gas dissolution is neglectable (Johansen, 2000).

However, in deep waters, the travel time for the gas through the water column is longer, also rising the dysphasic flow time. Adding to this the fact that the gas solubility increases with the environmental pressure (Johansen, 2000), it is observed frequently that under natural conditions of low temperature and high pressure. The gas tends to form hydrates, which significantly change the ascension velocity of the gaseous plume along the water column (Chen and Yapa, 2001; Johansen, 2003; Topham, 1984). The first models plume evolution of gas developed did not foresee in their equations these two mechanisms (dissolution and hydration), limiting itself to its application in deeper ocean areas (Chen and Yapa, 2001). Yapa and Zheng (1997), for instance, proposed a set of equations to predict the space-time evolution of plumes formed by spills in intermediate waters, considering only the advective transport of the gas as function of its characteristics (volumetric composition) and the environmental thermodynamic conditions (temperature fields, salinity, pressure and density). In the 90's these important mechanisms were introduced into the modeling of a plume of gas in the marine environment (Chen and Yapa, 2001; Reed *et al.,* 1999; Yapa *et al.,* 2001; Zheng and Yapa, 2000).

In this work will be analyzed the dilution capacity of the oil/gas effluents overflow in a blowout event as a result of the simultaneous effects of sea currents, winds and surface and subsurface thermodynamic processes. Three different locations were selected at the continental shelf of Brazil, near the Amazon River mouth and adjacent oceanic areas. This analysis will be held through mathematical modeling of hydrodynamics and gas/oil dispersion plumes in the study region.

STUDY AREA

The Amazon Continental Shelf is a high priority area for the conservation of biodiversity (dos Santos *et al.,* 2016; da Silva Junior and Magrini, 2014) and the Amazon River mouth represents the limit of the distribution of several sponges, lobster, stony corals and snapper and others shallow water fishes, among other groups of coastal and reef organisms (Moura *et al.,* 2016). Our region of study is framed in 52°-40°W/4°S-10°N with 0.25° of resolution, covering an area of 9464500 km2. Fig. 1 shows the bathymetry with the positioning of points P1, P2 and P3 over the continental shelf in the northern coast of Brazil and the location of the deepwater oil exploration blocks.

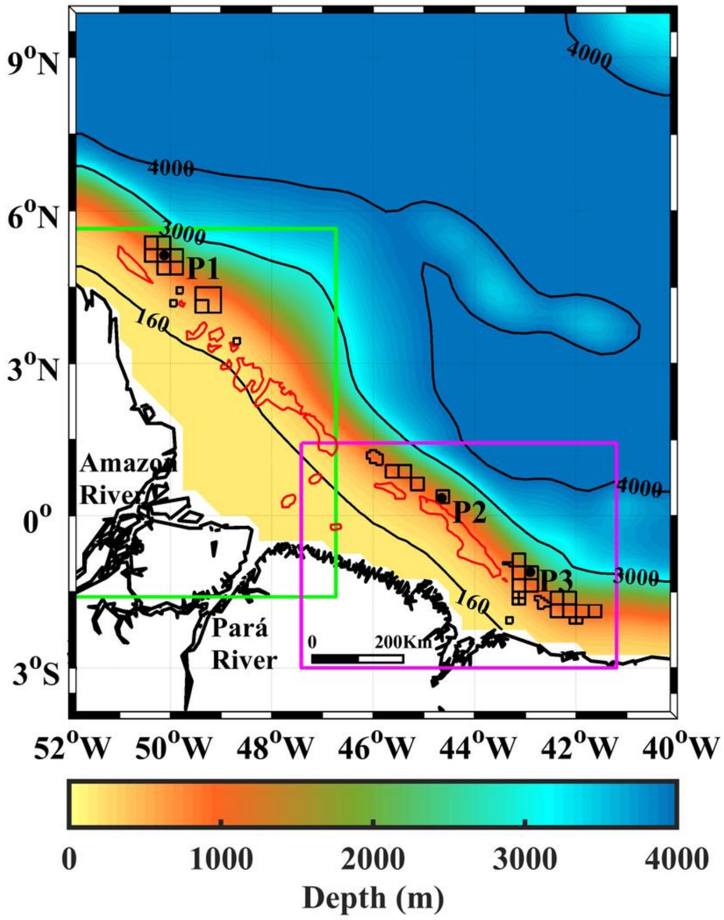

Figure 1. The bathymetry and distribution of the slope in the continental shelf off northern Brazil are represented the isobaths of 160, 3000 and 4000 m in black continuous lines. The green rectangle represents the Amazon mouth basin and the magenta one represents Pará-Maranhão-Barreirinhas basin. The oil and gas exploration blocks are represented by black polygons. The location of P1, P2 and P3 is represented by blue points above of exploration blocks where P1, P2 and P3 are placed - block FZA-M-88 (P1), block PAMA-M-337 (P2) and block BAR-M-21 (P3). The coral reef appears in red color.

The most important oceanic currents around the Amazon region are North Brazil Current (NBC), North Equatorial Countercurrent (NECC) and South Equatorial Current (SEC). According to Stramma and England (1999) the SEC is divided into four branches: the Southern South Equatorial Current (sSEC), the Central South Equatorial Current (cSEC), the northern South Equatorial Current (nSEC) and equatorial South Equatorial Current (eSEC). The eSEC and cSEC give origin to NBC; the latter is also fed by nSEC. At each season the SEC has a strong flow the westwards (about 0.3 ms^{-1}) near the equator and weaker (0.1-0.15 ms^{-1}) in a broad band south of 10°S (Peterson and Stramma, 1991).

NBC flows from northwestward (Lentz, 1995) along the northeastern continental margin of Brazil as a coastal current developing an retroflexion in rings form (Dessier and Donguy, 1994; Fratantoni *et al.,* 1995; Goes *et al.,* 2005; Johns *et al.,* 1990; da Silveira *et al.,* 2000). This makes a turn to the east driven by the wind and feeds the NECC, the NBC reaches speeds of 0.75-1.00 ms^{-1} (Arnault *et al.,* 1999). During the summer, in response to a shift towards the north of the trade winds, the NECC forms eastwards, intensifying significantly during the winter (Grodsky and Carton, 2002; Richardson and Walsh, 1986). The NECC is located between 3-10°S and is considered as the northern boundary for SEC (Peterson and Stramma, 1991). The nSEC is a water source that reinforces the NECC (Stramma and England, 1999). The northern limit of NECC when present is the North Equatorial Current (NEC). The mean speed eastward of NECC is 0.42 ms^{-1} (Fratantoni, 2001).

THE REGIONAL OCEAN MODELING SYSTEM (ROMS)

The ROMS model was used to reproduce climatological and spatial-time variability of oceanic circulation and thermohaline variability in the study area. ROMS is an open source programming, which is effectively created by an extensive group of engineers and researchers, with more than 400000 lines of FORTRAN code, coordinating primitive conditions in a rotational arrangement of free surface, utilizing the Boussinesq approximation, the hydrostatic guess and the adjust of the vertical force (Panzer *et al.,* 2013; Shchepetkin and McWilliams, 2005; Song and Haidvogel, 1994). This was adjusted to various geographic areas of the world where great outcomes were gotten (Haidvogel *et al.,* 2000; Penven *et al.,* 2000; Silva *et al.,* 2009).

The area used for the ROMS model simulations is framed in 60.5°-14.5°W/15.5°S-24.5°N. The bathymetry grid has 183 x 159 nodes with 32 levels in the vertical, of which 20 are in the upper 500 m depth. The ETOPO2 (Smith and Sandwell, 1997) topography database was used in the vertical discretization with 2 min of horizontal resolution. The surface forcings were obtained from monthly mean climatology of Comprehensive Ocean Atmosphere Data Set (COADS05) (Da Silva *et al.,* 1994) with 0.5° of horizontal resolution. Tides are an important process in mixing the river freshwater plumes with the open ocean and are obtained from the TPXO7 (Egbert and Erofeeva, 2002; Egbert *et al.,* 1994), which has altimetry data from several satellites to improve the accuracy of the results obtained through the hydrodynamic model (D'Onofrio *et al.,* 2012;Wang, 2004). All lateral boundaries are considered open. For the lateral boundary and initial conditions all variables were obtained from the monthly mean of World Ocean Atlas 2009 (WOA2009) (Antonov *et al.,* 2010; Locarnini *et al.,* 2010) with horizontal resolution of 1°. The monthly mean river discharge was obtained from Obidos and Tucurui gauge stations (Dai and

Trenberth, 2002), while the monthly climatology of sea surface temperature (SST) in the rivers discharge points was also obtained from WOA2009.

We have carried out a numerical experiment with ROMS model to characterize the hydrodynamic: salinity, temperature, and currents on the western tropical north Atlantic (WTNA) taking into account the discharges of the Amazon and Pará Rivers. These rivers release freshwater into the WTNA, giving the geographical configuration of Amazon River Delta. There are four inputs from the river to WTNA: Canal do Norte, Baia de Santa Rosa, Canal Perigoso and Canal do Jurupari and they were placed in four cells of the grid. Considering the width of each channel the contribution was calculated for each one with the same monthly temperature distribution for the four inputs nodes in the Amazon River Delta and different in the input node of the Pará River. We run ROMS model for 11 years but our analysis are restrict to the last 3 years of simulation.

The model validation of sea surface salinity (SSS), SST, potential salinity and temperature on the surface was implemented using the Simple Ocean Data Assimilation (SODA) version 2.2.4 (Carton *et al.,* 2000). This dataset presents a spatial resolution of 0.5° and was used for a period of 20 years (1991 to 2010).

THE GAS_DOCEAN MODEL

Pollutant dispersion models have been developed to the ocean, combining analytical expressions, Eulerian or Lagrangian formalism (De Dominicis *et al.,* 2013). One of the advantages of these models is their flexibility to assimilate different types of dataset, as the case with the output data of other models, such as the ROMS model (North *et al.,* 2011) or even using in situ current and thermohaline data (Leite *et al.,* 2014).

In this study the evolution of the oil/gas plumes through the water column was estimated based on the theory proposed by Chen and Yapa (2004), Fannelop and Sjoen (1980), Friedl and Fanneløp (2000), Yapa *et al.,* (2001), Zheng and Yapa (1998), Zheng and Yapa (2000) and Zheng and Yapa (2002). These studies were used for the elaboration of computational routines that represent the simultaneous transport of oil and natural gas. This model was previously used by Leite *et al.* (2014) in the evaluation of natural gas plumes that resulted from an eventual blowout in the oceanic floor. The new implementations to the GAS_DOCEAN code (version 3.0) allow the simulations of simultaneous evolution of the plumes of oil and natural gas. The adopted methodology follows the theoretical-experimental approach proposed by Chen and Yapa (2004).

Hogh pressure and temperature may induce the formation of hydrates starting from lighter hydrocarbon chains (Chen and Yapa, 2004; Zheng and Yapa, 2002). With the formation of hydrates, the upwelling time for the gas along the water column will be incremented, since their presence will induce the reduction of ascending velocity of the gas plume (Chen and Yapa, 2001; Johansen, 2003; Topham, 1984). The physical-chemical characteristics of the oil, necessary for simulations, were then calculated from each depth through parameterized equations inserted in the mathematical model, and taken from experimental curves obtained in laboratory.

In order to estimate time step (Δt), Lee and Cheung (1990) suggested Eq. 1 and was later used by Dasanayaka and Yapa (2009), Premathilake *et al.* (2016) and Yapa and Zheng (1997) obtaining good results

$$\Delta t = 0.1\frac{b_0}{|V_0|} \qquad /1/$$

where Δt is time step in s, b_o is ratio of initial control-volume in m and V_o is initial blowout velocity in ms^{-1}.

SCENARIOS FOR THE SIMULATION OF OIL AND GAS PLUMES

The points P1, P2 and P3 (Fig. 1) were selected according to the position of the oil and gas exploration blocks in the north continental shelf of Brazil and the analysis of oil sensitivity charts (SAO charts) of the areas subject to oil spill and blowouts in the region comprising the continental shelves of Amazon and Pará-Maranhão-Barreirinhas basins. P1 is located at 50°W,5.25°N and belongs to the FZA-M-88 exploration block; P2 at 44.5°W,0.5°N, corresponds to the PAMA-M-337 exploration block and P3 it is located in BAR-M-21 exploration block at 42.75°W,1°S (ANP, 2017). The parameters used in the simulations of oil/gas plumes are those reported by Chen and Yapa (2004) with the exception of those shown in the Tab. 1.

Table 1. Parameterization of GAS_DOCEAN.

Parameters	Value
Ratio between the bubble core width and the buoyant jet diameter	0.8
Gas density	5×10^{-3} kg m^{-3}
Initial shear entrainment coefficient	0.083
Gas flow	50 kg s^{-1}
Oil flow	100 kg s^{-1}
Mass transfer coefficient of dissolution	10^{-9} m s^{-1}

OCEAN CIRCULATION AND THERMOHALINE STRUCTURE

The main variables influencing the behavior of oil spills and blowouts are temperature, salinity and marine currents. The vertical profiles of the speed of the current are corroborated using the SODA dataset, with spatial resolution of 0.25°. Also the average values of the zonal component are compared in region Western North Equatorial Countercurrent (WNECC) framed at (50°−40°W/5°−8°N), whose average values were reported by Richardson and Reverdin (1987).

Fig. 2 depicts that the numerical mean seasonal currents are able to reproduce the advection patterns already reported by many authors (Fratantoni, 2001; Grodsky and Carton, 2002; Haidvogel *et al.,* 2000; Malanotte-Rizzoli *et al.,* 2000), The fundamental actor in the area ins the NBC, which forms large anticyclonic rings shed by the current of the northwestern whirl along the Norte Brazilian continental shelf.

The Amazon plume is transported along the Brazilian continental shelf by the NBC to the northwest during December-January-February (DJF) (Fig. 2), increasing its transportation in the months March-April-May (MAM) and reaching its maximum during June-July-August (JJA) (Muller-Krager *et al.,* 1988; Salisbury *et al.,* 2011). When NBC retroflexion occurs, it is transported eastward by the NECC during the period of September-October-November (SON) (Coles *et al.,* 2013; Foltz *et al.,* 2015; Moon and Song, 2014; Muller-Krager *et al.,* 1988).

The NECC is the main current that transports the Amazon plume eastward. Varona et al. (unpublished data) compared the zonal component (u) differences between ROMS model results and Surface Currents from Diagnostic model (Maximenko and Hafner, 2010) in an area associated to the east of the NECC, located at 48°−41°W/2°−8°N (EPLUME). Concluding that values of u indicate a gradually increasing from 0.2 ms^{-1} to 0.3 ms^{-1}, from JJA to SON, between 4.5° and 9.5°N, finding the maximum bias (0.2 ms^{-1}) between 5.5° and 6.5°N in July and between 4° and 5°N in October. The mean bias is 0.1 ms^{-1}. These results reveal that ROMS model represents quite well the dynamics of the NECC variability. The average of the zonal component in WNECC is 0.384 ms^{-1} during SON, according to reported by Richardson and Reverdin (1987), being 0.410 ms^{-1}.

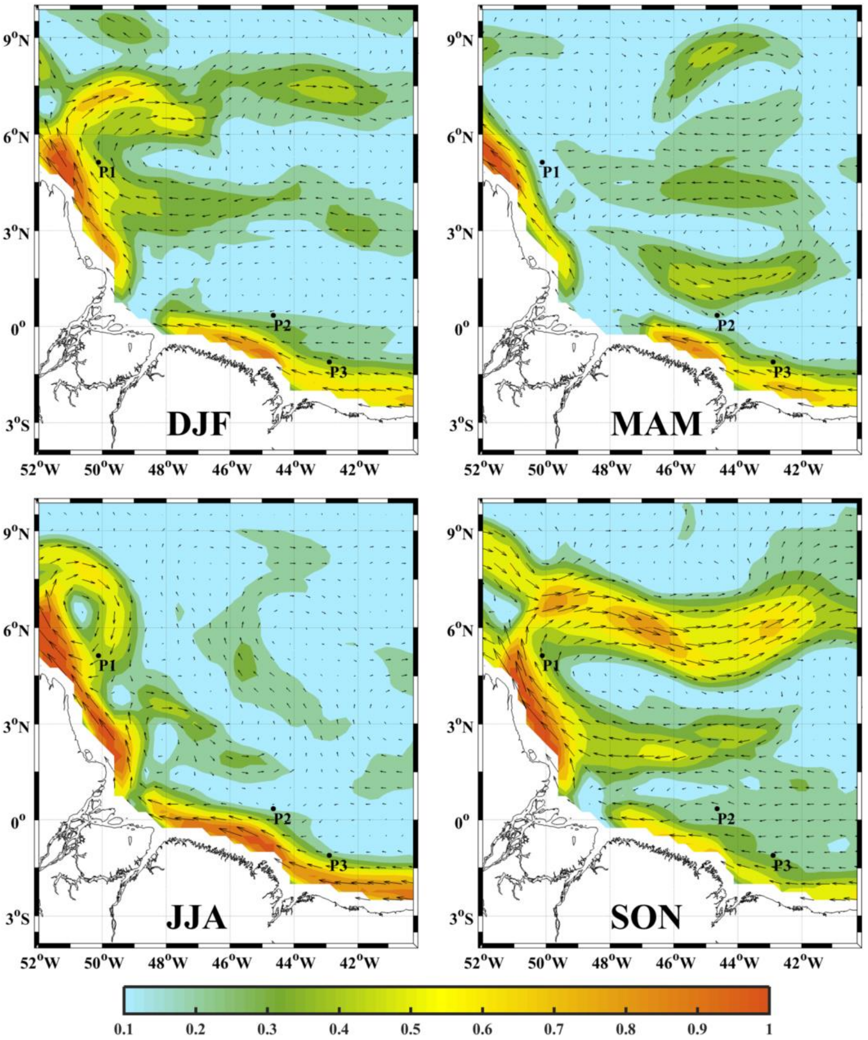

Figure 2. ROMS model outputs of the seasonal marine currents during the boreal winter (DJF-December, January, February), spring (MAM-March, April, May), summer (JJA-June, July, August), and fall (SON-September, October, November). The magenta polygon represents the Amazon River plume.

Fig. 3 shows the comparison of SST between the ROMS model and SODA dataset. SST presents higher temperatures than the SODA dataset in the area of the NBC retroflection, mainly during SON to DJF and in the NECC area. The cause of this large seasonal variation is probably a dynamic adjustment due to changes in the wind forcing over the tropical Atlantic and both local and remote wind stress that may play an important role in the SST variability (Bourles *et al.,* 1999; Johns *et al.,* 1998; Sharma *et al.,* 2009). Tab. 2 summarizes the main results of simulated SST and SODA dataset, evidencing greater difference in DJF (1.27°C), when the plume feeds the NECC. The ROMS model is well balanced in JJA.

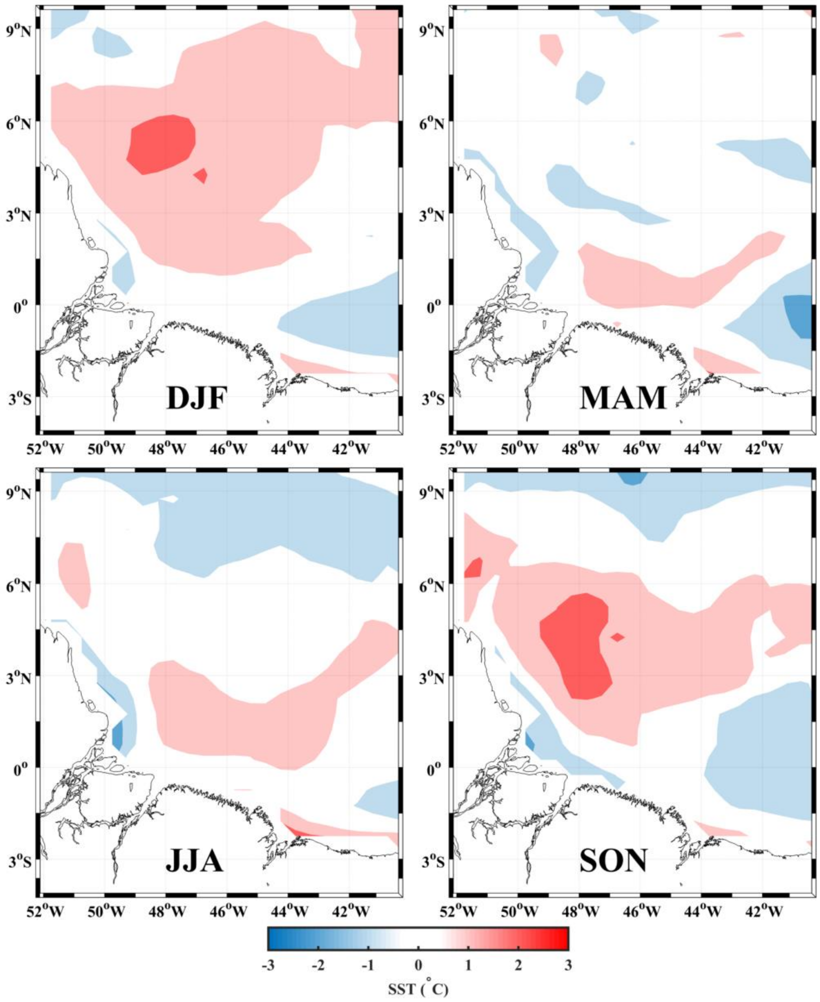

Figure 3. Mean seasonal cycle of the difference between the SST (◦C) of the ROMS model and the SODA dataset During the boreal winter (DJF-December, January, February), spring (MAM-March, April, May), summer (JJA-June, July, August), and fall (SON-September, October, November).

Table 2. Seasonal comparison of salinity and temperature at surface between the ROMS model and SODA dataset in EPLUME area. Mean value ± standard deviation.

	SSS		**SST**	
	SODA (psu)	**ROMS (psu)**	**SODA (°C)**	**ROMS (°C)**
DJF	35.97 ± 0.02	35.89 ± 0.06	27.43 ± 0.05	28.35 ± 0.15
MAM	35.85 ± 0.09	36.02 ± 0.03	27.41 ± 0.07	27.72 ± 0.14
JJA	35.32 ± 0.09	35.66 ± 0.11	27.95 ± 0.02	28.43 ± 0.09
SON	35.54 ± 0.06	35.41 ± 0.10	28.01 ± 0.03	28.99 ± 0.09

The difference of sea surface salinities between the ROMS model and SODA dataset is shown in Fig. 4. Mean simulated SSS presents lower salinities than SODA dataset in the area of the NBC retroflection mainly during MAM. In the months of SON, lower values of SSS follow the NECC.

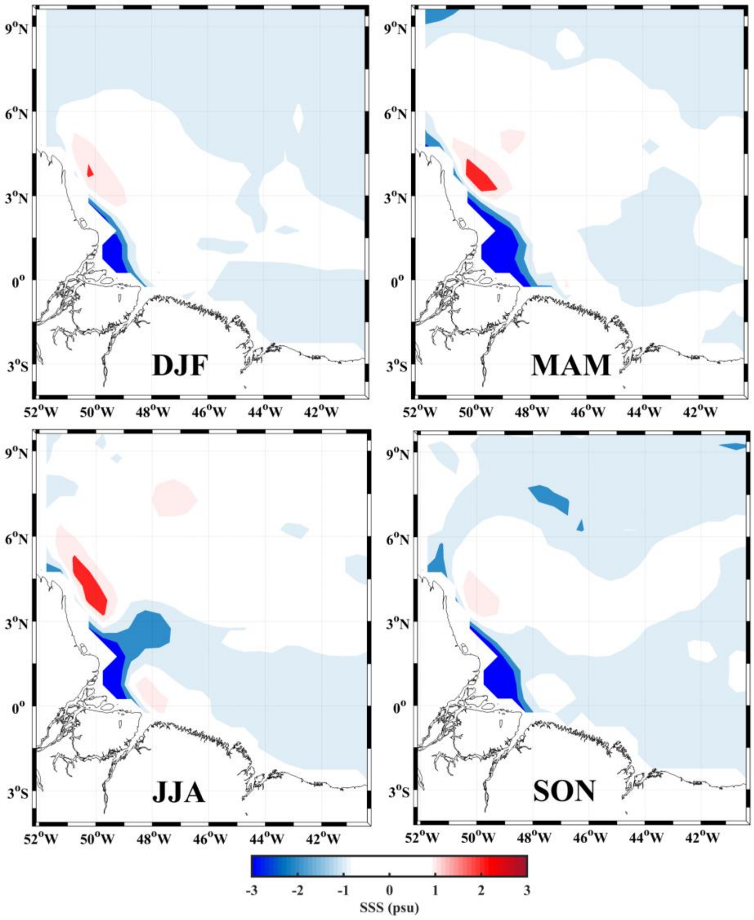

Figure 4. Mean seasonal cycle of the difference between the SSS (psu) of the ROMS model and the SODA dataset During the boreal winter (DJF-December, January, February), spring (MAM-March, April, May), summer (JJA-June, July, August), and fall (SON-September, October, November).

Tab. 2 above also shows a summary of the mean seasonal salinity cycles for the EPLUME area. The maximum difference observed was in JJA (0.34 psu) and the minimum difference was in DJF (0.08 psu). The ROMS model overestimate the SST, the with DJF period being the worst-agreement and the MAM, the best one.

Fig. 5(a) shows the vertical profiles of the temperature at point P1 of the SODA dataset and the ROMS model in the DJF and JJA periods. The vertical profiles of the temperature are better adjusted below 300 m depth in both periods. In depths above 300 m the ROMS model overestimates the temperature and the main differences range between 0.7 to 1.7°C. In JJA period there is a maximum difference of 0.04 ms^{-1} below 300 m and above this depth, the average difference was 0.17 ms^{-1} with a maximum difference of 0.21 ms^{-1} from 150 to 180 m depth (Fig. 5(b)). The profile of the current speed is well adjusted below the 300 m depth in the DJF period. The maximum difference in the DJF period was 0.18 ms^{-1} on the surface.

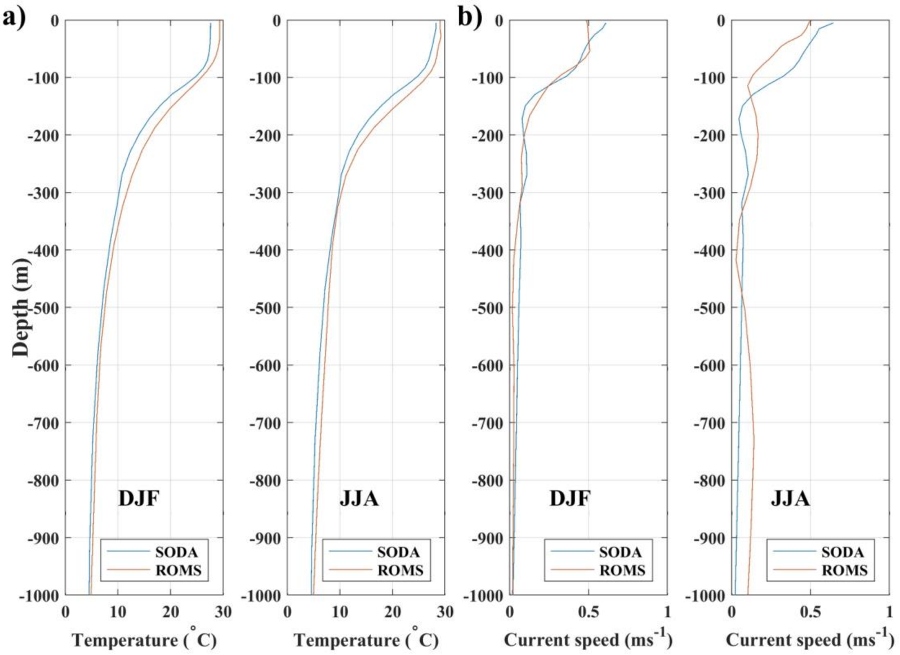

Figure 5. (a) Temperature and (b) current speed vertical profiles in DJF (December-January-February) and JJA (June-July-August) periods for SODA and ROMS at point P1.

In the north coast of Brazil, the continental shelf extends from 2 to 3° from the coast, followed by the continental slope with an approximate width of 1° varying the depths from 500 to 1900 m depth. The numerical simulation of oil/gas blowouts were located at 3 points of this continental slope.

Fig. 6(a) shows the mean seasonal velocity of the marine current, averaged between the surface and 100 m depth. The most intense currents form a band approximately wide and confined to the coastline, corresponds to the NBC. This current is more intense in the winter especially over the northwest part of the coast where it turns toward the east (in correspondence with the NBC retroflection), reaching speeds higher than 0.9 ms^{-1}. In the spring, we found the less intense currents of the whole year with maximum values eastward of the Amazon River mouth, reaching up to 0.7 ms^{-1}. In the summer, the currents in the NBC intensify vary from 0.5 ms^{-1} to speeds higher than 0.9 ms^{-1}. In the autumn, as in the winter, the turn of the current to the east appears, better defining the NBC retroflection. Higher speeds are found along the coast more to the northwest and in the NBC retroflection, oscillating the current speed from 0.5 ms^{-1} to speeds higher than 0.9 ms^{-1}.

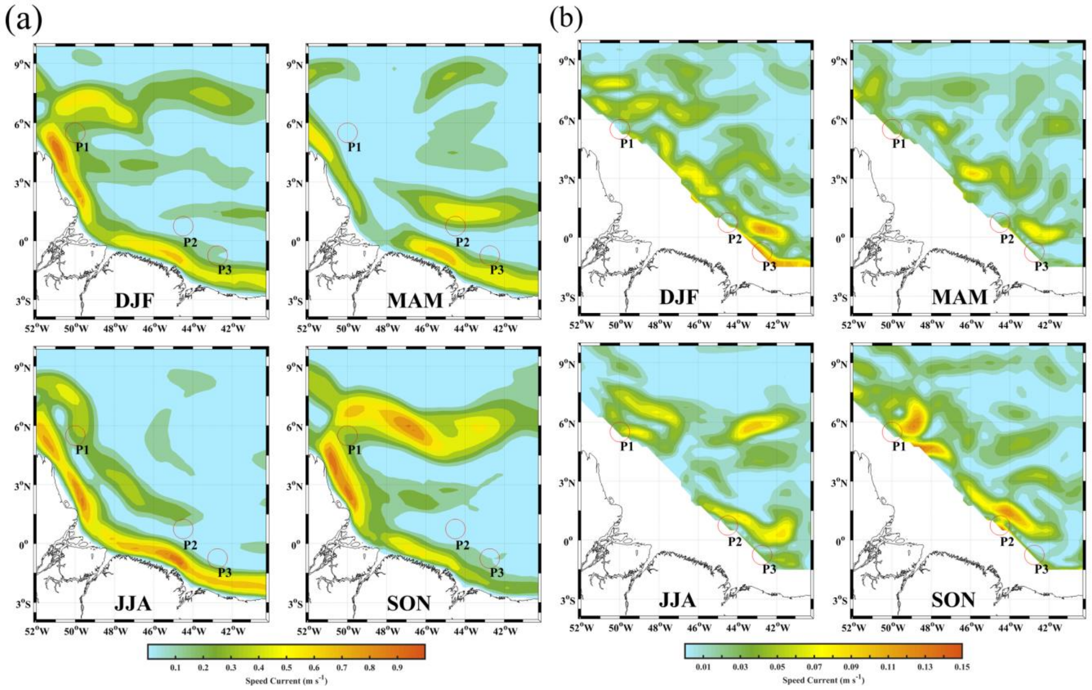

Figure 6. ROMS output of mean seasonal cycle of the currents measured (a) between the surface and 100 m depth (b) between 1000 and 1200 m depth during the winter (DJF-December, January, February), spring (MAM-March, April, May), summer (JJA-June, July, August), and fall (SON-September, October, November). The centers of the red circle represent the positions of the simulation points P1, P2 and P3.

The center of the red circles represents the positions of the P1, P2 and P3 simulation points. In winter the average speed is 0.25 ms^{-1}, at P1, extremely low (0.01 ms^{-1}) at P2 and it reaches 0.15 ms^{-1} at P3. In the spring, we find the lowest speeds of the year at P1, P2 and P3, oscillating between 0.01 and 0.25 ms^{-1}. In the summer and in the autumn at P2 and P3, current speeds reach the minimum value (0.01–0.15 ms^{-1}), increasing at P1 with respect to spring.

Fig. 6(b) shows the mean seasonal behavior of marine currents between 1000 and 1200 m depth. In general, at these depths the currents are very low, oscillating their speed between 0.01 and 0.15 ms^{-1}. These currents are slightly less intense in the spring and a little more intense in the fall, mainly above 4°N and between 47 and 50°W; and between 0.5-2°N and 42-45°W, reaching 0.15 ms^{-1}, moving this last pattern towards the southeast in the winter.

In the winter we find speeds of 0.15 ms-1 at P3 and between 0.01−0.03 ms^{-1} at P1 and P2. The least intense currents are in the spring at all 3 points (0.03 − 0.04 ms^{-1}). Similar speeds are found at P2 and P3 in the summer, increasing slightly at P1 to 0.06 ms^{-1}. In the autumn, speeds at P3 do not differ from the summer, being somewhat lower at P1 and reaching up to 0.15 ms^{-1} at P2.

OIL AND GAS PLUMES EVOLUTION

Fig. 7 shows the monthly evolution of oil/gas plumes at P1. During the entire evaluated period, the plumes were type 3, with exception to September, where they reached the maximum diameter below 1000 m depth. Above this level, the diameter of the plumes began to decrease gradually until reaches the surface, oscillating between 54−76.5 m. The plumes reached the largest diameter in August, November and December and the lowest diameter was observed between May-July (Tab. 3).

Table 3. Monthly diameter and displacement of oil/gas plumes at points P1, P2 and P3.

	P1			P2			P3		
	Mean diameter (m)	Displacement (m)	Evolution Time (hours)	Mean Diameter (m)	Displacement (m)	Evolution Time (hours)	Mean Diameter (m)	Displacement (m)	Evolution Time (hours)
Jan	56.4	(0.71, -0.70)	8.04	75.5	(-0.30, 0.20)	7.26	58.9	(0.37, -0.32)	6.30
Feb	65.3	(0.50, -0.45)	7.97	60.1	(-0.35, 0.26)	7.25	58.7	(-0.13, 0.22)	6.30
Mar	62.1	(0.71, -0.71)	8.06	54.1	(-0.33, 0.24)	7.25	58.7	(-0.09, 0.23)	6.30
Apr	63.3	(0.36, -0.36)	7.96	58.4	(0.14, -0.15)	7.26	58.7	(-0.19, 0.26)	6.30
May	54.5	(0.69, -073)	8.05	60.7	(-0.10, 0.15)	7.25	58.8	(0.20, -0.18)	6.30
Jun	54.0	(0.30, -0.28)	7.95	55.3	(-0.52, 0.34)	7.26	58.8	(0.18, 0.24)	6.30
Jul.	54.3	(0.38, 0.41)	7.96	73.1	(-0.54, 0.32)	7.27	58.8	(0.10, -0.03)	6.30
Aug	74.1	(-0.24, 0.22)	7.96	61.0	(-0.56, 0.30)	7.26	58.8	(-0.44, 0.64)	6.33
Sep	60.3	(-0.02, -0.01)	7.96	56.5	(-0.47, 0.25)	7.26	58.7	(-0.28, 0.36)	6.30
Oct	61.4	(0.35, -0.33)	7.97	79.5	(-0.44, 0.26)	7.25	58.7	(-0.39, 0.47)	6.31
Nov	70.6	(0.36, -0.24)	7.97	54.5	(-0.42, 0.19)	7.25	58.7	(-0.19, 0.32)	6.30
Dec	76.5	(0.54, -0.69)	8.02	79.7	(-0.26, 0.16)	7.26	58.7	(-0.37, 0.55)	6.32

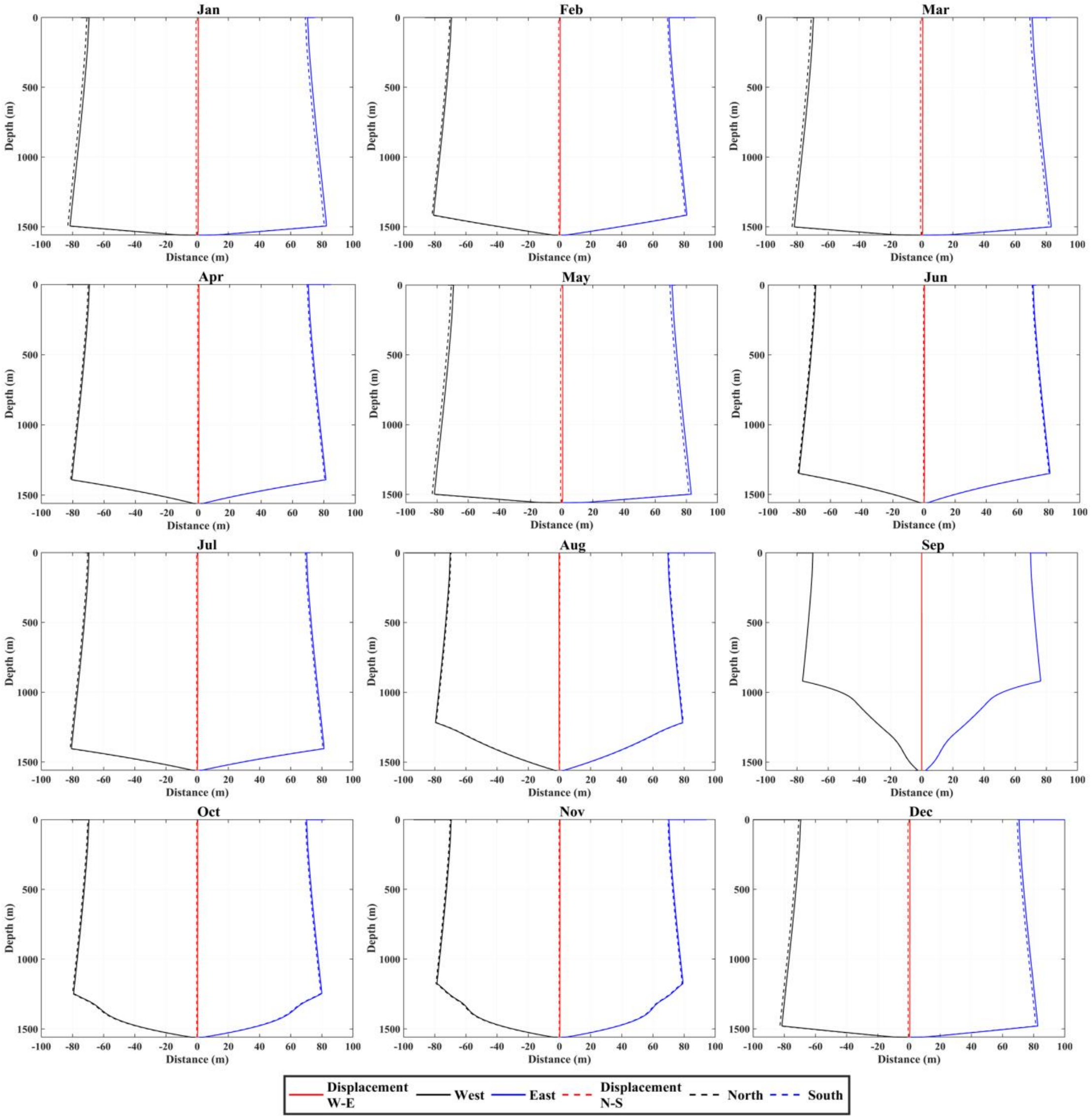

Figure 7. Monthly oil/gas plume evolution at P1. The solid lines represent the west (-) and east (+) directions. The dashed lines represent the north (-) and south (+) directions. The red color is the displacement of the plumes from the bottom. The black color represents the radius to the west and north. The blue color represents the radius to the east and south.

The largest displacements of the plume from the blowout point were approximately 1 m in January and May. The mean arrival time of the oil/gas plumes to the surface was 7.99 hours and difference between the months was minimal.

Fig. 8 shows the monthly evolution of the oil/gas plumes at P2. As already verified in P1, all the plumes are were of type 3. All the plumes reach their maximum diameter below 1000 m, decreasing their diameter until they reach the surface (54.1-79.7 m). The largest diameters in the surface corresponded to the months of January, October and December. The largest displacements of P2 plume occurred from June to August and were approximately 0.64 m (Tab. 3). The average time of arrival at the surface was 7.26 hours.

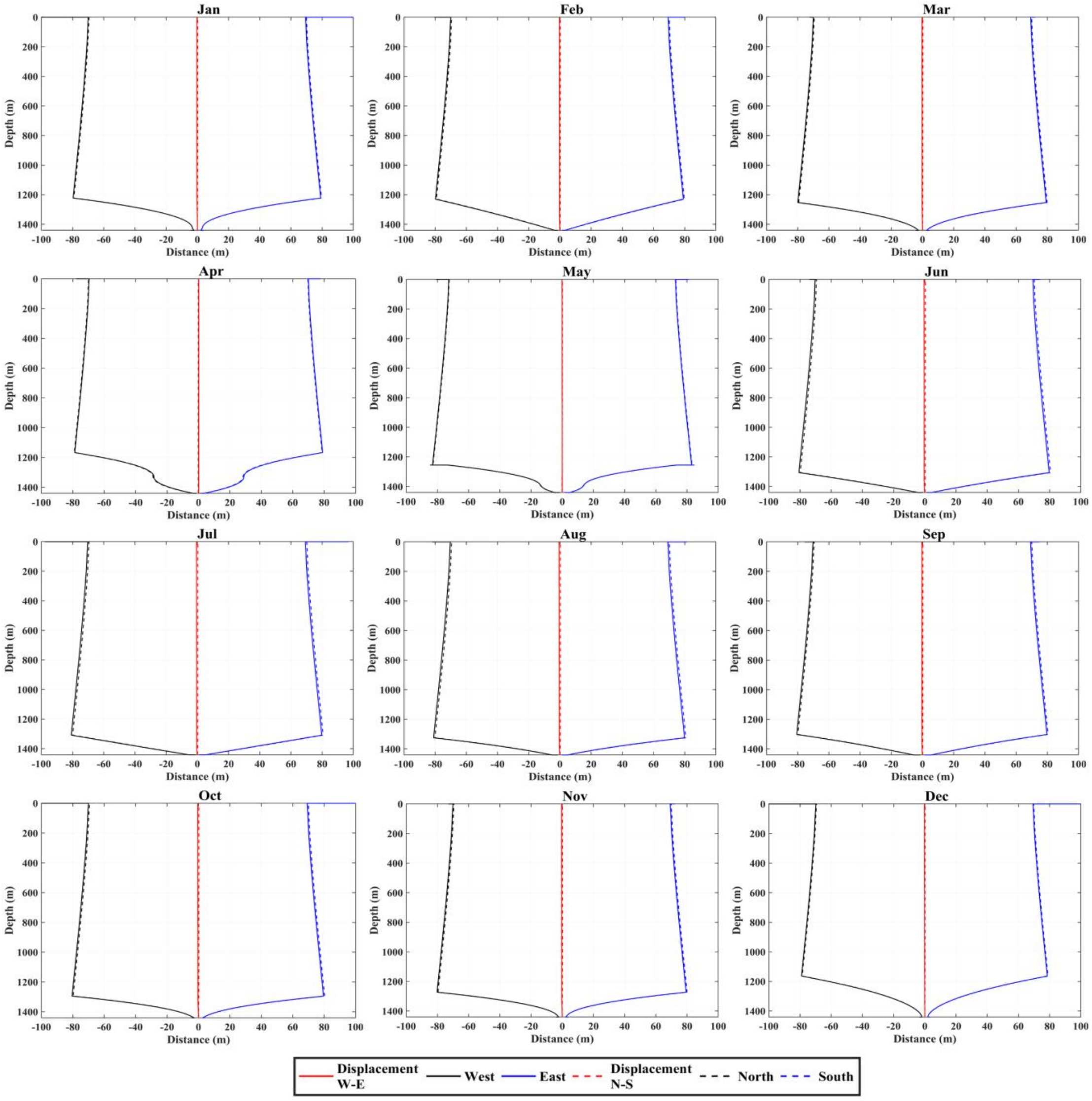

Figure 8. Monthly oil/gas plume evolution at P2. The solid lines represent the west (-) and east (+) directions. The dashed lines represent the north (-) and south (+) directions. The red color is the displacement of the plumes from the bottom. The black color represents the radius to the west and north. The blue color represents the radius to the east and south.

The pattern of oil/gas plume evolution already observed at the points P1 and P2 (type 3) was also verified at P3 (Fig. 9). The plumes at P3 reaching its largest diameter below 1000 m depth except for the months of May and July, where the diameter at the surface was almost invariant during all months (58.7−58.9 m). As shown in Tab. 3, the displacement of the plumes from its point of origin occurred in August and was 0.78 m. The plumes evolution time was practically the same, oscillating between 6.30 and 6.33 hours.

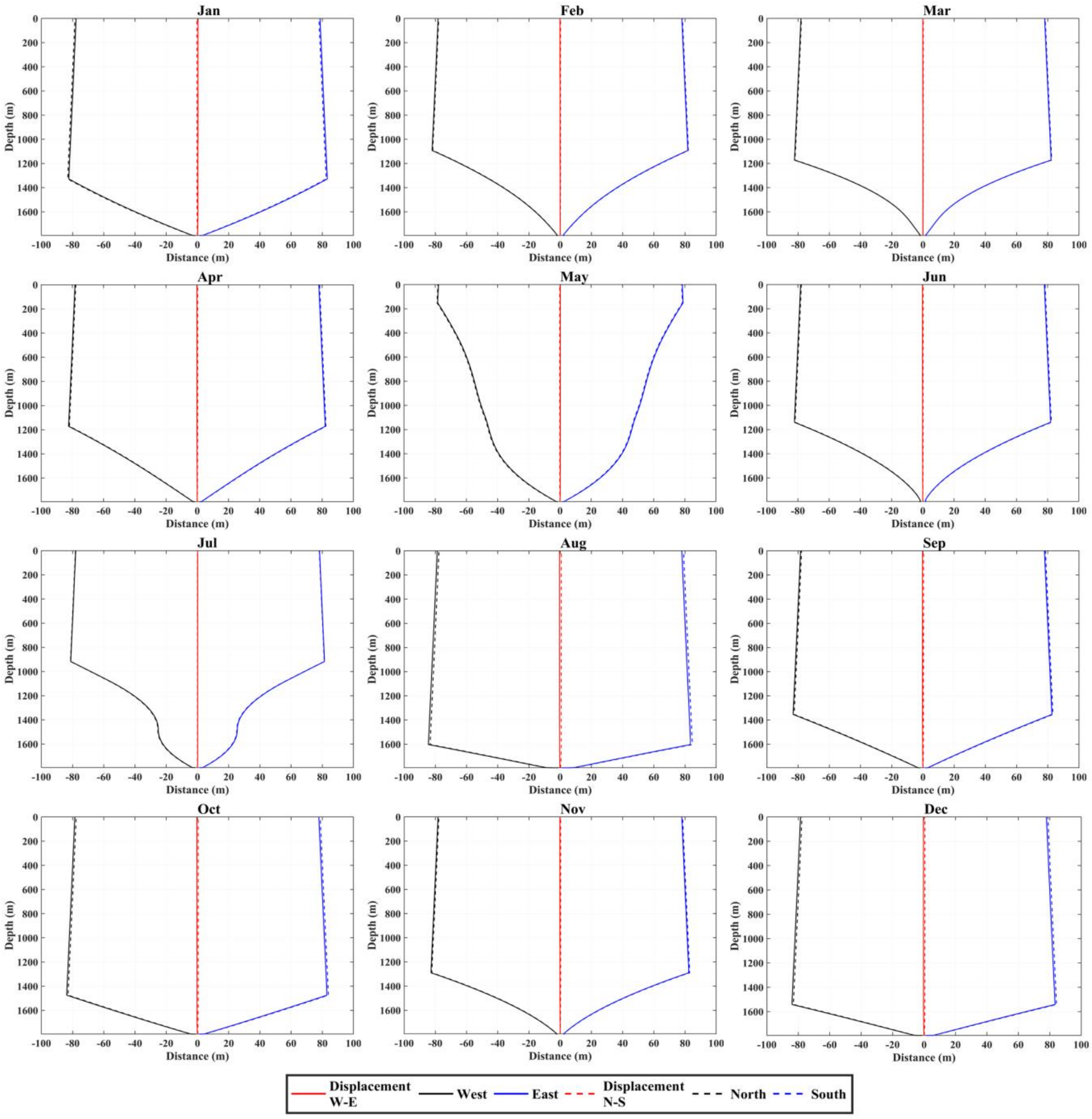

Figure 9. Monthly oil/gas plume evolution at P3. The solid lines represent the west (-) and east (+) directions. The dashed lines represent the north (-) and south (+) directions. The red color is the displacement of the plumes from the bottom. The black color represents the radius to the west and north. The blue color represents the radius to the east and south.

Fig. 10(a) shows the vertical profiles of the current velocity for March at point P1 and for November at point P3. In both profiles, the plume simulations show that the maximum diameters of these were reached below 1000 m depth (Fig. 7 and Fig. 9). The bottom speed of points P1 and P3 is greater than 0.1 ms-1 and less than 0.2 ms-1, thus maintaining the entire water column up to 200 m depth. This behavior is very similar to the rest of the profiles at all points, with the exception of September, at point P1, and of May and July, at point P3.

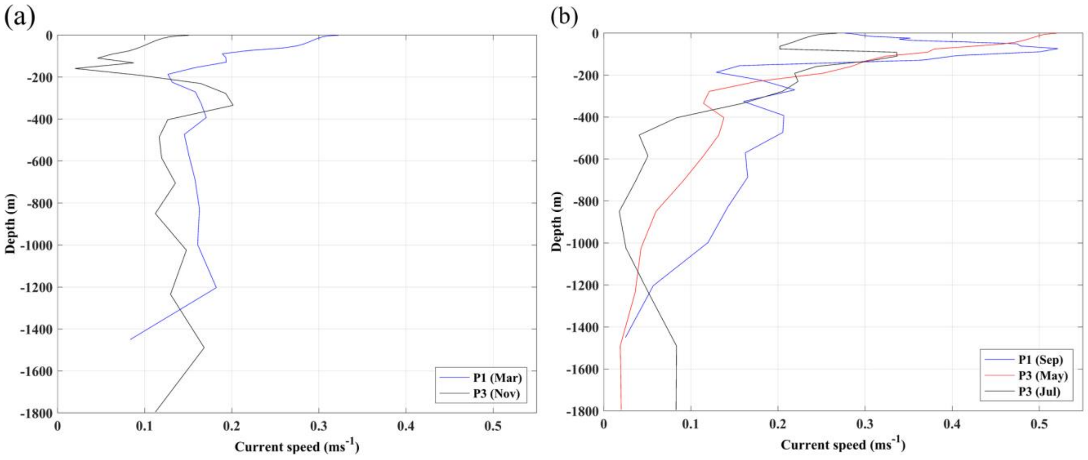

Figure 10. Vertical profiles of the current speed (a) at P1 (March) and P3 (November) and (b) at P1 (September) and P3 (May and July).

In September, at P1 (Fig. 10(b)), the current speed at the bottom was almost zero (approximately 0.02 ms-1). From the bottom, the velocity grew very slowly as the depth decreased to 1000 m (0.12 ms-1). The speed began to increase a little faster from 1000m depth to the surface, which means that the maximum diameter was reached between 900 and 1000 m depth. In May at P3 (Fig. 10(b)) the behavior of the plume in the bottom was also almost zero, but the increase in speed began near the 1500 m depth, which was much slower than in the previous case. Up to almost 200 m depth the speed did not exceed 0.2 ms-1 and, above that, where the plume reached its maximum diameter, it began to grow sharply until exceeding 0.5 ms-1 on the surface. At this same point, in July (Fig. 10(b)), the current speed was less than 0.1 ms-1 and maintained that value up to 1500 m depth. It began to decrease to approximately 850 m depth and then, it increased from above this depth, reaching its maximum diameter.

Using the coefficient 0.2 in the Eq. 1 did not get good results because the bottom current speed at the three points was very small, |V_0 |→0, which this implied that Δt→∞. Thus it was necessary to adjust the coefficient to estimate Δt. The Eq. 2 below was then considered.

$$\Delta t = \begin{cases} 0.025\dfrac{b_0}{|V_0|} & \text{for P1 and P2} \\ 0.0375\dfrac{b_0}{|V_0|} & \text{for P3} \end{cases} \qquad /2/$$

CONCLUSION

This study characterizes the behavior of the plumes produced by the oil/gas blowouts in deep waters located at the continental slope in the northwest coast of Brazil, combining the ROMS and the GAS_DOCEAN models. The salinity and temperature of the hydrodynamic model were well adjusted to the SODA dataset, both on the surface and in the vertical profiles. All oil/gas plumes were type 3 and the oceanographic characteristics in the 3 points of the numerical simulations similar.

At P1, the mean diameter at the surface varied between 54−76.5 m and, at the bottom, the plume displacement from its origin was approximately 1 m. The average time it took to reach the surface was 7.99 hours; however, it was slower than in p2 (7.26 hours). The largest distance of displacement from P2 point of origin was 0.64 m and its average diameter on the surface ranged 54.1−79.7 m.

At P3, the displacement of the plume from its origin was 0.78 m. The mean diameter on the surface at this point varied between 58.7 and 58.9 m. The plume evolution time to the surface remained almost invariant (6.30−6.33 hours). The small plume displacement from its origin is was due to the low speeds in the vertical profile.

To obtain good results in the numerical simulations of the plumes, it was necessary to adjust the coefficient for Δt computation. The equation suggested by Lee and Cheung (1990) was modified to $\Delta t = 0.025\, b_0/|V_0|$ for P1 and P2; and $\Delta t = 0.0375\, b_0/|V_0|$ for P3.

ACKNOWLEDGEMENTS

The first author thanks to Human Resources Program (PRH-47) of the Agência Nacional do Petróleo (ANP) for the concession of PhD scholarships. This work is also part of the Project Pólo de Interação para o Desenvolvimento de Estudos conjuntos em Oceanografia do Atlântico Tropical (PILOTE) and is a contribution of the Project Simulating the Amazon River Plume and its Impacts using Climate Models (CAPES-TAMU, Grant 99999.003440/2015-00).

REFERENCES

Abimbola, M., Khan, F. and Khakzad, N. (2014), Dynamic safety risk analysis of offshore drilling, *Journal of Loss Prevention in the Process Industries*, Vol. 30, pp. 74–85.

de Andrade, M.M.N., Szlafsztein, C.F., Souza-Filho, P.W.M., dos Reis A.A. and Gomes, M.K.T. (2010), *Journal of Environmental Management*, Vol. 91, n. 10, pp. 1972–1980

Agência Nacional do Petróleo, Gás Natural e Biocombustíveis (ANP) (2017), *Dados Georreferenciados dos Blocos em Exploração e Campos de Produção* (Georeferenced Data of Blocks in Exploration and Production Fields), em: http://www.brasil-rounds.gov.br/portugues/mapas_de_concessoes.asp. (accessed in January 12, 2018). Only in Portuguese.

Antonov, J., Seidov, D., Boyer, T., Locarnini, R., Mishonov, A., Garcia, H., Baranova, O., Zweng, M. and Johnson, D. (2010), Salinity, in Levitus, S. (Ed.), *World Ocean Atlas 2009*, US Gov. Print. Off., Washington, DC, vol. 2.

Arnault, S., Bourles, B., Gouriou, Y. and Chuchla, R. (1999), Intercomparison of upper layer circulation of the western equatorial Atlantic Ocean: In situ and satellite data, *Journal of Geophysical Research*, Vol. 104, pp. 21171–21194.

Bourles, B., Gouriou, Y. and Chuchla, R. (1999), On the circulation in the upper layer of the western Equatorial Atlantic, *Journal of Geophysical Research*, Vol. 104, pp. 21151–21170.

Carton, J.A., Chepurin, G. and Cao, X. (2000), A Simple Ocean Data Assimilation Analysis of the Global Upper Ocean 1950–95. Part I: Methodology, *Journal of Physical Oceanography*, Vol. 30, pp. 294-309.

Carvalho, M. and Gherardi, D.F.M. (2003), Uso de transformação IHS e classificação não supervisionada por regiões para o mapeamento da sensibilidade ambiental ao derramamento de óleo, in XI Simpósio Brasileiro de Sensoriamento Remoto, Belo Horizonte (MG). *Anais...* Belo Horizonte, pp. 1515–1523.

Charrouf, Z. and Guillaume, D. (2008), Argan oil: Occurrence, composition and impact on human health, *European Journal of Lipid Science and Technology,* Vol. 110, n. 7, pp. 632-636.

Chen, F. and Yapa, P.D. (2001), Estimating hydrate formation and decomposition of gases released in a deep-water ocean plume, *Journal of Marine Systems*, Vol. 30, pp. 21–32.

Chen, F. and Yapa, P.D., (2004), Modeling gas separation from a bent deep-water oil and gas jet/plum, *Journal of Marine Systems*, Vol. 45, pp. 189–203.

Coles, V.J., Brooks, M.T., Hopkins, J., Stukel, M.R., Yager, P.L. and Hood, R.R. (2013), The pathways and properties of the Amazon river plume in the tropical North Atlantic Ocean, *Journal of Geophysical Research: Oceans,* Vol. 118, pp. 6894–6913.

Da Silva, A., Young, A.C. and Levitus, S. (1994), Atlas of surface marine data 1994, volume 1: Algorithms and procedures, Technical Report 6.

Dai, A. and Trenberth, K.E., (2002), Estimates of Freshwater Discharge from Continents: Latitudinal and Seasonal Variations, *Journal of Hydrometeorology*, Vol. 3, pp. 660–687.

Dasanayaka, L.K. and Yapa, P.D. (2009), Role of plume dynamics phase in a deep-water oil and gas release model, *Journal of Hydro-environment Research*, Vol. 2, pp. 243–253.

De Dominicis, M., Pinardi, N., Zodiatis, G. and Lardner, R., (2013), MEDSLIK-II, a Lagrangian marine surface oil spill model for short-term forecasting–Part 1: Theory, *Geoscientific Model Development*, Vol. 6, pp. 1851–1869.

Dessier, A. and Donguy, J.R. (1994), The sea surface salinity in the tropical Atlantic between 10 S and 30 N-seasonal and interannual variations (1977-1989), *Deep Sea Research Part I: Oceanographic Research Papers*, Vol. 41, pp. 81–100.

D'Onofrio, E., Oreiro, F. and Fiore, M. (2012), Simplified empirical astronomical tide model—An application for the Río de la Plata estuary, *Computers & Geosciences*, Vol. 44, pp. 196–202.

Egbert, G.D., Bennett, A.F. and Foreman, M.G.G. (1994), TOPEX/POSEIDON tides estimated using a global inverse model, *Journal of Geophysical Research: Oceans*, Vol. 99, pp. 24821–24852.

Egbert, G.D. and Erofeeva, S.Y., (2002), Efficient inverse modeling of barotropic ocean tides, *Journal of Oceanic and Atmospheric Technology*, Vol. 19, pp. 183–204.

E&P Forum/UNEP - United Nations Environment Programme (1997), *Environment management in oil and gas exploration and production*: An overview of issues and management approach, Technical Report 37.

Fannelop, T. and Sjoen, K. (1980), *Hydrodynamics of underwater blowouts*, in: 18th Aerospace Sciences Meeting, 219p.

Foltz, G.R., Schmid, C. and Lumpkin, R. (2015), Transport of Surface Freshwater from the Equatorial to the Subtropical North Atlantic Ocean, *Journal of Physical Oceanography*, Vol. 45, pp. 1086–1102.

Fratantoni, D. (2001), North Atlantic surface circulation during the 1990's North Atlantic surface circulation during observed with satellite-tracked drifters, *Journal of Geophysical Research: Oceans,* Vol. 106, pp. 22067–22093.

Fratantoni, D.M., Johns, W.E. and Townsend, T.L. (1995), Rings of the North Brazil Current: Their structure and behavior inferred from observations and a numerical simulation, *Journal of Geophysical Research*, Vol. 100, pp. 10633–10654.

Friedl, M.J. and Fanneløp, T. (2000), Bubble plumes and their interaction with the water surface, *Applied Ocean Research*, Vol. 22, pp. 119–128.

Garza-Gil, M.D., Prada-Blanco, A. and Vázquez-Rodríguez, M.X. (2006), Estimating the short-term economic damages from the Prestige oil spill in the Galician fisheries and tourism, *Ecological Economics*, Vol. 59, n. 4, pp. 842–849.

Goes, M., Molinari, R., da Silveira, I. and Wainer, I. (2005), Retroflections of the north Brazil current during February 2002, *Deep Sea Research Part I: Oceanographic Research Papers*, Vol. 52, pp. 647–667.

Grodsky, S.A. and Carton, J.A. (2002), Surface drifter pathways originating in the equatorial Atlantic cold tongue, *Geophysical Research Letters*, Vol. 29, n. 23, pp. 62(1)- 62(4).

Gundlach, E.R. and Hayes, M.O. (1978), Vulnerability of coastal environments to oil spill impacts, *Marine Technology Society Journal*, Vol. 12, pp. 18–27.

Haidvogel, D., Arango, H., Hedstrom, K., Beckmann, A., Malanotte-Rizzoli, P. and Shchepetkin, A. (2000), Model evaluation experiments in the North Atlantic basin: Simulations in nonlinear terrain-following coordinates, *Dynamics of Atmospheres and Oceans*, Vol. 32, pp. 239–282.

International Energy Agency (IEA) (2009), *World Energy Outlook*, Paris, 698p.

International Energy Agency (IEA) (2011), *World Energy Outlook*, Paris, 666p.

International Tanker Owners Pollution Federation (ITOPF) (2016), Oil Tanker Spill Statistics, em: http://www.itopf.com/knowledge-resources/data-statistics/statistics/ (accessed in July 7, 2017).

Johansen, Ø. (2000), DeepBlow–a Lagrangian plume model for deep water blowouts, *Spill Science & Technology Bulletin*, Vol. 6, pp. 103–111.

Johansen, Ø. (2003), Development and verification of deep-water blowout models, *Marine Pollution Bulletin*, Vol. 47, pp. 360–368.

Johns, W., Lee, T., Schott, F., Zantopp, R. and Evans, R. (1990), The North Brazil Current Retroflection: Seasonal Structure and Eddy Variability, *Journal of Geophysical Research*, Vol. 95, pp. 22103–22120.

Johns, W.E., Lee, T.N., Beardsley, R.C., Candela, J., Limeburner, R. and Castro, B. (1998), Annual cycle and variability of the North Brazil Current, *Journal of Physical Oceanography*, Vol. 28, pp. 103–128.

Lara, I. (2014), Geopolítica y governance de los hidrocarburos, *Relaciones Internacionales*, Vol. 23, n. 46, pp 149-175.

Lee, J.H. and Cheung, V. (1990), Generalized Lagrangian model for buoyant jets in current, *Journal of Environmental Engineering,* Vol. 116, pp. 1085–1106.

Leite, F.S., Silva, M.A., Araujo, M., Silva, R.A. and Droguett, E.L. (2014), Modeling Subsurface Gas Release in Tropical and Shallow Waters: Comparison with Field Experiments off Brazil's Northeast Coast, *Human and Ecological Risk Assessment: An International Journal*, Vol. 20, 150–173.

Lentz, S.J. (1995), The Amazon River Plume during AMASSEDS: Subtidal current variability and the importance of wind forcing, *Journal of Geophysical Research: Oceans*, Vol. 100, pp. 2377-2390.

Locarnini, R., Mishonov, A., Antonov, J., Boyer, T., Garcia, H., Baranova, O., Zweng, M. and Johnson, D. (2010), Temperature, in Levitus, S. (Ed.), *World Ocean Atlas 2009*, US Gov. Print. Off., Washington, DC, vol. 1, 184 p.

Malanotte-Rizzoli, P., Hedstrom, K., Arango, H. and Haidvogel, D.B. (2000), Water mass pathways between the subtropical and tropical ocean in a climatological simulation of North Atlantic, *Dynamics of Atmospheres and Oceans*, Vol. 32, pp. 331–371.

Maximenko, N. and Hafner, J. (2010), *SCUD: Surface Currents form Diagnostic model*, Technical Report 5.

Mendelssohn, I.A., Andersen, G.L., Baltz, D.M., Caffey, R.H., Carman, K.R., Fleeger, J.W., Joye, S.B., Lin, Q., Maltby, E. and Overton, E.B. (2012), Oil impacts on coastal wetlands: implications for the Mississippi River Delta ecosystem after the Deepwater Horizon oil spill, *BioScience*, Vol. 62, n. 6, pp. 562-574.

Michel, J., Hayes, M.O. and Brown, P.J. (1978), Application of an oil spill vulnerability index to the shoreline of lower Cook Inlet, Alaska, *Environmental Geology*, Vol. 2, pp. 107–117.

Moon, J.H. and Song, Y.T. (2014), Seasonal salinity stratifications in the near-surface layer from Aquarius, Argo, and an ocean model: Focusing on the tropical Atlantic/Indian Oceans, *Journal of Geophysical Research: Oceans*, Vol. 119, pp. 6066–6077.

Moura, R.L., Amado-Filho, G.M., Moraes, F.C., Brasileiro, P.S., Salomon, P.S., Mahiques, M.M., Bastos, A.C., Almeida, M.G., Silva, J.M., Araujo, B.F., Brito, F.P., Rangel, T.P., Oliveira, B.C.V., Bahia, R.G., Paranhos, R.P., Dias, R.J.S., Siegle, E., Figueiredo Jr, A.G., Pereira, R.C., Leal, C.V., Hajdu, E., Asp, N.E., Gregoracci, G.B., Neumann-Leitão, S., Yager, P.L., Francini-Filho, R.B., Fróes, A., Campeão, M., Silva, B.S., Moreira, A.P.B., Oliveira, L., Soares, A.C., Araujo, L., Oliveira, N.L., Teixeira, J.B., Valle, R.A.B, Thompson, C.C., Rezende, C.E. and Thompson, F.L. (2016), An extensive reef system at the Amazon River mouth, *Science Advances,* Vol. 2, n. 4, pp. e1501252.

Muller-Krager, F.E., McClain, C.R. and Richardson, P.L. (1988), The dispersal of the Amazons water, *Nature*, Vol. 333, pp. 56–59.

Neff, J.M., Rabalais, N.N. and Boesch, D.F. (1987), Long-term environmental effects of offshore oil and gas development, in Boesch, D.F. Rabalais, N.N. (Eds.), *Offshore oil and gas development activities potentially causing long-term environmental effects*, pp. 149–173, London (UK), [Chapter 4].

North, E.W., Adams, E., Schlag, Z.Z., Sherwood, C.R., He, R.R., Hyun, K.H.K. and Socolofsky, S.A. (2011), Simulating oil droplet dispersal from the Deepwater Horizon spill with a Lagrangian approach, in Monitoring and Modeling the Deepwater Horizon Oil Spill: A Record-Breaking Enterprise, *Geophysical Monograph Series*, Vol. 195, pp. 217–226.

O'Rourke, D. and Connolly, S. (2003), Just oil? The distribution of environmental and social impacts of oil production and consumption, *Annual Review of Environment and Resources*, Vol. 28, n. 1, pp. 587-617.

Panzer, I., Lines, S., Mak, J., Choboter, P. and Lupo, C., (2013), *High Performance Regional Ocean Modeling with GPU Acceleration*, IEEE/MTS OCEANS.

Penven, P., Roy, C., Colin de Verrdière, A. and Largier, J. (2000), Simulation of a coastal jet retention process using a barotropic model, *Oceanologica Acta*, Vol. 23, pp. 615–634.

Peterson, R.G. and Stramma, L. (1991), Upper-level circulation in the South Atlantic Ocean, *Progress in Oceanography*, Vol. 26, pp. 1–73.

Prates, C.P.T., Pierobon, E.C., da Costa, R.C. and de Figueiredo, V.S. (2006), *Evolução da oferta e da demanda de gás natural no Brasil*, BNDES Setorial, Rio de Janeiro, n. 24, pp. 35–68.

Premathilake, L.T., Yapa, P.D., Nissanka, I.D. and Kumarage, P., (2016), Impact on water surface due to deepwater gas blowouts, *Marine Pollution Bulletin*, Vol. 112, pp. 365–374.

Reed, M., Johansen, Ø., Brandvik, P.J., Daling, P., Lewis, A., Fiocco, R., Mackay, D. and Prentki, R. (1999), Oil spill modeling towards the close of the 20th century: overview of the state of the art, *Spill Science & Technology Bulletin*, Vol. 5, pp. 3–16.

Richardson, P.L. and Reverdin, G. (1987), Seasonal cycle of velocity in the Atlantic North Equatorial Countercurrent as measured by surface drifters, current meters, and ship drifts, *Journal of Geophysical Research: Oceans*, Vol. 92, pp. 3691–3708.

Richardson, P.L. and Walsh, D. (1986), Mapping climatological seasonal variations of surface currents in the tropical Atlantic using ship drifts, *Journal of Geophysical Research*, Vol. 91, pp. 10537–10550.

Salisbury, J., Vandemark, D., Campbell, J., Hunt, C., Wisser, D., Reul, N. and Chapron, B. (2011), Spatial and temporal coherence between Amazon River discharge, salinity, and light absorption by colored organic carbon in western tropical Atlantic surface waters, *Journal of Geophysical Research*, Vol. 116, C00H02, pp 1-14.

dos Santos, V.F., Mendes, A.C. and da Silveira, O.F.M. (2016*), Atlas de sensibilidade ambiental ao óleo da Bacia Marítima da Foz do Amazonas*, Macapá: IEPA.

Sharma, N., Anderson, S.P., Brickley, P., Nobre, C. and Cadwallader, M.L. (2009), *Quantifying the Seasonal and Interannual Variability of the Formation and Migration Pattern of North Brazil Current Rings*, IEEE. pp. 1–7. Conference paper: OCEANS 2009, MTS/IEEE Biloxi - Marine Technology for Our Future: Global and Local Challenge.

Shchepetkin, A.F. and McWilliams, J.C. (2005), The regional oceanic modeling system (ROMS): a split-explicit, free-surface, topography-following-coordinates oceanic model, *Ocean Modelling*, Vol. 9, pp. 347–404.

Silva, M., Araujo, M., Servain, J., Penven, P. and Lentini, C.A.D. (2009), High-resolution regional ocean dynamics simulation in the southwestern tropical Atlantic, *Ocean Modelling*, Vol. 30, pp. 256–269.

da Silva Junior, O.M. and Magrini, A. (2014), Exploração de hidrocarbonetos na Foz do Rio Amazonas: perspectivas de impactos ambientais no âmbito das áreas ofertadas na 11o rodada de licitações da Agência Nacional do Petróleo, *Revista GeoAmazônia*, Vol. 2, pp. 159–172.

da Silveira, I.C., Brown, W.S. and Flierl, G.R. (2000), Dynamics of the North Brazil Current retroflection region from the Western Tropical Atlantic Experiment observations, *Journal of Geophysical Research: Oceans*, Vol. 105, pp. 28559–28583.

Skogdalen, J.E., Utne, I.B. and Vinnem, J.E. (2011), Developing safety indicators for preventing offshore oil and gas deepwater drilling blowouts, *Safety Science*, Vol. 49, n. 8-9, pp. 1187–1199.

Skogdalen, J.E. and Vinnem, J.E. (2012), Quantitative risk analysis of oil and gas drilling, using Deepwater Horizon as case study, *Reliability Engineering and System Safety*, Vol. 100, pp. 58–66.

Small, M.J., Stern, P.C., Bomberg, E., Christopherson, S.M., Goldstein, B.D., Israel, A.L., Jackson, R.B., Krupnick, A., Mauter, M.S. and Nash, J. (2014), *Risks and risk governance in unconventional shale gas development*, ACS Publications.

Smith, W.H.F. and Sandwell, D.T. (1997), Global sea floor topography from satellite altimetry and ship depth soundings, *Science*, Vol. 277, pp. 1956–1962.

Song, Y. and Haidvogel, D.B. (1994), A Semi-implicit Ocean Circulation Model Using a Generalized Topography-following Coordinate System, *Journal of Computational Physics*, Vol. 115, pp. 228–244.

Stramma, L. and England, M. (1999), On the water masses and mean circulation of the South Atlantic Ocean, *Journal of Geophysical Research*, Vol. 104, pp. 20863–20883.

Teal, J.M. and Howarth, R.W. (1984), Oil spill studies: a review of ecological effects, *Environmental Management*, Vol. 8, n. 1, pp. 27–43.

Topham, D. (1984), The formation of gas hydrates on bubbles of hydrocarbon gases rising in seawater, *Chemical Engineering Science*, Vol. 39, pp. 821–828.

Ugochukwu, C.N.C. and Ertel, J. (2008), Negative impacts of oil exploration on biodiversity management in the Niger De area of Nigeria, *Impact Assessment and Project Appraisal*, Vol. 26, n. 2, pp. 139-147.

U.S. Department of Energy, (U.S. DOE) (1999), *Environmental benefits of advanced oil and gas exploration and production technology*, 168p.

U.S. Energy Information Administration (U.S. EIA) (1998), *Future Supply Potential of Natural Gas Hydrates*, Report DOE/EIA-0484, pp. 73–90.

U.S. National Ocean Industries Association (U.S. NOIA) (2005), *What are environmental challenges and regulatory barriers to expanding our natural gas supply and how can they be remedied?*, in Natural Gas Conference, Senate Energy and Natural Resources Committee, pp. 9–11.

Wang, Y. (2004), *Ocean Tide Modeling in the Southern Ocean,* Technical Report 471, Department of Civil and Environmental Engineering and Geodetic Science, The Ohio State University, Columbus, Ohio.

Yapa, P.D. and Zheng, L. (1997), Simulation of oil spills from underwater accidents I: Model development, *Journal of Hydraulic Research*, Vol. 35, pp. 673–688.

Yapa, P.D., Zheng, L. and Chen, F. (2001), A model for deep-water oil/gas blowouts, *Marine Pollution Bulletin*, Vol. 43, pp. 234–241.

Zheng, L. and Yapa, P.D. (1998), Simulation of oil spills from underwater accidents II: Model verification, *Journal of Hydraulic Research*, Vol. 36, pp. 117–134.

Zheng, L. and Yapa, P.D. (2000), Buoyant velocity of spherical and nonspherical bubbles/droplets, *Journal of Hydraulic Engineering*, Vol. 126, pp. 852–854.

Zheng, L. and Yapa, P.D. (2002), Modeling gas dissolution in deep-water oil/gas spills, *Journal of Marine Systems*, Vol. 31, pp. 299–309.

A PAPER "AMAZON RIVER PLUME INFLUENCE IN THE WESTERN TROPICAL ATLANTIC DYNAMIC VARIABILITY"

This annex presents the manuscript entitled *Amazon River plume influence in the Western Tropical Atlantic dynamic variability*, submitted July 7, 2017 in *Dynamics of Atmospheres and Oceans*. Current status: Submit Revision.

The main objective is quantify how much the Amazon River plume impacts on the dynamics of the Western Tropical North Atlantic. The role of Amazon and Pará Rivers plumes in the temperature, salinity and dynamics of the main surface currents is investigated.

Amazon River plume influence on Western Tropical Atlantic dynamic variability

H. L. Varona[a,*], D. Veleda[a], M. Silva[a], M. Cintra[b], M. Araujo[a,c]

[a]*Department of Oceanography, DOCEAN, Federal University of Pernambuco, Recife-PE, Brazil.*
[b]*Federal University of Rio Grande do Norte, Natal-RN, Brazil.*
[c]*Brazilian Research Network on Global Climate Change, Rede CLIMA, S. José dos Campos-SP, Brazil.*
**Corresponding author: humberto.varona@yadex.com*

Abstract

This study focuses on analysing the potential impact of the Amazon and Pará Rivers on the salinity, temperature and hydrodynamics of the Western Tropical North Atlantic (WTNA) region between 60.5°-24°W and 5°S-16°N. The Regional Ocean Model System (ROMS) was used to simulate ocean circulation with 0.25° horizontal resolution and 32 vertical levels. Two numerical experiments were performed considering river discharge and river input. Temperature and salinity distributions obtained numerically were compared with Simple Ocean Data Assimilation (SODA) and in situ observations from the Prediction Research Moored Array in the Tropical Atlantic (PIRATA) buoys located at 38°W8°N and 38°W12°N. Surface currents were compared with Surface Currents from Diagnostic model (SCUD). Once we verified that model results agreed with observations, scenarios with and without river discharges were compared. The difference between both simulations in the Sea Surface Temperature distribution was smaller than 2°C, whereas the Sea Surface Salinity (SSS) changed by approximately 8 psu in the plume area close to the coast from August to December and reaching SSS differences of approximately 4 psu in the region of the North Equatorial Counter Current (NECC). The surface current velocities are stronger in the experiment with river discharge, mainly in the NECC area from September to December and close to the coast in June to August. The results show that river discharges also cause a phase shift in the zonal currents, anticipating the retroflection of the North Brazil Current by two months and enhancing eastward NECC transport, which is in agreement with observations. The Mixed Layer Depth and Isothermal Layer Depth in the presence of river discharge is 20−50 m shallower over the entire extension of the Amazon plume compared with the situation without continental inflows. As a consequence, stronger Barrier Layers develop in the river plumes, reducing the Oceanic Heat Content in the WTNA.

Keywords: ROMS, Western Tropical North Atlantic, Amazon River discharge, Ocean circulation, Mixed Layer, Barrier Layer, Oceanic Heat Content.

1 Introduction

The circulation in the Western Tropical North Atlantic Ocean (WTNA) performs an important role in the interhemispheric transport of mass, heat, and salt and in the thermohaline overturning cell (Schmitz Jr. and McCartney, 1993; Bourlès et al., 1999a; Silva et al., 2009a; Veleda et al., 2012). Furthermore, a strong western boundary current, the North Brazil Current (NBC) is the main conduit for cross-equatorial transport of South Atlantic upper-ocean water as part of the Atlantic meridional overturning cell (Johns et al., 1998). This current flows north westward, intercepting the Amazon and Pará River freshwater discharges along the Brazilian north coast.

The Western Tropical North Atlantic Ocean is also a region with a complex system of zonal currents and counter-currents forced by subtropical gyres and the action of the trade winds in both hemispheres (Stramma et al., 2005). The NBC is considered a low latitude strong western-boundary current (Garzoli et al., 2004; Fratantoni and Richardson, 2006; Akuetevi and Wirth, 2015), and it is periodically retroflected near 6-8°N and separated away from the boundary, turning anti-cyclonically for more than 90°, and forming anticyclonic eddies exceeding 450 km in overall diameter (Richardson et al., 1994; Garzoli et al., 2004; Fratantoni and Richardson, 2006). The NBC retroflection feeds the North Equatorial Counter Current (NECC), an eastward zonal current that contributes to the formation of the anticyclonic current rings (Castelão and Johns, 2011). The NBC rings are a significant contributor to transporting water across current gyres and between hemispheres in the tropical Atlantic (Bourlès et al., 1999a; Johns et al., 1998; Schott et al., 2003; Stramma et al., 2005).

The Amazon River plume flows into the WTNA near the equator and is carried north westward along the Brazilian shelf by the NBC (Muller-Krager et al., 1988; Salisbury et al., 2011). This is the main source of freshwater in the world, with an average discharge of approximately 222,800 m^3s^{-1}, it deposits almost 20% of the global river discharge onto the equatorial Atlantic Ocean continental shelf (Goulding et al., 2003; Barthem et al., 2004). The Amazon River plume extends thousands of kilometres over the North Atlantic Ocean arriving at the Caribbean Sea (Müller-Karger et al., 1989; Johns et al., 1990). Strong seasonal variations in this current system occur in response to trade wind variability and seasonal migration of the atmospheric Intertropical Convergence Zone (ITCZ) between its southern position in boreal winter, and its northern position in boreal summer (Xie and Carton, 2004). This leads to northward transport of Amazon waters in boreal winter, and eastward transport of Amazon water in the NECC in boreal spring through autumn (Muller-Krager et al., 1988; Lentz, 1995; Fratantoni and Glickson, 2002; Coles et al., 2013; Foltz et al., 2015). Thus, the influence of Amazon water is felt far from the river mouth through enhancement of surface stratification leading to the formation of barrier layers (Silva et al., 2005; Ffield, 2007; Coles et al., 2013; Grodsky et al., 2014). Thus, the Amazon River plume is thought to influence the surface ocean heat balance and its interaction with the atmosphere in the WTNA.

The Western Tropical North Atlantic ocean is a region with intense land-ocean interaction, characterised by complex material transport, mixed layer depth changes (Grodsky et al., 2012; Coles et al., 2013) and high biogeochemical activity (Lefèvre et al., 2010; Ibánhez et al., 2017; Araujo et al., 2014, 2017), giving rise to alterations in local and remote oceanic processes. For example, river discharge use to be a small component of the open ocean salinity balance, but the magnitude of the Amazon freshwater source is so important that the discharged volume reaches two-fold the net evaporation minus precipitation budget over the north western tropical Atlantic (Ferry and Reverdin, 2004). Thus, in addition to the physical and weather/climate impacts, the Amazon and Pará Rivers also inject terrestrially derived sediments, nutrients, and coloured as well as transparent dissolved organic matter that can also be traced thousands of kilometres from the river mouth (Hu et al., 2004). The Biological community structure is strongly influenced by these terrigenous inputs of dissolved organic matter and nutrients, as well as by the induced changes in the stratification in the upper ocean (Stukel et al., 2014), leading to a globally significant uptake of atmospheric carbon dioxide in the river plume area (Cooley et al., 2007; Subramaniam et al., 2008; Yeung et al., 2012).

Several recent studies have used in situ observation data, satellite products, general circulation models (OGCMs) and regional models to explain the spatial and temporal variability of the Amazonian plume and its interaction with the NBC rings (Fratantoni and Glickson, 2002; Ffield, 2007; Korosov et al., 2015). Schmidt et al. (2011), for example, implemented an operational forecasting system using a high-resolution model to resolve the migration rate of the NBC rings on a short time scale. Other recent work links the intensification of hurricanes to the spreading of Amazonian freshwater discharges due to the impact of haline stratification on reduction of the vertical heat flux (Balaguru et al., 2012; Grodsky et al., 2012; Newinger and Toumi, 2015) and the periodic movement of the NBC rings (Ffield, 2007).

In this work, we used a climatological modelling approach to investigate the role of the Amazon and Pará River plumes on the circulation and thermohaline variability in the Amazon River-Ocean continuum (Araujo et al., 2017). Two numerical experiments were conducted, contrasting the scenarios with and without the contribution of continental freshwater to the tropical Atlantic. We focused here on the impact of river inflows on the circulation (NBC-NECC system) and temperature/salinity distributeons, which induce important changes in isothermal/mixed/barrier layer formation and oceanic heat content in the Western Tropical North Atlantic Ocean. The model configuration, simulation scenarios, observational dataset and analysis procedures are described in Section 2. In addition to simulation considering the discharges of the Amazon and Pará Rivers in the presence of islands (Scenario RRF), an idealised configuration without continental contributions was also simulated (Scenario NRF). The results from scenario RRF are compared with the available observational datasets in order to validate the simulation. Then, differences between two scenarios are examined. Simulation results, including model validation, are presented and discussed in Section 3. The last section provides the conclusions and outcome perspectives of this work.

2 Data and methodology

2.1 Numerical modelling experiments

In this work, we use the Regional Ocean Modeling System (ROMS), an open source software, which has been continuously developed by a large community of scientists, with more than 400,000 lines of FORTRAN code. ROMS integrates the primitive Reynolds equations in a rotational free surface system of free surface, using the Boussinesq approximation, the hydrostatic approximation and the balance of vertical momentum (Shchepetkin and McWilliams, 2005; Song and Haidvogel, 1994; Panzer et al., 2013). This was adapted to different geographic regions of the world where good results were obtained (Haidvogel et al., 2000; Penven et al., 2000; Silva et al., 2009a; Tchamabi et al., 2017).

The region of study is framed in 60.5°-24°W and 5°S-16°N (Fig. 1) with 0.25° of resolution (approximately $27.8\,km$), covering an area of $4916 \cdot 10^3 km^2$ corresponding to a 183×159 node grid with 32 levels in the vertical, 12 of which are in the upper 100 m and 20 in the $500\,m$. The ETOPO2 (Smith and Sandwell, 1997) topography database was used in the vertical discretisation with 2 *min* of resolution. The red rectangles in Fig. 1 indicate the regions used to evaluate model performance where strong seasonal changes in ocean circulation and thermohaline structure are observed; REG1 corresponds to the NBC retroflection region, and REG2 represents the NECC area. The locations of PIRATA buoys are also plotted in the figure.

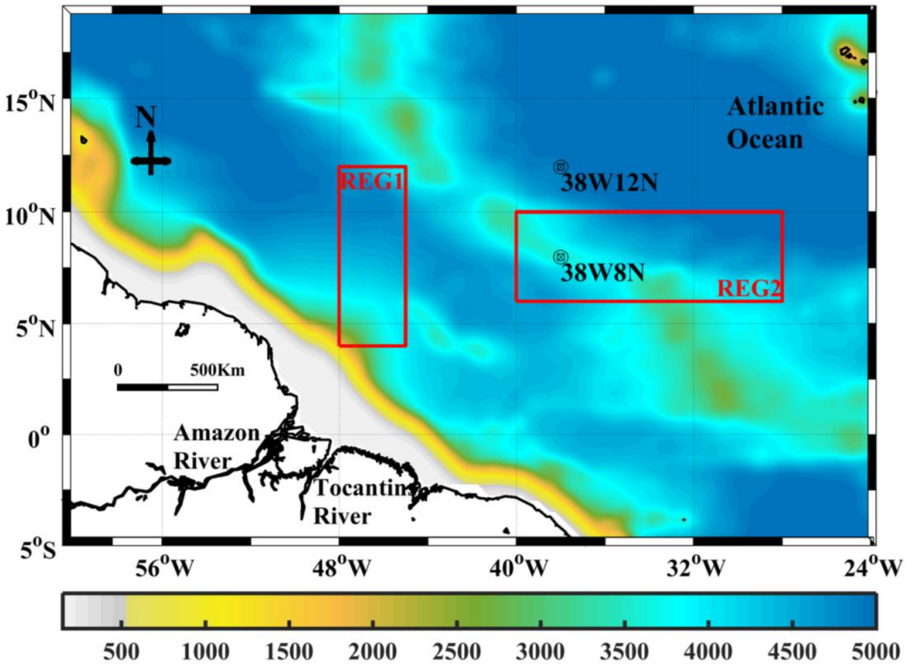

Figure 1: The model domain framed in 60.5°-24°W/5°S-16°N. The colour bar represents ocean bathymetry and the red rectangles correspond to two regions used for model validation: REG1 (48-45°W/4-12°N) and REG2 (40-28°W/6-10°N). PIRATA buoys at 38°W8°N and 38°W12°N are also indicated in the figure.

Four lateral boundaries are considered open in simulations. In the lateral boundary and initial conditions all variables were constrained by the monthly mean of the 2009 World Ocean Atlas, WOA2009 (Locarnini et al., 2010; Antonov et al., 2010) with a resolution of 1°. The surface forcings were obtained from the monthly mean climatology of the Comprehensive Ocean-Atmosphere Data Set (COADS05) (Da Silva et al., 1994) with 0.5° of resolution. Tides are an important process in mixing the river freshwater plumes with the open ocean and are obtained from the TPXO7 (Egbert et al., 1994; Egbert and Erofeeva, 2002), which has altimetry data from several satellites to improve the accuracy of the results obtained through the hydrodynamic model (Wang, 2004; D'Onofrio et al., 2012). The monthly mean river discharge was obtained from the Obidos and Tucurui gauge stations (Dai and Trenberth, 2002), and the monthly climatology of Sea Surface Temperature (SST) in the river discharge points was also obtained from WOA2009.

We performed two numerical experiments to estimate the potential impact of the Amazon and Pará Rivers on the salinity, temperature and surface currents of the WTNA. In the first experiment, hereafter referred to as River Runoff (RRF), the Amazon and Pará Rivers release freshwater into the WTNA. Given the geographical configuration of the Amazon River Delta, there are four inputs from the river to the WTNA (Fig. 2(a)): Canal do Norte, Baia de Santa Rosa, Canal Perigoso and Canal do Jurupari. The inputs are placed in four cells of the grid. Considering the channel width, the contribution was calculated for each one, distributed as 14.47%, 37.27%, 29.13% and 19.13%, respectively (Fig. 2(b)), with the same monthly temperature distribution for the four input nodes in the Amazon River Delta and different in the input node of the Pará River (Fig. 2(c)). In the second experiment, the No-River Runoff (NRF), the Amazon and Pará Rivers do not release freshwater into the WTNA, keeping the same model parametrisation and initial and boundary conditions. We ran each experiment for 11 years (spin-up), but our analyses are focused on the last simulation year.

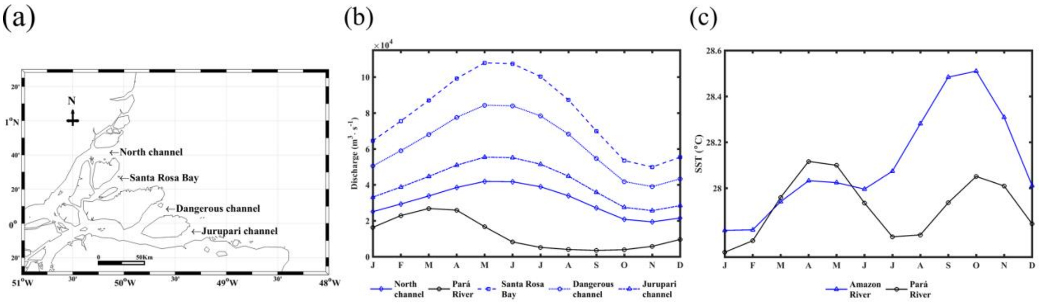

Figure 2: (a) Location map of the Amazon River delta and its four inputs (North channel, Santa Rosa Bay, Dangerous channel and Jurupari channel) from the river to WTNA. (b) Monthly distribution of discharge (m^3s^{-1}) of the Amazon River (blue lines) and Pará River (black line), from the Obidos and Tucuruí gauge stations. (c) Monthly distribution of temperature ($\circ C$) of of the Amazon River (blue line) and Pará River (black line).

2.2 Mixed layer depth (MLD), isothermal layer depth (ILD), barrier layer thickness (BLT) and oceanic heat content (OHC) criteria

The MLD was defined as the depth where the density increases from the surface value due to a prescribed temperature decrease of 0.2°C ($\Delta T = -0.2°C$) while maintaining constant surface salinity. The MLD was mathematically defined by Sprintall and Tomczak (1992) and de Boyer Montégut et al. (2007) as

$$\Delta\sigma = \sigma(T + \Delta T, S, P_0) - \sigma(T, S, P_0)$$

where $\Delta\sigma$ is the density difference for the same change in temperature ΔT at constant salinity, T and S are the values of temperature and salinity at the reference depth (Z_{REF}) and P_0 is the pressure at the ocean surface. The ILD is the depth at which the temperature is equal to $T + \Delta T$. In this study, we consider Z_{REF}=0, corresponding to the SST obtained in simulations.

The Barrier Layer (BL) may prevent heat exchange between the oceanic mixed layer (MLD) and deeper water, influencing the SST and ensuring greater isolation along the Mixed Layer Depth (MLD). The thicker the BL is, the less heat exchange exists between deep cold water and the oceanic mixed layer. The BLT is calculated as

$$\mathrm{BLT}=\mathrm{ILD}-\mathrm{MLD}$$

The transfer of mass, momentum and energy through the mixing layer is an important feature influencing oceanic circulation and changes with the atmosphere. The ILD determines the heat content and the mechanical inertia of the layer that interacts directly with the atmosphere (de Boyer Montégut et al., 2004). Changes in oceanic heat content play an important role in sea level rise due to thermal expansion. The quantity of energy stored per unit area in the ocean (OHC) between levels Z_{REF} and h is defined according to Jayne et al. (2003) as

$$\mathrm{OHC}=\rho_0 C_p \int_{Z_{REF}}^{h} T(z)\,dz$$

where *OHC* is Oceanic Heat Content in Jm^{-2}, $\rho_0 = 1025$ kg m^{-3} is the representative density of seawater at the sea surface, $C_p = 4 \cdot 10^3 J(\text{kg}-°C)^{-1}$ is the specific heat of seawater at constant pressure at the sea surface (Levitus et al., 2005), $T(Z)$ is a vertical temperature ($°C$), *Z* is Depth (m), Z_{REF}=0 and h is the maximum depth to calculate the *OHC*.

As the depth increases, the temperature oscillation decreases and below the active ocean layer, there are practically no annual variations in temperature. The OHC is more related to the thickness of the isothermal layer than to the temperature directly; thus, we plan to study only the quantity of heat in the active layer of the ocean, numerically integrating the temperature in each vertical profile in the grids of the RRF and NRF experiments, from surface to $h = ILD$.

2.3 Model validation: Comparison with observations

For model validation, we compare numerical Sea Surface Temperature and Sea Surface Salinity (SSS) variability with the Simple Ocean Data Assimilation (SODA) version 2.2.4 (Carton et al., 2000a, 2000b; Carton and Giese, 2008), which has a spatial resolution of 0.5° and integration period of 20 years (1991-2010).

Surface currents are compared with the Surface Current form Diagnostic model (SCUD) (Maximenko and Hafner, 2010), with spatial resolution of 0.5° and period of 2000-2008. To compare numerical results to previous findings reported by Richardson and Reverdin (1987), the average values of the zonal component of surface velocity were also calculated for two different regions of the NECC: the Western NECC (WNECC - 50-40°W/5-8°N), and the Eastern NECC (ENECC - 30-25°W/5-8°N).

Other than considering the overall differences between the RRF and NRF scenarios at the whole integration domain, the river induced circulation and thermohaline changes were examined at two highly dynamic areas of the WTNA (red rectangles in Fig. 1): (i) the REG1 region (48-45°N/4-12°N) corresponding to an NBC retroflection area; and (ii) the REG2 region (40-28°W/6-10°N), representing the zonal band NECC pathway.

Subsurface temperature and salinity distributions and variability obtained from the RRF scenario were compared to the observed climatology of the PIRATA buoys located at 38°W8°N and 38°W12°N (Servain et al., 1998; Bourlès et al., 2008), constructed during 2000-2015. The

PIRATA mooring design allows high frequency measurements of ocean temperature at 11 levels (i.e., 1, 20, 40, 60, 80, 100, 120, 140, 180, 300, 500 m), salinity at 4 levels (1, 20, 40, 120 m), and meteorological variables at the sea surface, that are transmitted and kept immediately available on the Web after their validation (https://www.pmel.noaa.gov/gtmba/).

Except the previously mentioned comparison of the zonal component of current velocity, the results presented and discussed in the next section focus on the differences between the RRF and NRF experiments during: boreal winter (DJF: December, January, February); boreal spring (MAM: March, April, May), boreal summer (JJA: June, July, August) and boreal autumn (SON: September, October, November).

3 Results and discussion

3.1 Model evaluation: Validation of the RRF experiment

The ROMS monthly climatology output is compared with the SODA dataset to evaluate model results and validate the RRF experiment. The differences in Sea Surface Salinity between the model simulation and SODA climatology (RRF-SODA) are shown in Fig. 3. The results indicate that lower SSS values were obtained from ROMS simulations than from SODA in the area of the NBC retroflection (during April to June - boreal spring) and in some meanders of the NECC zonal corridor (during October to December - boreal autumn).

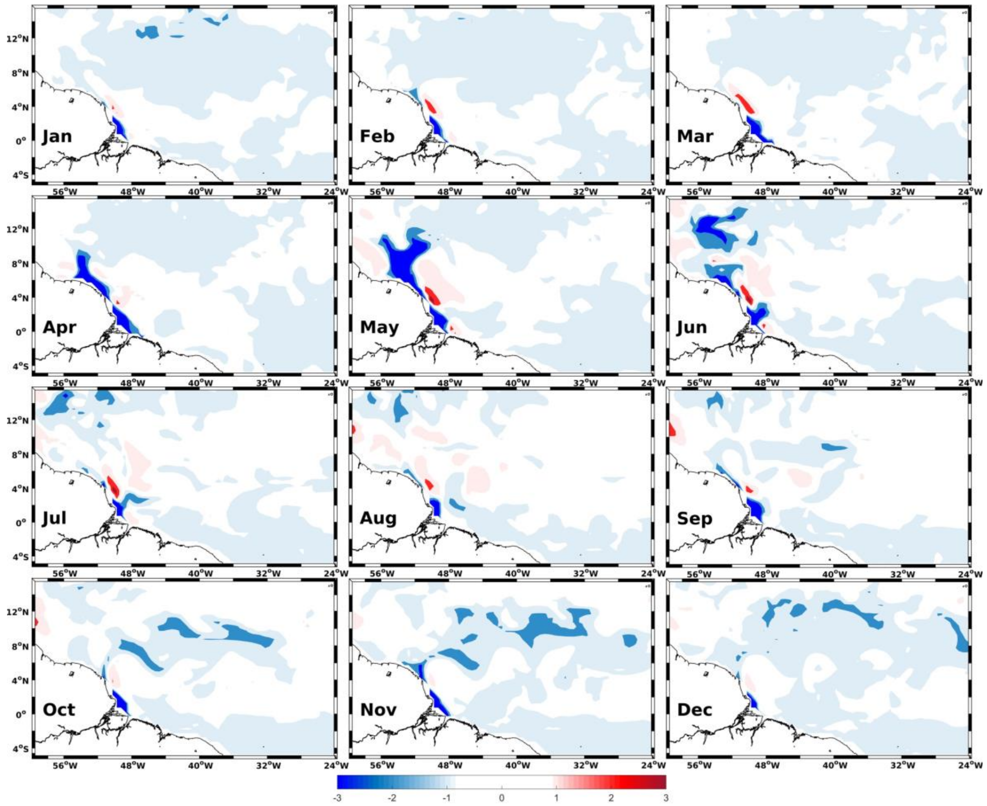

Figure 3: Seasonal variability of the differences in SSS distributions (psu) between the RRF experiment and SODA climatology in the WTNA.

The differences between the SST climatology obtained from simulation and from SODA are shown in Fig. 4. The modelled mean SSTs present in general higher monthly averaged temperatures than SODA in the area of the NBC retroflection and the NECC, mainly during boreal autumn and early/mid-winter.

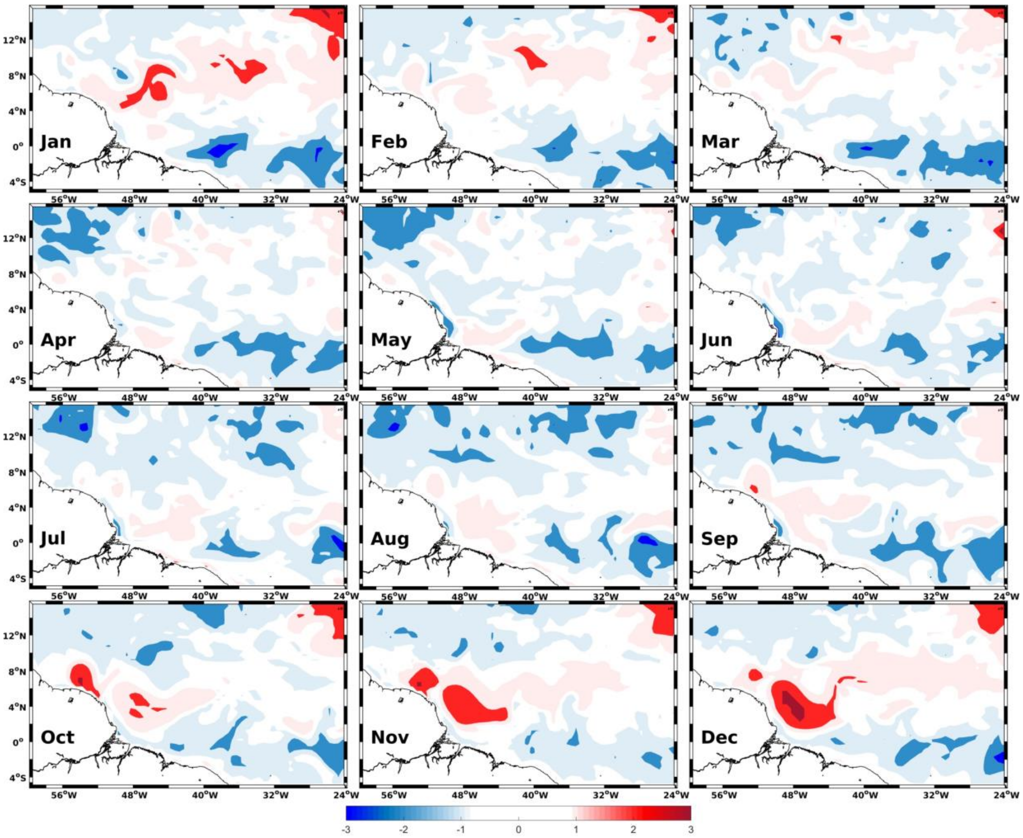

Figure 4: Seasonal variability of the differences in SST distributions (ºC) between the RRF experiment and SODA climatology in the WTNA.

A comparison between seasonal averaged SSS (columns 1 and 2) and SST (columns 3 and 4) values obtained from simulations (RRF) and from SODA in REG2 area (NECC region, Fig. 1) is shown in Tab. 1. The mean value±standard deviation is indicated in the first set of rows, and the range (minimum−maximum) in the second set for each season. The results indicate overall good agreement between SST and SSS generated by the RRF scenario and SODA. The maximum SSS difference in area REG2 (0.27 *psu*) is verified during boreal summer (June to August) and a minimum SSS difference (0.06 *psu*) during boreal spring (March to May). For SST, columns 3 and 4 in Tab. 1 show greater differences between RRF simulation and SODA in the REG2 area during boreal winter (December to February) (1.27°C), when we still have the Amazon river plume feeding the NECC. The RRF simulation is better adjusted during boreal summer (June to August).

Table 1: Comparison between seasonal SSS (columns 1 and 2) and SST (columns 3 and 4) values obtained from simulations (RRF scenario) and from SODA in the REG2 area (NECC region, Fig. 1). The mean value±standard deviation is indicated in the first rows, and value ranges (minimum−maximum) in the second rows.

Period	SSS		SST	
	SODA (psu)	RRF (psu)	SODA ($^{\circ}C$)	RRF ($^{\circ}C$)
DJF	35.86±0.02 (35.56−36.10)	35.63±0.07 (34.94−36.19)	26.90±0.04 (26.02−27.48)	28.17±0.14 (26.47−29.12)
MAM	36.09±0.02 (35.87−36.32)	36.15±0.01 (35.81−36.47)	26.74±0.10 (25.60−27.61)	27.05±0.27 (25.73−28.31)
JJA	35.82±0.03 (35.43−36.15)	36.09±0.05 (35.46−36.51)	27.77±0.07 (27.15−28.30)	27.77±0.23 (26.27−28.84)
SON	35.41±0.07 (34.89−35.87)	35.23±0.13 (34.19−36.26)	28.26±0.04 (27.84−28.74)	28.63±0.13 (27.63−29.69)
Annual	35.79±0.03 (35.44−36.11)	35.78±0.08 (35.10−36.36)	27.42±0.07 (26.65−28.03)	27.91±0.19 (26.53−28.99)

Fig. 5 shows the comparison between near surface (0-120 m depth for salinity and 0-500 m depth for temperature) seasonal variation of the vertical distributions of temperature and salinity obtained from the RFF scenario and from PIRATA observations at 38°W8°N and 38°W12°N. This figure indicates generally good agreement between model results and in situ measurements, but in order to have a statistical confirmation of model capacity to reproduce observations, we performed two-sample t-test. Prior to performing t-test, in situ and numerical profiles were normalised since the initial dataset showed non-normal distributions as verified by the one-sample Kolmogorov-Smirnov test.

The simulated salinity at the position 38°W8°N (Fig. 5(a)) shows a seasonal evolution of vertical structure similar to that observed from PIRATA data, in particular during boreal spring (August to December), when lower salinity Amazonian waters are transported eastward by the NECC. The main differences are verified from June to October, in the first 40 m, just after the beginning of NBC retroflection, when the freshwater river plume starts to feed the NECC (Coles et al., 2013; Grodsky et al., 2014). T-test indicated no statistically significant differences between vertical distributions of salinity issued from the RRF experiment and PIRATA data (p=0.9966, $\alpha = 0.05$). The temperature evolution obtained numerically is also well adjusted to measurements (Fig. 5(b)), with no significant differences between the potential model and PIRATA data (p=0.8287, $\alpha = 0.05$).

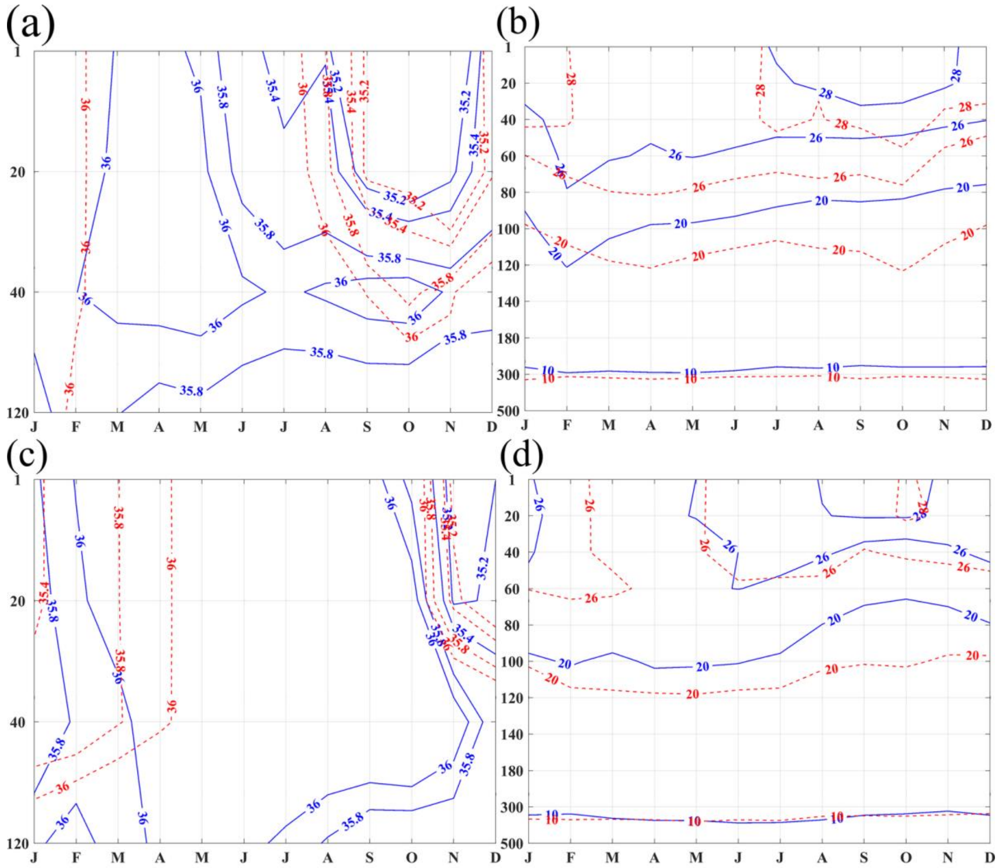

Figure 5: Hovmöller diagrams of temperature and salinity obtained from model simulation (red dashed lines) and PIRATA observations (blue solid lines) at: 38°W8°N (a) salinity (psu) and (b) temperature ($°C$); and $38°W12°N$ (c) salinity (psu) and (d) temperature ($°C$).

The vertical profiles of modelled salinity are in general agreement with in situ measurements at the position of the PIRATA buoy 38°W12°N (Fig. 5(c)). A mean difference of $0.4 psu$ is seen and no significant differences were found between model outputs and observations (p=0.9857, $\alpha = 0.05$). The evolution of near surface vertical temperature structure is also similar to the measurement along the year (Fig. 5(d)), with some discrepancies between 100−120 m depth, just below the thermocline depth. Again, t-test indicated no significant differences between the model and measurements (p=0.8137) for a significance level of 0.05.

The NECC is the main current transporting the Amazon River plume eastward (Grodsky et al., 2014). We now compare the seasonal evolution of the zonal components of surface velocity longitudinally averaged in the REG2 limits (40-28°W) obtained numerically (RRF scenario) (Fig. 6(a)) to that issued from the SCUD dataset (Fig. 6(b)). Both cases show a gradual increase of the zonal component from July to October, between 4.0 and 10°N, and decreasing during boreal autumn (September to November). The maximum difference between the model and SCUD was found between 5.5 and 6.5°N in July and between 4 and 5°N in October, with an averaged difference of 0.1 ms^{-1}. These results reveal that the model simulation represents the dynamics of the NECC variability in the WTNA quite well.

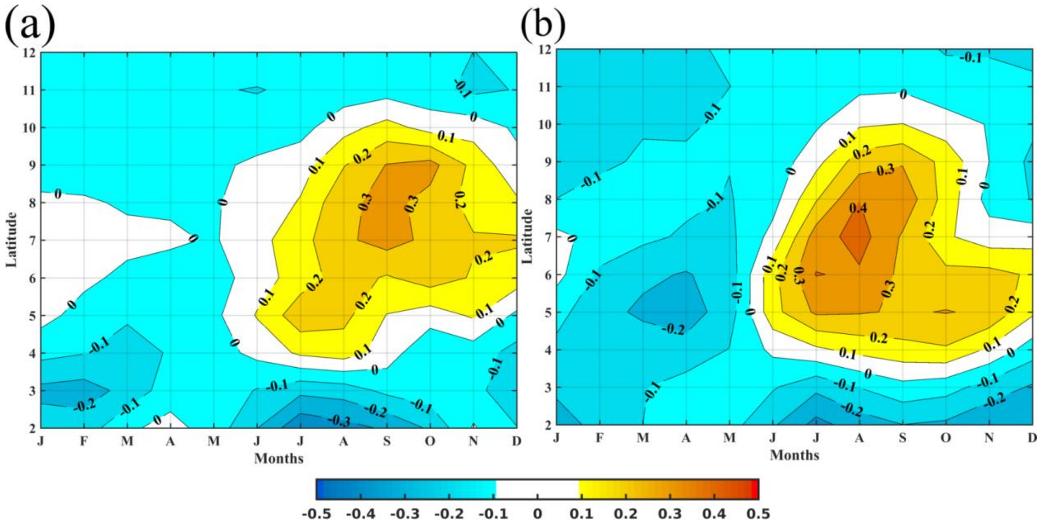

Figure 6: Hovmöller diagrams of the zonal component of surface velocity longitudinally averaged in the REG2 limits (40-28°W): (a) Model (RRF) simulation; (b) SCUD dataset.

Finally, to compare model results to previous in situ observations, we calculated the averaged zonal component of surface velocity obtained numerically during boreal autumn at the WNECC and ENECC regions as 0.384 ms^{-1} and 0.226 ms^{-1}, respectively. These values are very close to those reported by Richardson and Reverdin (1987) for the same period and regions (0.410 ms^{-1} and 0.215 ms^{-1}, respectively).

3.2 Impact of river plumes: Comparison between the RRF and NRF experiments

In this section, we compare the seasonal evolution of the differences between the RRF and NRF scenarios (RRF-NRF). It aims to investigate the influence of river discharges on the surface ocean circulation and thermohaline structure in the WTNA.

3.2.1 Impacts of thermohaline structure and changes on ILD, MLD, BLT and OHC

Fig. 7(a) shows the seasonal variation of the difference of SSS distributions in the WTNA obtained from model results with (RRF) and without (NRF) the Amazon and Pará River discharges. The RRF experiment shows lower salinity confined to the coast from December to February. From March to May, the RRF scenario shows evidence of lower salinity at the NBC retroflection area. From June to August, the plume spreads northward, and from September to

November, the plume is transported eastward by the NECC. The river scenario shows 10−12 psu lower salinity values along the coast than does the NRF case, which represents the seasonal cycle of the Amazon plume well. In the NECC area, the continental inflows generate lower SSS values of 4 psu. These results are in agreement with previous observations and modelling efforts (Silva et al., 2009b, 2010; Coles et al., 2013; Korosov et al., 2015; Newinger and Toumi, 2015; Araujo et al., 2017).

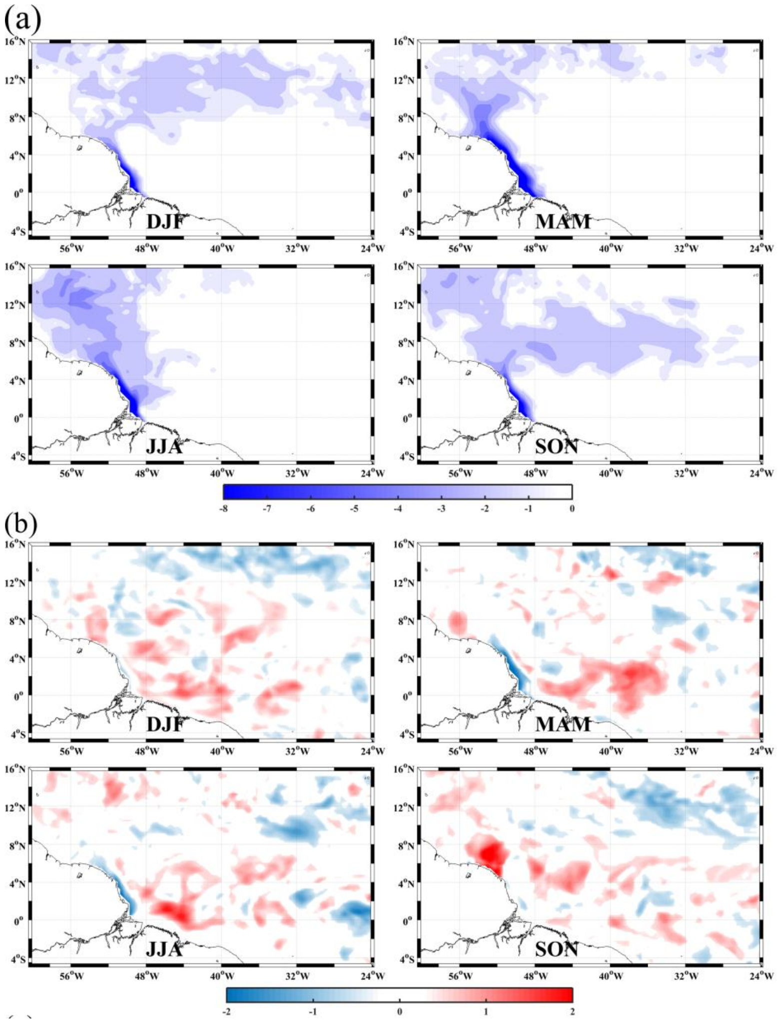

Figure 7: Seasonal evolution of the difference of: (a) SSS (psu); and (b) SST (ºC) between the RRF (River discharges) and NRF (No-river discharges) simulations during boreal winter (DJF:

December, January, February), boreal spring (MAM: March, April, May), boreal summer (JJA: June, July, August), and boreal autumn (SON: September, October, November).

Fig. 7(b) shows the differences in seasonal SST distributions for both situations (RRF-NRF). Although not significant, the results indicate that river discharges induce a warming near the Amazon River mouth, in particular during boreal spring/summer and at the NBC retroflection area in boreal autumn. A small cooling is also verified very close to the coastline at the left side of the river mouth. In the open ocean SST changes are not very sensitive to the river inputs. These results are in agreement with previous observations (Silva et al., 2010; Newinger and Toumi, 2015; Araujo et al., 2017).

Changes in temperature and salinity distributions due to the inflow of Amazon and Pará River freshwater modify the thickness and evolution of the Isothermal (ILD), Mixed (MLD) and Barrier layers (BLT) in the WTNA. Fig. 8(a) indicates that oceanic mixed layers are shallower in the RRF experiment than in the situation simulated with no-river input. These changes are located in the regions (and periods) where (when) river plumes spread into the WTNA. Indeed, the low-density layer formed by the freshwater river discharge induces MLD 20 m to 50 m shallower over the entire extension of the plume. The MLD minimum for the RRF experiment is 6 m throughout the year and the maximum fluctuates between 88 m and 100 m, being deeper in the SON period. In contrast, whereas minimum MLD values are approximately 6 m, the maximum mixed layer depth oscillates between 100 m and 120 m in the absence of river plumes (NRF experiment).

Fig. 8(b) shows the spatial distribution of the differences in the seasonally averaged distributions of ILD between the RRF and NRF experiments. Although less intense than MLD, we also find shallower ILDs in the presence of river discharges than in the simulations without continental contribution (NRF), in particular during boreal summer (JJA) and autumn (SON). As expected, there is a clear influence of SST changes over the ILD, being up to 1°C higher in the plume area for the RRF scenario than for the No-rivers simulation (Fig. 7(b)).

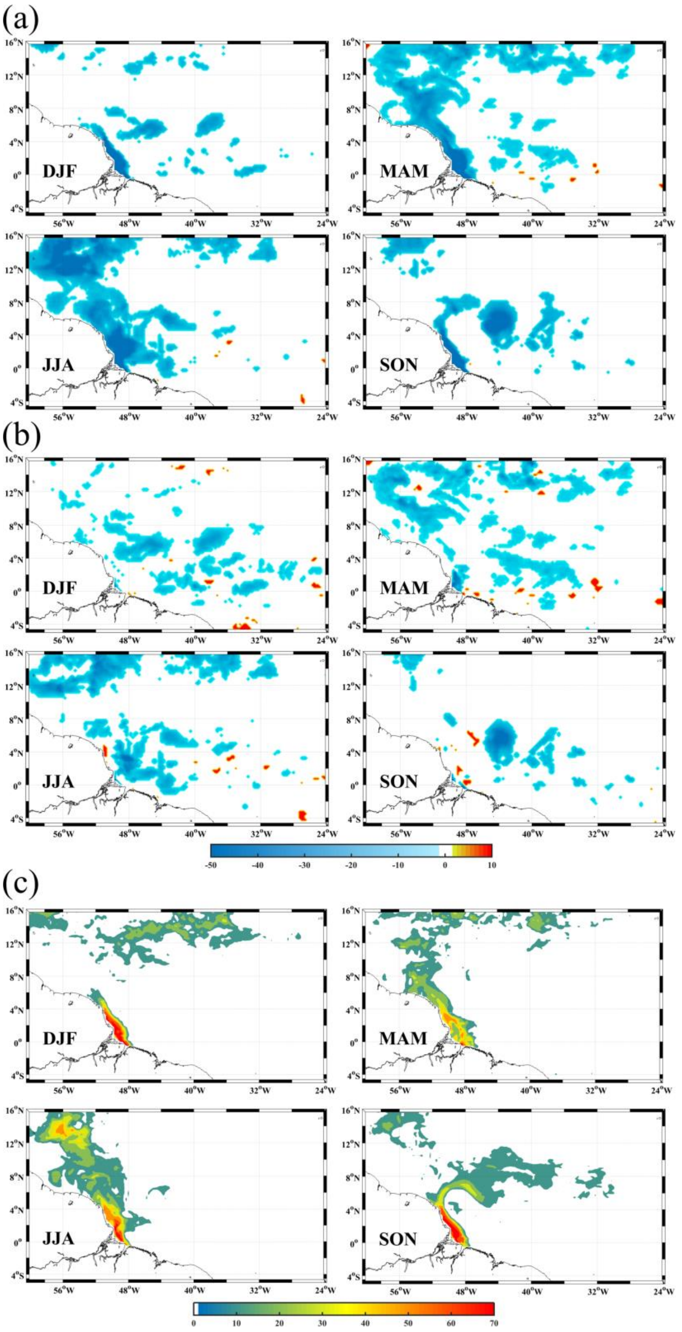

Figure 8: Seasonal evolution of the difference of: (a) MLD (m), (b) ILD (m), and (c) BLT (m) between the RRF (River discharges) and NRF (No-river discharges) simulations during boreal

winter (DJF: December, January, February), boreal spring (MAM: March, April, May), boreal summer (JJA: June, July, August), and boreal autumn (SON: September, October, November).

As presented for MLD and ILD, Fig. 8(c) shows the spatial distribution of the seasonally averaged differences of BLT distributions between the RRF and NRF experiments. The discharge of freshwater from the rivers plays a fundamental role in the formation of barrier layers along the extensions of the river plume spreading into the WTNA. The maximum difference in BLT is verified at the Amazon mouth extending north westward when the river plume is transported towards the Caribbean Sea. During boreal autumn (SON) the differences in BLT extend to the east following plume transport by the NECC. In the absence of rivers, the BL is almost non-existent in the plume area, and we find 100% of the BLT in the range of 1−35 m. In the RRF experiment the BLT reaches 82−94 m in the DFJ, MAM and JJA periods and up to 110 m in boreal autumn (SON). Similar magnitudes and BLT distributions were reported by the in situ observations of Pailler et al. (1999) and Silva et al. (2005, 2009b and 2010).

It is expected that space and time modifications to temperature distribution due to river inflows should also induce changes in oceanic heat content (OHC) in the WTNA. Simulation results indicate that higher accumulations of heat in the ILD without rivers varied from 1.1 to $1.3 \cdot 10^{10}\,Jm^{-2}$, whereas the maximum values of OHC in the RRF experiment ranged from 1.0 to $1.2 \cdot 10^{10}\,Jm^{-2}$. Fig. 9 presents the seasonally averaged differences in OHC between the simulations with and without rivers (RRF-NRF) indicating that rivers reduce oceanic heat storage, in particular along the plume spreading areas. The largest differences ranged between -0.7 and $-0.3 \cdot 10^{10}\,Jm^{-2}$, during the periods of MAM, JJA and SON, confirming that variation in ILD is the main factor influencing the OHC difference between the RRF and NRF experiments.

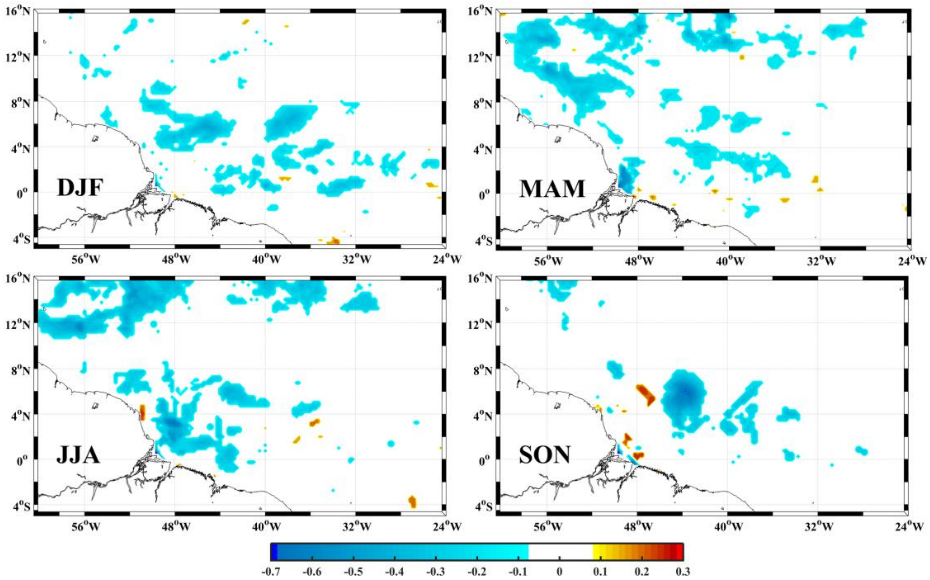

Figure 9: Mean seasonal cycle of difference in *OHC* ($J\ m^{-2}$) integrated from Z_{REF} to *ILD*. Boreal winter (DJF: December, January, February), boreal spring (MAM: March, April, May), boreal summer (JJA: June, July, August), and boreal autumn (SON: September, October, November).

3.2.2 Impact on ocean circulation and changes to NBC and NECC

Fig. 10 shows the differences in ocean surface circulation between numerical results obtained from the RRF and NRF scenarios. The seasonal cycle provides evidence of the rivers’ impact on the WTNA regions under the influence of freshwater plumes (NBC retroflection and NECC areas). Stronger surface velocities are present from June to November and a well-defined meandering/ring structure is highlighted from September to November. These differences (reaching 1 ms^{-1}) emphasize the role of the Amazon river plume in the dynamics of the NBC-NECC system, including NBC retroflection, formation of NBC rings and eastward NECC meandering/transport.

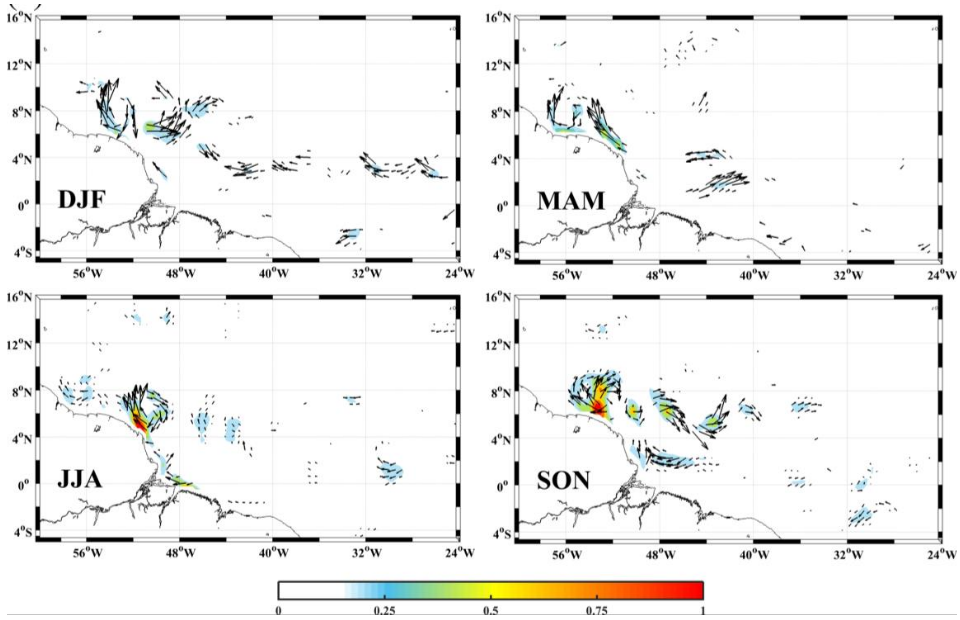

Figure 10: Seasonal evolution of the difference in surface currents (ms^{-1}) between the RRF (River discharges) and NRF (No-river discharges) simulations during boreal winter (DJF: December, January, February), boreal spring (MAM: March, April, May), boreal summer (JJA: June, July, August), and boreal autumn (SON: September, October, November).

To evaluate the influence of Amazon inflow on the dynamics of the NBC retroflection we compare the evolution of the longitudinally averaged (REG1 limits 48-45°W) zonal component of the surface currents obtained from the RRF and NRF experiments (Fig. 11(a) RRF and (b) NRF). The results show overall similar patterns in both simulations with the zonal current intensity reaching a maximum of 0.5 ms^{-1}. In both cases, stronger zonal velocity appears in January-February (between 7° and 8°N), with a core of less intense but still significant eastward transport centred at 9°N in March-April. However, during the second half of the year, when river discharges are stronger (Goulding et al., 2003; Barthem et al., 2004; Araujo et al., 2014), there is evidence for differences in the space and time evolution of zonal currents between the RRF and NRF scenarios. Although eastward currents start to occur in the middle of August in both scenarios, stronger and broader eastward transport is verified when the Amazon and Pará Rivers are considered. The period of maximum zonal current values is also different for both situations, whereas the cores of high eastward velocity are verified since the beginning of August in the RRF simulation; those maximum values are shifted to mid-September in the NRF case. The differences in intensity and space-time evolution of the zonal surface currents in the second part of the year reveals how river plumes change ocean circulation in the WTNA, in particular over the NBC retroflection area and the NECC pathway (see also Fig. 10).

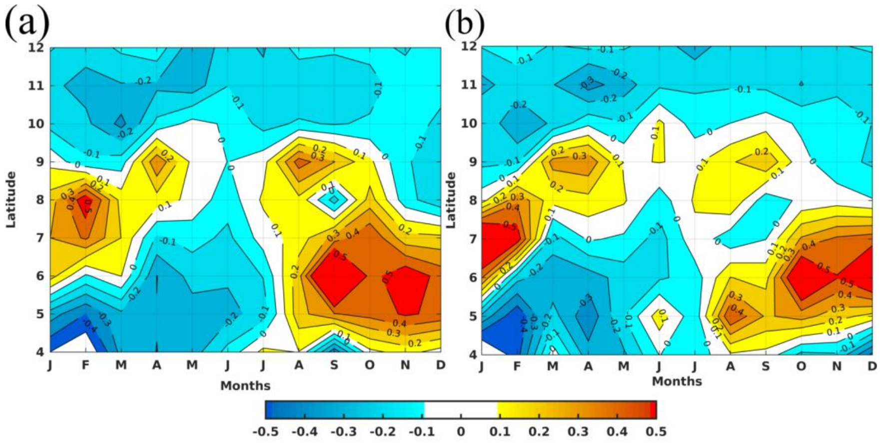

Figure 11: Hovmöller diagrams of the zonal component of surface velocity longitudinally averaged in the REG1 limits (48-45°W): (a) RRF scenario (River discharges); (b) NRF scenario (No-river discharges).

4 Conclusions

This study uses observations and numerical modelling to investigate the influence of the Amazon and Pará Rivers' discharge on the surface ocean circulation and thermohaline variability in the Western Tropical North Atlantic Ocean (WTNA). Regional climatological modelling is used to conduct two numerical experiments with (RRF) and without (NRF) continental freshwater inflow. Our analyses focused on the impact of rivers on the circulation (NBC-NECC system) and temperature/salinity distribution that induce changes in the isothermal/mixed/barrier layer formation and oceanic heat content.

The model results considering real situations (with rivers) are in good agreement with previous observations and reanalysis efforts, showing similar patterns of thermohaline distribution and ocean surface circulation in the WTNA. The rivers' impact on sea surface salinity variability is evident. The space and time variability of SSS in the area of the NBC retroflection and NECC is clearly identified, showing a confinement of the lower salinity waters near the coast from December to February and spreading eastward along the NECC pathway from September to November. The SST fields change near the Amazon River mouths, reducing the salinity by approximately 8 psu.

A warm core of SST is concentrated at the left side of the Amazon mouth from September to November, following the NBC retroflection area, due to the influence of warmer river temperature. However, in the open ocean, SST changes are not significantly sensitive to river discharges.

The computed differences between the RRF (Rivers discharges) and NRF (No-rivers discharges) scenarios indicate a strong impact of river plumes on ocean circulation in the WTNA. Compared to the NRF experiment, the RRF experiment increases the surface current up to 1 ms^{-1}. Stronger velocity occurs from June to November and well-defined meandering/ring generation structures are highlighted from September to November. The results also emphasize the role of the Amazon plume in the dynamics of the NBC retroflection, as well as in the eastward NECC transport. The comparisons of longitudinally averaged zonal components of surface currents in the NBC retroflection area for the RRF and NRF experiments show overall similar patterns during the first half of the year, when river discharges are lower. However, during the second semester, the beginning of maximum eastward transport (zonal currents reaching 0.5 ms^{-1}) is two months delayed in the absence of continental inflows, and is also weaker and limited to a narrower latitude band compared to the observed RRF scenario.

The Amazon and Pará Rivers also impact the isothermal/mixed/barrier layer dynamics in the WTNA. Induced MLD and ILD are 20−50 m shallower over the entire extension of the river plumes when river discharges are considered, resulting in the maximum BLT at the river mouths, extending north westward as the plume is transported towards the Caribbean during boreal spring and summer. Higher values of BLT are observed along the zonal NECC pathway during boreal autumn, after eastward NBC retroflection.

Changes in near surface thermohaline structure drive oceanic heat content. The results indicate that modifications in isothermal/mixed/barrier layers due to river input result in less oceanic heat storage in the WTNA. Differences up to $0.1 \cdot 10^{10}\, Jm^{-2}$ are verified in the large portion of the Western Tropical North Atlantic occupied by less salty plume waters.

In summary, the results indicate the Amazon and Pará Rivers' discharges impact the thermohaline structure in the WTNA as follows: (i) modifying seasonal salt distribution variability in the river plume area, (ii) inducing shallower Mixed and Isothermal layers as a response to salinity changes, (iii) enhancing Barrier Layer formation and increasing its depth, and (iv) reducing Ocean Heat storage capacity. Furthermore, ocean surface circulation is modified by the following factors: (v) anticipating the NBC retroflection (by about two months), and (vi) enhancing the eastward NECC transport/spreading of low salinity water into the central tropical Atlantic.

Considering all the evidence for the influence of the Amazon and Pará Rivers on the dynamics of the WTNA Ocean, it seems interesting as a next step to investigate the effects of these physical alterations and of the riverine nutrient and organic material contributions on the biogeochemical cycles of the Western Tropical North Atlantic region. In this case, in addition to the analyses of observations and in situ measurements, the use of coupled physical-biogeochemical modelling appears to be an exciting research method to be explored.

Acknowledgements

The first author thanks to Human Resources Program (PRH-47) of the Agência Nacional do Petróleo (ANP) for the concession of PhD scholarships. This paper is a contribution of the Brazilian Research Network on Global Climate Change, FINEP/ Rede CLIMA Grant Number 01.13.0353-00. The authors thank to the Brazilian National Institute of Science and Technology for Tropical Marine Environments“ INCT AmbTropic (CNPq/FABESB grants 565054/2010-4 and 8936/2011), the Project Simulating the Amazon River Plume and its Impact using Climate Models, Grant CAPES-TAMU 003440/2015-00, the Project Modeling the light field in the waters of Equatorial Atlantic under the effects of the Amazon River discharge: implication to biogeochemical processes and primary production, MEC/MCTI/CAPES/CNPq/FAPs Grant: 401326/2012-8; D. V. thanks to Project ProdPluma - Modelo Regional de Produtividade PrimÃ¡ria da Pluma do Amazonas (CNPq grant 460687/2014-0).

References

Akuetevi, C.Q.C., Wirth, A., 2015. Dynamics of turbulent western-boundary currents at low latitude in a shallow-water model. Ocean Science 11, 471–481. doi: 10.5194/os-11-471-2015.

Antonov, J., Seidov, D., Boyer, T., Locarnini, R., Mishonov, A., Garcia, H., Baranova, O., Zweng, M., Johnson, D., 2010. World Ocean Atlas 2009, vol. 2: Salinity, edited by: Levitus. S., NOAA Atlas NESDIS 69, 184.

Araujo, M., Noriega, C. E. D., Lefèvre, N., 2014. Nutrients and carbon fluxes in the estuaries of major rivers flowing into the tropical Atlantic. Frontiers in Marine Science, 1:10, doi: 10.3389/fmars.2014.00010.

Araujo, M., Noriega, C., Hounsou-Gbo, G. A., Veleda, D., Araujo, J., Bruto, L., Feitosa, F., Flores-Montes, M., Lefèvre, N., Melo, P., Otsuka, A., Travassos, K., Schwamborn, R., Neumann-Leitão, S., 2017. A Synoptic Assessment of the Amazon River-Ocean Continuum during Boreal Autumn: From Physics to Plankton Communities and Carbon Flux. Frontiers in Microbiology, doi: 10.3389/fmicb.2017.01358.

Balaguru, K., Chang, P., Saravanan, R., Leung, L.R., Xu, Z., Li, M., Hsieh, J.S., 2012. Ocean barrier layers' effect on tropical cyclone intensification. Proceedings of the National Academy of Sciences 109, 14343–14347.

Barthem, R.B., Charvet-Almeida, P., Montag, L.F.A., Lanna, E., 2004. Amazon Basin, GIWA Regional assessment 40b. UNEP .

Bourlès, B., Gouriou, Y., Chuchla, R., 1999b. On the circulation in the upper layer of the western Equatorial Atlantic. Journal of Geophysical Research 104, 21151–21170.

Bourlès, B., Molinari, R.L., Johns, E., Wilson, W.D., Leaman, K.D., 1999a. Upper layer currents in the western tropical North Atlantic (1989-1991). Journal of Geophysical Research 104, 1361–1375.

Bourlès, B., Lumpkin, R., McPhaden, M. J., Hernandez, F., Nobre, P., Campos, E., Yu, L., Planton, S., Busalacchi, A. J.,Moura, A. D., Servain, J., Trotte, J., 2008: The PIRATA Program: History, Accomplishments, and Future Directions. Bulletin of the American Meteorological Society, doi: 10.1175/2008BAMS2462.1

de Boyer Montégut, C., Madec, G., Fischer, A.S., Lazar, A., Iudicone, D., 2004. Mixed layer depth over the global ocean: An examination of profile data and a profile-based climatology. Journal of Geophysical Research 109, C12003.

de Boyer Montégut, C., Mignot, J., Lazar, A., Cravatte, S., 2007. Control of salinity on the mixed layer depth in the world ocean: 1. General description. Journal of Geophysical Research: Oceans 112.

Carton, J.A., Chepurin, G., Cao, X., 2000a. A Simple Ocean Data Assimilation Analysis of the Global Upper Ocean 1950–95. Part I: Methodology. Journal of Physical Oceanography 30, 294–309, doi:10.1175/1520-0485.

Carton, J.A., Chepurin, G., Cao, X., 2000b. A Simple Ocean Data Assimilation Analysis of the Global Upper Ocean 1950–95. Part II: Results. Journal of Physical Oceanography 30, 311–326, doi: 10.1175/1520-0485.

Carton, J.A., Giese, B.S., 2008. A reanalysis of ocean climate using Simple Ocean Data Assimilation (SODA). Monthly Weather Review 136, 2999–3017. doi:10.1175/2007MWR1978.1.

Castelão, G.P., Johns, W.E., 2011. The sea-surface structure of North Brazil Current Rings derived from shipboard and moored acoustic Doppler current profiler observations. Journal of Geophysical Research 116.

Coles, V.J., Brooks, M.T., Hopkins, J., Stukel, M.R., Yager, P.L., Hood, R.R., 2013. The pathways and properties of the Amazon river plume in the tropical North Atlantic Ocean. Journal of Geophysical Research C: Oceans 118, 6894–6913.

Cooley, S.R., Coles, V.J., Subramaniam, A., Yager, P.L., 2007. Seasonal variations in the Amazon plume-related atmospheric carbon sink. Global Biogeochemical Cycles 21, 1–15.

Da Silva, A., Young, A.C., Levitus, S., 1994. Atlas of sur face marine data 1994, volume 1: Algorithms and procedures. Technical Report 6. NOAA, NESDIS.

Dai, A., Trenberth, K.E., 2002. Estimates of Freshwater Discharge from Continents: Latitudinal and Seasonal Variations. Journal of Hydrometeorology, 3, 660–687, doi: 10.1175/1525-7541.

D'Onofrio, E., Oreiro, F., Fiore, M., 2012. Simplified empirical astronomical tide model—An application for the Río de la Plata estuary. Computers & Geosciences 44, 196–202.

Egbert, G.D., Bennett, A.F., Foreman, M.G.G., 1994. TOPEX/POSEIDON tides estimated using a global inverse model. Journal of Geophysical Research: Oceans 99, 24821–24852.

Egbert, G.D., Erofeeva, S.Y., 2002. Efficient inverse modeling of barotropic ocean tides. Journal of Oceanic and Atmospheric Technology 19, 183–204.

Ferry, N., Reverdin, G., 2004. Sea surface salinity interannual variability in the western tropical Atlantic: An ocean general circulation model study. Journal of Geophysical Research: Oceans 109, 1–11. doi:10.1029/2003JC002122.

Ffield, A., 2007. Amazon and Orinoco River Plumes and NBC Rings: Bystanders or Participants in Hurricane Events? Journal of Climate 20, 316–333.

Foltz, G.R., Schmid, C., Lumpkin, R., 2015. Transport of Surface Freshwater from the Equatorial to the Subtropical North Atlantic Ocean. Journal of Physical Oceanography 45, 1086–1102.

Fratantoni, D.M., Glickson, D.a., 2002. North Brazil Current Ring Generation and Evolution Observed with SeaWiFS*. Journal of Physical Oceanography 32, 1058–1074.

Fratantoni, D.M., Richardson, P.L., 2006. The evolution and demise of North Brazil Current rings. Journal of Physical Oceanography 36, 1241–1264.

Garzoli, S.L., Ffield, A., Johns, W.E., Yao, Q., 2004. North Brazil Current retroflection and transports. Journal of Geophysical Research 109, 1–14.

Goulding, M., Barthem, R., Ferreira, E., 2003. Smithsonian Atlas of the Amazon. Smithsonian Institution Press. 1 edition.

Grodsky, S.A., Reul, N., Lagerloef, G., Reverdin, G., Carton, J.A., Chapron, B., Quilfen, Y., Kudryavtsev, V.N., Kao, H.Y., 2012. Haline hurricane wake in the Amazon/Orinoco plume: AQUARIUS/SACD and SMOS observations. Geophysical Research Letters 39, 4–11.

Grodsky, S.A., Reverdin, G., Carton, J.A., Coles, V.J., 2014. Year-to-year salinity changes in the Amazon plume: Contrasting 2011 and 2012 Aquarius/SACD and SMOS satellite data. Remote Sensing of Environment 140, 14–22.

Haidvogel, D., Arango, H., Hedstrom, K., Beckmann, A., Malanotte-Rizzoli, P., Shchepetkin, A., 2000. Model evaluation experiments in the North Atlantic basin: Simulations in nonlinear terrain-following coordinates. Dynamics of Atmospheres and Oceans 32, 239–282.

Hu, C., Montgomery, E.T., Schmitt, R.W., Muller-Karger, F.E., 2004. The dispersal of the Amazon and Orinoco River water in the tropical Atlantic and Caribbean Sea: Observation from space and S-PALACE floats. Deep Sea Research Part II: Topical Studies in Oceanography 51, 1151–1171.

Ibánhez, J.S.P., Flores, M., Lefèvre, N., 2017. Collapse of the tropical and subtropical North Atlantic CO_2 sink in boreal spring of 2010. Scientific Reports 7, 41694. doi:10.1038/srep41694.

Jayne, S.R., Wahr, J.M., Bryan, F.O., 2003. Observing ocean heat content using satellite gravity and altimetry. Journal of Geophysical Research: Oceans 108, doi:10.1029/2002JC001619.

Johns, W., Lee, T., Schott, F., Zantopp, R., Evans, R., 1990. The North Brazil Current Retroflection: Seasonal Structure and Eddy Variability. Journal of Geophysical Research 95, 22103–22120.

Johns, W.E., Lee, T.N., Beardsley, R.C., Candela, J., Limeburner, R., Castro, B., 1998. Annual cycle and variability of the North Brazil Current. Journal of Physical Oceanography 28, 103–128.

Korosov, A., Counillon, F., Johannessen, J.A., 2015. Monitoring the spreading of the Amazon freshwater plume by MODIS, SMOS, Aquarius, and TOPAZ. Journal of Geophysical Research C: Oceans 120, 268–283.

Lefèvre, N., Diverrès, D., Gallois, F., 2010. Origin of CO_2 undersaturation in the western tropical Atlantic. Tellus B 62, 595–607.

Lentz, S.J., 1995. The Amazon River Plume during AMASSEDS: Subtidal current variability and the importance of wind forcing. Journal of Geophysical Research C: Oceans 100, 2377–2390.

Levitus, S., Antonov, J., Boyer, T., 2005. Warming of the world ocean, 1955–2003. Geophysical Research Letters 32.

Locarnini, R., Mishonov, A., Antonov, J., Boyer, T., Garcia, H., Baranova, O., Zweng, M., Johnson, D., 2010. World Ocean Atlas 2009, vol. 1, Temperature, edited by S. Levitus, 184 pp. US Gov. Print. Off., Washington, DC .

Maximenko, N., Hafner, J., 2010. SCUD: Surface CUrrents form Diagnostic model. IPRC Technical Note No. 5. International Pacific Research Center - School of Ocean and Earth Science and Technology - University of Hawaii http://iprc.soest.hawaii.edu/users/hafner/NIKOLAI/SCUD/BAK/SCUD_manual_02_16.pdf.

Müller-Karger, F.E., McClain, C.R., Fisher, T.R., Esaias, W.E., Varela, R., 1989. Pigment distribution in the Caribbean Sea Observations from space. Progress in Oceanography 23, 23–64.

Müller-Krager, F.E., McClain, C.R., Richardson, P.L., 1988. The dispersal of the Amazons water. Nature 333, 56–59.

Newinger, C., Toumi, R., 2015. Potential impact of the colored Amazon and Orinoco plume on tropical cyclone intensity. Journal of Geophysical Research: Oceans 120, 1296–1317.

Pailler, K., Bourlès, B., Gouriou, Y., 1999. The barrier layer in the western tropical Atlantic Ocean. Geophysical Research Letters 26, 2069–2072.

Panzer, I., Lines, S., Mak, J., Choboter, P., Lupo, C., 2013. High Performance Regional Ocean Modeling with GPU Acceleration. IEEE/MTS OCEANS .

Penven, P., Roy, C., Colin de Verrdière, A., Largier, J., 2000. Simulation of a coastal jet retention process using a barotropic model. Oceanologica Acta 23, 615–634.

Richardson, P.L., Hufford, G.E., Limeburner, R., Brown, W.S., 1994. North Brazil Current retroflection eddies. Journal of Geophysical Research 99, 5081–5093.

Richardson, P.L., Reverdin, G., 1987. Seasonal cycle of velocity in the Atlantic North Equatorial Countercurrent as measured by surface drifters, current meters, and ship drifts. Journal of Geophysical Research: Oceans 92, 3691–3708.

Salisbury, J., Vandemark, D., Campbell, J., Hunt, C., Wisser, D., Reul, N., Chapron, B., 2011. Spatial and temporal coherence between Amazon River discharge, salinity, and light absorption by colored organic carbon in western tropical Atlantic surface waters. Journal of Geophysical Research 116, C00H02.

Schmidt, A.C.K., Science, M., Brickley, P., Marine, H., 2011. A Feature Oriented Regional Modeling System for the North Brazil Current Rings Migration after Retroflection. Offshore Technology Conference .

Schmitz Jr., W.J., McCartney, M.S., 1993. On the North Atlantic Circulation. Reviews of Geophysics 31, 29–49.

Schott, F.A., Dengler, M., Brandt, P., Affler, K., Fischer, J., Bourlès, B., Gouriou, Y., Molinari, R.L., Rhein, M., 2003. The zonal currents and transports at 35 W in the tropical Atlantic. Geophysical Research Letters 30, 1349.

Servain, J., Busalacchi, A.J., Mcphaden, M.J., Moura, A.D., Reverdin, G., Vianna, M., Zebiak, S.E., 1998. A pilot research moored array in the tropical Atlantic (PIRATA). Bulletin of the American Meteorological Society 79, 2019–2031.

Sharma, N., Anderson, S.P., Brickley, P., Nobre, C., Cadwallader, M.L., 2009. Quantifying the Seasonal and Interannual Variability of the Formation and Migration Pattern of North Brazil Current Rings, in: OCEANS 2009, MTS/IEEE Biloxi-Marine Technology for Our Future: Global and Local Challenges, IEEE. pp. 1–7.

Shchepetkin, A.F., McWilliams, J.C., 2005. The regional oceanic modeling system (ROMS): a split-explicit, free-surface, topography-following-coordinates oceanic model. Ocean Modelling 9, 347–404.

Silva, A. C., Araujo, M., Medeiros, C., Silva, M., Bourlès, B., 2005. Seasonal changes in the mixed and barrier layers in the western equatorial Atlantic. Brazilian Journal of Oceanography 53(3/4), 83-98.

Silva, M., Araujo, M., Servain, J., Penven, P., Lentini, C.A.D., 2009a. High-resolution regional ocean dynamics simulation in the southwestern tropical Atlantic. Ocean Modelling 30, 256–269.

Silva, A. C., Bourlès, B., Araujo, M., 2009b. Circulation of the thermocline salinity maximum waters off the Northern Brazil as inferred from in situ measurements and numerical results. Annales Geophysicae 27, 1861-1873.

Silva, A. C., Araujo, M., Bourlès, B., 2010. Seasonal variability of the Amazon River plume during REVIZEE Program. Tropical Oceanography 38, 70-81.

Smith, W.H.F., Sandwell, D.T., 1997. Global sea floor topography from satellite altimetry and ship depth soundings. Science 277, 1956–1962.

Song, Y., Haidvogel, D.B., 1994. A Semi-implicit Ocean Circulation Model Using a Generalized Topography-following Coordinate System. J. Comput. Phys. 115, 228–244. doi:10.1006/jcph.1994.1189.

Sprintall, J., Tomczak, M., 1992. Evidence of the barrier layer in the surface layer of the tropics. Journal of Geophysical Research: Oceans 97, 7305–7316.

Stramma, L., Rhein, M., Brandt, P., Dengler, M., Böning, C., Walter, M., 2005. Upper ocean circulation in the western tropical Atlantic in boreal fall 2000. Deep Sea Research Part I: Oceanographic Research Papers 52, 221–240.

Stukel, M.R., Coles, V.J., Brooks, M.T., Hood, R.R., 2014. Top-down, bottom-up and physical controls on diatom-diazotroph assemblage growth in the Amazon River plume. Biogeosciences 11, 3259–3278.

Subramaniam, A., Yager, P.L., Carpenter, E.J., Mahaffey, C., Björkman, K., Cooley, S., Kustka, A.B., Montoya, J.P., Sañudo-Wilhelmy, S.A., Shipe, R., Capone, D.G., 2008. Amazon River enhances diazotrophy and carbon sequestration in the tropical North Atlantic Ocean.

Proceedings of the National Academy of Sciences of the United States of America 105, 10460–5.

Tchamabi, C. C., Araujo, M., Silva, M., Bourlès, B., 2017. A study of the Brazilian Fernando de Noronha Island and Rocas Atoll wakes in the tropical Atlantic. Ocean Modelling, doi: 10.1016/j.ocemod.2016.12.009.

Veleda, D., Araujo, M., Zantopp, R., Montagne, R., 2012. Intraseasonal variability of the North Brazil Undercurrent forced by remote winds. Journal of Geophysical Research 117, C11024.

Wang, Y., 2004. Ocean Tide Modeling in the Southern Ocean. Technical Report 471. Department of Civil and Environmental Engineering and Geodetic Science. The Ohio State University. Columbus, Ohio.

Xie, S.P., Carton, J.A., 2004. Tropical Atlantic variability: Patterns, mechanisms, and impacts. Earths Climate: The Ocean–Atmosphere Interaction, Geophys. Monogr. 147, Amer. Geophys. Union 100, 121–142. doi:10.1029/147GM07.

Yeung, L. Y., Berelson, W. M., Young, E. D., Prokopenko, M. G., Rollins, N., Coles, V. J., Montoya, J. P., Carpenter, E. J., Steinberg, D. K., Foster, R. A., Capone, D. G., Yager, P. L., 2012. Impact of diatom-diazotroph associations on carbon export in the Amazon River plume. Geophysical Research Letters, 39, doi:10.1029/2012GL053356.